Effects of retrogressive thaw slumping on particulate organic carbon dynamics in the Northwest Territories, Canada

by

Sarah Shakil

A thesis submitted in partial fulfillment of the requirements for the degree of

Doctor of Philosophy

in

Ecology

Department of Biological Sciences

University of Alberta

ABSTRACT

Climate change is increasing the frequency and intensity of thermokarst and accelerating the delivery of terrestrial organic material from previously sequestered sources to aquatic systems, where it is subject to further biochemical alteration. Rapid climate change in the glacially conditioned ice-rich and ice-marginal terrain of the Peel Plateau, western Canada, is accelerating thaw-driven mass wasting in the form of retrogressive thaw slumps, which are rapidly increasing in area, volume and thickness of permafrost thawed. Permafrost thaw can mobilize substantial amounts of organic carbon to streams where it can be decomposed to greenhouse gases during transport or re-sequestered in sediments. While studies have shown that organic carbon in dissolved form can be readily decomposed in aquatic systems, a substantial portion of organic carbon released to aquatic systems because of permafrost thaw can also occur in particulate form. Few studies have examined how permafrost thaw can alter the composition of particulate organic material in aquatic systems, and none have properly assessed the degree to which the organic carbon portion of this particulate organic matter (POC) can be decomposed. The purpose of this thesis is to examine the mobilization (Chapter 2), in-stream processing (Chapter 3), and downstream transport (Chapter 4) of POC from thaw slumps. We found that organic carbon mobilized to streams from thaw slumps can increase by orders of magnitude, though the magnitude of increase varies substantially in relation to slump morphology, stream power, and landscape position. Furthermore, increases in organic carbon are almost entirely due to mobilization of POC which is relatively more recalcitrant than organic carbon in unaffected streams (Chapter 1). Experiments provide further evidence that slump-mobilized POC is resistant to biodegradation in stream water and mineral-associated processes (e.g., sorption, chemoautolithotrophy) could act to protect and sequester carbon (Chapter 2). Finally, while material eroded by slumps can exceed the

transport capacity of streams creating centuries to millennial scale sedimentary deposits in valley bottoms (Chapter 1), the order of magnitude increases in TOC can be sustained for kilometers downstream and have likely resulted in a regime shift in the Peel River organic carbon loads (Chapter 3). This research highlights particle flux as a key variable in the release of permafrost carbon from abrupt thaw. Targeted quantification of the multitude of biotic and abiotic processes acting on the carbon, organic matter, and minerals associated with these particles will be of critical importance in accurately predicting the affect of continued regional permafrost erosion on the carbon cycle and aquatic systems affected.

PREFACE

This work was a component of Dr. Suzanne Tank's research program investigating permafrost thaw, land-water linkages, and carbon cycling in the western Canadian Arctic. Each chapter in this thesis reflects collaborative efforts between many colleagues participating in or collaborating with this program, including partnerships between academic and government researchers, that have resulted in manuscripts published, in-review, or in preparation for submission to peer-reviewed journals. Chapters are structured in accordance with the guidance provided by the journals to which they are or will be submitted to. For all chapters, Sarah Shakil led the design, data collection, analyses, and writing under the supervision of Dr. Suzanne E. Tank. Further details on author contributions are provided within each chapter.

Chapter 2: Shakil S, Tank SE, Kokelj SV, Vonk, JE, Zolkos S. 2020. Particulate dominance of organic carbon mobilization from thaw slumps on the Peel Plateau, NT: Quantification and implications for stream systems and permafrost carbon release, *Environmental Research Letters*, 15, 114019. https://doi.org/10.1088/1748-9326/abac36

> ***Dataset:*** *Shakil S, Tank S, Kokelj SV, Zolkos S. 2020. The effect of retrogressive thaw slumps on the delivery of organic matter and nutrients to downstream freshwater systems in the Peel Plateau region, Northwest Territories. Waterloo, Canada: Canadian Cryospheric Information Network (CCIN). https://doi.org/10.21963/13160*

Chapter 3: Shakil S, Tank SE, Vonk JE, Zolkos S. In Review. Low biodegradability of particulate organic carbon mobilized from thaw slumps on the Peel Plateau, NT, and possible chemosynthesis and sorption effects, *Biogeosciences Discussions*. https://doi.org/10.5194/bg-2021-150

> ***Dataset:*** *Shakil, S., Tank, S., Vonk, J. & Zolkos, S. 2021. Incubation Data Assessing Biodegradability of Organic Carbon Mobilized from Permafrost Thaw Slumps (Peel Plateau, NT, Canada). Waterloo, Canada: Canadian Cryospheric Information Network (CCIN). https://doi.org/10.21963/13237*

Chapter 4: Shakil S, Tank SE, Kokelj SV, Vonk JE, Zolkos S, Kokoszka J. Downstream persistence of particulate organic carbon released from permafrost thaw slumps. In preparation for submission to *Journal of Geophysical Research: Biogeosciences*.

> ***Dataset:*** *To be made available in Polar Data Catalogue*

DEDICATION

Dedicated to

زبیده اصغر علی (۱۹۲٦ - ۲۰۱۸)
Zubeda Asgharali (1926 – 2018)

اصغر علی غلام حسین (۱۹۱۷ - ۲۰۰۳)
Asghar Ali Ghulam Hussain (1917 – 2003)

خدیجة محمد حسین وهره (۱۹۲۵ - ۱۹۷۳)
Khadija Mohammed Husain Vora (1925 – 1973)

محمد حسین تراب علی وهره (۱۹۱۵ - ۲۰۰۱)
Mohammed Husain Turabali Vora (1915 – 2001)

This thesis was written by ساره شکیل

Shakil, Fatima, and Bastian helped write out the names here.

ACKNOWLEDGEMENTS

Fieldwork for this research took place within the Gwich'in settlement region. Thank you to the Teetł'it Gwich'in community at Fort McPherson who allowed us to stay within their community for weeks to months at a time across multiple summers. Thank you to Christine Firth, Elizabeth Jerome, Billy Wilson, Dempster Colin, Andrew Koe, and Keith Colin, who were invaluable guides to field sites, assisted with measurements, and provided thoughtful conversation and insight into the nature of the watersheds we visited. Thank you to staff at the Tetlit Renewable Resource Council in Fort McPherson, at the Aurora Research Institute, Western Arctic Research Centre for their vital logistical support with a special thanks to Bessie Rogers, Erika Hille, Jolie Gareis, and Hailey Verbonac. Many funding sources made this research possible: NSERC Discovery Grant and Northern Supplement, the Polar Continental Shelf Program, Environment and Climate Change Canada, the Northern Scientific Training Program, UAlberta North, the Weston Family Foundation, the Arctic Institute of North America. Personal funding was provided through NSERC CGS-M and CGS-D, Queen Elizabeth II Graduate Scholarships, the Weston Award for Northern Research, Walter H. John's Graduate Fellowship, the UofA's Master's Scholarship, the MSc and PhD recruitment awards, and the Green and Gold Student Leadership and Professional Development Grant (travel support for the Radiocarbon Training Program).

Thank you to my supervisor, Dr. Suzanne Tank, a key support for most of my academic career, and a door-opener to the world of research. Thank you to my supervisory committee, Dr. Jorien Vonk and Dr. Rolf Vinebrook, for their time, expertise, and continuous encouragement and to members of my candidacy and defense committee, Dr. Alberto Reyes, Dr. Kevin Devito, Dr. Dolly Kothawala, for their enthusiasm in discussing my research. Dr. Steve Kokelj and his colleagues, including Justin Kokoszka, Jurjen van der Sluijs, and Dr. John Tunnicliffe, and other staff at the NWT Geological Survey provided an important geomorphic and landscape-level perspective for this work. Shawne Kokelj provided meteorological data used in this thesis.

The rotator in chapter 3 was created by Technical Services staff in the Department of Mechanical Engineering, supervised by Roger Marchand. Staff at the Biogeochemical Analytical Service Laboratory, the UC Davis Stable Isotope Facility, and the Andre Lalonde Radiocarbon Facility and Jan Veizer Laboratory at the University of Ottawa provided invaluable high quality analytical services critical for this thesis and were always friendly and open to providing advice

for tricky samples. The Radiocarbon Training Program at the Andre Lalonde Radiocarbon Facility gave me hands-on training in radiocarbon analysis of POC and sediments. Thank you as well to many lab group technicians: Jennifer Lloyd (critical support in setting up multiple instruments), Christine Ridenour, Maria Cavaco. Thank you to our field and lab assistants: Luke Gjini, Joyce Kendon, Maya Guttman, Lindsey Stephen, Erin MacDonald, Rosemin Nathoo. Special thanks to J. Kendon and M. Guttman for enduring through many troublesome experiments. Thank you to staff at the BioSci storeroom for shipping and purchasing support and at Information Services & Technology for technological support. Thank you to Tom Hantos for lab safety tips including autoclave training, and Jeff Johnston (BioSci Fab-Lab) for creation of field and lab equipment. Thank you to many lab members from multiple groups over the years, including Cara Littlefair and Chelsea Willis (submitting time-sensitive field samples and advocates for enjoying life outside of work); Kyra St. Pierre (so many things); Melodie Kunegel (models, stats, R); Jessica Serbu and Sasiri Bandara (lab tips); Scott Zolkos; and many others.

Thank you to Dr. Kathy Young and Dr. Anna Abnizova for providing me with my first opportunity in research and their encouragement to continue, and many friends who helped make environmental sciences fun (including Tina Chiu, Kenneth Abas, and Osamah Ali). Thank you to each person I've crossed paths with during this degree that has brightly coloured this journey, helped beyond any expectation, inspired me to think bigger, triggered laughter when it was most needed (and even when not!), and has had to deal with multiple office drop ins and e-mail follow-ups. To individually name each person would go beyond the 2-page acknowledgement limit I'm allowed (!) but know that I am grateful.

Finally, thank you to my

siblings, Sakina, Ali, Husain, and Bastian,

and the many people beyond I am lucky to call family. Most importantly, thank you to my

parents, Fatima Shakil and Shakil Asgharali,

who somehow got us to adulthood.

TABLE OF CONTENTS

LIST OF TABLES

LIST OF FIGURES

Chapter 1. General Introduction

1.1. Background

1.1.1. Global Climate Change, the Cryosphere, and the Arctic

Human activity has warmed the climate at a rate that is unprecedented in at least the last 2,000 years, due to increased greenhouse gas concentrations in the atmosphere (Gulev et al. 2021, IPCC 2021). Current best estimates suggest that atmospheric carbon dioxide, methane, and nitrous oxide concentrations have increased by 47%, 156%, and 23% since 1750 (Gulev et al. 2021, IPCC 2021) and that human activity has increased the global surface temperature by 1.07°C from the period of 1850-1900 to the period of 2010-2019 (IPCC 2021). The consequences of these changes to the Earth's climate system are already being felt in every inhabited region of the globe, through multiple changes including weather and climate extremes (Seneviratne et al. 2021; IPCC 2021).

The cryosphere, frozen components of the Earth system, has been particularly responsive to global warming with changes occurring that can directly and indirectly affect all of Earth's inhabitants. Over the last few decades, warming has caused mass loss in ice sheets and glaciers, reductions in snow cover, Arctic Sea ice extent and thickness, and increases in permafrost temperatures (IPCC 2019). Many of the changes that are being observed (e.g., glacial retreat and reduction in Arctic Sea ice extent) are unprecedented over many centuries to many thousands of years (IPCC 2021). Over the last two decades, Arctic surface air temperature has increased at more than double the global average, a phenomenon, known as Arctic amplification, that occurs due to multiple positive feedback mechanisms (e.g., land surface and ocean albedo) as the Arctic atmosphere, ocean, and land surfaces change in response to warming (Meredith et al. 2019). Change in the region is already directly impacting the ~4 million people living permanently in the Arctic region (IPCC 2019). In addition, as an integral part of the Earth system, changes in the Arctic will move through shared ocean, atmosphere, and ecological and social systems to affect inhabitants across the world.

1.1.2. Permafrost thaw and carbon

Frozen ground can typically be considered within three categories: (a) the active layer near the surface which thaws and refreezes every summer and winter respectively; (b) permafrost,

defined as ground (rock, soil, ice) at a temperature of <0°C for at least 2 consecutive years; and (c) a transient layer with a higher ice content than the active layer that has likely alternated in and out of permafrost over decades to centuries (French 2013). The permafrost zone, where permafrost coverage ranges sporadic and isolated patches of permafrost to "continuous permafrost", occupies ~24% of the exposed land surface in the Northern Hemisphere (Brown et al. 2002). However, presence of permafrost is not static. Its depth and extent are dependent on regional and global climate conditions, dynamics of ecosystems and their ecological succession, and human activities (Schuur and Mack 2018). Current permafrost extents in the Arctic are projected to decrease with continued climate warming (IPCC 2021, Chadburn et al. 2017, Hjort et al. 2018).

Over millennia, low soil temperatures, poor drainage, cryoturbation in high latitudes has enabled the accumulation of a globally significant pool of soil organic carbon (SOC) within the permafrost region (Hugelius et al. 2014, Davidson and Janssens 2006). The current best estimates suggest that the total permafrost region SOC stock is ~1460 to 1600 PgC, of which 800 – 1000 PgC is contained within perennially frozen soils (Hugelius et al. 2014). This is almost double the carbon currently estimated to be within the atmosphere (~850 ± 10 Pg C, Ussiri et al. 2017) and more than double the estimates for carbon contained within global forest above-ground biomass (~426 – 571 Pg, Santoro et al. 2021). Thaw and exposure of this organic carbon to accelerated mineralization to greenhouse gases may result in permafrost thaw acting as a significant source of carbon dioxide and methane (Schuur et al. 2015). Recent estimates suggest that emissions only from gradual permafrost thaw (see below) could be up to 150 Pg C by 2100 if climate mitigation policies are weak (Natali et al. 2021). Even with strong mitigation efforts, emission have been projected to range from ~6 to 118 Pg C by 2100 (Natali et al. 2021). However, there is low confidence in the timing and magnitude of this release, with much of this uncertainty associated with uncertainty and lack of representation of the diverse ways in which permafrost thaw can manifest (e.g., abrupt thaw, IPCC AR6, Technical Summary pg 60). If this source of carbon is not fully accounted for in climate mitigation efforts, the remaining allowable carbon budget that makes it probable to limit warming to 1.5°C or 2°C could be overshot (Natali et al. 2021).

The nature of permafrost thaw, composition of carbon contained within soils, and the environment that organic carbon is released to after thaw varies substantially across the Arctic. This variability, in part, is based on variability in permafrost ice-content, landscape relief,

permafrost extent, parent material, and geologic history (Tank et al. 2020). Two categories have emerged to characterize major differences in the rate at which permafrost will thaw and expose carbon stocks contained within: press vs. pulse disturbances. Gradual changes in the thermal regime as the climate warms (i.e., active layer deepening) is often referred to as a "press" disturbance (Schuur and Mack 2018). This gradual thaw will provide access to previously frozen materials at the top of the permafrost table that can differ in composition from the active layer ranging from being more mineral rich to a greater accumulation of organics (e.g., Lacelle et al. 2014, Keller et al. 2010, Strauss et al. 2017). In contrast, rapid thaw caused by, for example, the thaw of ice-rich ground and the formation of thermokarst, is often characterized as "pulse" disturbance, and are still not fully represented in Earth system models. This type of permafrost thaw can manifest in diverse ways (Kokelj and Jorgensen 2013) and when occurring on hillslopes can dramatically increase the erosion of terrestrial materials to streams (Kokelj et al. 2013). Although this marked increase in sediment will carry with it particle-associated carbon and nutrients, there has been little direct investigation of how this change will affect the broader carbon cycle. Some estimates suggest that abrupt thaw processes could be equivalent to 40% of the emissions from gradual thaw (Turetsky et al. 2020), and therefore not accounting for abrupt thaw processes may substantially underestimate the amount of carbon released with permafrost thaw.

1.1.3. Land-to-ocean linkages and the importance of inland waters within the global carbon budget

The Arctic Ocean watershed encompasses over 15% of the global terrestrial landmass and this landmass is experiencing some of the most rapid changes in response to global warming (Tank et al 2012, IPCC 2019, also see section 1.1.1). The stream and river networks that drain these landscapes carry signals of change occurring across their watersheds. The Arctic Ocean contains only 1% of the global ocean volume, yet it receives ~11% of global river discharge (McClelland et al. 2012). As a result, water, heat, and terrestrial materials delivered via river inputs can have a greater effect on the Arctic Ocean than in any other ocean basin and changes in these fluxes can have significant effects on the physical structure (e.g., stratification), energy balance, and food web dynamics of the Arctic Ocean (e.g. IPCC 2019; Terhaar et al. 2021). Climate model simulations project a warmer and wetter Arctic (Krasting et al. 2013 in Meredith et al. 2019), including intensification of precipitation across northern watersheds (Meredith et al. 2019).

Between 1976 and 2017, discharge has been increasing by 3.3 ± 1.6 % in Eurasian and 2.0 ± 1.8 % in North American rivers flowing into the Arctic Ocean (Holmes et al. 2018, Meredith et al. 2019). In combination with widespread landscape changes across the Arctic, including permafrost thaw, the flow of materials to the Arctic Ocean can be significantly affected.

In addition to being important linkages between terrestrial and marine systems, streams and rivers are also important active components of global biogeochemical cycles themselves (Battin et al. 2009, Cole et al. 2007, Aufdenkamp et al. 2011). Studies have increasingly shown that lateral export of carbon is an important component of the net ecosystem exchange of terrestrial systems and not accounting for them can result in discrepancies in the scale of the terrestrial carbon sink (Cole et al. 2007). Changes in vegetation combined with increasing disturbances such as wildfires and thawing permafrost can significantly affect the carbon balance of high latitude regions. Accounting for the lateral fluxes and processing of carbon in inland waters is necessary to determine how these changes will affect the regional and global carbon balance (e.g., Hutchins et al. 2020, Karlsson et al. 2021, Kondo et al. 2019) and is still a major knowledge gap.

1.1.4. Particulate Organic Carbon

Organic carbon in inland waters is extremely chemically diverse and exists across a size spectrum (Simon et al. 2002) but is often separated into two categories: particulate organic carbon (POC) and dissolved organic carbon (DOC). These two fractions of organic carbon are often defined based on the pore size of filters used to separate the dissolved and particulate fraction, typically ranging from 0.45 - 1 μm. Studies examining the impact of permafrost thaw on organic matter composition and biodegradability in streams have almost exclusively examined changes in the dissolved phase (Vonk et al. 2015). Many studies have shown that permafrost thaw can release DOC that is highly biodegradable (Abbott et al. 2014, Spencer et al. 2015, Littlefair and Tank 2018). In some landscapes, this elevated lability has been attributed to preservation and/or accumulation of biolabile compounds in permafrost (Ewin et al. 2015, Strauss et al. 2017), while in others it may be due in part to biochemical processes occurring when multiple soil profiles mix prior to delivery to stream systems (Littlefair and Tank 2018). However, the elevated lability of permafrost-derived organic matter is not consistent throughout the Arctic (Burd et al. 2020, Wickland et al. 2018), highlighting the need to contextualize the fate of organic matter mobilized by permafrost thaw in relation to landscape state factors (Tank et al. 2020).

Organic matter and carbon in particulate form is a further complication. Accessibility of carbon associated with particles can be reduced compared to material in the dissolved phase (Battin et al. 2008), potentially in part due to higher energy costs as enzymatic dissolution is required or due to physical protection via mineral association (Opfergelt et al. 2020, Einarsdóttir et al. 2020). However, these particles can be hotspots of microbial activity that can be missed if studies only focus on material in the dissolved phase (Attermeyer et al. 2018). The combination of most of the organic carbon mobilized from hillslope thermokarst features being in the form of POC (Vonk et al. 2013), combined with the paucity of studies examining the mobilization and fate of particulate material from thawing permafrost, leaves the assessment of the mobilization and fate of POC a major knowledge gap in our understanding of the effects of permafrost thaw on carbon release and northern streams and rivers.

1.1.5. A Hotspot of Change: The Peel Plateau

Rising air temperature and intensification of precipitation has accelerated retrogressive thaw slump activity and the degradation of ice-rich terrain in landscapes positioned along former glacial margins (Kokelj et al. 2017, Segal et al. 2016). Situated at the former western limit of the Laurentide Ice Sheet (Kokelj et al. 2017), the Peel Plateau is underlain by ice-rich permafrost that is highly susceptible to collapse and the formation of hillslope thermokarst features, namely retrogressive thaw slumps (Kokelj et al. 2015, Kokelj et al. 2021). From 1986 – 2018 climate-driven permafrost erosion via retrogressive thaw slumping has increased by two orders of magnitude (Kokelj et al. 2021). Much of this thaw driven mass wasting has occurred along first and second order stream networks that eventually drain into the Arctic Ocean (Kokelj et al. 2021). In particular, the Peel Plateau is a major hot spot of climate-driven mass wasting occurring along headwater streams (Kokelj et al. 2021).

1.2. Objectives

To address knowledge gaps in our understanding of the effect of permafrost thaw on northern freshwater systems and the permafrost carbon-climate feedback I undertook a series of studies within the watersheds of the Peel Plateau, in the western Canadian Arctic. I focused on quantifying and characterizing the release of POC to stream systems because of retrogressive thaw slump

activity, and the fate of this carbon. These studies focused on three main objectives addressed individually in three data chapters:

Chapter 2: Assess the impacts of retrogressive thaw slumps on the delivery of organic matter to the immediate downstream environment, and the relative importance of carbon delivery in the dissolved vs. particulate phase

Chapter 3: Experimentally test the extent to which POC mobilized by thaw slumps can be mineralized to carbon dioxide vs. re-sequestered in downstream sediments

Chapter 4: Examine the degree to which POC mobilized by thaw slumps is available for transport downstream and can contribute to organic carbon fluxes in the Peel River

Finally, **Chapter 5** summarizes the research present throughout, and discusses the implications of this work as change continues with global warming along with potential avenues for future research.

Chapter 2. Particulate dominance of organic carbon mobilization from permafrost thaw slumps on the Peel Plateau, NT

2.0. Summary

Climate change is increasing the frequency and intensity of thermokarst, and accelerating the delivery of terrestrial organic material from previously sequestered sources to aquatic systems, where it is subject to further biochemical alteration. Rapid climate change in the glacially conditioned ice-rich and ice-marginal terrain of the Peel Plateau, western Canada, is accelerating thaw-driven mass wasting in the form of retrogressive thaw slumps, which are rapidly increasing in area, volume and thickness of permafrost thawed. Despite major perturbation of downstream sedimentary and geochemical fluxes, few studies have examined changes in flux and composition of particulate organic carbon (POC) in streams and rivers as a result of permafrost thaw. Here we show that the orders of magnitude increase in total organic carbon, nitrogen, and phosphorus mobilized to streams from thaw slumps on the Peel Plateau is almost entirely due to POC and associated particulate nitrogen and phosphorus release. Slump-mobilized POC is compositionally distinct from its dissolved counterpart and appears to contain relatively greater amounts of degraded organic matter, as inferred from base-extracted fluorescence of particulate organic matter. Thus, slump mobilized POC is potentially more recalcitrant than POC present in non-slump affected stream networks. Furthermore, a substantial portion of POC mobilized from thaw slumps will be constrained within primary sediment stores in valley bottoms, where net accumulation is currently exceeding net erosion, resulting in century to millennial scale sequestration of thermokarst-mobilized POC. This study highlights the pressing need for better knowledge of sedimentary cascades, mobilization, and storage reservoirs in slump-affected streams, and baseline assessments of the biodegradability of POC and cycling of particulate nutrients within a sedimentary cascade framework. Explicit incorporation of POC dynamics into our understanding of land-water carbon mobilization in the face of permafrost thaw is critical for understanding implications of thermokarst for regional carbon cycling and fluvial ecosystems.

2.1. Introduction

Abrupt climate-driven permafrost thaw (i.e. thermokarst) is prevalent across the circumpolar north (Olefeldt et al 2016, Kokelj et al 2017a) and is accelerating in ice-rich glaciated landscapes

(Segal et al 2016, Lewkowicz and Way 2019). Degradation of ice-rich ground liberates sequestered materials, saturates thawing soils and sediments, and enables mixing of various soil layers that may substantially differ in composition (Vonk et al 2015, Kokelj et al 2015, Lacelle et al 2019). Thermokarst on slopes can rapidly translocate large volumes (102 to 106 m^3) of previously frozen materials downslope (Kokelj et al 2015, van der Sluijs et al 2018) to new storage reservoirs in valley bottoms where material is subject to fluvial erosion and entrainment (Kokelj et al 2013), thereby exposing material to light, dissolution, and microbial degradation (Vonk et al 2015).

The growing need to include thermokarst processes (Kokelj and Jorgenson 2013) into Earth system or land surface models (Turetsky et al 2020) has advanced research on quantifying carbon storage in thermokarst landscapes (Olefeldt et al 2016, Fuchs et al 2018, 2019) and measuring carbon fluxes and composition from thermokarst features (Vonk et al 2015, Littlefair et al 2017, Tanski et al 2017, Ramage et al 2018). However, studies on organic carbon mobilization from thermokarst features have predominantly focused on dissolved organic carbon (DOC) (e.g. Mann et al 2015, Abbott et al 2015, Littlefair et al 2017), with effects varying from orders of magnitude increases in concentrations (Manning et al 2015) to little response or a decrease in concentrations (Littlefair et al 2017) due to a combination of landscape state factors that control organic matter accumulation in permafrost and its release (Ewing et al 2015, Mu et al 2017, Tank et al 2020). Most work examining thermokarst-mobilized particulate organic carbon (POC) flux has focused on coastal erosion (Vonk et al 2012, Tanski et al 2017, Ramage et al 2018), and studies detecting signatures of permafrost thaw in major northern rivers (Guo and Macdonald 2006, Guo et al 2007, Wild et al 2019, Bröder et al 2020), the latter of which have noted POC is more aged than dissolved or colloidal phases, thus reflecting a greater degree of mobilization from deeper permafrost deposits. Although work on Melville Island has shown that active layer detachments can increase the delivery of aged POC to stream networks (Lamoureux and Lafreniere 2014, Beel et al 2020), studies on POC mobilization in fluvial systems is extremely limited.

Organic matter is a vital source of energy and nutrients to the microbial base of aquatic food webs (Manning et al 2015). The composition of organic matter, such as its C: N: P stoichiometry, molecular structure, and degree of mineral association, can impact the relative importance of carbon transfer through food webs, relative to mineralization to CO2 (Sardans et al 2012, Manning et al 2015, Welti et al 2017). Thermokarst may alter the relative abundance of organic matter from different sources (Wauthy et al 2018) and phases (particulate vs. dissolved)

in recipient systems. If sources of organic carbon differ substantially in their composition, then rapid transfer of terrestrial material via thermokarst processes may have the potential to abruptly alter energy transfer to and through aquatic systems. 'Autochthonous' organic matter, derived from living material in the stream channel (e.g. algae) is generally considered to be more labile and of greater nutritional quality for upper trophic levels than terrestrial organic matter, partly due to the lower carbon-to-nutrient ratios, higher algal polyunsaturated fatty-acid content, and the complex amorphous structure of terrestrial organic matter (Guo et al 2016, Brett et al 2017). However, the origin and nature of terrestrial deposits can vary. Lipid degradation proxies have suggested that permafrost-sourced particulate organic matter (POM) in the Kolyma river is more labile than POM in a headwater stream with POM dominated by in-stream production and recent vegetative sources (Bröder et al 2020). Pautler et al (2010) also found elevated microbial activity in soil organic matter redistributed by active layer detachments on Melville Island, suggesting the release of labile soil organic matter from thawing permafrost. Many studies have found permafrost-derived DOC to be more biodegradable than relatively more modern DOC present in adjacent aquatic systems (Abbottet al 2014, Spencer et al 2015, Littlefair and Tank 2018). In some landscapes, this elevated lability has been attributed to the preservation and/or accumulation of biolabile compounds in permafrost (Ewing et al 2015, Strauss et al 2017), while in others it may be due in part to biochemical processes occurring when multiple soil profiles mix prior to delivery to stream systems (Littlefair and Tank 2018). However, the elevated lability of permafrost-derived organic matter is not consistent throughout the Arctic (Burd et al 2020, Wickland et al 2018) highlighting the need for contextualizing the fate of organic matter mobilized by permafrost thaw in relation to landscape state factors that may control the diagenetic state of terrestrial organic matter and how it is released during thaw (Tank et al 2020). But assessments on thermokarst-mobilized organic matter composition and lability are dominantly made for the dissolved phase. Across boreal aquatic ecosystems, POC can have significantly elevated mineralization rates relative to DOC (Attermeyer et al 2018), which suggest assessments based on DOC could be inaccurate for total organic carbon pools if POM and associated POC are the dominant form of organic matter and carbon mobilized to recipient aquatic systems.

One of the most dramatic forms of thermokarst is the retrogressive thaw slump (henceforth 'thaw slump'). Thaw slumps occur at high densities in glacially conditioned permafrost landscapes including ice-marginal moraine systems, and glaciofluvial, glaciolacustrine, and glaciomarine

deposits (Rudy et al 2017, Kokelj et al 2017a, Ward Jones et al 2019). Thaw slumps develop as ice-rich permafrost thaws and collapses, and saturated materials flow over sloping terrain, transporting material downslope to streams, lakes, or coastal environments. These dynamic thermokarst systems predominantly affect low order streams where they overwhelm transport capacity and can transform long-term sediment flux (Kokelj et al 2017a, Kokelj et al under review). On the Peel Plateau in the western Canadian Arctic, a warming and wetting climate has intensified thaw slump activity (Kokeljet al 2015, Segalet al 2016). The region has one of the highest density of large thaw slumps in northwestern Canada with most features occurring in headwater streams of east-flowing tributaries of the Peel River (Kokelj et al 2017a). As thaw slumps erode hillslopes, they can increase sediment loads in streams by orders of magnitude (Kokelj et al 2013), and expose materials normally unavailable for transport to stream systems, such as glacial tills maintained in permafrost since the Pleistocene (Lacelle et al 2013, 2019). The degree to which thaw slumping changes the nature and quantity of organic matter mobilized to streams may depend on the characteristics of surficial materials and thickness of permafrost thawed, in addition to ground-ice content, topography, and intensity of climate conditions that drive slope thermokarst processes (Kokelj et al 2015, 2017a, Lacelle et al 2019).

Here, we target three key goals. First, we quantify the relative magnitude of POC vs. DOC mobilization to stream water columns on the Peel Plateau. Second, we assess how thaw slumping affects the source and composition of organic matter present in recipient streams. Third, we examine how changes in the quantity and composition of mobilized organic matter varies in relation to thaw slump morphology and landscape variation. We undertake this work across a series of thaw slump features that vary in their morphology and landscape position as it relates to the nature of materials mobilized by thaw. Assessing POC mobilization and its overall composition is critical to understand and predict the impacts of abrupt permafrost thaw on aquatic ecosystems and carbon cycling, and to advance our understanding of the biogeochemical effects of permafrost thaw within aquatic networks.

2.2. Methods

2.2.1. Study Region

The Peel Plateau is a 24 000 km2 glacially conditioned landscape characterized by ice-rich, fluvially incised terrain that is representative of other permafrost preserved glaciated landscapes across northwestern Canada, Alaska, and Siberia (Kokelj et al 2017b) (**Figure 2-1**). The headwaters of east flowing Peel River tributaries originate in mountainous unglaciated terrain where surficial materials are dominated by colluvium, and transition to glacial till with decreasing topographic relief towards the east (Duk-Rodkin and Hughes 1992, Kokelj et al 2017b). The transition from tundra to shrub to stunted boreal forest in lowlands is associated with the regional topographic gradient that generally occurs West to East (O'Neillet al 2015) and may affect the organic carbon content in active layer and Holocene-age permafrost (Dyke 2005).

The region's ice-rich, fluvially-incised landscape is characterized by a high density of thaw slumps (Segal et al 2016) compared to many glaciated permafrost landscapes to the east (Kokelj et al 2017b). In the late-Pleistocene (ca. 18, 000 to 15, 000 cal. yr. BP; Lacelle et al 2013), the region was briefly covered by the Laurentide Ice Sheet (LIS). During this time, glacial tills, glaciofluvial and glaciolacustrine materials were deposited in a dynamic ice-marginal setting (Lacelle et al 2013) and preserved as permafrost was established following glacial retreat (Lacelle et al 2004, 2013). Early Holocene warming was associated with an increase in active layer thickness to ~1.5 fold that of present-day conditions (ca. 9000 cal. yrs. BP, Burn et al 1997), and an acceleration of mass-wasting (e.g. thaw slumping) and development of colluvial deposits. These processes enabled soil formation, geochemical modification and the incorporation of organics to the depths of maximum thaw, followed by a cooling period and upwards aggradation of the permafrost table (Lacelle et al 2019). These modified deposits have been preserved in a 'relict-thaw layer' situated immediately below present-day active layer soils, distinguished from the unmodified tills below by a thaw unconformity (Lacelle et al 2019). Thus, the relict-thaw layer can be comprised of a paleo-active layer and/or sediments deposited at the base of a hillslope from past slumping activity (colluvial deposits, Lacelle et al 2019).

Considering this history, we refer to three main categories of terrestrial material eroded by thaw slumps: (1) the currrent active layer, where soil has developed from the relict-thaw layer; (2) Holocene-age permafrost containing previously thawed diamicton (relict-active layer) and colluvium (slumped sediments); and (3) Pleistocene-age permafrost containing tills that have remained preserved within permafrost. Headwall height, scar zone area, and debris tongue length

(**Figure 2-2**a–b) vary by orders of magnitude (**Table 2-1**, Kokelj et al under review), potentially affecting the relative contributions of different sources exposed in headwalls and their delivery to streams.

2.2.2. Site selection

Eight thaw slump sites were selected for sampling within the Stony Creek and Vittrekwa River watersheds on the Peel Plateau (**Figure 2-1**, **Table 2-1**). Sites were selected based on the following criteria in order of importance: (1) connection of channelized runoff to a stream network; (2) provision of a range of variation in slump morphology; and (3) availability of data from previous studies to build on a baseline body of knowledge (Kokelj et al 2013, Littlefair et al 2017). This selection was constrained by accessibility of sites due to the remote location of the region. The Stony Creek and Vittrekwa watershed were targeted due to the ability to access sites from the Dempster Highway.

Sites were visited two to three times from June to August 2015. Samples were obtained from: channelized runoff within each thaw slump (IN); a downstream location where all channelized runoff entered the valley-bottom stream (DN); and an unimpacted reference stream that was usually directly upstream of the slump inflow (UP). FM2-UP is an exception being an unimpacted tributary flowing into the downstream sampling point, but not directly upstream. Given the requirement for unimpacted upstream sites, all sites are located on independent subcatchments with the exception that FM2-DN is downstream of FM3-DN. Downstream locations typically integrated channelized runoff and materials entrained by channel erosion of the debris tongue, along with potentially enhanced sideslope erosion (Kokelj et al 2015, van der Sluijs et al 2018).

2.2.3. Stream sample collection

Water samples were collected in pre-acid-leached high-density polyethylene (HDPE) bottles or DI-leached low-density polyethylene (LDPE) cubitainers when greater volumes were needed for suspended particulate parameters. Both containers were triple sample-rinsed. Due to high sediment loads, water samples for dissolved constituents were allowed to settle for ~24 h prior to vacuum filtration (following Littlefair et al 2017) through pre-combusted glass fibre filters (Whatman, GF/F, 0.7 µm). Dissolved constituents included DOC, total dissolved nitrogen (TDN)

and phosphorus (TDP), dissolved inorganic nitrogen (DIN: NH_4^+ & NO_3^- + NO_2^-), and soluble reactive phosphorus (SRP). Dissolved organic nitrogen (DON; TDN-DIN) and organic phosphorus (DOP; TDP-SRP) were calculated from measured nutrient species. Any DOP concentrations below the limit of quantitation for TDP (4.9 µg l^{-1}) were replaced with half the limit's value (supplementary S1.2). Suspended particulate material was collected on pre-weighed and pre-combusted (450◦C, 5 h) glass fibre filters (Whatman, GF/F) within 24 h of collection and stored frozen for analysis of POC & POδ^{13}C, particulate nitrogen (PN) & Pδ^{15}N, particulate organic phosphorus (POP), and PO^{14}C. PO^{14}C samples were collected from three of our eight sites (FM2, FM3, SD, capturing slump morphology range; **Table 2-1**) on pre-combusted (500 ◦C, 5 h) quartz fibre filters (Whatman, QM/A, 2.2 µm). In 2016, sites accessible by foot (5 of 8) were re-visited to obtain samples to measure optical characteristics of base-extracted particulate organic matter (BEPOM) (Osburn et al 2012, Brym et al 2014). For further details on sample collection, see Appendix A1.1.

2.2.4. Quantification of organic carbon delivery (Goal 1)

We calculated instantaneous yields of POC, DOC, and total organic carbon (TOC) upstream and downstream of thaw slumps using paired measurements of constituent concentration and stream discharge, and watershed areas delineated in ArcGIS (A1.4.3). We determined slump effects on TOC yields with linear mixed effects models using the R package lme4 (Bates et al 2015; supplementary S5). We included random slope and random intercept terms, accounting for repeated measures by allowing the slope (i.e. slump effect) and intercept to vary per slump site.

2.2.5. Source contributions to stream organic carbon (Goal 2)

Stream periphyton and headwall samples were collected at six slump sites in 2017 for POδ13C end member values (Appendix A1.6). Headwall sources consisted of an upper active layer (O-horizon), lower active layer (resembling A and/or B soil horizons), and Holocene and Pleistocene permafrost. Headwall samples were additionally analyzed for Pδ15N, and %POC, %PN, and %POP. FM2 and FM3 headwalls were also sampled for PO14C to match 2015 stream PO14C. Contributions of sources to upstream, within, and downstream POC were quantified using a dual carbon (13C, 14C) mixing model (MixSIAR, Stock et al 2018; A1.7).

2.2.6. Assessment of compositional changes in particulate organic material via geochemical analyses (Goal 2)

We used linear mixed effects models (Appendix A1.5) to examine slumping effects on: POC:PN and POC:POP stoichiometry (Sardans et al 2012, Manning et al 2015); POδ^{13}C and Pδ^{15}N, used as metrics of organic matter source (Finlay and Kendall 2008) and stage of decay (^{13}C enrichment via anaerobic decomposition; Gundelwein et al 2007); and percent POC (%POC; as POC:TSS), used as a metric of organic carbon content of sediments. We further examined DOC:DON and DOC:DOP ratios to compare the dissolved and particulate response. We used principal components analysis (PCA) to (a) build upon our linear mixed models and assess broad patterns in geochemical parameters across sites, and (b) compare the geochemical composition of streamwater particulate organic matter (POM) to headwall sources (2.2.1). Variables with highly skewed and non-normal distributions were transformed prior to analysis.

2.2.7. Assessments of compositional changes via optical analyses of base-extracted particulate organic matter (BEPOM) (Goal 2)

Absorbance and fluorescence spectra of BEPOM were analysed following Osburn et al (2012) and Brym et al (2014). We calculated spectral slopes, slope ratios (SR), and total absorbance from 250–450 nm per unit of suspended sediment ($a_{tot/TSS}$, Helms et al 2008, Brym et al 2014) as proxies for molecular weight and relative quantity of extractable chromophoric organic matter per unit of sediment. A parallel factor analysis (PARAFAC) model was fit to excitation-emission matrices (drEEM toolbox in MATLAB; Murphy et al 2013) to resolve fluorescent components associated with fluorescent organic matter pools with different bulk molecular structure. To increase the sample size for a more robust model, samples collected upstream, within, and downstream of thaw slump sites in 2016 (n=17) were combined with samples collected in 2017 from streams with and without active slumps in the watershed across the Stony Creek and Vittrekwa (n = 39; thus n_{total} = 56). Further details regarding PARAFAC are in (Appendix A1.2.4).

Relative contribution of components to sample fluorescence was determined by normalizing maximum fluorescence intensities (F_{max}) of each component to the sum of component intensities for a given sample (%C = $F_{max}/(\sum F_{max})$). Excitation-emission matrices were corrected and smoothed prior to any calculations and modelling. Further details are in A1.2. To aid component interpretations, we calculated commonly-used fluorescence indices (Table A2-5,

A1.2.5), and assessed relationships between these indices and our PARAFAC components using PCA, transforming any highly skewed or non-normal variables (A1.3.2). Follow-up analyses on variables of interest were conducted using repeated measures ANOVA (A1.8).

2.2.8. Landscape and environmental controls on composition and delivery (Goal 3)

We used a linear model (*lm()* in R) to examine the relative importance of morphological, meteorological, and landscape effects on variation in upstream vs. within and upstream vs. downstream comparisons (i.e. slump effects) across slump sites. Slump effects were represented by extracting the random slopes per slump site from the aforementioned linear mixed effects models of TOC yield (2.2.4) and %POC (2.2.6, **Table 2-2**). We ran two separate models for upstream vs. within and upstream vs. downstream random slopes. Explanatory variables consisted of: debris tongue length and maximum headwall height (morphological effects; Littlefair et al 2017, Zolkos et al 2019); total rainfall over the 96 h preceding sampling (meteorological effects; Kokelj et al 2015); and longitude of slump site and stream power immediately downstream of the RTS (landscape effects). Maximum slope across the scar zone to immediate valley bottom was also used as a landscape variable for the TOC yield model. Through our study design we attempted to control meteorological variation by sampling all sites close in time, but meteorological variables were included to account for the fact that sites were sampled on a series of sequential days. For further details on explanatory variables see A1.9.

2.3. Results

2.3.1. The effects of slumping on TOC and nutrient delivery to streams (Goal 1)

POC accounted for the majority of organic carbon present within the channelized runoff of slumps. Within-slump POC concentrations reached greater than 9000 mg l^{-1}, while the maximum DOC concentration recorded was 33.6 mg l^{-1}. Within-slump sediment concentrations at some sites (FM2, SE) accounted for 10%–30% of the water volume, further decreasing per-volume DOC estimates and increasing the importance of POC fluxes and yields. Instantaneous total organic carbon (TOC) yields increased, on average, by an order of magnitude downstream of thaw slumps ($p = 0.005$, **Table 2-2**, **Figure 2-2**a and d). Increases in POC yields accounted for 85%–100% of TOC increases, except for two out of three instances at SD, where POC accounted for 31% of TOC

increases, and in one instance, TOC yield decreased downstream by ~ 6 mg s^{-1} km^{-2} due to decreases in DOC yield (**Figure 2-2**a and e). In 43% of our observations, DOC yields decreased downstream of slumps. With the exception of site SD, the high concentrations of particles mobilized from within-slump shifted streams from being DOC to POC dominated (**Figure 2-2**a, **Figure 2-3**a and d).

Increases in suspended sediment delivery and associated PN and POP to streams also led to orders of magnitude increases in instantaneous total nitrogen (as TDN + PN) and phosphorus (as TDP + POP) yields (**Figure 2-2**b–c, **Figure 2-3**b–c). Greater DON and DOP concentrations within slumps relative to upstream did not result in elevated downstream concentrations relative to upstream (Figure **2-3**e–f). Across stream locations, POC:POP ratios were lower than DOC:DOP ratios (Figure **2-3**l). POC:PN ratios were also lower than DOC:DON and DOC:DIN ratios at all downstream locations with the exception of one sample downstream of SC (**Figure 2-3**j–k).

High DIN concentrations within slump runoff did result in elevated concentrations downstream, largely driven by increases in NH_4^+ (Figure **2-3**h). In contrast, no consistent difference was noted in SRP concentrations (**Figure 2-3**i). TDN:TDP ratios were often more than double the Redfield ratio of 16:1, a guideline for nutrient limitation in marine and freshwater systems (**Figure 2-3**g). With the exception of site SE, ratios were elevated within-slump, relative to upstream sites, sometimes leading to elevated ratios downstream relative to upstream (**Figure 2-3**g).

2.3.2. The effect of slumping on sources of stream POC and DOC (Goal 2)

Terrestrial sources accounted for upwards of 80% of POC upstream, within, and downstream of sites incorporated in the dual-carbon isotope model (SD, FM2, and FM3, **Figure 2-4**, Table A1-5). Across all eight sites, upstream POδ^{13}C was variable and sometimes more ^{13}C depleted than active layer sources (**Figure 2-5**b), indicating differing contributions from ^{13}C depleted in situ sources (i.e. periphyton, POδ^{13}C = −33.39 ± 4.19, mean ± SD) across sites. Slumping increased POC mobilization from both Pleistocene-age and Holocene-age permafrost, but POC from Pleistocene-age permafrost appeared to contribute more on average to within-slump and downstream POC (Figure **2-4**b). The small permafrost contributions to upstream POC are due to incorporation of FM3-UP in the model, which began to experience streambank erosion and has more ^{14}C-depleted POC than other upstream sites (**Figure 2-4**(a)). DOδ^{13}C (Zolkos et al 2018) and

DOΔ^{14}C (Littlefair et al 2017) suggest DOC is also predominantly terrestrial, with upstream DOC sourced from O-horizon soils (Figure **2-4**a). Similar to upstream POδ^{13}C, upstream DOδ^{13}C values were more ^{13}C depleted than within-slump DOδ^{13}C, suggesting relatively greater contributions from ^{13}C depleted periphyton to upstream DOC. However, within-slump DOC is relatively more ^{14}C-enriched than within-slump POC (i.e. younger; **Figure 2-4**a).

2.3.3. The effects of slumping on organic matter geochemical composition in streams (Goal 2)

Slumping effects on DOM and POM composition were most pronounced for POδ^{13}C and %POC. When compared to upstream values, within-slump runoff significantly differed in %POC, POδ^{13}C, POC:POP, DOC:DOP, and DOC:DON (**Table 2-2**). Differences in POC:PN and Pδ^{15}N could not be tested statistically. However, POC:PN ratios upstream (11.4 ± 2.7, mean± SD), within (11.6 ± 3.3), and downstream (10.8 ± 1.9) overlapped substantially (**Figure 2-3**k), as did Pδ^{15}N values upstream (1.53 ± 0.89), within (1.48 ± 0.67), and downstream (1.60 ± 0.40). When comparing downstream to upstream locations, only %POC and POδ^{13}C were significantly different (**Table 2-2**).

A principal components analysis of DOM and POM composition showed two major gradients (**Figure 2-5**a). Only %POC, POC:POP, POC:PN, and POδ^{13}C variables had arrow lengths greater than the circle of equilibrium for the PCA analysis. Therefore, these variables contributed the most to dispersion of sites in the reduced space and we focus on them for description of the gradients. PC1 (29%) clearly separated within-slump and downstream sites from upstream locations along a gradient that was indicative of variation in POM diagenetic state and periphytic contributions to POM, as indicated by %POC and POδ^{13}C. Along PC1, within-slump and downstream sites were more mineral- and ^{13}C-enriched relative to upstream sites, suggesting slump sediments had a greater proportion of degraded terrestrial material relative to fresher terrestrial material or in situ production (^{13}C depleted periphyton, **Figure 2-5**b) characteristic of POC upstream (**Figure 2-4**). No slump effect was apparent along PC2 (24%). Instead, PC2 reflected variation in POC: PN: POP stoichiometry. Runoff and upstream POM showed greater variability than downstream POM along this gradient, driven by nutrient-poor POM from active layer-dominated runoff (shallow slump SD) and an upstream site draining a catchment near the

mountains (SE). This variation disappears for downstream samples, where POM is more universally nutrient enriched.

Incorporating headwall end-member sources into a PCA of POM geochemistry resulted in similar gradients of organic matter diagenesis/in situ contribution (along %POC and POδ^{13}C; PC1) and nutrient composition (POC:POP and POC:PN; **Figure 2-5**b, PC2). Organic matter from Holocene and Pleistocene permafrost was compositionally indistinguishable between horizons and from most within-slump samples. The upper active layer (O-horizon) had a greater organic carbon content (%POC) than permafrost and lower active layer samples, was more closely associated with upstream and within-slump runoff samples from SD (the shallowest slump) and was generally more nutrient depleted than permafrost sources. Both upper and lower active layer sources had greater variability in POC:PN and POC:POP than permafrost sources, which clustered at the more nutrient enriched end of PC2. Decreasing C:N ratios from upper active layer to permafrost has also been noted by Lacelle et al (2019) and is attributed to carbon mineralization, and thus degradation of organic matter since production.

2.3.4. The effects of slumping on the optical properties of based-extracted POM (Goal 2)

Five components were identified by PARAFAC (Figure A**1-1**, Table A1-1) (available online at stacks. iop.org/ERL/15/114019/mmedia), and matched components reported in other studies at Tucker congruences exceeding 0.95 (C1–C4) and 0.90 (C5) (www.openfluor.org; Murphy et al 2014). C1–4 were associated with terrestrial humic-/fulvic-like peaks, while C5 was associated with a tyrosine-/protein-like peak (Table A1-1). Components 1–4 contributed upwards of 92% of Fmax upstream, within-slump, and downstream of slumps, in agreement with findings of terrestrial organic matter dominance from mixing model results. C2 is similar to a component previously described as soil fulvic-like (Table A1-1), and contributed similar proportions to Fmax upstream (18% ± 2 se), within (20% ± 3 se), and downstream (19% ± 1 se) of slumps.

A PCA of BEPOM-derived optical characteristics revealed two clear gradients (**Figure 2-5**c). The first was driven by contributions of C1, C3, and $a_{tot/TSS}$. Increasing $a_{tot/TSS}$ indicates greater chromophoric organic matter per unit sediment (i.e. Stubbins et al 2014), while C1 and C3 contrast two pools of terrestrial humic-like materials (see below). Along this gradient, within and downstream locations had greater values of %C1, but lower values of %C3 and $a_{tot/TSS}$ than

upstream locations. We found a significant difference in %C1, the variable most strongly associated with this gradient, between stream locations (repeated measures ANOVA, $F_{2,4} = 8.34$, $p = 0.011$) due to differences between upstream %C1 (29 ± 3 se) vs. within (43 ± 3 se) and downstream (40 ± 3 se) locations (least-squared means; Lenth 2016). The second gradient in PCA space separated more biogeochemically-processed material (indicated by HIX, peak A:B and C:B; Table A1-2) with greater molecular weight (SR, Helms et al 2008) from 'fresh' or protein-like organic material (%C5). Across all sites, within-slump and downstream locations tended to be most closely associated with the more processed end of this gradient (**Figure 2-5**c).

The %C1–%C3 gradient described above reinforces that slump sediments are more biogeochemically processed. C1 strongly resembles C1 of Stubbins et al (2014), which was identified as, 'an aggregation of highly diverse, relatively high molecular weight' terrigenous molecules that were 'carbon-rich and nitrogen poor'. In contrast, C3 resembles Stubbins-C3 and -C4 which both had greater nitrogen content, less conjugation or lower molecular weight, and greater homogeneity, suggesting these components have undergone less reworking since production. Thus, these results are consistent with inferences made from POM bulk geochemistry that within-slump and downstream material are relatively more degraded since production than upstream material (2.3.3).

2.3.5. The effects of morphological, meteorological, and landscape factors on slump-enabled changes in TOC yields and POM source and composition (Goal 3)

While TOC yields increased universally with slumping, this effect ranged from approximately two-fold to two orders of magnitude across sites (**Figure 2-2**a) in association with headwall height ($\beta_{std\text{-}height} = 0.366 \pm 0.062$, $p = 0.004$), stream power ($\beta_{std\text{-}spower} = 0.251 \pm 0.055$, $p = 0.011$), and increasing westward location on the Peel Plateau ($\beta_{std\text{-}long.} = -0.203 \pm 0.062$, $p = 0.031$). Headwall height ($\beta_{std\text{-}height} = 0.169 \pm 0.034$, $p = 0.007$, **Table 2-3**) and longitude ($\beta_{std\text{-}long} = -0.154 \pm 0.031$, $p = 0.008$, **Table 2-3**) were also significant predictors of differences in $(\%POC)^{-1}$ between upstream and within-slump locations. Upstream:within $(\%POC)^{-1}$ differences increased with increasing headwall height and westward location. In contrast, upstream: downstream variation in %POC was not explained by landscape or slump-associated variables, likely because %POC was less variable across downstream sites (**Figure 2-5**).

Contributions of permafrost-origin materials to within-slump and downstream POM increased with headwall height (**Figure 2-4**a, Table A1-5). Holocene- and Pleistocene-age permafrost contributions to downstream POC increased from 18.5 ± 18.5% and 14.4 ± 15%, respectively (mean ± se) at SD (~ 2 m max. height, **Table 2-1**) to 31.5 ± 34.4% and 50 ± 35.3% at FM3 (~10.3 m max. height) and 31.4 ± 32.1% and 49.6 ± 29.1% at FM2 (~25 m max. height). In particular, POC from Pleistocene-age permafrost doubled in contribution from SD to FM2. Within-slump POM molecular structure, inferred from BEPOM, also varied with headwall height, and this variation was similarly lost downstream. Within-slump BEPOM fluorescence ranged from being indistinguishable from upstream sites at the shallowest slump (SD), to being substantially enriched in %C1 at the largest features (FM2; **Table 2-1**; **Figure 2-5**c). This variation did not persist downstream as POM downstream of FM2 and SD became more similar to other slump sites.

2.4. Discussion

Slumping caused orders of magnitude increases in TOC and nutrient delivery to streams via the thaw-driven mobilization of sediments. This mobilization was dominantly in the form of POC, PN, and POP, shifting streams from dissolved to particulate dominated systems. Slumping increased permafrost organic carbon in stream networks, however within-slump POC values were more ^{14}C-depleted (older) than values previously recorded for DO^{14}C (**Figure 2-4**a), Littlefair et al 2017) indicating POC mobilizes a greater degree of aged organic matter from deeper permafrost deposits. Optical properties of base-extracted POM indicated slump-mobilized POM was more processed since production than material present upstream.

Slumping increased TOC yields to a greater degree at sites with greater maximum headwall height and downstream stream power. Increasing thickness of permafrost thawed, associated with headwall height, may increase hydrologic input from melting of massive ice (Rudy et al 2017) which can increase sediment transport at baseflow (Kokelj et al 2013). Across the Peel Plateau, headwall heights and the depth of permafrost thawed generally increase as slumping intensifies and connects to streams, with slump-stream connectivity typically occurring at maximum headwall heights greater than ~2 m (Kokelj et al under review). Thus, as slumping intensifies, stream TOC yields may increase due to increased delivery of POC. However, this increase will also depend on the stream's transportation potential (i.e. stream power), which we discuss further in 2.4.2. Landscape position also played an important role as TOC yields increased to a greater degree

westwards on the Peel Plateau, with closer proximity to late-glacial limits, where elevation and relative relief is greater, tundra vegetation is sparser, and fine-grained tills, with a greater abundance of glaciofluvial/glaciolacustrine deposits, are veneered over bedrock (Duk-Rodkin and Hughes 1992). Since maximum scar-valley slope was not a significant predictor of TOC yields, the combination of sparse vegetation and fine-grained, ice-rich deposits veneering bedrock appear to make the terrain near the western margin of the glacial limit particularly susceptible to thaw-driven erosion. Headwall height and landscape position also affected the organic carbon content of within-slump particles and divergence from upstream particles, with headwall height also increasing the proportion of more decayed organic matter of within-slump POM (2.3.5). However, we found no significant predictors of differences in composition between upstream and downstream %POC, and site variation in upstream-to-within BEPOM differences decreased downstream of thaw slumps, despite the fact that Holocene- and Pleistocene-age permafrost contributions to downstream POC were greater at sites with greater headwall heights. We discuss this further in section 2.4.3. Finally, though our study focused on actively eroding slumps, slump stabilization, which can occur if collapsed debris accumulates at the base of the headwall and insulates exposed ice (Kokelj et al 2015), was evident at FM4 where most of the headwall was not actively eroding during our sampling period. This may be why TOC concentrations did not increase substantially and within-slump POC, PN, and POP concentrations are more similar to SD, the smallest slump in this study. Notably, POC yields still increased downstream of slump FM4, likely due to stream erosion of the ~1 km debris tongue.

2.4.1. Significance of thermokarst-derived POC and implications for permafrost-carbon release and fate

Particulate dominance of organic carbon mobilization is likely common in hillslope thermokarst systems throughout the circumpolar Arctic, based on previous records of high POC and sediment concentrations within or downstream of thermokarst features in Siberia (Vonk et al 2013), the Eastern Canadian high Arctic (Lamoureux and Lafreniere 2014, Beel et al 2020), and Alaska (Bowden et al 2008). Furthermore, the Peel Plateau shares similarities to permafrost preserved glaciated landscapes observed to contain thaw slumps in Alaska and Siberia (Kokelj et al 2017a). Yet studies assessing controls on mobilization (Bröder et al 2020, Tanski et al 2017) and mineralization (Attermeyer et al 2018, Tanski et al 2019) of permafrost-origin POC are sparse,

particularly in comparison to DOC, despite particles being noted as important sites for carbon mineralization in streams (Attermeyer et al 2018), or, conversely, agents of carbon sequestration (Hemingway et al 2019).

On the Peel Plateau, slump-mobilized POC appears to be at a greater stage of decay than relatively more modern material present upstream, as inferred from depleted organic carbon content, and relative increase in a fluorescent component (C1) that has been described as a diverse array of relatively high molecular weight molecules (Stubbins et al 2014). This suggests reduced bioavailability of stream POC. This is in agreement with Lacelle et al (2019) where 13C NMR analysis of slump headwalls has shown that active layers contain young and more biodegradable forms of organic carbon (O-alkyl-C and narrow Alkyl-C), while undisturbed permafrost and relict-thaw layers, if not comprised of colluvium from past slumping, contain older and relatively more recalcitrant aromatic compounds. Calibrated dates of Pleistocene-age permafrost in this study are > 40 000 yrs B.P. (Table A1-4), in agreement with previous work that suggests a significant amount of soil organic carbon within Pleistocene-age permafrost likely originates from regional vegetation growing prior to the advance of the LIS (Lacelle et al 2019). However, shale bedrock, including black shales with > 2 wt% TOC (Allen et al 2015), was likely also eroded and entrained in glacial till (Norris 1985, Calmels et al 2007). Thus petrogenic organic carbon, which is 'radiocarbon dead', cannot be excluded as another important component of material preserved within Pleistocene-age deposits.

Our findings of relatively more decayed slump-mobilized POC broadens previous findings that slump-derived DOC on the Peel Plateau has reduced aromaticity and molecular weight, and elevated biolability compared to that from unimpacted streams (Littlefair et al 2017, Littlefair and Tank 2018). This suggests that DOM and POM pools are compositionally distinct and slumping affects the two pools in contrasting ways. Compositional differences could be due in part to different source contributions to the POC vs. DOC pools. $\Delta^{14}C$ values suggest that organic carbon from Pleistocene-age permafrost contributes proportionately less to DOC than POC, which is further supported by ground ice measurements on the Peel Plateau that show that DOC concentrations are greater in Holocene-age permafrost (15.36 ± 14.16 mg l^{-1}; Zolkos and Tank 2019) than Pleistocene-age permafrost (2.58 ± 2.19 mg l^{-1}; mean ± SD, n = 8). Furthermore, DOM stoichiometry is starkly different from POM stoichiometry, the latter of which closely resembles Holocene and Pleistocene headwall organic matter stoichiometry. This difference could be due to

ongoing processing of DOM in permafrost porewaters (Ewing et al 2015) and partial sorption/desorption that preferentially enables aliphatic moieties to remain dissolved (Littlefair and Tank 2018). These findings are corroborated by work on Herschel Island, an ice marginal feature along the Yukon north coast, where the degradation of permafrost material exposed in slump headwalls was largely driven by degradation in the dissolved phase (Tanski et al 2019). Given that tills on Herschel Island contain a greater proportion of marine sediments, and thus likely differ somewhat in their composition to those from the Peel Plateau (Kokelj et al 2002, Lane et al 2012, Tanski et al 2017), this result suggests that our findings may be relevant across the broader glacial margin region of the western Canadian Arctic.

In terms of the broader Arctic, our finding of more decayed slump-mobilized POC does contrast with recent findings that permafrost-influenced POM in the Kolyma River is less degraded than that derived from a headwater stream primarily influenced by in-stream production and recent vegetation, as assessed by lipid degradation proxies (Bröder et al 2020). This difference may be due to differences in the sources and genesis of permafrost between the two regions. While permafrost on the Peel Plateau was formed following the deposition of glacial tills within which petrogenic organic carbon is likely an important component (see below), permafrost thaw in the Kolyma River region unearths deposits in the Yedoma domain, formed from the simultaneous accumulation of ground ice and sediment/organic matter eposition (syngenetic) in non-glaciated regions typically with low topographic relief (Schirrmeister et al 2013, Strauss et al 2017). Contrasts in geological origins of these two permafrost environments may also influence the nature of material mobilization. The remobilization of sediments and organic carbon to fluvial networks in the Yedoma domain tends to be documented along larger rivers and coastlines, while direct impacts to fluvial networks on the Peel Plateau predominantly occur in headwater streams where fluvial incision has engendered high topographic relief (Tank et al 2020, Kokelj et al under review). Thus we need more studies examining/including thermokarst-POC mobilization in different landscapes to understand its release and fate in relation to landscape state factors (Tank et al 2020).

Petrogenic organic carbon, likely an important component of Pleistocene-origin POC in this study, is generally considered resistant to remineralization (Blattmann et al 2018). However, the balance between oxidation of petrogenic organic carbon, a source of CO_2 (Horan et al 2019) and burial of biospheric organic carbon, a sink of CO_2 (Hilton et al 2015) plays an important role

in determining the status of the Mackenzie River basin as a net source or sink to the atmosphere (Horan et al 2019). Thus enhanced erosion of organic carbon via thaw slumps on the Peel Plateau highlights the importance of asessing the reactivity of slump-mobilized POC and emphasizes the growing recognition of fluvial networks as important components of carbon cycling in northern ecosystems (Plaza et al 2019), particularly in thermokarst terrains (Turetsky et al 2020).

2.4.2. Implications of sediment transport limitation for permafrost-carbon fate

Our study focuses on suspended particles, yet the majority of terrestrial material eroded via slumping accumulates within valley-bottom debris tongues (Kokelj et al under review, Kokelj et al 2015, van der Sluijs et al 2018). Fluvial erosion of these deposits are limited by the stream's transport capacity as illustrated by the significant role stream power plays in explaining suspended TOC yield variations in this study. At FM2 and FM3, ~ 30% of the terrestrial volume excavated by slumping is contained within slump debris tongues (Kokelj et al under review, van der Sluijs et al 2018). When accounting for the fact that the upper 10 m of permafrost can contain greater than 50% ground ice content (Malone et al 2013, Lacelle et al 2015), the debris tongue likely contains greater than 80% of the soils and sediments evacuated by slumping, since melted ground ice is lost via runoff and evaporation. Debris tongues at FM3 and the immediately downstream FM2 have estimated volumes of 19.5 and 1.5 105 m^3 (van der Sluijs et al 2018, Kokelj et al under review). If we assume a single density of sediments (2.65 g cm^{-3}; Armanini et al 2018) and estimate 2% of sediment is POC (using suspended sediment %POC data from FM2-DN and FM3-DN in this study), this 15.95 km^2 catchment contains ~ 1.1×10^{11} g slump-origin POC in debris tongue deposits. We estimate that POC may remain within these primary sediment stores (Murton and Ballantyne 2017) for hundreds (~1.4×10^2) to thousands (~1.1×10^3) of years. This estimate is based on scaling of average downstream suspended POC fluxes (FM2-DN, this study) through the active thaw season (April 30th to September 30th inclusive, 154 d, O'Neill et al 2015), with an error range of −75% to + 100%. Our error range is roughly based on differences noted between scaling average SD fluxes vs calculations with turbidity calibrated by TSS flux and %POC data (supplementary S10) and uncertainty in the duration of active stream erosion throughout the year. This storage estimate does not take stream bedload transport into account, and we recommend future studies include measurements of bedload transport to increase accuracy of storage estimates. The intensification of thaw slump activity and disturbance enlargement is causing a rapid, net accumulation of materials in valley bottom debris tongue deposits (van der Sluijs et al 2018, Kokelj

et al under review). Though not located in the valley bottom, preserved organic matter within colluvial deposits of headwalls suggests that the accumulation of thawed material may inhibit organic matter decomposition (Lacelle et al 2019, Zolkos and Tank 2020). POC that is transported away from the thaw site by the stream will also fluctuate between deposition and transport, dependent on particle density and size. When settled out, mineralization of organic carbon can be reduced ~50% (Richardson et al 2013) or more, particularly if contained in anoxic sediments (Peter et al 2016), though DOC can diffuse from sediments to be mineralized in oxic waters (Peter et al 2016). Across the western Canadian Arctic, the volume of terrestrial material excavated from landscapes by slumping is accelerating (Kokelj et al 2015, Kokelj et al under review, Lewkowicz and Way 2019), with slumping primarily occurring on low order streams with less power for sediment transportation than the larger Peel and Mackenzie rivers (Kokelj et al 2017a, Kokelj et al under review). This suggests that hillslope thermokarst models, where the majority of carbon is laterally exported and a substantial proportion is assumed to be mineralized (e.g. one-third, Turetsky et al 2020), may overestimate carbon mineralization. Improved prediction of the fate of permafrost carbon released by slope thermokarst requires that sediment cascade frameworks, and assessments of organic carbon reactivity within that framework, be integrated into modelling efforts.

2.4.3. Ecological implications for stream systems

Increasing sediment mobilization due to thermokarst activity can directly decrease foodweb production by decreasing stream benthic invertebrate abundance (Chin et al 2016), and by shifting food webs to become more reliant on decomposition of terrestrial organic carbon than in-stream primary production, as a result of the negative effects of sediments on autochthonous production (Levenstein et al 2018). Thus, the composition of terrestrial inputs may play an important role in changes in stream ecological function and the basal energy resources that support higher trophic level production.

Differential organic matter composition is a well-established driver of variation of microbial metabolism (Sinsabaugh and Follstad Shah 2012, Ward and Cory 2015, Roiha et al 2016, Panneer Selvam et al 2017, Jain et al 2019). Thus, the divergent composition of permafrost-origin DOM and POM in this study suggests that DOM-based assessments of microbial production and mineralization rates are unlikely to be accurate for POM. In our study, the low POC:POP ratios

relative to DOC:DOP, are closer to mean C:P values of aquatic microbial biomass obtained from the literature (166 with approximately three-fold variation; Sinsabaugh et al 2013), suggesting that microbial biomass production could be greater on POM than estimates based solely on DOM, if organisms are P-limited and if the lower C:P ratios in POM is not solely due to living microbial biomass (Sinsabaugh and Follstad Shah 2010, Franklin et al 2011). TDN:TDP ratios were typically more than double Redfield ratios and, in some cases, increased downstream due to high TDN:TDP within slump ratios, suggesting limited phosphorus supply in the dissolved phase and that POM could be an important source of phosphorus to microbes. Yet the diagenetic state of POM in this study suggests low lability, thus low C:N and C:P ratios may be due to incorporation of N and P in humic complexes (Grandy and Neff 2008, Sinsabaugh and Follstad Shah 2011). In addition, some particulate nitrogen may be inorganic nitrogen sorped to clay structures (Schubert and Calvert 2001). Complexation in combination with non-competitive sorption of enzymes to mineral and organic colloids in particle-rich environments, may decrease metabolic efficiency (Schimel and Weintraub 2003, Grandy and Neff 2008) and microbial growth rates (Moorhead and Sinsabaugh 2006). This highlights the need to include particle-associated microbial communities and enzymes in assessments of rates of microbial production and mineralization (Sinsabaugh and Shah 2012) to understand how the abrupt shift in the quantity and composition of organic matter delivered to streams may affect resource flow through stream food webs (Sinsabaugh and Shah 2013), and thus stream ecological function and it is role in regional or global biogeochemical cycles.

Despite differences in within-slump POM, consistent convergence of downstream POM composition suggests that slump-POM material is well mixed prior to entry into modern stream networks. Headwall ablation, accumulation of a saturated slurry of thawed materials, and downslope sediment transport by surface flow and deeper seated flow contributes significantly to physical mixing of slumped materials (Kokelj et al 2015, van der Sluijs 2018) that were previously distinguishable in stratigraphy. Furthermore, biochemical processing within the slump scar zone (Abbott et al 2015, Tanski et al 2017) may be enhanced by the warm and wet conditions that distinguish this environment (Kokelj et al 2009, van der Sluijs et al 2018). This suggests that compositional differences between slumps may be less important than the quantity of POM for driving differences in downstream microbial processing between slump sites and/or that the initial unimpacted stream system state is important in understanding the effect of slumping on change to

a stream system since upstream locations in this study had greater variation than downstream locations. Further long-term studies of changing biogeochemical function as slumps undergo variations in headwall erosion rates would help assess this. Of course, this interpretation is limited by the sensitivity of our analyses. Further work detailing specific organic compounds (e.g. via solid-state NMR, Mccallister et al 2018; or Pyrolysis-Gas Chromatography-Mass Spectrometry, Py-GC/MS; Ma et al 2018) is required. In addition, the shift of streams from DOC to POC dominated systems highlights the need to use tools that can be applied to both dissolved and particulate phases of organic matter and associated microbial activity.

Finally, slump-associated particle release along fluvial networks creates potential for ecological and biogeochemical effects to be carried far from the site of thaw. The headwaters of the Peel Plateau drain into the Peel River, which has an annual sediment flux greater than most major Russian-Arctic Rivers (Holmes et al 2002). Currently, the contribution of thermokarst-derived sediments and POC to this flux is an important unknown. Using turbidity data and relationships between turbidity and TSS, POC, PN, and POP (supplementary S10) we estimate that POC, PN, and POP yields downstream of the smallest slump in this study (SD) are approximately 3.0×10^5, 3.9×10^4, and 1.0×10^4 kg km^{-2} from mid-June to mid-August (supplementary S10, figure S7). These estimated yields are orders of magnitude greater than the combined dissolved and particulate carbon and nitrogen yields of any of the major Arctic rivers, including the Mackenzie River (Mcclelland et al 2016). Thaw slumping along these headwaters is thus likely to increase downstream nutrient and organic carbon subsidies and act as a hotspot for nutrient and organic matter transfer from land to fluvial networks. Though the majority of material excavated from thaw slumps is being temporarily contained within debris tongue deposits, these primary sediment stores are readily available for stream transport and will cascade through a sequence of storage reservoirs through downstream systems over the coming millennia (Kokelj et al under review). This also highlights, as previously noted (Kokelj et al 2015, Beel et al 2018), that hydrometeorological change will play an important role in propagation of effects to downstream systems.

2.5. Conclusions

In permafrost regions where slope thermokarst is a dominant mechanism of thaw-driven change, we show that the vast majority of organic carbon mobilization to stream networks occurs

via POC. Particulate organic matter mobilized from thaw slumps, and associated POC, is compositionally distinct from the dissolved phase, in part due to the range of distinct material types that have been preserved by permafrost. This will likely translate into differences in carbon mineralization rates and roles in nutrient cycling between the two phases. Estimated yields from slumps suggest that these features create a hotspot for particulate C, N, and P release to fluvial networks. While the majority of material mobilized by thaw slumping is deposited in valley-bottom stores, these massive repositories of readily-mobilized material can switch streams from dissolved- to particulate-dominated systems and will create a step change in the ecological and biogeochemical functioning of downstream systems that is irreversable over century to millenial timescales. The dominance of sediment-associated C, N, and P release from thaw slumps highlights the pressing need for better knowledge of sedimentary cascades, mobilization, and storage reservoirs in slump-affected streams, and baseline assessments of the microbial processing of POM and cycling of particulate nutrients within a sedimentary cascade framework.

2.6. Acknowledgements

We are thankful for support from the Tetlit Gwich'in Renewable Resources Council and Aurora Research Institute, and field assistance of Joyce Kendon, Luke Gjini, Maya Guttman, Lindsay Stephens, Christine Firth, Elizabeth Jerome, Billy Wilson, Keith Colin, Rosemin Nathoo, and Erin MacDonald. Cara Littlefair provided invaluable advice on field logistics, and was involved in initial site selection of HA, HB, HD, and SD. Shawne Kokelj provided meteorological data. Alberto Reyes provided advice on headwall source sampling. Christopher Osburn advised laboratory BEPOM analyses and he and Ashley Dubnick provided advice on PARAFAC modelling. Christine Ridenour assisted with BEPOM analyses. Casey Beel provided advice on interpretation of turbidity sensor data. Research was financially supported by the Aurora Research Fellowship, Garfield Weston Foundation, Northern Scientific Training Program, UAlberta North, Natural Sciences and Engineering Research Council of Canada, Environment Canada Science Youth Horizons Program, Arctic Institute of North America, and Polar Continental Shelf Program. Northwest Territories Geological Survey (NTGS) contribution #0128. Finally, thank you to two anonymous reviewers whose comments improved this manuscript.

2.7. Tables

Table 2-1 Maximum headwall heights, slump area, estimate scar volumes, debris tongue volumes, debris tongue lengths, distance to late glacial limit, elevation, and maximum scar-valley slope for the eight slump sites included in this study. Delineated watershed areas for the upstream and downstream location at each slump site is also provided. ND indicates no data.

Site	Lat (DD)	Long (DD)	Headwall height[a] (~m, max)	Area[b] (10^4 m^2)	Est. scar vol. [c] (10^4 m^3)	Debris tongue volume[d] (2017, 10^4 m^3)	Debris tongue length[e] (m)	Dist. to late GL[f] (m)	Elevation[g] (m, max)	Max. scar-valley slope (%)	Watershed Area (km^2)	
											UP	DN
FM2	67.25770	-135.23694	25	31.7	240 (600)	195	1529	18918	373	67	0.73	15.95
SE	67.14862	-135.71803	23	1.5	3.1	ND	30	-3452	576	123	5.33	5.54
FM4	67.27798	-135.15955	17	8.8	38	ND	960	22901	296	98	3.41	4.35
HD	67.40057	-135.33413	11.7	1.8	4.0	ND	137	23713	323	65	17.94	18.30
FM3	67.25335	-135.27281	10.3	6.1	23 (50)	14.7	576	17312	399	34	3.18	3.75
HA	67.15074	-135.68652	7.3	5.9	22	ND	288	-3015	530	80	0.90	1.08
HB	67.24054	-135.82028	7.1	13.6	71	ND	257	-3215	666	35	0.69	1.02
SD	67.18030	-135.72717	2	<1	<1.7	ND	0	-3914	594	67	0.92	1.09

[a]Sources: Zolkos et al. (2019)

[b] Sources: Littlefair et al. (2017), SE approximated from Google Earth, based on 2016 imagery

[c] Pre-disturbance scar volume estimated from scar volume vs. scar area relationships, bracketed values show measured values in 2017 [Kokelj et al. under review; log(vol) = -1.44 + 1.42(log(area))]

[d] based on 2017 data, Van der Sluijs et al. (2018) and Kokelj et al. under review

[e] Sources: Littlefair et al. (2017); Zolkos et al. (2018)

[f] Distance from late glacial limit of the Laurentide Ice Sheet, negative values are West, positive values are East (supplementary S9). The late glacial limit used was mapped at the continental scale, potentially increasing its location error in our study area, which may be why some slumps are "positioned west" of the limit.

[g]Maximum elevation within ~100m of the headwall (supplementary S9)

Table 2-2 Results of the linear mixed effects regression models (estimate, error, degrees of freedom [df], t-statistic [t], and p-value [p]) comparing organic matter composition upstream, within, and downstream of thaw slump runoff. Estimate shows the effect of change in stream location (upstream vs. downstream, upstream vs. within-slump) on dependent variables and error shows standard error of the estimate.

	Upstream vs. Downstream					Upstream vs. Within-slump					Random Effects in model
Variable	Estimate	Error	df	t	p	Estimate	Error	df	t	p	
log (TOC yield)	0.9303	0.2374	7.3	3.92	0.005	N/A					(1 + StreamLocation|SlumpSite)
log (POC: POP)	-0.0461	0.0725	53.5	-0.636	0.527	0.1215	0.0725	53.5	1.676	0.010	(1|SlumpSite)
POC:PN	Not assessed, singular fit warnings for all models										
$(PO\delta^{13}C)^{-1}$	-0.0006	0.0001	53.25	-7.168	<0.001	-0.0008	0.0001	53.25	-9.727	<0.001	(1|SlumpSite)
$P\delta^{15}N$	Not assessed, singular fit warnings for all models or failure to converge										
$(\%POC)^{-1}$	0.2779	0.0450	7.13	6.189	<0.001	0.2140	0.0640	7.06	3.342	0.012	(1 + StreamLocation|SlumpSite) + (1|Jday)
log (DOC: DOP)	-0.0381	0.0748	53.6	-0.509	0.613	-0.3676	0.0748	53.6	-4.913	<0.001	(1|SlumpSite)
log (DOC: DON)	-0.0844	0.0668	51.5	-1.262	0.213	-0.3515	0.0660	51.4	-5.329	<0.001	(1|SlumpSite)

Table 2-3. Effects of morphological, landscape, and stream power variables on variation in log (TOC yield) and (%POC-1) across slump sites. Only explanatory variables retained in final models are shown. Estimates are standardized. Starting variables for all models consisted of maximum headwall height, debris tongue length, total rainfall over the past 96 hours, longitude of the slump site, and downstream stream power (except for the upstream: within model). Maximum slope was also used for the TOC yield model.

Variable (scaled and centered)	Estimate	Error	t	P
upstream: downstream log (TOC yield)	($R^2_{adj.}$ = 0.8677)			
Max. Headwall Height (m)	0.366	0.062	5.914	0.004
Downstream stream power	0.251	0.055	4.530	0.011
Longitude	-0.203	0.062	-3.265	0.031
Intercept	0.000	0.051	0.000	1.000
upstream: within (%POC^{-1}) [a]	($R^2_{adj.}$ = 0.8112)			
Max. Headwall Height (m)	0.169	0.034	5.031	0.007
Longitude	-0.154	0.031	-4.951	0.008
Total Rainfall (mm, past 96 hours) [b]	0.040	0.030	1.330	0.254
Intercept	0.000	0.026	0.000	1.000
upstream: downstream (%POC^{-1})				
No explanatory variables found to be significant				

[a] stream power was not entered as a variable in the starting model
[b] retained to improve model residuals

2.8. Figures

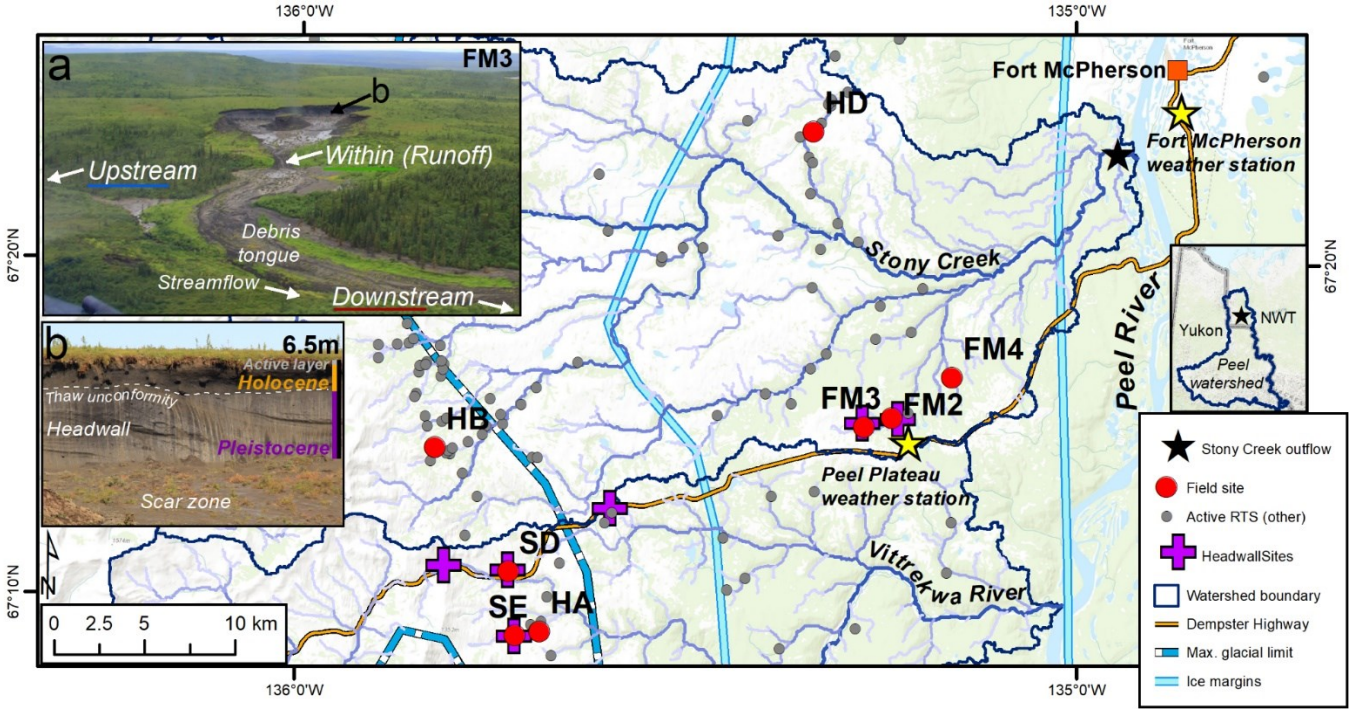

Figure 2-1. Location of slump sites sampled for stream water chemistry on the Peel Plateau, NWT. Inset (a) shows stream sampling points relative to a slump site. Inset (b) shows headwall units of a slump. Active RTS features are from Segal et al. (2016). Note that glacial limits presented were mapped at the continental scale, potentially increasing its location error in our study area, but is presented here to demonstrate east-west gradients. Adapted from Zolkos et al. (2018).

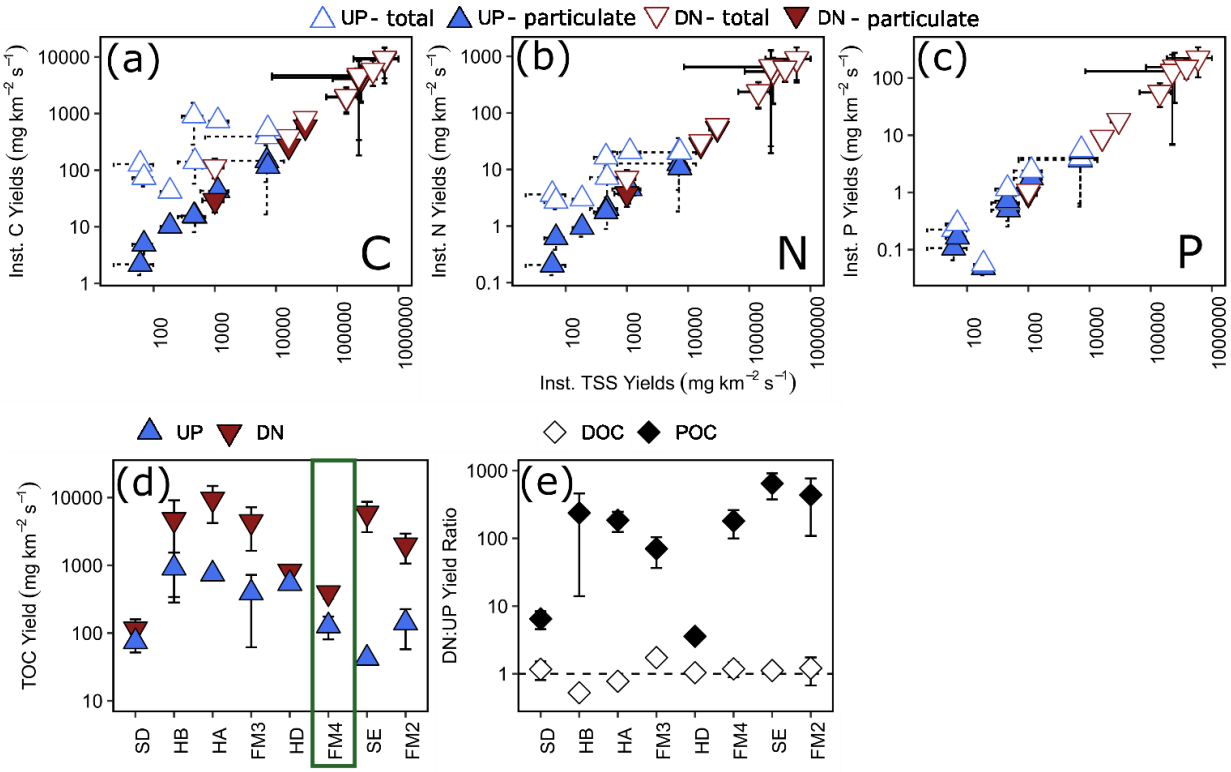

Figure 2-2. (a) Instantaneous suspended carbon (C), (b) nitrogen (N), and (c) phosphorus (P) yields vs total suspended sediment (TSS) yields, upstream and downstream of thaw slumps. Filled triangles show particulate organic carbon (POC), particulate nitrogen (PN), and particulate organic phosphorus (POP) yields, while empty triangles show total organic carbon (TOC), total nitrogen (TN = total dissolved nitrogen + PN), and total phosphorus (TP = total dissolved phosphorus + POP) yields. (d) Suspended TOC yield upstream and downstream of thaw slump sites. (e) Downstream: upstream ratios (DN:UP) of particulate (POC) and dissolved (DOC) organic carbon yields. Whiskers represent standard error. There is only one HD upstream sample. The green box highlights slump FM4; most of the 'FM4' headwall was not actively thawing during the sampling period. Slump sites on the x-axis are ordered left to right by increasing headwall height.

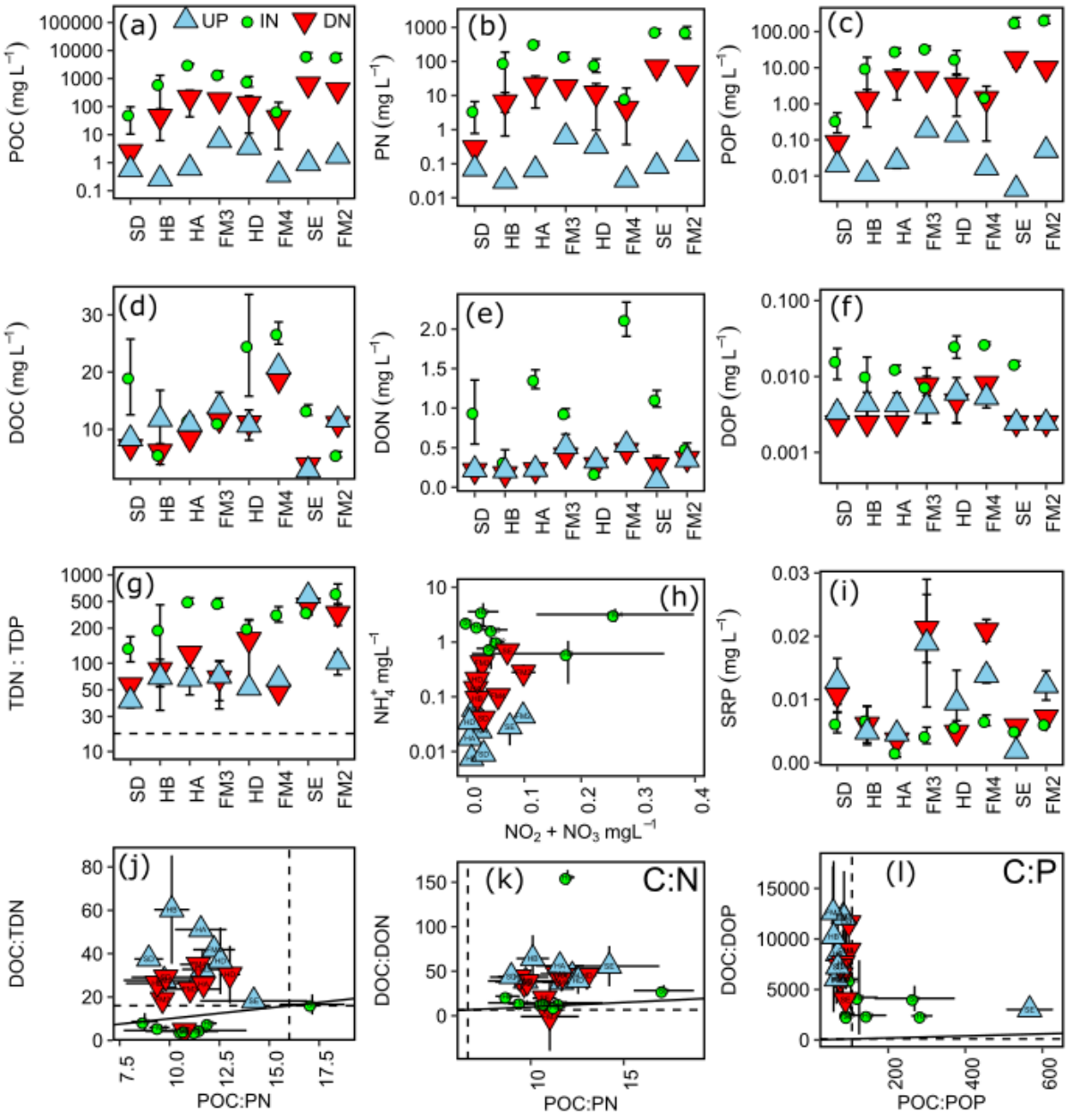

Figure 2-3. Upstream, within, and downstream comparisons of: (a-c) concentrations of particulate organic carbon (POC), particulate nitrogen (PN), and particulate organic phosphorus (POP); (d-f) concentrations of dissolved organic carbon (DOC), nitrogen (DON), and phosphorus (DOP); (g) total dissolved nitrogen vs. total dissolved phosphorus ratios

(TDN:TDP); (h) NH_4^+ vs NO_2^- + NO_3^- concentrations; (i) soluble reactive phosphorus (SRP) concentrations; (j) organic carbon to total nitrogen atomic ratios in the dissolved and particulate phase; (k) DOM vs. POM C:N atomic ratios, assuming PN here accurately represents PON; (l) DOM vs POM C:P atomic ratios. Where, applicable, slump sites on the x-axis are ordered left to right by increasing headwall height. Dashed lines on ratio plots demarcate Redfield ratios, a guideline for which higher values may indicate marine and freshwater nutrient limitation, while solid lines indicate the 1:1 ratio. Legend is in (a).

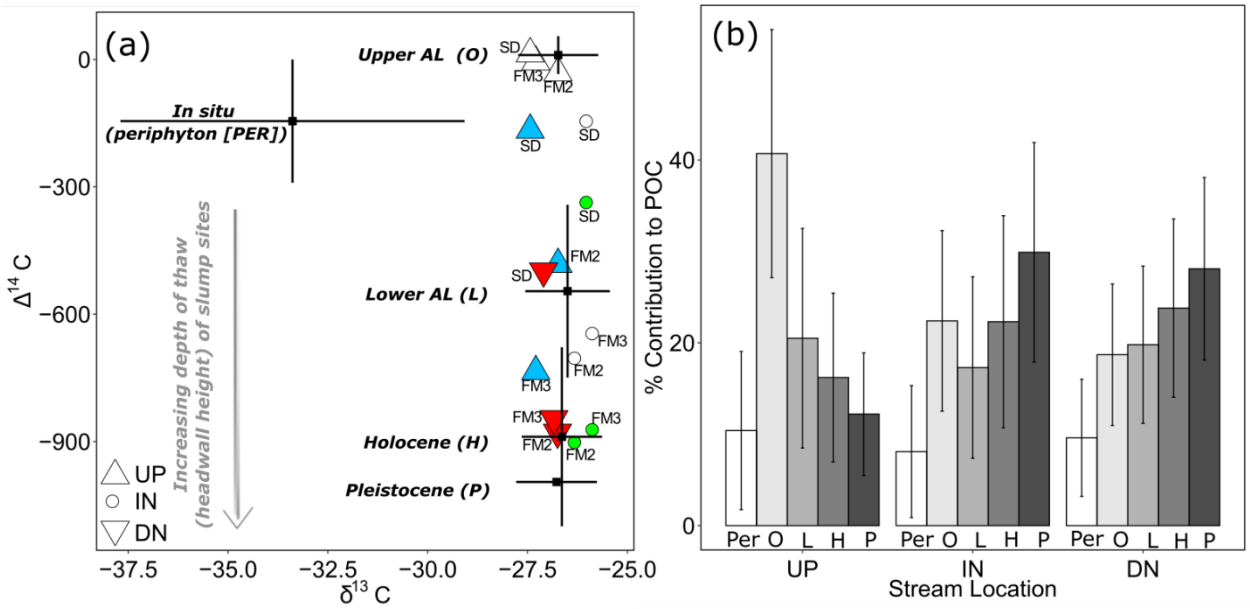

Figure 2-4. (a) Isospace plot of $\delta^{13}C$ vs. $\Delta 14C$ (‰) of POC sources and stream samples upstream, within, and downstream of select slump sites. Means ± 1 standard deviation of potential headwall [including Upper (O) and Lower (L) Active Layer, Holocene permafrost (H), and Pleistocene permafrost (P)] and in situ production [periphyton (PER)] sources are plotted (further details in supplementary S7). PO$\delta^{13}C$ standard deviations include ± 1‰ discrimination factor allowed in mixing model. Estimates of DO$\delta^{13}C$ and DO$\Delta 14C$ are shown via hollowed shapes using seasonal average values obtained from Zolkos and Tank (2019) and Littlefair et al. (2017) respectively. (b) Mean and standard error of % contributions of sources in (a) upstream, within, and downstream locations for FM2, FM3, and SD.

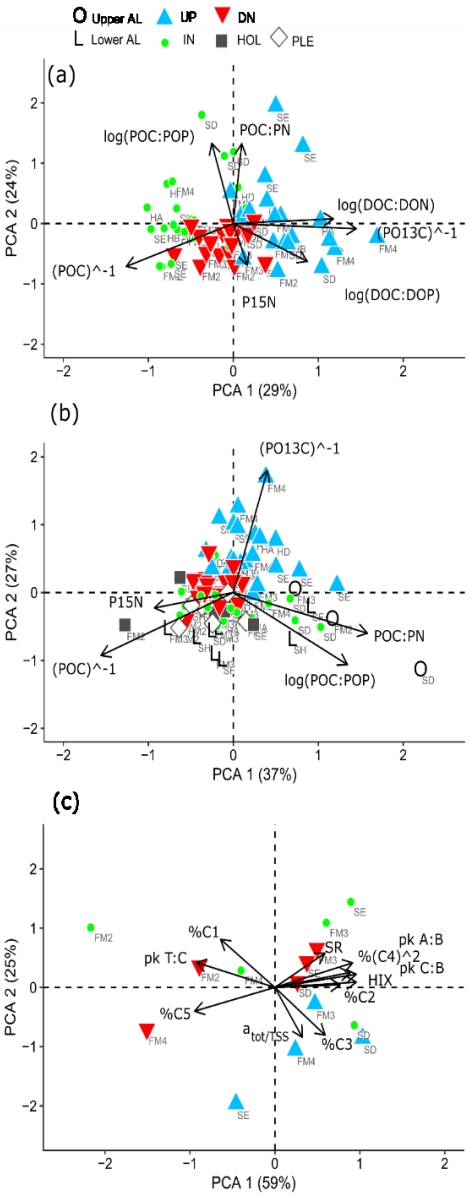

Figure 2-5. PCA results for: (a) Geochemical composition of suspended particulate organic matter (POM) and dissolved organic matter (DOM) in runoff and stream water. (b) Geochemical composition of suspended POM in stream water, and values from stratigraphic samples for slump headwalls [Upper (O) and Lower (L) Active Layer, Holocene permafrost (HOL), and Pleistocene permafrost (PLE) are shown]. (c) Base extracted POM [BEPOM] fluorescent components (%C1-5) and optical indices (see Table A**1-2**).

Chapter 3. Low biodegradability of particulate organic carbon mobilized from thaw slumps on the Peel Plateau, NT, and possible chemosynthesis and sorption effects

3.0. Summary

Warming and wetting in the western Canadian Arctic are accelerating thaw-driven mass wasting by permafrost thaw slumps, increasing total organic carbon delivered to headwater streams by orders of magnitude primarily due to increases in particulate organic carbon (POC). Upon thaw, permafrost carbon entering and transported within streams may be mineralized into CO_2 or re-sequestered into sediments. The balance between these processes is an important uncertainty in the permafrost-carbon-climate feedback. Using aerobic incubations of POC from streams affected by thaw slumps we find that slump-mobilized organic carbon undergoes minimal (~ 4%) oxidation over a 1-month period, indicating that this material may be predominantly destined for sediment deposition. Simultaneous measurements of POC and dissolved organic carbon (DOC) suggest that mineralization of DOC accounted for most of the total organic carbon loss. Our results indicate that mobilization of mineral-rich tills in this region may protect carbon from mineralization via adsorption to minerals and also promote inorganic carbon sequestration via chemolithoautotrophic processes. With intensification of hillslope mass wasting across the northern permafrost zone, region-specific assessments of permafrost carbon fates and inquiries beyond organic carbon decomposition are needed to constrain drivers of carbon cycling and climate feedbacks within stream networks affected by permafrost thaw.

3.1. Introduction

Permafrost soils comprise the single largest pool of terrestrial organic carbon (OC) (Schuur et al., 2015; Hugelius et al., 2014), half of which may be vulnerable to rapid mobilization into

modern biogeochemical cycles via abrupt thaw processes (Turetsky et al., 2020; Olefeldt et al., 2016). Permafrost dissolved organic carbon (DOC), typically defined as compounds < 0.7μm, is often highly susceptible to biotic mineralization into CO2 within aquatic systems (Vonk et al., 2015a; Littlefair and Tank, 2018; Abbott et al., 2014; Mann et al., 2015). Abrupt thaw can mobilize orders of magnitude more particulate organic carbon (POC, typically > 0.7μm) than DOC, yet the biodegradability of permafrost POC is not well understood (Shakil et al., 2020; Tank et al., 2020; Vonk et al., 2015b).

Suspended particles can be important sites for mineralization (Attermeyer et al., 2018) or mineral protection (Hemingway et al., 2019; Opfergelt, 2020; Groeneveld et al., 2020). In addition to molecular composition and a host of environmental factors that typically affect organic matter decomposition (e.g., microbial activity, nutrient availability) (Kothawala et al., 2021), mineralization of POC in stream networks depends on transport vs. deposition. When settled out, mineralization of POC can be reduced by ~50% (Richardson et al., 2013) or more, particularly if contained in anoxic sediments (Peter et al., 2016), though carbon release can shift to be in the form of methane (Schaedel et al. 2017). Fractions of POC with different density and size therefore not only experience a different settling and transport trajectory, but also may have differing processes and rates affecting OC dynamics (Tesi et al., 2016). If biodegradability varies across size and density fractions, this could alter realized mineralization during transport relative to measurements on bulk OC (Tesi et al., 2016).

Warming and intensifying precipitation across the ice-rich terrain of the Peel Plateau in western Canada has triggered an acceleration of thaw-driven landscape erosion in the form of retrogressive thaw slumps (hereafter, slumps) (Kokelj et al., 2020). Thaw slumping along stream sites in this region can increase TOC yields by orders of magnitude, almost entirely due to increases in POC (Shakil et al. 2020). Slump-derived DOC in the region is relatively more labile than background DOC, as shown by chemical composition and incubations (Littlefair et al., 2017; Littlefair and Tank, 2018). Slump-derived POC chemical composition suggests lower

bioavailability as POC sources shift from the active layer and some periphyton material to Pleistocene-aged organic carbon and petrogenic organic carbon mobilized from permafrost (Shakil et al., 2020; Bröder et al., 2021). However, POC bioavailability has not been experimentally assessed. Given that slump-released carbon occurs almost entirely as POC in this region (Shakil et al., 2020), understanding the fate of this carbon remains a critical knowledge gap.

Our objectives were to assess the potential for slump POC to be mineralized to CO2 during transport in streams. To do this, we undertook experimental incubations to: (a) determine whether slump-POC differs in biodegradability from POC present in unimpacted waters; and (b) quantify and assess the biodegradability of slump-POC fractions relative to their transport potential. This work provides insight into the fate of an understudied component of permafrost-mobilized OC.

3.2. Methods

3.2.1. Region and field sampling

Slumping occurs across the Peel Plateau (**Figure 3-1**) and typically mobilizes terrestrial material from three distinct sources: (1) Pleistocene-age tills that have remained preserved within permafrost since deposition by the Laurentide Ice Sheet and subsequent permafrost aggradation; (2) Holocene-age permafrost developed from tills following active layer deepening and/or slumping in previous warm periods, followed by permafrost aggradation during a cooler climate; and (3) a contemporary active layer. Thus, the relative contribution of biogeochemical substrate from these three terrestrial sources to streams can depend on thaw depth (Shakil et al., 2020; Bröder et al., 2021). Source composition can also vary west-east as vegetation (elevation) and geology changes along this gradient (Shakil et al., 2020).

Sampling occurred during July-August, within the Stony Creek and Vittrekwa River watersheds of the Gwich'in Settlement Region on the Peel Plateau (**Figure 3-1**). In 2015, substrate from streams near and within three slump sites (HA, HB, HD) was used to test if mobilization of slump-POC and nutrient release affect biodegradability of OC in streams. Stream water samples were obtained from: channelized runoff within each thaw slump (IN); a downstream location where all runoff entered the valley-bottom stream (DN); and an unimpacted reference stream upstream of slump inflow (UP) (**Figure 3-1**b). Site HD-UP experienced some encroachment of slump runoff, and thus was not a fully unimpacted site (Figure A**2-5**). In 2016, substrate was collected upstream, within, immediately downstream, and 2.79 km downstream of slump SE to assess variations in biodegradability with transport potential. In 2019, substrate was collected within and downstream of slump FM3 to follow-up results from 2015 and 2016 (details below). Slump sites had varied elevation and morphology, with maximum headwall heights (**Figure 3-1**a) ranging from 7.1 to 23m (see Shakil et al., 2020). All samples were processed (i.e., filtered) within 24 hours of collection, apart from within-slump and downstream samples used for adding particles to "unfiltered" treatments in 2016 that were stored in the dark at 4°C until the start of the experiment. Experiments were started within 24 hours (2015, 2019) or 48 hours (2016) after processing. The extra hold time for the 2016 experiment was due to the extra time needed for size fractionation of samples (see below and supplementary S2). For further sample collection details, see Appendix.2.

3.2.2. Biodegradation experiments

3.2.2.1. Effects of POC source, dissolved constituents, and settling (2015)

To test the effect of POC source (**Table 3-1**, Figure **3-2**), we incubated unfiltered upstream water (upstream POC; treatment "UU") and filtered upstream water with a 2 mL addition of slump runoff (slump POC; "SU") in 120 mL glass serum bottles for 7 days at ca.

20°C in the dark, with continuous end-over-end rotation (4 rpm; Richardson et al. 2013) (A2.2, Figure **3-2**). Control bottles accounted for DOC contained in filtered upstream water alone (no POC control; "UF"). Additionally, we tested for: (a) the effect of particle deposition by allowing a replicate set of SU bottles to settle out ("SS"); and (b) the slump-derived release of additional solutes (e.g., nutrients) by mixing slump POC with filtered downstream water ("SD"). Bottles were filled to have no headspace.

3.2.2.2. Variability as a function of transport potential (2016)

SE within-slump runoff was split into three sieve size fractions (63 – 2000 µm, 20 – 63 µm, < 20 µm) by sieving a 0.5 mL aliquot and adding the resultant size fractions to filtered downstream water in 60 mL glass BOD bottles (A2.2, Figure **3-2**). An unfractionated control (0.5 mL in 60 mL downstream water) was also created, and bottles were incubated for 8 days in the dark at ca. 20°C as above. Since relative concentrations of each size fraction were maintained, the <20 µm fraction had orders of magnitude greater total suspended solid (TSS) concentrations than the larger two fractions (Table A2-2). We also incubated filtered and unfiltered (but diluted, Table A2-2) stream water from sites upstream, downstream, and 2.79 km downstream of SE to accompany size fraction incubations. We characterized POC differences between size fractions using: (a) ^{14}C age, (b) percent POC (%POC; POC : TSS), and (c) absorbance and fluorescence spectra of base-extracted particulate organic matter (BEPOM) (Osburn et al., 2012)(A2.3). Bottles were filled to have no headspace.

3.2.2.3. Measurements

We measured: (a) concentrations of DOC, POC, and TOC, and $SUVA_{254}$ (an optical proxy for dissolved organic matter (DOM) aromaticity) (Weishaar et al., 2003) at the beginning and end of incubations; and (b) O_2 concentrations approximately daily (PreSens, Fibox4, SP-PSt3-NAU-D5-YOP) to provide insight on rate of change (Richardson et al. 2013). We

assumed heterotrophic breakdown of OC would be the dominant O_2 consumption pathway, as respiratory quotients across several freshwater sites have been noted to vary around 1 (Berggren et al., 2012). Incubation O_2 concentrations presented never dropped below 2 mg L^{-1}; a threshold well above O_2 limiting concentrations for different bacterial species (Stolper et al., 2010 and references therein). One exception was one of four replicates for the SE unfractionated treatment, which was removed and replaced with the mean of replicates for statistics. Our experiments aimed to mimic conditions downstream of slump inflows, thus slump-affected incubations had POC concentrations ranging from 1.4 to 18.6 times DOC concentrations. Samples for TSS concentration were collected alongside POC. Further details are available in A2.4.

3.2.2.4. Follow-up experiments

To assess processes that could consume O_2 and/or generate OC (due to O_2 losses coupled with OC gains observed in 2015 and 2016) we undertook two follow-up experiments. First, we combined 0.15 mg of sterilized HD debris tongue sediments (collected in 2016)(Zolkos and Tank, 2020) with 18.2 Ω Milli-Q (MQ) water to assess abiotic O_2 loss. MQ water was sourced from a machine with a carbon filter and was quality controlled to have less than 10 ppb TOC. We incubated 60 mL glass BOD bottles on a shaker table in the dark at ca. 20°C for 7 days, monitoring O_2 as above. Second, we measured change in dissolved and particulate inorganic carbon (DIC, PIC), in addition to change in DOC and POC, in an incubation combining FM3 slump runoff with downstream water, including sterilized replicates. The treatments were designed to replicate treatment "SD" in 2015. Sterilization was achieved by autoclaving and adding $ZnCl_2$ as a poison and was validated using plate counts (A2.5). We hypothesized chemosynthesis associated with nitrification and sulfide oxidation (eqns. 1-4) could generate OC and so we additionally measured dissolved inorganic nitrogen (NH_4^+, NO_3^-, NO_2^-) via automated colorimetry and sulfate (SO_4^{2-}) via ion chromatography at

the Canadian Association of Laboratory Accreditation (CALA)-certified Biogeochemical Analytic Service Laboratory (BASL; University of Alberta, further details in supplementary A2.4.

$NH_3 + 1.5O_2 \leftrightarrow NO_2^- + H^+ + H_2O$ (Eq. 1a) (Summ and Morgan 2012)

$NO_2^- + 0.5O_2 \leftrightarrow NO_3^-$ (1b) (Stumm and Morgan 2012)

$CO_2 + H_2S + O_2 + H_2O \leftrightarrow [CH_2O] + H_2SO_4$ (Eq. 2) (Klatt and Polerecky, 2015)

$FeS_2 + 3.75O_2 + 3.5H_2O \leftrightarrow + 2H_2SO_4 + Fe(OH)_3$ (Eq. 3) (Percak-Dennett et al., 2017)

$H_2SO_4 + 2(Ca, Mg)CO_3 \leftrightarrow 2(Ca^{2+}, Mg^{2+}) + SO_4^{2-} + 2HCO_3^-$

(Eq. 4) (Calmels et al. 2007, Zolkos and Tank 2020)

Note that equation 2 is a general equation of chemolithoautotrophic reduced sulfur oxidation that can have a variable stoichiometry and assumes sulfur oxidizing bacteria exclusively produce SO_4^{2-}, rather than both SO_4^{2-} and S^0 (Klatt and Polerecky, 2015; Nelson et al., 1986). Equation 3 shows a net reaction for a model of pyrite oxidation at circumneutral-pH (Percak-Dennett et al., 2017). We note that pH in the streams in this study can be quite variable but tend to be circumneutral, often varying around pH7 and most ranging from pH 6 – 8 (see supplementary data of Shakil et al. 2020). This sulfide oxidation can generate sulfuric acid that can weather carbonates (e.g., eq. 4) or silicates (Zolkos and Tank, 2020; Zolkos et al., 2020).). Sediments in sterilized and unsterilized bottles were characterized using X-ray diffraction (XRD) (A2.4.4).

3.2.3. Data analyses

Two-way ANOVAs, with site and treatment as fixed effects, were used to assess the effect of POC presence (UF vs SU), source (UU vs SU), dissolved matrix (SU vs SD), and settling (SU vs SS) on percent changes in OC (DOC, POC, and TOC), DOM aromaticity ($SUVA_{254}$) and O_2 loss rate. One-way ANOVAs were also used to assess differences in the aforementioned

changes between size fractions (2016 experiment). Two-way ANOVAs were used to assess the effect of distance and filtration (fixed effects) for the 2016 transect experiments. Significant main effect interactions were followed up with Tukey-adjusted pair-wise t-tests (Zar, 2010). We also calculated 95% confidence intervals to evaluate whether OC changes significantly differed from zero. Principal components analyses were used to visualize differences in optical indices between size fractions (2016), and changes in DOM and BEPOM (2019). To assess factors controlling in situ CO_2 and O_2 dynamics we calculated departures of O_2 and CO_2 from atmospheric equilibrium (Vachon et al. 2019) using 2015 in situ measurements of dissolved O_2 at several slump sites (Shakil et al., 2020) and coupled CO_2 departures (Zolkos et al., 2019). For further details, see Appendix.2.

3.3. Results

3.3.1. Effects of POC presence and source (2015)

Across experiments, declines in POC were not observed, and in some cases, POC increased (Figure **3-3**). Slump runoff addition into filtered upstream water (SU) did not significantly alter %ΔDOC (the percent change in DOC from beginning to end of the experiment), $\Delta SUVA_{254}$ (change in DOM aromaticity), or %ΔTOC ($p>0.05$; Table **3-2**, Figure **3-3**) relative to the upstream filtered control (UF). Similarly, POC source (slump [SU] vs. unfiltered upstream [UU]) did not significantly affect %ΔTOC or $\Delta SUVA_{254}$ ($p>0.05$, **Table 3-2**, Figure **3-3**). However, %ΔPOC was significantly lower when particles were sourced from slump runoff (SU vs. UU; $p<0.001$, Table A2-1), potentially because particle concentrations were orders of magnitude lower in upstream bottles (Table **3-3**). DOC increased in the presence of upstream particles (UU) but decreased in the presence of slump particles (SU), though this difference was marginally insignificant (Table **3-2**, $p = 0.053$). Despite no effect on %ΔTOC (Table **3-2**), the addition of slump particles (SU) did significantly increase rates of O_2

consumption compared to upstream filtered and unfiltered treatments (UF and UU; Figure **3-3** a-c), though this effect was dependent on slump site (significant interactions, **Table 3-2**; note lack of increase for site HD where slump runoff encroached upstream site).

3.3.2. Effects of background dissolved constituents and settling (2015)

Changing filtrate to downstream water, which has higher ion and nutrient concentrations (Shakil et al. 2020), had no significant effect on any parameter measured in the experiment (SU vs. SD, **Table 3-2**). Allowing slump particles to settle (SU vs SS) did not affect %ΔTOC but did significantly reduce O_2 consumption rates. Mean DOC concentrations also switched from decreasing (SU) to increasing (SS) (Figure **3-3**d), though the difference was not significant ($p=0.10$, **Table 3-2**).

3.3.3. Variability dependent on transport potential (2016)

Based on ^{14}C age, %POC, and relative contribution of fluorescent peak C (Coble, 2007), larger particle size fractions appeared to be associated with fresher terrestrial-origin organic matter than smaller size fractions (A2.3). POC associated with particles < 20 µm dated to > 27,000 cal BP, while POC associated with particles ranging from 20 – 63 µm and 63 – 2,000 µm dated to ~ 19,600 cal BP and ~8,000 cal BP respectively (Table **3-5**). The majority of POC (73%, Table **3-5**) was associated with particles less than 20 µm.

Only bottles containing particles <20 µm displayed significant gains in TOC (95% CI; Figure **3-3**g-i) but we did not find a significant difference in %ΔTOC or %ΔPOC between size fractions (ANOVA; **Table 3-3**). DOC losses occurred in all treatments downstream of slumps, to a greater degree when particles were present (i.e., unfiltered treatments) (Figure **3-3**h-i, $p<0.05$,

Table 3-4), and were significantly greater when particles were <20 µm ($p<0.05$, Figure **3-3**g, **Table 3-3**). Increases in $SUVA_{254}$ were also significantly greater for <20µm particle treatments ($p<0.05$ **Table 3-2** and **Table 3-6**), as were TSS concentrations (Table A2-2). %DOC loss was also significantly greater 2.79 km downstream of SE compared to immediately downstream (

Table 3-4).

3.3.4. O_2 vs. carbon

Change in O_2 and TOC generally did not follow the 1:1 trend expected if heterotrophic respiration dominated metabolic processing (Figure **3-4** a-c). The greatest deviations from 1:1 was observed in treatments containing slump runoff, where despite large losses in O_2, we saw non-significant changes to gains in TOC. Increases in TOC from upstream, filtered, and 2.79 km downstream bottles were within the range of experimental blanks (Figure **3-4**c).

Although the rate of O_2 consumption within and across experiments was generally greater in treatments with greater initial TSS (Figure **3-4**d), there was no consistent relationship between TOC changes and initial TSS (Figure **3-4**e). However, some of the greatest TOC increases occurred during incubations of slump SE particles <20 μm and slump HA particles in upstream (SU) and downstream (SD) filtrate, treatments amongst those with the greatest initial TSS (Figure **3-4**a, b, e).

In-situ comparisons of O_2 vs. CO_2 showed within-slump samples to have the greatest excess CO_2, with several samples substantially departing from the 1 CO_2: -1 O_2 stoichiometry associated with heterotrophic respiration (Figure **3-4**f). In contrast, several downstream and upstream sites displayed measurements close to atmospheric equilibrium for CO_2 but were supersaturated for O_2, potentially due to temperature changes and lower solubility of O_2 (Vachon et al., 2020).

3.3.5. Follow-up experiments

3.3.5.1. Sterilized debris sediments in Milli-Q water (2018)

Oxygen was completely consumed (~226 μM) in bottles containing sterilized HD debris tongue material suspended in MQ water within 4-5 days, exceeding the O_2 loss rates previously observed (Table A2-1, Figure A**2-3**a). Bottles containing sterilized sediments had lower pH (5.52 – 6.09) following incubation than MQ controls (6.53 – 6.91).

3.3.5.2. Inorganic carbon changes and potential chemolithoautotrophy (2019)

Oxygen consumption occurred in sterilized treatments (-15 ± 6 μM, mean ± 95% CI, t = 27 days) but was more pronounced in unsterilized bottles (-124 ± 15 μM). The pronounced O_2 decline in unsterilized bottles was accompanied by a significant loss of DOC (-83 ± 26 μM) and a non-significant loss of POC (-85 ± 261 μM), balancing to a non-significant loss of TOC (-170 ± 262 μM, Figure **3-5**). Total inorganic carbon (TIC) increased significantly in unsterilized treatments, driven by increases in DIC. In sterilized bottles, modest oxygen losses were accompanied by significant DOC losses (-93 ± 51 μM), significant POC gains (141 ± 33 μM), balancing to a modest non-significant gain in TOC (48 ± 66 μM). TIC in sterilized bottles had a minor significant decrease (-25 ± 20 μM), driven by losses in DIC.

Ammonium (NH_4^+) decreased from 8.68 ± 0.47 μM to below detection (0.2 μM) in unsterilized bottles, while NO_3^- + NO_2^- increased by 2.58 ± 2.36 and 1.33 ± 1.67 μM, respectively. In sterilized bottles, NH_4^+increased by 6.74 ± 1.80 μM alongside negligible changes in nitrate or nitrite. Sulfate (SO_4^{2-}) generation was greater in unsterilized (90 ± 6 μM) than sterilized (54 ± 23 μM) bottles, but for both treatments SO_4^{2-} increased more than would be expected via pyrite oxidation (Figure **3-5**d, based on oxygen stoichiometry in eq. 3). However, the only sulfur-bearing mineral detected in sediments (XRD; 1-5% detection limit) was pyrite (Table A2-3).

A biplot of PCA components 1 and 2 did not reveal any shifts in BEPOM or DOM optical characteristics during incubation of unsterilized treatments (Figure **3-5**d-e). However, DOM

from sterilized treatments shifted towards lower molecular weight (SR, slope ratio), lower aromatic material ($SUVA_{254}$) of greater biological origin (BIX). PC1 separated DOM in sterilized and unsterilized bottles, suggesting the sterilization processes increased the proportion of simple compounds. Since the sterilization process itself appears to increase the proportion of simple compounds, the results caution against its use as an abiotic baseline.

3.4. Discussion

Our incubations, coupled with multiple studies examining slump-POC composition (Shakil et al., 2020; Bröder et al., 2021; Keskitalo et al., 2021) indicate that slump-mobilized POC in glacial landscapes of western Canada has low biodegradability on the Peel Plateau. We found no significant losses of POC or TOC or evidence that %ΔTOC increased in streams due to the presence of slump-mobilized POC. This finding was consistent across slump sites and for varying size fractions and distances downstream of slump inputs. While %ΔTOC did not significantly differ across size fractions of slump SE particles, particles most likely to remain in transport (< 20 μm) enabled the greatest loss in DOC (linked to greater TSS) and significant gains in TOC. A coupled transect experiment showed that downstream of SE, TOC gains were not significant or were within error of blanks (2.79 km downstream), though both downstream treatments had orders of magnitude lower TSS than the <20 μm size fraction treatment sourced directly from slump runoff.

The lack of loss in TOC and POC contrasted with elevated O_2 consumption rates downstream of slumps, except for slump HD, where slump runoff encroached into the upstream site (Figure A**2-5**). Despite a lack of TOC or POC loss, oxygen consumption rates in treatments containing particles were always elevated relative to their DOC controls, highlighting that oxygen consumption could not be solely accounted for by DOC mineralization. Instead, TOC gains suggest potential for chemoautotrophic carbon sequestration. Further, abiotic processes (e.g., mineral oxidation) appear to have the potential to consume oxygen rapidly enough to

decouple oxygen and carbon dynamics from the 1:1 relationship associated with heterotrophic respiration, as suggested by sterile incubations of HD debris material. The excess in situ CO_2 concentrations we observe are likely from mineral weathering that can generate CO_2 in this system (Zolkos et al., 2018).

Our finding of low POC biodegradability is likely conservative since incubations focus on the most labile period (initial 7-27 days) (Richardson et al., 2013). Our longest incubation (27 d; **Figure 3-5** non-sterile) did not show significant TOC losses, though 95% error spanning losses expected from a 1:1 relationship with O_2 suggests that detection of change may be masked by error in POC measurements (**Figure 3-5**a). Using ΔTIC as an alternate metric of carbon mineralization, we estimate that ~ 4% of the initial TOC pool may have been mineralized within 27 d. The difference in the landscape position and slump morphology of the slump site (SC is further east than slumps HA, HB, and SE) and the longer time period of the incubation (27 days vs. 7-8 days) could have both played a role in the average loss in TOC versus the gain seen in previous comparable experiments where slump material was added to downstream water. Time series experiments on TOC degradation from similarly glacially-conditioned Qikiqtaruk (Herschel Island) indicate that CO_2 production tied to organic matter mineralization ceased by the end of a 120-day incubation, and greater than half (~58%) of total CO_2 was produced within the first 27 d (Tanski et al. 2019). Assuming a similar rate for OC mineralization, we can scale up our findings beyond the time of our incubation to estimate that ~7% of slump-mobilized TOC on the Peel Plateau may be mineralized during the entirety of time it is transported in streams. These findings are consistent with measures of little change in CO_2 concentrations downstream relative to upstream of slumps (Zolkos et al., 2019), despite orders of magnitude increases in POC and thus TOC (Shakil et al., 2020). The maximum of 7% TOC mineralization observed in this study may be elevated relative to slow rates of mineralization within permafrost (Leewis et al. 2020) but is considerably lower than the assumption used by Turetsky et al. (2020) that 2/3rds of DOC/POC mobilized by hillslope

abrupt thaw will be mineralized on a decadal timescale (Table S1 in Turetsky et al. 2020). The higher rate of mineralization used by Turetsky et al. (2020) is cited to be based on mineralization rates observed for DOC in Pleistocene Yedoma landscapes (Vonk et al. 2013). While rates of mineralization similar to, or greater than, this have been noted in several studies (e.g. Vonk et al. 2013, Spencer et al. 2015, Abbott et al. 2014), these findings have not been consistent in landscapes across the Arctic (e.g. Burd et al. 2020) likely due to differences in landscape factors including the nature of permafrost genesis (e.g. syngenetic vs. epigenetic permafrost, Tank et al. 2020). Further, none of these studies included POC within their assessments of % loss despite the fact that POC concentrations within thaw streams could be an order of magnitude greater (Vonk et al. 2013, Shakil et al. 2020). Percent TOC loss within this study is also lower than % DOC loss observed for this study area (Littlefair et al.2018) likely due to substantial differences in biochemical processes occurring in the DOC vs. POC pool upon thaw and interaction with mineral surfaces exposed (see further discussion below) and contrasting sources (Shakil et al. 2020). However, our estimate of 7% loss is comparable to Tanski et al. (2019) who observed 2% to 9% TOC loss rates for incubations of permafrost, including POC, mixed with seawater and incubated at 16°C for 120 days.

This study and work by Tanski et al. (2019) both suggest DOC contributes more to heterotrophic CO_2 production than POC in glacial margin landscapes even where hillslope thermokarst increases fluvial POC by orders of magnitude (Shakil et al. 2020). This seemingly contrasts protection of DOM by adsorption to mineral surfaces (Littlefair et al., 2017), however adsorption onto minerals tends to favour humic-like, oxygen-rich compounds, typically considered recalcitrant, over protein-like compounds (Groeneveld et al., 2020). Thus, sorption could "sort" labile carbon into the dissolved phase and relegate intrinsically recalcitrant ("humic-like", aromatic) carbon to mineral protection as POC. Evidence of this includes elevated lability of slump-mobilized DOM relative to upstream DOM (Littlefair et al., 2017; Littlefair and Tank, 2018), low lability of slump POM (Shakil et al., 2020; this study) and

striking compositional similarity of DOC from slump-impacted streams on the Peel Plateau to that from other circumpolar regions with mineral soils (Wologo et al., 2021). Where RTS sediments continue to selectively sequester aromatic DOM and release labile DOM during fluvial transport, the relative increase in lability in the remaining DOM pool may promote microbial OC oxidation and CO_2 production downstream. However, when particles settle out, anoxia could result in release of adsorbed DOC to the overlying water column (Peter et al., 2016), which may explain the switch from mean DOC decreases to DOC increase in comparisons between rotated and settled slump treatments. Sorption appeared to occur in 2019 sterilized bottles as DOC concentrations declined but POC increased, and DOM aromaticity and molecular weight decreased. No change in DOM in unsterilized bottles may reflect sorption (loss of aromaticity) and degradation (gain of aromaticity) acting simultaneously, which underlines challenges in quantifying process by measuring OC changes in bulk incubations and why DOC declines were not consistently followed by increases or decreases in $SUVA_{254}$ across experiments, even when losses were consistent as in 2016.

We note that rapid within-slump processing of labile components prior to entrainment within streams may still occur, as supported by high NH_4^+ concentrations (Shakil et al., 2020) indicative of decomposition (Tanski et al., 2017), low representation of labile compounds in the slump scar zone and stream sediments relative to headwall sources (active layer)(Keskitalo et al., 2021), and excess CO_2 in slump runoff resulting from both heterotrophic respiration and geogenic production (Zolkos et al., 2019)(Figure **3-4**f). Past work indicates that OC rapidly lost within-slump may predominantly originate from the active layer (Bröder et al., 2021) and Holocene-age permafrost in areas where organic material buried in colluvial deposits from past slumping has preserved organics (Lacelle et al., 2019).In addition to serving as a possible marker for decomposition, high concentrations of ammonia may stimulate nitrification and associated chemosynthetic carbon sequestration. Though we did not see significant TOC gains in our 2019 experiment, ammonia loss coupled with nitrite production suggests active

nitrification. Nitrifying bacteria have slow growth rates (Sinha and Annachhatre, 2007; Bock and Wagner, 2013), with the molar ratio of NH_4^+ consumed to carbon fixed ranging from 25 – 100 (Ward 2013). Using this stoichiometry and initial NH_4^+ concentrations estimated across 2015-16 incubations (Table A2-4) indicates that nitrification would be unlikely to fix more than 1 µM, in comparison to OC gains of 601 ± 459 µM (mean ± 95% CI of SE <20 µm incubation, Figure **3-4**b, Table A**2-4**). Chemolithoautotrophy by sulfur oxidizing bacteria can also sequester carbon (Klatt and Polerecky, 2015) with the ratio of CO_2 sequestered to O_2 consumed ranging from 0.09 – 0.41 for aerobic thiosulfate oxidizers (Klatt and Polerecky 2015). The process has been noted to be an important carbon sequestration mechanism in mine-tailings (Li et al. 2019). Although the role of aerobic microorganisms in sulfide oxidation is commonly associated with acidic-pH conditions as in Li et al. (2019), this process can also occur at circumneutral pH (Percak-Dennett et al. 2015). Given the high sediment concentration in streams affected by slumping (can exceed 800 g L^{-1}, Shakil et al. 2020), and the prevalence of sulfide minerals and oxidation across the Peel Plateau (Zolkos et al., 2018), chemolithoautotrophy associated with sulfide oxidation is a mechanism worth exploring as a counterbalance to OC mineralization. Precise techniques such as isotope labelling (Spona-Friedl et al., 2020) and the tracking of genes associated with carbon fixation processes (Percak-Dennett et al., 2017) may circumvent challenges associated with POC measurement errors and tracking multiple processes acting on OC end-point measurements.

3.5. Conclusion

Permafrost thaw slumping is increasing TOC concentrations in streams across the Peel Plateau (Canada) by orders of magnitude, almost entirely in the form of POC (Kokelj et al., 2020; Shakil et al., 2020; Keskitalo et al., 2021). Across incubations conducted including slump-POC, we found a maximum of 4% of the initial total organic carbon was lost within 27 days and estimate that this would scale to approximately 7% of slump-derived TOC being lost

during transport in streams. Further changes in DOC and POC concentrations alongside previous observations of high biolability of slump-DOC (Littlefair et al. 2018) and recalcitrant composition of slump-POC (Shakil et al. 2020, Keskitalo et al. 2021) suggest this loss is primarily driven by losses in DOC. Across our experiments, we find slump-POC has low biodegradability in streams. This, alongside observations that majority of POC mobilized by slumps is likely to be contained within debris tongues for centuries to millennia (Shakil et al. 2020) suggests slump-mobilized POC is predominantly destined to be re-sequestered in sediments. While our experiments examine material exiting rather than within the slump scar zone, thus missing degradation that may happen within the scar zone, our estimates are far lower than assumptions used in Turetsky et al. (2020) that 2/3rds of POC/DOC released will be mineralized. This highlights the need to contextualize permafrost-carbon release within different landscapes. Further, increased input of minerals alongside increases in organic carbon into streams creates significant potential for carbon sequestration via abiotic (sorption, mineral protection) and biotic (chemolithoautorophy) processes. Targeted investigations of these multiple processes acting simultaneously on carbon dynamics require specific quantification in landscapes experiencing rapid change.

3.6. Acknowledgements

This work took place within the Gwich'in Settlement Region, and we are thankful for support from the Tetlit Gwich'in Renwable Resources Council and Western Arctic Research Centre. We are further thankful for the field assistance of Christine Firth, Elizabeth Jerome, Andrew Koe, Joyce Kendon, Maya Guttman, Luke Gjini, and Lindsay Stephen. Maya Guttman and Joyce Kendon also helped experiment set up and sample processing. Hailey Verbonac assisted with O_2 measurements during our 2015 experiments conducted in Inuvik. This manuscript also benefitted from helpful discussions with: Steve Kokelj with regards to field sampling and perspectives on landscape changes in the region; and Matthias Koschorreck and

Rafael Marcé with regards to chemoautotrophic processes, and Alex Wolfe who first provided advice to broaden consideration of what affects oxygen and carbon dynamics. The rotator used for incubations was designed and manufactured by Technical services staff in the Department of Mechanical Engineering at the University of Alberta, supervised by Roger Marchand. Funding for this study was provided by the Natural Sciences and Engineering Research Council (NSERC), Polar Continental Shelf Program (Natural Resources Canada), Campus Alberta Innovates Program, ArcticNet, CiCan Cleantech Internship Program, Environment Canada Science Youth Horizons Internship, Northern Scientific Training Program, University of Alberta and UAlberta North, and the Aurora Research Institute. Personal support to SS was provided by NSERC and the Garfield Weston Foundation. Research for this paper was conducted under NWT research licences: 15685 (2015); 15685 (2016); 15887 (2017); 16575 (2019).

3.7. Tables

Table 3-1. Summary of experiments and main results with reference to figures and text sections for details.

Year	Field Sampling	Exp. Details	#days	Test	Treatments	Main result	Considerations
2015	UP, IN, and DN of slumps HA, HB, HD	3.2.2.1, Fig. 3-2	7	POC presence	SU (slump in filtered upstream) vs. UF (filtered upstream)	between treatments: no effect on %ΔTOC but increased O_2 loss; (2) within treatments: no sig. TOC loss (Fig 3-3, Table 3-2)	
				POC source	SU vs. UU (unfiltered upstream)		
				Dissolved constituents	SU vs. SD (slump in filtered downstream)	Between treatments: no effect on %ΔTOC or O_2 loss; (2) within treatments: no sig. TOC loss (Fig 3-3, Table 3-2)	
				Settling	SU vs. SS (SS off rotator to allow settling)	(1) Between treatments: no effect on %ΔTOC, reduced O_2 loss; (2) within treatments: no sig. TOC loss *(Fig 3-3, Table 3-2)*	
2016	UP, IN, DN, and 2.79 km DN of slump SE	3.2.2.2, Fig. 3-2	8	Biodegradability vs. transport potential	Sieve size fractions: (1) 2000-63µm (2) 63-20µm <20µm). + unfractionated reference	No sig. diff. in %Δ TOC or %Δ POC changes between size fractions but sig. TOC gain and largest DOC loss for particles <20 µm (Fig 3-3, Table 3-3)	↓ [TSS] in two larger size fractions relative to smallest, two largest also within MQ error

			Transect validation	unfiltered and filtered DN vs. 2.79 km DN. + UP reference	Change in downstream distance: no effect on %ΔTOC; within treatments: no sig. TOC loss (Fig 3-3, Table 3-4)	UP and 2.79 km DN within MQ blank error
2018	HD debris tongue material	3.2.2.4 7	Abiotic O_2 loss	Sterilized debris tongue sediments in Milli-Q (MQ) water vs. MQ control	Rapid O_2 loss in absence of microbial activity (Fig A2-3a)	MQ may accelerate weathering, HD debris sediments an extreme weathering endmember
2019	IN and DN of slump SC	3.2.2.4, 27 Fig. A2-8	paired inorganic carbon changes & chemo-lithotrophy	Unsterilized mimic of SD (2015 treatment) vs. sterilized SD. + MQ blanks	Prior gains not replicated but only ~4% of TOC mineralized, greater sulfate gains and nitrification in unsterilized treatments *(Fig. 3-5)*	SC slump in a different landscape type than SE and HA where prior gains were observed, sterilization treatments may not be a true abiotic control

Table 3-2. Two-way ANOVAs of tests of sources, filtrate, and settling on biodegradability of POC in 2015 experiments. Follow-up tukey-adjusted pair-wise t-tests are shown where significant interactions were present. Since SU treatments were tested 3 times and multiple outcomes were tested, p-values reported in two-way ANOVAs were corrected for false discovery rate (FDR) (19 tests). Degrees of freedom associated with treatment, site, interaction, and residuals are 1, 2, 2, and 12 respectively for all tests.

Effect		Treatment				Site		Treatment*Site	
Test	Variable	estimate	error	F/t[a]	p	F	p	F	p
Control (SU-UF)	$\Delta SUVA_{254}$	-	-	1.45	0.48	1.64	0.37	1.42	0.66
	%ΔDOC	-	-	0.54	0.75	0.02	0.98	0.54	0.81
	%ΔTOC	-	-	0.49	0.75	0.07	0.98	0.98	0.80
	ln(k)	-	-	305.57	0.00	6.43	0.04	8.92	0.04
	HA	2.01	0.17	11.80	<<.001	-	-	-	-
	HB	2.02	0.17	11.83	<<.001	-	-	-	-
	HD	1.13	0.17	6.64	<<.001	-	-	-	-
Source (SU-UU)	$\Delta SUVA_{254}$			2.22	0.34	0.14	0.98	6.51	0.08
	HA	0.40	0.11	3.80	0.00	-	-	-	-
	HB	-0.06	0.11	-0.52	0.61	-	-	-	-
	HD	-0.07	0.11	-0.70	0.50	-	-	-	-
	%ΔDOC	-7.06	2.46	8.22	0.05	1.13	0.47	1.53	0.66
	log(%POC+50)	-0.19	0.04	27.40	0.00	5.08	0.07	2.39	0.42
	%ΔTOC	-	-	2.22	0.34	1.73	0.37	0.78	0.80
	ln(k)			172.43	0.00	43.21	0.00	67.84	0.00
	HA	1.69	0.15	11.60	<<.001	-		-	
	HB	1.90	0.15	13.04	<<.001	-		-	
	HD	-0.28	0.15	-1.89	0.08	-		-	
Filtrate	$\Delta SUVA_{254}$	-	-	2.52	0.34	11.81	0.01	0.41	0.81

(SD-SU)	%ΔDOC	-	-	0.05	0.87	2.71	0.21	2.90	0.42
	%ΔPOC	-	-	0.11	0.85	2.66	0.21	0.20	0.89
	%ΔTOC	-	-	0.37	0.75	2.66	0.21	0.72	0.80
	k	-	-	0.24	0.81	20.12	0.00	0.19	0.88
Settling (SS-SU)	$\Delta SUVA_{254}$	-	-	0.10	0.85	10.46	0.01	0.77	0.80
	%ΔDOC	-	-	5.84	0.10	0.11	0.98	0.39	0.81
	%ΔPOC	-	-	0.38	0.75	1.08	0.47	0.21	0.88
	%ΔTOC	-	-	0.00	0.96	1.36	0.43	0.43	0.81
	ln(k)	-0.67	0.07	81.68	0.00	11.47	0.01	2.46	0.42

[a]F-values are reported for two-way ANOVAS, t-values are reported for follow-up pairwise t-tests

10

Table 3-3. Welch's ANOVA and follow-up Games-Howell pair-wise t-tests of differences between size fractions (2016 experiment). P-values for main ANOVAs are adjusted for false-discovery rate to account for multiples outcomes tested (5 tests). Follow-up tests were only conducted when main ANOVA tests showed a significant difference. Size fractions: SN = 63 – 2000 µm, SL= 20 – 63 µm, SMSC = <20 µm.

					Follow-up tests				
Variable	F	df_{num}	df_{denom}	p	Estimate	95% error	t	df	p
$\Delta SUVA_{254}$[a]	41.63	2	5.8	0.001					
	SL vs SN				2.00E-02	1.75E-01	0.46	5.2	0.894
	SMSC vs SN				3.80E-01	1.75E-01	7.14	5.0	0.002
	SMSC vs SL				3.60E-01	2.60E-01	8.62	6.0	<0.001
%ΔDOC	22.21	2	4.9	0.007					
	SL vs SN				-6.09E+00	1.97E+01	2.00	4.8	0.200
	SMSC vs SN				-1.45E+01	2.00E+01	5.40	3.4	0.018
	SMSC vs SL				-8.39E+00	1.12E+01	5.20	4.3	0.012
%ΔPOC	2.81	2	4.5	0.161					
%ΔTOC	5.13	2	4.4	0.089					
ln(k)	66.66	2	5.9	<0.001					
	SL vs SN				-4.34E-05	4.01E-03	-0.01	9.0	0.992
	SMSC vs SN				3.87E-02	4.01E-03	9.66	9.0	<<0.001
	SMSC vs SL				3.87E-02	4.01E-03	9.67	9.0	<<0.001

Table 3-4. Two-way ANOVAs for transect experiment examining effects of filtrations (unfiltered vs. filtered) and distance (immediately downstream vs. 2.79 km downstream) from slump SE and interactions between the two. Since multiple (4-5) parameters from the same experiment are tested, p-values were corrected for false discovery rate. Degrees of freedom associated with distance, filtration, interaction, and residuals are 1, 1, 1, and 12 respectively for all tests.

Variable	Distance		Filtration		Distance*Filtration		Follow-up tests				
	F	p	F	p	F	p	Est.	se	t	df	p
ΔSUVA254	0.21	0.659	5.59	0.048	12.44	0.013					
DN vs 2.79 km DN (filtered)							-0.09	0.04	-2.174	12	0.050
DN vs 2.79 km DN (unfiltered)							0.12	0.04	2.815	12	0.016
%ΔDOC	7.39	0.031	17.00	0.003	10.87	0.013					
DN vs 2.79 km DN (filtered)							0.67	1.64	0.409	12	0.689
DN vs 2.79 km DN (unfiltered)							-6.96	1.64	-4.253	12	0.001
%ΔPOC[a]	12.01	0.031	-	-	-	-					
%ΔTOC	1.71	0.269	1.99	0.184	0.00	0.949					
ln(k)	12.65	0.020	55.96	0.000	0.95	0.466					

[a]Percent change in POC not tested for filtration or interaction effect because negligible POC concentrations in filtered treatments

Table 3-5. Characteristics of size fractions used in 2016 experiment. %POC indicates POC: TSS. sd = standard deviation. SEM = standard error of the mean.

Size Fraction Category	Unfractionated	0.063 - 2mm	0.020 - 0.063 mm	<0.020 mm
Mean particle size	11.9	48.9	21.67	5.78
sd	3.78	4.6	2.9	2.79
$F^{14}C$	NA	0.4113	0.1332	0.056
sd	NA	0.0019	0.0012	0.0006
calBP (percent representation)	NA	8020 - 7926 (88.3%) 7896 - 7871 (7.1%)	19791 - 19292 (95.4%)	27640 - 27250 (95.4%)
%POC	1.6	3.12	1.35	1.67
SEM	0.03	0.09	0.02	0.02
% of sum initial POC across fractions	NA	12%	15%	73%

Table 3-6. Absolute changes in $SUVA_{254}$ in 2015-16 experiments.

Year	Treatment	Site	$\Delta SUVA_{254}$	95% error	n
2015	Filtered upstream (F)	HA	0.08	0.36	3
		HB	0.11	0.70	3
		HD	0.02	0.08	3
	Unfiltered upstream (U)	HA	-0.25	0.20	3
		HB	-0.06	0.35	3
		HD	-0.02	0.44	3
	Slump in filtered upstream (SU)	HA	0.16	0.47	3
		HB	-0.11	0.16	3
		HD	-0.09	0.15	3
	Slump in filtered downstream (SD)	HA	0.20	0.28	3
		HB	-0.07	0.06	3
		HD	0.04	0.12	3
	SU settle (SS)	HA	0.19	0.41	3
		HB	-0.05	0.20	3
		HD	-0.20	0.60	2
2016	Unfractionated	SE	0.46	0.41	4
	2 - 0.063 mm	SE	0.06	0.15	4
	0.063 - 0.020 mm	SE	0.09	0.10	4
	< 0.020 mm	SE	0.45	0.09	4
	Upstream	SE	-0.07	0.11	4
	Upstream filtered control	SE	-0.07	0.07	4
	Downstream	SE	-0.10	0.17	4
	Downstream filtered control	SE	0.07	0.05	4
	2.79k Downstream	S2	-0.01	0.03	4
	2.79k Downstream filtered control	S2	-0.05	0.07	4

3.9. Figures

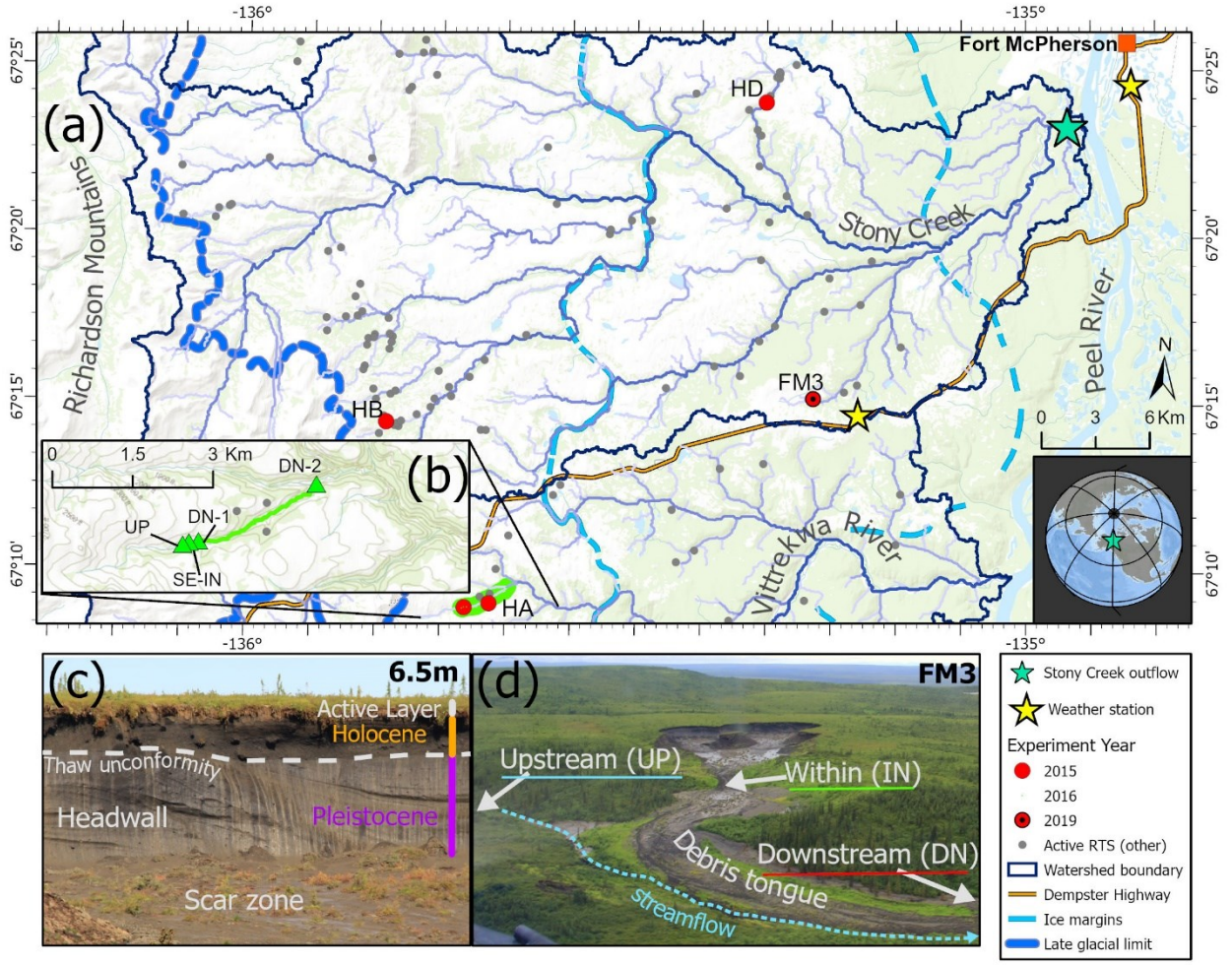

Figure 3-1. (a) Location of slump sites sampled for experiments. (b) 2016 sampling points (green triangles) show sampling locations along a transect which began just upstream of the point where slump SE runoff enters a valley bottom stream. Panel (c) shows headwall units of a slump. Panel (d) shows stream sampling points relative to a slump site, as sampling design used in the 2015 experiment. HA, HB, HD, SE and FM3 are slump site IDs. Active RTS features are from Segal et al. (2016). Former glacial limits of the Laurentide Ice Sheet (ice margins and late-glacial limit) are delineated from Duk-Rodkin and Hughes (1992). Service Layer credits: (1) World Topographic Map: Northwest Territories, ESRI, © OpenStreetMap contributors 2020, HERE, Garmin, USGS, NGA, EPA, USDA, NPS, AAFC, NRCan. Distributed under the Open Data Commons Open Database License (ODbL) v 1.0. (2) World Ocean Base: Esri, Garmin, GEBCO, NOAA NGDC, and other contributors. (3) World Continents.

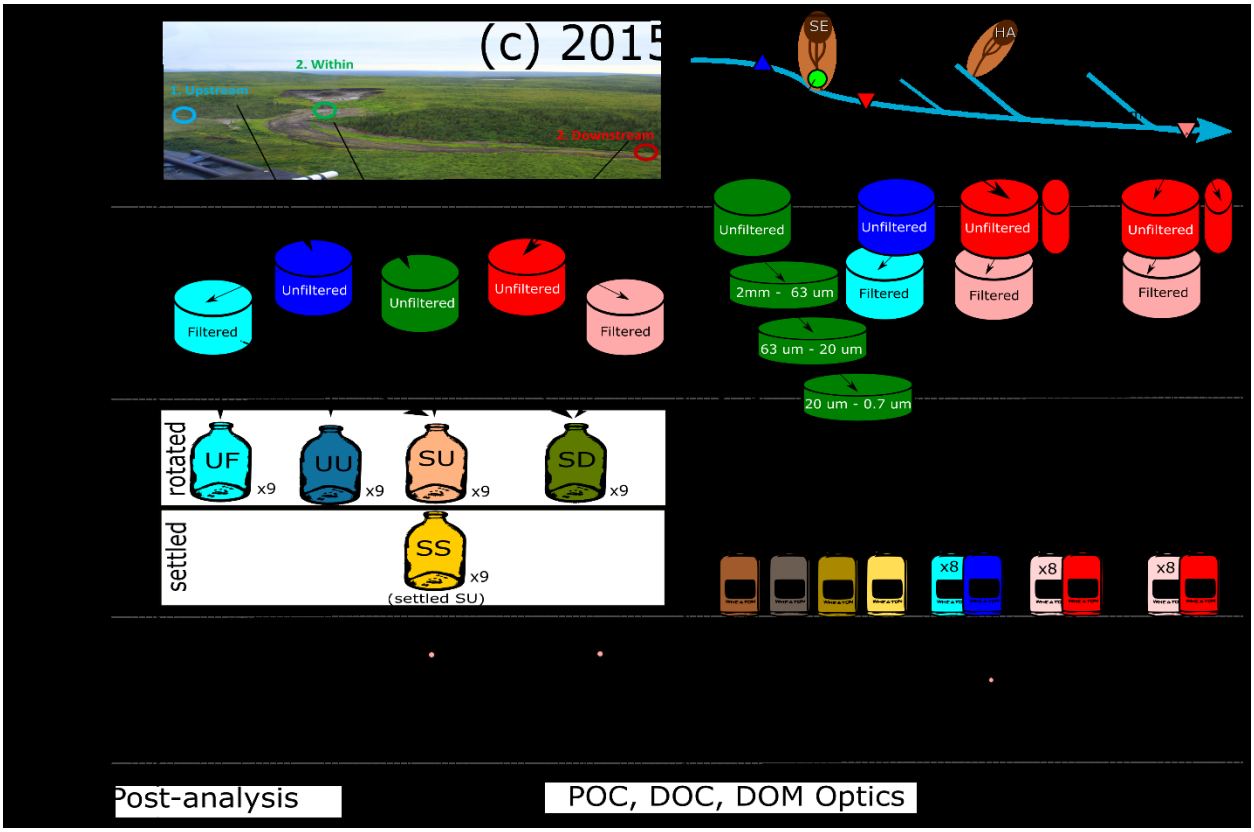

Figure 3-2. Flow chart for processing of (a) 2015 and (b) 2016 experiment. Note, timepoint 2 for 2015 (a) did not last for much longer than timepoint 1 due to rapid oxygen loss. Due to this, and the fact that some bottle replicates had to be removed because of anoxia, data is not presented in the main manuscript. Analyses show particulate (POC) and dissolved (DOC) organic carbon and dissolved organic matter (DOM) optics (SUVA254). Larger diagrams are available in the supplementary. Flow chart for 2019 is in Appendix 2.

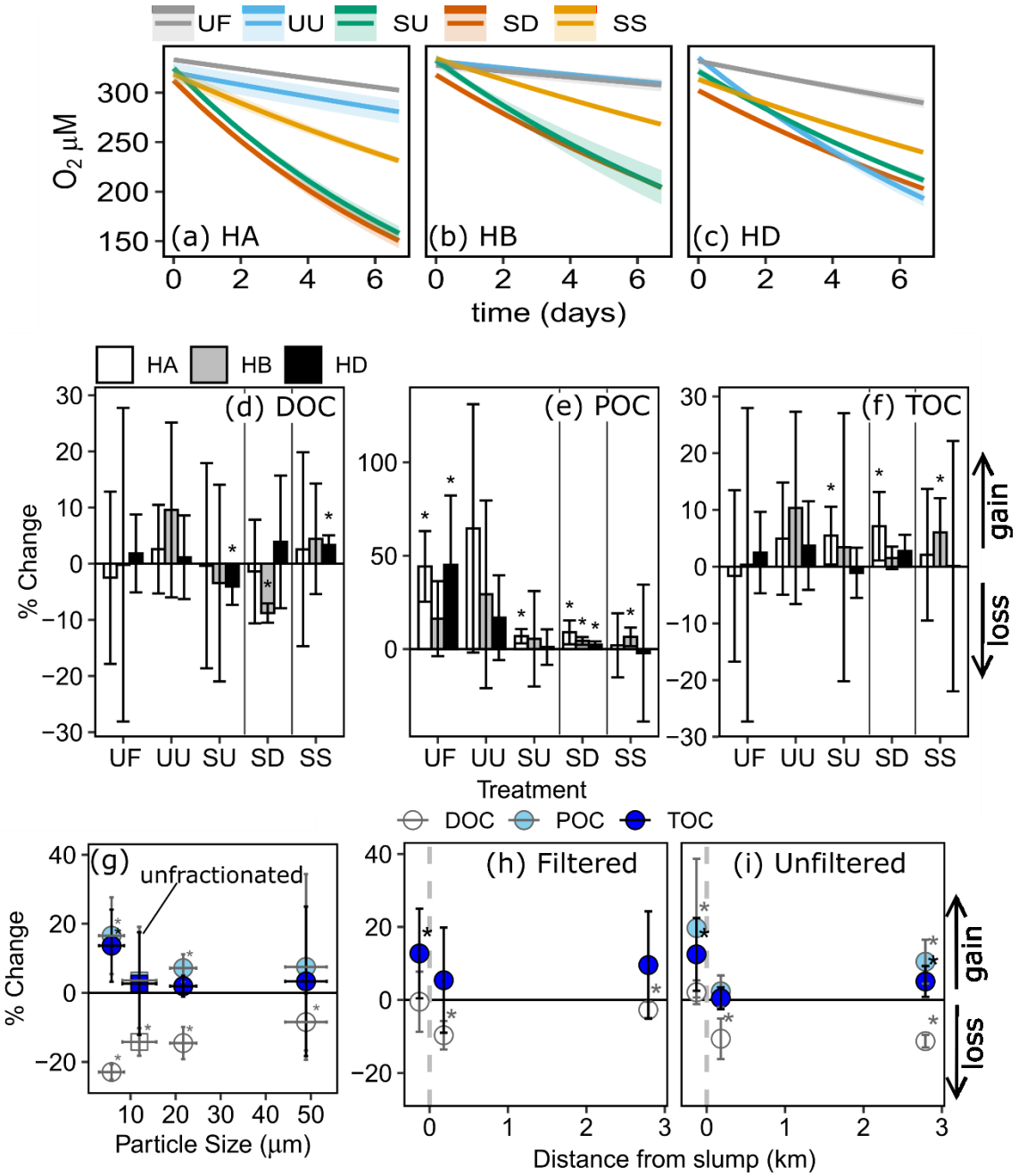

Figure 3-3. (a-c) Modelled (line) O2 (mg L-1) across combinations of source material and settling effects. Percent change in DOC, POC, and TOC in comparison to: (d-f) combinations of source material and settling effects; (g) geometric mean particle size; and (h-i) distance from slump site. Vertical errors are 95% confidence intervals with asterisks marking significant differences from zero. Horizontal errors (e) are particle size geometric standard deviation. Codes (a-f): filtered (UF) and unfiltered (UU) upstream, slump material in upstream (SU) and downstream (SD) filtrate, and SU settled out (SS). HA, HB, and HD are slump sites.

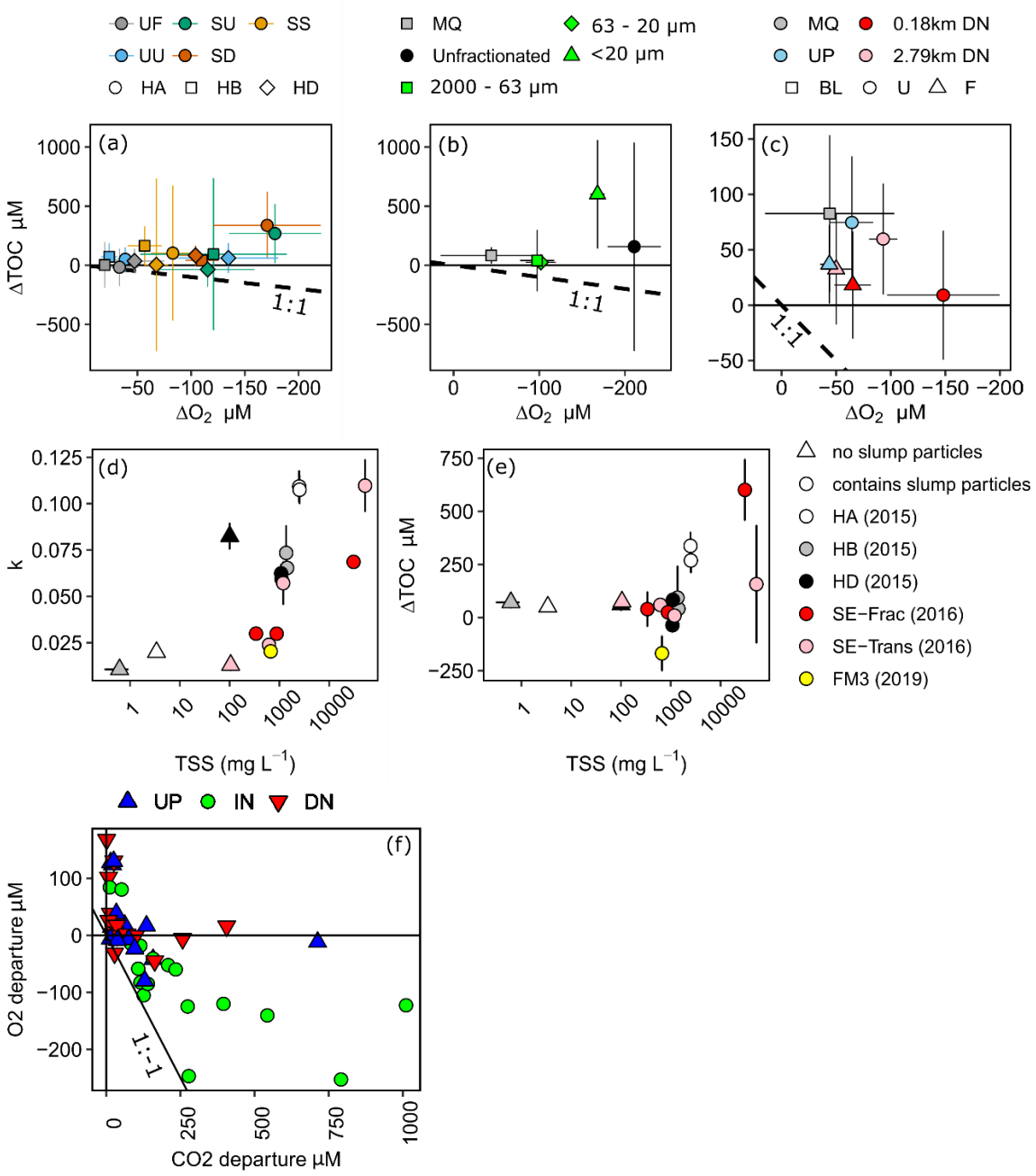

Figure 3-4. Changes in TOC vs. changes in dissolved O2 for: (a) test of biodegradability; (b) site SE fractionation experiment; and (c) site SE transect experiment. Dashed lines in a-c represent predicted loss of OC for respiratory quotient=1 and error bars show 95% confidence intervals. (d-e) Exponential rate of O2 consumption (k) or changes in TOC vs. initial TSS for treatments across experiments, excluding filtered, settled, and sterilized treatments from a-c. SE-Frac indicates the fractionated treatments from panel (b). (f) Departures of O2 and CO2 from atmospheric equilibrium in samples collected upstream (UP), downstream (DN) and within (IN) a series of slump sites on the Peel Plateau. Error bars in (d) and (e) show standard error of the mean. Codes in (a): filtered (UF) and unfiltered (UU) upstream, slump material in upstream (SU) and downstream (SD) filtrate, and SU settled out (SS). HA, HB, and HD are slump sites.

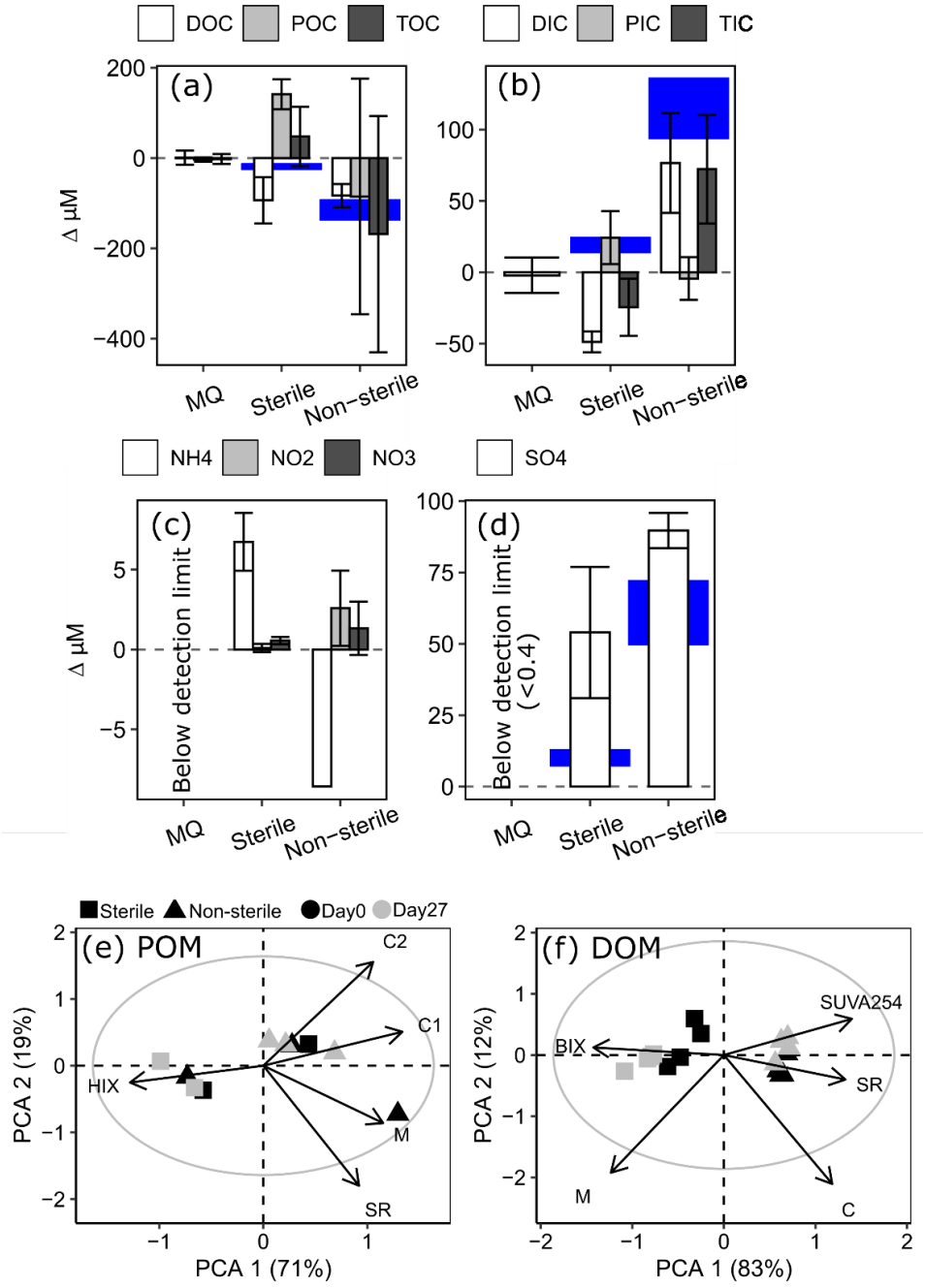

Figure 3-5. Changes in millimolar concentrations of: (a) organic carbon; (b) inorganic carbon; (c) ammonium (NH4+), nitrite (NO2-), and nitrate (NO3-); and (d) sulfate (SO42-) in 2019 test of interferences. Note difference in scales between panels. Blue shades highlight potential carbon gains or losses based on O2 loss and a respiratory quotient of 1 (a-b) and potential SO42– generated from pyrite oxidation (eq. 3). Error bars and blue heights both show a range representing 95% confidence intervals. (e-f) PCA biplot of components 1 and 2 showing variation in POM (e) and DOM (f) optical properties. Grey circle outlines circle of equilibrium contribution, plot shown in scaling 1. Abbreviations of optical indices are provided in Table A**2-5**.

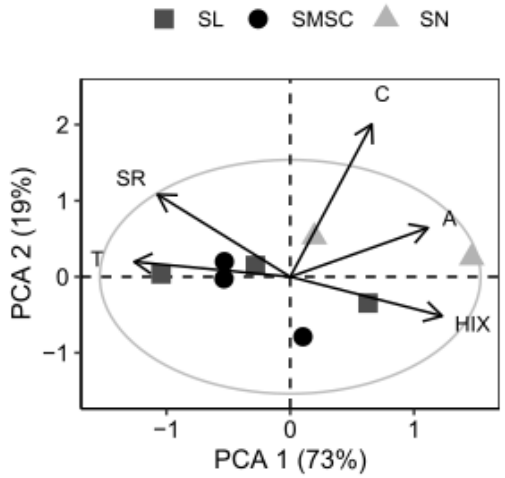

Figure 3-6. Principal components analysis of optical indices for BEPOM of different size fractions. PCA is shown in scaling 1. The grey circle marks the circle of equilibrium contribution. Abbreviations of optical indices are as in Table A**2-5**; SN = 63 – 2000 µm, SL= 20 – 63 µm, SMSC = <20 µm.

Chapter 4. Downstream persistence of particulate organic carbon from permafrost thaw slumps on the Peel Plateau, NT

4.0. Summary

Climate-driven erosion of permafrost terrain via retrogressive thaw slumping in the western Canadian Arctic has increased by two orders of magnitude since the 1980s. This intensification in permafrost erosion primarily occurs along first and second order streams, many of which run across the Peel Plateau and drain into the Peel River. Yet, the degree to which this material can be transported downstream and alter the organic carbon regime of downstream receiving waters has not been documented to date. Here, we show that large loads of organic carbon, primarily in the form of old and degraded particulate organic carbon (POC) from Pleistocene-age permafrost, can be transported tens of kilometers downstream from headwaters on the Peel Plateau into the Peel River. Since the volume of terrestrial material eroded from hillslopes by thaw slumps to headwater streams exceeds the ability of streams to transport it, long term reservoirs are created in the valley bottom to feed future flux. Historical records of organic carbon dynamics in the Peel River suggest that intensification of thaw slumping across the Peel Plateau is resulting in a non-linear increase in total organic carbon loads on the Peel River, caused by increased delivery of POC. Thus, changes in terrestrial erosion, which are affecting less than 1% of the terrestrial area, are already resulting in major changes in the regime of the Peel River, which are poised to cascade through fluvial networks to affect organic carbon and nutrient supplies and quality throughout the Mackenzie Delta and nearshore Arctic Ocean.

4.1. Introduction

Permafrost is a fundamental structural component of Arctic ecosystems (Schuur and Mack 2018). It is a climate-sensitive and globally significant reservoir of carbon (Hugelius et al. 2014, Schuur et al. 2015, Schuur and Mack 2018) and its distribution controls the flow of materials across Arctic landscapes (e.g. water, carbon, nutrients; Walvoord and Kurylyk 2016, Vonk et al. 2019). Across the Arctic, permafrost is warming following trends in increasing air temperatures in the Northern Hemisphere (Biskaborn et al. 2019) and its thaw has the potential to have significant

effects on regional Arctic landscapes and the global climate system (Schurr et al. 2015, Turetsky et al. 2020).

Thaw-driven mass wasting is eroding thousands of cubic metres of terrestrial material, much of which was previously sequestered within permafrost in post-glacial-margin landscapes across the circumpolar Arctic (Kokelj et al. 2021, Kokelj et al. 2017). Though these mass wasting processes may only affect a limited percent of the terrestrial landscape (e.g., <1%, Lewkowicz and Way 2019) their effects on aquatic systems can be extensive (Bowden et al. 2008, Kokelj et al. 2005, Kokelj et al. 2021). In the western Canadian Arctic, retrogressive thaw slumping is intensifying along headwater streams, increasing the rate of erosion of terrestrial material beyond the stream's transport capacity (Kokelj et al. 2021, Shakil et al. 2020). As a result, these features can elevate sediment and particle-associated organic carbon and nutrient concentrations by orders of magnitude and alter the biogeochemical and ecological functioning of affected aquatic systems (Shakil et al. 2020, Chin et al. 2016, Levenstein et al. 2018, Zolkos et al. 2020, Keskitalo et al. 2021).

Quantifying the scales over which materials mobilized by thaw slump features propagate downstream is important for a number of reasons. First, it enables us to determine how intensifying erosion on the landscape will affect downstream aquatic systems and land-ocean linkages (McClelland et al. 2016). Second, it can improve our design of downstream measurements used to understand broader landscape changes (Shogren et al. 2019). Third, it can better constrain the effects of permafrost thaw on global biogeochemical cycles (Hilton et al. 2015). Organic carbon is of particular interest because the balance between its burial and oxidation en route to marine sediments may significantly alter the regional and global carbon cycle (Hilton et al. 2015, Schuur et al. 2015). Furthermore, organic carbon can be an important source of energy for aquatic foodwebs and its transport, along with associated nutrients, within aquatic networks may affect downstream and coastal foodweb dynamics (Casper et al. 2014, Terhaar et al. 2021).

The biogeochemical effects of permafrost-related mass wasting on downstream environments depends on both the magnitude and composition of material travelling through fluvial networks, and how these materials are selectively processed and maintained in suspension during transport. Thaw slumps erode sediments from both permafrost and the active layer (Lacelle et al. 2010, Kokelj and Jorgensen 2013). These sources differ in their chemical composition, decomposition rate, and transportation potential (Bröder et al. 2021, Keskitalo et al. 2021, Shakil et al. 2020). The

ability to detect slump-mobilized organic carbon at increasing watershed scales may also be complicated by additional inputs of particulate organic matter via bank undercutting and erosion (Kokelj et al. 2017). Further, increased inputs of dissolved organic carbon (DOC) at larger watershed scales may decrease the importance of particulate organic carbon (POC) relative to the total organic carbon (TOC) load of a watershed. These "dilutions" by additional sources of particulate and dissolved organic matter (POM, DOM) may reduce the relative importance of slumping on fluvial biogeochemistry as watershed scales increase.

The goals of this study were to: (a) determine the degree to which POC mobilized by thaw slumps is transported downstream; (b) quantify the relative contribution of slump-origin carbon to organic carbon fluxes in slump-impacted watersheds in the western Canadian Arctic; and (c) determine whether long term trends in organic carbon fluxes within the Peel River have been altered by changes in upstream climate-driven permafrost erosion. This was achieved by (a) conducting transect surveys of POC downstream of active thaw slumps and along the mainstem of a slump-impacted watershed on the Peel Plateau, NT, Canada; (b) determining geospatial drivers of organic carbon flux and composition across an impacted watershed on the Peel Plateau; and (c) analyzing historical trends in sediment and organic carbon fluxes in the Peel River, which receives inputs from a series of slump-impacted catchments.

4.2. Methods

4.2.1. Study Region

We undertake this work on the Peel Plateau, a 24, 000 km^2 glacially conditioned landscape characterized by ice-rich, fluvially incised terrain that is representative of other permafrost preserved glaciated landscapes across northwestern Canada, Alaska, and Siberia (Kokelj et al. 2017b) (**Figure 4-1**). The headwaters of east flowing Peel River tributaries originate in mountainous unglaciated terrain where surficial materials are dominated by colluvium, and transition to glacial till with decreasing topographic relief towards the east (Kokelj et al. 2017b, Duk-Rodkin and Hughes 1992). These include the Stony Creek and Vittrekwa River watersheds, which have the second and third greatest density of thaw slumps of watersheds across the Peel Plateau and the greatest density of thaw slumps of Peel Plateau watersheds draining directly into the Peel River (Lacelle et al. 2015). A transition from tundra to shrub to stunted boreal forest in

lowlands is also associated with the regional topographic gradient that generally occurs east-west (O'Neill et al. 2015) and may affect the organic carbon content in active layer and near surface permafrost (see below; Dyke 2005, Burn et al. 1997). On the Peel Plateau, the area affected by slumping has increased by two orders of magnitude since the 1980s and this intensification has increased the number of thaw slumps connected to hydrological networks.

In the late-Pleistocene (ca. 18, 000 to 15, 000 cal. yr. BP, Lacelle et al. 2013), the region was briefly covered by the Laurentide Ice Sheet (LIS). During this time, glacial tills, glaciofluvial and glaciolacustrine materials were deposited in a dynamic ice-marginal setting (Lacelle et al. 2013) and preserved as permafrost was established following glacial retreat (Lacelle et al. 2004, Lacell et al. 2013). Subsequent early Holocene warming was associated with an increase in active layer thickness to ~1.5 fold that of present day conditions (ca. 9,000 cal. yrs. BP, Burn et al. 1997), and an acceleration of mass-wasting (e.g. thaw slumping) and development of colluvial deposits. These processes enabled soil formation, geochemical modification and the incorporation of organics, followed by a cooling period and upward aggradation of the permafrost table (Lacelle et al. 2019). These modified deposits have been preserved in a "relict-thaw layer" situated immediately below present-day active layer soils, demarcated from the unmodified tills below by a thaw unconformity (Lacelle et al. 2019). Thus, the relict-thaw layer can be comprised of a paleo-active layer and/or sediments deposited at the base of hillslopes from past slumping activity (colluvial deposits, Lacelle et al. 2019).

Considering this history, we refer to three main categories of terrestrial material eroded by thaw slumps: (1) the active layer, where soil is developed from the relict-thaw layer, incorporating modern organics; (2) Holocene-age permafrost containing previously thawed diamicton (relict-active layer) and colluvium (slumped sediments); and (3) Pleistocene-age permafrost containing tills that have remained preserved within permafrost. Headwall height, scar zone area, and debris tongue length vary by orders of magnitude across slump features (Kokelj et al. 2021), potentially affecting the relative liberation of different sources exposed in headwalls and their delivery to streams. Bank undercutting and erosion can additionally become increasingly important sources of sediment inputs as watershed scale increases (Kokelj et al. 2017a). Erosion of banks may also be enhanced in smaller watersheds (<10 km^2) as debris tongues entering valleys actively erode the adjacent streambank.

4.2.2. Transportation downstream (Goal 1)

To address our first objective, transect sampling was conducted in a sub-watershed of the Vittrekwa River watershed (**Figure 4-1**). In 2015, two transects were established from the point where thaw slump runoff of an active slump entered a "pristine" stream to 0.4-1km downstream of this inflow. Samples for total suspended solids (TSS), POC, and the ^{13}C signature of POC ($\delta^{13}C_{POC}$) were collected along evenly spaced transects three times from June to August. Discharge measurements were taken at the beginning and end of transects to assess possible dilution via inputs of subsurface flow. Transects were conducted downstream of two slumps representing morphological endmembers. Slump SD is a small slump with thaw depth of ~2m at the time of sampling, while slump SE is a larger slump with a thaw depth of ~23 m, putting these features on opposite ends of the range of thaw depths that can be found for slumps across northwestern Canada (Kokelj et al. 2021). In 2015, average TSS and organic carbon concentrations during the thaw season immediately downstream of SE were orders of magnitude greater than downstream of SD (Shakil et al. 2020). In 2017, measurements were taken at 11 sites along a ~72 km transect in the Stony Creek mainstem from unimpacted headwaters to the outlet of the Peel River (**Figure 4-1**). Sampling was conducted from July 10th – August 7th, with the western-most eight sites sampled on July 25th and July 27th, and sites near the outlet sampled to bookend the transect sampling (July 10th and August 7th, see Table A**3-2**). At these sites, discharge, POC and DOC concentrations, $\delta^{13}C_{POC}$, compositional measures of POM (as base extracted POM; BEPOM, see below), and the ^{14}C signature of POC ($F^{14}C_{POC}$) were obtained.

4.2.3. Contribution to watershed organic carbon fluxes (Goal 2)

To address our second objective, we examined instantaneous POC and DOC fluxes during the middle of the thaw season (mid-July to mid-August) across 34 "end-member" sub-catchments within the Stony and Vittrekwa watersheds, with watershed areas ranging from 0.2 to 105 km^2. Sites were selected for accessibility and to capture the variability in intensity of thaw impact, geology, and vegetation across these two watersheds. Sources and structure of organic matter associated with POC and DOC were characterized using $\delta^{13}C_{POC}$, BEPOM, and optical analyses of DOM. Bank sediment samples were collected where possible across endmember sites and analyzed for percent soil organic carbon content (%SOC), the ^{13}C signature of SOC ($\delta^{13}C_{SOC}$), and base-extracted soil organic matter (BESOM) to determine whether these sources can overlap in

composition with values previously measured for end-member sources to streams (active layer, Holocene and Pleistocene-age permafrost, and periphyton; Shakil et al. 2020). At select sites believed to represent end members of streambank inputs (eroding shale bedrock vs. vegetated banks), $F^{14}C_{SOC}$ of streambank sediments was also collected. Specific conductance and dissolved ion ($Ca^{2+,}$ Na^{+}, Mg^{2+}, Sr^{2+}, SO_4^{2-}) samples were taken as tracers of weathering of minerals exposed by thaw slumping (Malone et al. 2013, Zolkos et al. 2018). $\delta^{18}O_{H2O}$ samples were obtained as potential tracers of massive ice exposed via thaw slumping and potentially contributing to discharge (Lacelle et al. 2013, Littlefair et al. 2017).

4.2.4. Historical trends in the Peel River (Goal 3)

We analyzed long term trends in annual Peel River discharge, DOC, POC, and TSS fluxes by pairing long-term water chemistry from Environment Canada and historical discharge data from the Water Survey of Canada (station 10MC002) in LoadRunner software, which automates runs of the U.S. Geological Survey constituent load-modeling software LOADEST (Runkel et al., 2004). DOC was determined at the Taiga Environmental Laboratory in Yellowknife (NT), as NPOC using a Shimadzu Total Organic Carbon Analyzer on a 0.45 µm filtered sample. POC was determined at the Environment and Climate Change Canada Inorganic Analytical Laboratory via elemental analysis of sediments collected on GF/C filters (nominal pore size of 1.0 µm) using a Perkin Elmer Elemental Analyzer and a CE440 Elemental Analyzer. Years with discharge data gaps greater than seven consecutive days were removed (n=9). We evaluated trends with the nonparametric Mann-Kendall test in R (R Core Team, 2015), using the trend pre-whitening approach (Yue et al., 2002) in the *zyp* package (Bronaugh & Werner, 2013) to account for serial correlation. The years analyzed ranged from 1975 to 2017.

4.2.5. Stream channel characterization and discharge

We measured instantaneous discharge at each sampling point using a pygmy or Redback "AA" current meters and the velocity-area method (Gordon et al. 2005, pg. 93 – 96). Stream channel sections were modified, if necessary, to remove objects creating turbulence (rocks, twigs) and divided into equal subsections. A single velocity measurement was obtained for each subsection by recording the number of revolutions of a current meter at 0.6x the depth. Where the AA meter profile was too large for the stream section, a pygmy meter was used. Where both AA

meter and pygmy meter widths or heights were too large (i.e. very narrow or shallow streams) the float-area method was used to determine velocity in each subsection, where a small buoyant object (short twigs) was placed on the water surface at the center of the subsection and the time it took to travel a known distance was recorded. At 2017 sub-watershed sites, we measured channel slope using a clinometer (Gordon 2004) along three reaches comprising one full meander amplitude at each site. The meander was centered on the sampling site. Slope was calculated as the average of the three replicates with degree measurements converted to m m^{-1}. Slope and discharge measurements were then used to calculate stream power (see A1.9). At sites 2 – 10 of the Stony Creek transect, discharge could only be measured across part of the channel width, thus full estimated of discharge were calculated by scaling up the discharge in relation to the proportion of the channel width it represented. At site 11, discharge could not be reliably measured, thus fluxes are not reported.

4.2.6. Stream sampling

Water samples were collected in pre-acid-leached HDPE bottles or DI-leached LDPE cubitainers when greater volumes were needed for suspended particulate parameters. Both containers were triple sample rinsed. Water samples for $\delta^{18}O$ analysis were collected in the field using a syringe, filtered through a 0.45 µm cellulose acetate syringe filter into a glass vial, sealed with an air-tight cap and no headspace, and stored at 4°C in the dark until analysis. Suspended particulate material was collected on pre-weighed and pre-combusted (450 °C, 5h) glass fibre filters (Whatman GF/F; 0.7 µm nominal pore size) within 24 h of collection and stored frozen for analysis of POC & $\delta^{13}C_{POC}$, BEPOM, and Chlorophyll α concentration. Samples for $F^{14}C_{POC}$ collected on 25 mm pre-combusted quartz fiber (QM/A, 2.2 µm nominal pore size). Due to high sediment loads at some sites, when collecting for dissolved constituents, all water samples were allowed to settle for ~24 h prior to vacuum filtration (following Littlefair et al. 2017) through pre-combusted glass fibre filters (Whatman, GF/F). Filtrate for DOC analysis was stored in pre-combusted glass vials and preserved with 1 uL mL^{-1} of concentrated trace metal grade HCl (following Vonk et al. 2015). Filtrate for DOM absorbance was stored in pre-leached HDPE bottles. Filtrate for analysis of cations and trace metals (Ca^{2+}, Na^{+}, K^{+}, Mg^{2+}, Sr^{2+}, dissolved Fe (dFe)) was stored in 15 mL polyethylene centrifuge tubes (Corning ®) and preserved with 18% trace-metal grade HNO_3 to a pH of < 2.0. Filtrate for analysis of anions (SO_4^{2-}, Cl^{-}) was stored in

15 mL polyethylene centrifuge tubes (Corning ®). All filtrate sample bottles were triple sample rinsed and stored in the dark at ca. 4°C.

4.2.7. Streambed and streambank sampling

Across sub-catchments, streambed particle size was determined using the Wolman pebble count (Wolman 1954). Briefly, 100 'pebbles' were collected and sized along a transect zigzagging across the stream reach, with the size bin determine by the recording the largest hole size on a gravelometer that could retain the pebble (one less than smallest size it can pass through). Bins consisted of 180, 128, 90, 64, 45, 32, 22.6, 16, 11, 8, 5.6, 4, 2.8, 2, and <2 mm. Pebble counts spanned riffles, pools, and banks. The percent of bed material less than 2mm (%fines) was estimated using the *approx()* function in R stats (R Core Team 2013) when plotting cumulative percent against the mid-point of each bin size. At three sites, all 100 counts were recorded below 2mm so %fines were recorded as 100%. At seven sites, pebble count was not conducted because: (1) the streambed was primarily vegetation/algae or moss covering what appeared to be bedrock (four sites); or (2) selective difficulty picking up larger pebbles or stones from the streambed under cold conditions (3 sites). Streambank sediments were also collected across sub-catchment sites from areas that appeared to be actively eroded by the stream system to account for these additional sources of terrestrial material contributing to organic matter within the stream network. A pre-combusted stainless-steel scoopula was used to scoop material from the erosion face into a whirlpak bag for %SOC and $\delta^{13}C_{SOC}$ and two new polyethylene centrifuge tube (Corning ®), one for BESOM and one for $F^{14}C_{SOC}$ analysis. Material was stored in the dark at -20°C until shipment to the University of Alberta.

4.2.8. Laboratory Analyses

4.2.8.1. Dissolved Analyses

Dissolved organic carbon (DOC) concentration was determined as non-purgeable organic carbon from three injections with a coefficient of variation <2%, or most similar 3 of 5 injections on a Shimadzu TOC-V analyzer. Cations and trace metals (Ca^{2+}, Na^{+}, K^{+}, Mg^{2+}, Sr^{2+}, dFe) and anions (SO_4^{2-}, Cl^{-}) were analyzed at the University of Alberta Biogeochemical Analytical Services Laboratory by Inductively Coupled Argon Plasma Optical Emission Spectrometer (Thermo ICAP-

6300) and Ion Chromatography (Dionex DX-600) respectively. Methods were modified from US EPA 200.7 and US EPA 300.1 respectively. Detection limits were 0.0053 (Ca^{2+}), 0.0160 (Na^{+}), 0.0092 (K^{+}), 0.0103 (Mg^{2+}), 0.0157 (Sr^{2+}), 0.0161 (dFe) ppm, 0.04 (SO_4^{2-}) and 0.03 (Cl^{-}) ppm.

4.2.8.2. Particulate Analyses

Filters for POC, $\delta^{13}C_{POC}$, and $F^{14}C_{POC}$ were oven dried at 60 °C for 24 hours, weighed, and fumigated under heat (60 °C) for 24 hours by placing 25 mL of 12M trace metal grade HCl into a desiccator in an oven to remove carbonates and dolomites (Whiteside et al. 2011). Following fumigation, samples were air dried in a second desiccator and were then re-oven dried at 60 °C for 24 hours (Whiteside et al. 2011). NaOH pellets were kept in a weigh dish in the second desiccator to consume acidic fumes and reduced acidity of the filters prior to oven drying. Dried filters were packed into tin capsules and analyzed for POC and $\delta^{13}C_{POC}$ on an elemental analyzer interfaced to a PDZ Europa 20-20 isotope ratio mass spectrometer (UC Davis Stable Isotope Facility). $F^{14}C_{POC}$ was analyzed by Accelerator Mass Spectrometry following pellitization at the University of Ottawa (A.E. Lalonde AMS Laboratory).

4.2.8.3. Streambank sediment samples

At the University of Alberta, all sediment samples were freeze dried. Samples collected in whirlpak bags were ground with a stainless-steel coffee grinder, cleaned between samples using dilute HCl followed by a thorough rinse with 18.2 Ω Milli-Q water. Subsamples of ground sediments were weighed into silver capsules that were exposed to concentrated trace-metal grade HCl fumes for 24 hours (details of fumigation procedure in Shakil et al. 2020, following Whiteside et al. 2011). Silver capsules were sealed, packed into a tin capsule, and shipped to the UC Davis Stable Isotope Analysis laboratory for analysis of %SOC and $\delta^{13}C_{SOC}$ as described above. Samples selected for $F^{14}C_{SOC}$ analysis were disaggregated using a pre-combusted aluminum rod in the 15 mL centrifuge tube following freeze drying. Then, samples were spread on a pre-combusted glass petri-dishes and examined under a dissecting microscope to remove any large debris or material (e.g. twigs, large rocks) that contrasted the bulk background sediments. At the University of Ottawa Radiocarbon laboratory, subsamples of sediments were then pre-treated to remove carbonates using heated acid washes (HCl, 1M, 80°C, 30 min; “A” treatment from Crann et al.

2017). Acid washes were repeated until effervescence stopped occurring in the samples; across all samples two rounds of acid washes were sufficient.

4.2.8.4. Optical characterization of organic matter

Filters collected for BEPOM were base-extracted following Osburn et al. (2012). Extractions were analyzed for absorbance from 240 – 800 nm at 1 nm increments in a 10 mm cuvette using an integration time of 0.1 seconds (Horiba Aqualog). The same sample was then analyzed for fluorescence at excitation wavelengths from 230 – 800 nm at 5nm increments, emission wavelengths from 118.782 – 828.183 at ~2.3 nm increments, an integration time of 2 seconds, and Medium CCD Gain. Samples were diluted when optical density was greater than 0.4 at 240 nm (Osburn et al. 2012) or if counts on the machines exceeded 50,000 outside of the Rayleigh scatter lines. Raw excitation-emission matrices were blank-corrected, corrected for inner filter effects, and normalized to Raman Units. First and second order Rayleigh and Raman scatter were excised, and all excised scatter was interpolated over except for first order Rayleigh scatter. To understand variation in POM composition across sites and sample types, we applied a previously-published PARAFAC model that identified five components using a series of BEPOM samples from subcatchments within this study and sites upstream of, downstream of, and draining thaw slumps (Shakil et al. 2000). Further details on BEPOM extractions and PARAFAC modelling can be found in Shakil et al. (2020). Five components were identified by PARAFAC for BEPOM samples. P1-4 (BEPOM components 1-4) were associated with terrestrial humic-/fulvic-like peaks, while P5 was associated with a tyrosine-/protein-like peak (component descriptions in Shakil et al. 2020). P1 and P3 have been previously identified as components that undergo clear change in their contribution with the addition of slump material into streams, (with P1 representing degraded organic matter at a later diagenetic state, and P3 representing material that has undergone relatively less reworking (Shakil et al. 2020). Notably, P1 has a much higher contribution to the fluorescent POM pool at slump impacted sites, while P3 is proportionately much more important in BEPOM samples unimpacted by slumping (Shakil et al. 2020).

DOM absorbance was measured within seven days of collection using an Ocean Optics UV-VIS instrument with a Flame spectrometer module (FLMS01220). Scans were conducted from 220 – 800 nm using an integration time of 1.5s, the average of 10 scans per reading, and a boxcar width of 1. A reference measurement was conducted using 18.2 Ω Milli-Q water in the same quartz

cuvette. Samples were baseline corrected using the average absorbance from 700-800 nm and spectral slope (S_R, Helms et al. 2008) and Fe-corrected $SUVA_{254}$ (Weishaar et al. 2003, Poulin et al. 2014) were calculated.

4.2.9. Geospatial Analyses

Watershed delineations were based on gridded (30 m) Canadian Digital Elevation Model (CDEM) products from Natural Resources Canada (NRCan; https://open.canada.ca), stream networks vectorized in the National Hydro Network, and visible in multispectral imagery from Copernicus Sentinel data (2017; European Space Agency, https://sentinel.esa.int/; St. Pierre, Zolkos, and Shakil et al. 2018). Stream networks were delineated from the CDEM. Prior to delineation, CDEM data were reconditioned using stream vectors from the NRCan National Hydro Network (NHN). Prior to reconditioning, these stream vectors were modified solely for the sampled sites to match current stream networks. This was done by overlaying NHN networks on multispectral imagery from Copernicus Sentinel data (2017) (European Space Agency, http://sentinel.esa.int/). Stream networks in the 2017 Sentinel-2 imagery were found to match 2015 and 2016 stream networks and was used to ensure consistency in the stream network delineation used for related projects spanning 2015 – 2017 on the Peel Plateau.

To assess landscape controls on organic carbon flux and composition, we delineated active retrogressive thaw slumps (RTSs) (Kokoszka and Kokelj 2021, Zolkos et al. 2020) and derived: (a) terrain slope, roughness, and elevation; (b) percent watershed composition of geological units; (c) percent watershed composition of land cover units and lakes and ponds; (d) primary productivity and SOC content in the top 100 cm; and (e) thaw slump activity connected to streams in the watershed (Table A3-3). Mean watershed slope and elevation were derived from the CDEM using the Slope and Zonal Statistics tool in ArcGIS Pro 2.8. Percent shale in bedrock units was derived by intersecting polygons of geological units delineated from Norris (1985) with delineated watersheds. Similarly, percent surficial geology units were calculated by intersecting polygons of geological units from Côté (2013) with watersheds. Percent land cover was derived by converting the 2015 Land Cover raster data to polygons and intersecting them with watersheds. The average of total gross primary production from 2017-07-04 to 2017-08-13 (covering the period of study) was derived in Google Earth Engine by summing 8-day GPP MODIS data products, and then calculating the average per watershed area. Annual net primary production (NPP) for 2015 was

also averaged per watershed in Google Earth Engine using NPP derived from MODIS data. Soil organic carbon content in the top 1 m (kg C m^{-2}) (Hugelius et al. 2013) was also calculated as the area-weighted mean for each watershed. The stream distance to the nearest active slump was also determined in ArcGIS Pro 2.8 by manually selecting the nearest slump to the sampling point and calculating the path length using Network Analysis. Further details of spatial data are in Table A3-3.

4.2.10. Data Analysis

Two partial redundancy analyses (pRDA) analyses were used to determine drivers of organic carbon yields (DOC, POC, and TOC yields) and DOM and POM composition in the 34 end-member sub-catchments, which include both slump-affected and unaffected sites, with the effect of Julian day conditioned out. Dependent variables for DOM and POM composition were selected as metrics that have been shown to change with the input of slump material into streams, to assess whether any watershed characteristics aside from those quantifying slump impact might drive changes in these composition indices. These variables were $\delta^{13}C_{POC}$, %POC and the percent contribution of BEPOM PARAFAC components 1 and 3 (P1 and P3) for POM composition (Shakil et al. 2020) and $SUVA_{254}$ and S_R for DOM composition (Littlefair et al. 2017). For both pRDA analyses, explanatory variables consisted of variables that described water chemistry ($\delta^{18}O$ and Ca yield), soil and geology, landcover, thaw slumping, stream morphology, watershed slope, runoff (water yield), and rainfall (**Table 4-1**). Chlorophyll α concentrations were not included within water chemistry because they were below the detection limit (1 µg L^{-}) for most of the sites. Although distance to the nearest slump could not be included because many sites were not affected by any slumping, distance effects were examined in relation to streambed fines (see below). To reduce the effect of outliers on the correlations calculated for RDA, all variables were transformed using log(x+2), except for $\delta^{18}O$. To reduce effects of multi-collinearity and find the most parsimonious model we performed automated forward selection using the *ordiR2step* function from the R software (R Core Team, 2018) package *vegan* (Oksanen et al. 2018). The function builds the model forward to maximize the adjusted R^2 at every step and stops when the adjusted R^2 starts to decrease, or the permutation p-value exceeds 0.05, or the adjusted R^2 of the global model (containing all explanatory variables, specified using the *scope* term) is exceeded. Forward selection was used as the explanatory variable selection method because of the large number of

explanatory variables relative to sample size. Where effects on a single variable were of interest for further investigation (e.g. TOC yields alone), a linear regression was used, with the dependent variable log-transformed as needed to improve model residuals.

4.3. Results

4.3.1. Transportation downstream (Goal 1)

Compositional changes in sediments and POC were sustained for the entire distance of the 2015 transects (400 to 1000 m downstream of SD and SE respectively). Compared to upstream values, %POC decreased immediately downstream of slumping, and remained low throughout the transect at both slump sites (**Figure 4-2**a) while δ^{13}C-POC values increased and remained elevated for the duration of the transect (**Figure 4-2**b). There was no systematic decline in POC concentrations or fluxes with increasing distance downstream (**Figure 4-2**c-d), except for a slight decline in the first 400m during the August transect at site SE. In several instances POC concentrations and fluxes were greater at various downstream points along the transect than immediately downstream of both slump SD and SE.

Along our longer, 71 km transect, GPP, $\%RTS_{active}$, and %moraine increased from the headwaters towards the Stony Creek outlet, while watershed slope and %colluvial decreased (**Figure 4-3**b-c). While DOC concentration and flux generally increased downstream through the Stony Creek mainstem, DOC did not substantially increase as impacted watersheds began draining into the mainstem (**Figure 4-3**d). In contrast, POC concentration and flux increased from 0.309 to 74.3 mg L^{-1} and 1.45 to 269 g s^{-1} with the inflow of water from slump-affected watersheds (**Figure 4-3**e). After this initial spike, both POC concentration and flux decreased to 7.78 mg L^{-1} and 40.8 g s^{-1} respectively. POC concentrations remained within range of 12 – 23 mg L^{-1} until the outlet of the transect, while increasing discharge resulted in an increase in flux, except for a drop-off at the end of the transect likely due to the lower discharge on this sampling day (**Figure 4-3**a). Compositional parameters also changed in accordance with previous records of changes upstream and downstream of slumps (Shakil et al. 2020, **Figure 4-3**f-i). The contribution of the more degraded P1 to the overall fluorescent pool increased beyond the standard error associated with previous measurements upstream of thaw slumps to be closer to values previously measured immediately downstream of thaw slumps, while the relatively fresher P3 simultaneously decreased

to become more like contributions previously measured at downstream sites. This change was markedly greater at the first introduction of slump material into the mainstem where POC concentrations also spiked. $\delta^{13}C_{POC}$ increased, while %POC decreased. $F^{14}C_{POC}$ also decreased from 0.7 to less than 0.1 at the initial input of slumping and remained below 0.25 until the outlet. Notably, $F^{14}C_{POC}$ tracked changes in fluorescence contributions of P1 and P3 (**Figure 4-3**k). $F^{14}C$ values of DOC and streambank material collected at the Stony Creek outlet (sites 10 and 11) were substantially elevated relative to $F^{14}C_{POC}$, with DOC reflecting modern $F^{14}C$ values (**Figure 4-3**j).

4.3.2. Contribution to watershed organic carbon fluxes (Goal 2)

Total organic carbon fluxes were generally greater at higher stream orders, though some slump affected sub-catchments were transporting OC in quantities comparable to streams twice their order (**Figure 4-4**a). In slump-affected sub-catchments, most of the organic carbon moving through the stream network was in the form of POC (**Figure 4-4**b). However, while the proportion of TOC as POC could be 100% in second to fourth order slump-affected sub-catchments, this proportion fell to closer to 75% at Stony Creek mainstem sites of 6th order and greater (**Figure 4-4**b).

4.3.3. Drivers of variation within sub-catchments

The majority of the Stony Creek watershed (~80%) is underlain by bedrock containing shale. Most of the surficial material consists of colluvial (33%), piedmont (29%), and moraine (30%), followed by alluvial (5%) and organic (2%) materials. The majority of the landcover in the watershed is categorized as lichen/moss (47%) and shrubland (29%), followed by forests (13%) and barren-land (8%), with barren land primarily comprising area in the western mountainous region of the watershed. In 2017, the watershed was affected by 109 active slumps covering 0.37% of the watershed area. Less than 1% of the watershed (~0.8%) area is covered by lakes, while landcover classified as wetland accounted for less than 0.002% of the watershed area. Few to none of the sub-catchments studied had a proportion of their area classified as alluvial, bedrock, fluvial, glaciogenic, or organic, thus these surficial geology units were not used as geological drivers. Proportion of wetlands and urban land cover was similarly excluded because of its low coverage.

Across sub-watersheds, POC and TOC yields varied by 4-5 orders of magnitude ranging from 0.1 to 22, 112 mg s^{-1} km^{-2} and 2.6 to 22, 132 mg s^{-1} km^{-2}. DOC yields showed clear but more

muted variation from 2.52 to 160 mg s^{-1} km^{-2}. The explanatory variables selected as drivers of variation in DOC, POC, and TOC yields among watersheds consisted of water yield, GPP, and $\%RTS_{active}$ (**Table 4-1**). The adjusted R^2 of the model (78%) indicated these variables could explain most of the variation in the dataset with only 4% of the variation in the dataset conditioned out by Julian Day. A permutational ANOVA test found the overall model, RDA axes 1 and 2, and all three explanatory variables to be significant ($p<0.001$). Further variance partitioning with each explanatory variable and the conditioning term (Julian day) found that the adjusted R^2, while controlling for the effect of other variables, was greatest for $\%RTS_{active}$ (33%), followed closely by water yield (30%), and then GPP (12%). A biplot of RDA 1 and RDA2 (**Figure 4-4**c) revealed one gradient explaining variation in TOC and POC, and a second gradient explaining variation in DOC. Variation in POC and TOC yields were primarily driven by $\%RTS_{active}$ followed by GPP. Variation in DOC yields were largely be driven by water yield.

Further exploration of the variables driving TOC, POC and DOC yields used linear models to assess the relationship with $\%RTS_{active}$, GPP, and water yield. We found $\%RTS_{active}$ to be a significant predictor ($p<0.001$) for both TOC and POC yields, explaining 66% and 65% of the variation respectively. Estimates of model slopes suggested that TOC and POC yields increase by a factor of ~9 and 13 for every percent increase in $\%RTS_{active}$ (Eq. 1, errors of slope and intercept are shown in square brackets). Water yield was a marginally insignificant ($p=0.0684$) predictor of TOC yields but was retained in the model presented below, while neither water yield nor GPP were significant predictors of POC. $\%RTS_{active}$ was not a significant predictor of DOC yields, which was instead driven by GPP and water yield ($p << 0.001$ for both predictors).

$$\log(TOC_{yields}) = 0.893[\pm 0.110](\%RTS_{active}) + 0.019[\pm 0.010](\text{Water Yield}) + 1.159\ [\pm 0.161] \quad \text{(Eq. 1)}$$

$$\log(POC_{yields}) = 1.34[\pm 0.17](\%RTS_{active}) + 0.336\ [\pm 0.197] \quad \text{(Eq. 2)}$$

$$\log(DOC_{yields}) = 7.33[\pm 1.63](GPP) + 0.045\ [\pm 0.006](\text{Water Yield}) \quad \text{(Eq. 3)}$$

POC and DOC composition also showed broad variation across sub-catchments. Contributions of the first four BEPOM PARAFAC components, which represent POM of terrestrial origin, ranged from 71 – 94% of peak fluorescence across sites. Across sub-watersheds P1 (terrestrial organic matter at a later diagenic state) ranged from 24 to 57% and P3 (terrestrial organic matter relatively fresher than P1) from 5 to 43%. $\delta^{13}C_{POC}$ ranged from -31.19 to -26.71 and

%POC ranged from 0.66 to 33%. DOM variables S_R and $SUVA_{254}$ varied by 0.39 to 1.4 and 1.69 to 5.87 respectively. Reductions in the dataset to only use complete cases in the RDA resulted in some minor reductions in ranges of $\delta^{13}C_{POC}$ (-29.50 to -26.80), Sr (0.50 to 1.4) and SUVA254 (2.11 to 5.87).

The explanatory variables selected as drivers of variation in POM and DOM composition were calcium yield and GPP. Only 2% of the variation in the dataset was conditioned out and the adjusted R^2 of the model was 40%. Permutational ANOVAs found that the final model, RDA axis 1, and both terms were significant ($p<0.001$). RDA axis 2 was not found to significantly explain variation in the compositional data. While neither $\%RTS_{active}$ nor cumulative count of RTS were selected, a biplot of RDA 1 and 2 revealed that RDA1 separated watersheds affected by slumping from those not affected by slumping, with watersheds affected by slumping having a greater percentage of component P1, a more enriched $\delta^{13}C_{POC}$ signature, and lower molecular weight (greater S_R) and aromaticity (lower $SUVA_{254}$) of DOM. Thus, we re-ran the compositional RDA with the presence of slumping added in as a categorical variable. The final selected model consisted of slump presence, calcium yield, %area affected by moraine, stream power, and GPP, and the R^2_{adj} increased to 62%. Through variance partitioning we found calcium yields (R^2_{adj} = 24%) and presence vs. absence of active RTS affecting stream networks (16%) to account for the greatest variation in the dataset, when controlling for other variables in the final model (**Figure 4-4**e).

4.3.4. Changes in proportion of fine sediments across sub-catchments

Slumping also increased the proportion of fine sediments within sub-watershed streambeds. Streambeds sampled within watersheds that had any active slumping had significantly more %fines (increase of 22.74 ± 6.622 %, p=0.002, **Figure 4-5**a). The distance from the nearest slump did not have a significant effect on variation in %fines for sites affected by active slumping ($p>0.05$, **Figure 4-5**b).

4.3.5. Streambank source comparisons with thaw slump end members

%SOC and $\delta^{13}C_{SOC}$ of depositional streambank samples overlapped with multiple terrestrial end-member sources (**Table 4-2**). Average streambank $F^{14}C_{SOC}$ values in this study (0.195 ± 0.118 *mean* ± *se*) were similar to values previously observed for Holocene-age permafrost (0.112 ± 0.213) but were greater than those observed for Pleistocene-age permafrost (0.005 to

0.001). Stony Creek $F^{14}C_{POC}$ values (0.0981 – 0.2307) ranged from being below and above average values for streambank samples. Though the range in streambank samples indicate the possibility of streambanks samples (0.086 to 0.383) being more depleted than values observed in the Stony Creek mainstem, the minimum value, which was the only one below the most depleted values in the Stony Creek, was from one extreme end-member sample in a mountainous watershed where shale bedrock was exposed. (sub-catchment site 30).

4.3.6. Historical trends in the Peel River (Goal 3)

We found no significant linear trend in annual river discharge and annual POC and TSS loads in the Peel River from 1974 (TSS) / 1979 (POC) to 2017. However, annual DOC loads did increase significantly from 1979 - 2017 (**Figure 4-6** a-c). However, we do note that two major outliers in annual POC loads occurred in 2014 and 2016 and were ~20 Gmol y^{-1} greater than any other record during the period. Visual patterns in annual POC loads suggest that sometime between 2000 and 2010, a step change in the annual loads of POC occurred. This increase far exceeds any increase in DOC annual loads over the period. Variability in TSS loads appeared to substantially increase in the late 1990s. Like POC, the highest TSS annual loads on record occurred during 2014 and 2016, but these years were not outliers to the same degree as POC.

4.4. Discussion

4.4.1. Downstream transport of slump mobilized organic carbon (Goal 1) and contribution to watershed organic carbon fluxes (Goal 2)

Climate-driven permafrost erosion in the western Canadian Arctic has intensified by orders of magnitude over the past several decades, with this intensifying geomorphic activity occurring along first and second order headwater streams (Kokelj et al. 2021). Hillslope erosion by thaw slumps tend to erode sediments beyond the transport capacity of streams (Kokelj et al. 2021). Volume estimates of scar areas and debris tongues for slumps with scar areas of ~6 and 32 ha (FM3 and FM2 respectively), which range from the medium to large size of slumps in the western Canadian Arctic (Kokelj et al. 2021) suggest that 80% of the material originally eroded is retained within immediate valley bottom debris tongues (Shakil et al. 2020, Kokelj et al. 2021). Here, we find that the material that does enter suspension immediately downstream of slumps can continue

to be transported along shorter (400m to 1km) distances. Across these shorter-scale transects, we found no consistent decrease in POC concentration or flux, with values sometimes increasing downstream. In contrast, we did find major declines along in the 72 km transect along the Stony Creek mainstem between sites 3 and 4, where POC concentration and flux decrease by 90% and 85% respectively despite increasing discharge and antecedent rainfall, which are both important for sediment mobilization (Kokelj et al. 2015) (see below). Despite this, our results indicated that slump-derived POC was the dominant form of organic carbon exiting Stony Creek. This reinforces findings of Keskitalo et al. (2021) that recalcitrant organic carbon mobilized by slumps from permafrost can be traceable kilometers downstream.

Across first to fourth order streams, streams affected by slumping had orders of magnitude greater organic carbon than streams of the same order not affected by slumping. These large organic carbon fluxes increased or were maintained at 6th order streams including the outlet of the Stony Creek. Across all stream orders and the outlet, POC represented the majority (greater than 50%) of the organic carbon moving through the stream system. The proportion of POC contributing to total organic carbon in slump affected streams and at the outlet is likely equivalent to the proportion of slump-mobilized organic carbon contributing to TOC at the outlet during the periods within this study since (a) $F^{14}C_{DOC}$ values near the Stony Creek outlet suggest DOC primarily originates from modern material (e.g. leaching from vegetation and the active layer); (b) $\%RTS_{active}$ was the strongest predictor of POC and TOC yields across sub-catchments but was not a significant predictor of DOC; (c) compositional metrics indicate that outlet POC was most similar to POC mobilized from slumps; (d) streambank sediments that could be eroded into the stream near the Stony Creek outlet had consistently higher $F^{14}C$ values than the POC in the stream suspended load. We note that shale bedrock outcrops do occur along streams on the Peel Plateau, with shale having $F^{14}C_{SOC}$ values as depleted as the $F^{14}C_{POC}$ from the effectively radiocarbon dead values of Pleistocene-age permafrost. While POC loads in mountainous streams during our sampling periods were negligible compared to POC loads in slump-affected streams, storm events would enhance erosion of these outcrops and increase the contribution of this material to the mainstem. However, storm events would also enhance transport of loosely consolidated fine material in slump scar zones, debris tongues, and slump-origin material on streambeds, suggesting that material eroded via retrogressive thaw slumps would still be the dominant form of POC at the outlet.

Stream power has long been used as an important variable dictating the sediment transport capacity of a stream and can increase or decrease downstream with changes in discharge and slope, the two variables that, alongside gravity and water density, define stream power (Dingman 2002). The lack of change in POC in short distance transects downstream of slumps is likely due to consistency in discharge and slope across the duration of the transect. Generally, discharge tends to increase with increasing watershed scales, while channel slope decreases with drainage area on the Peel Plateau. A major reduction in POC concentration and flux between transect sites 3 and 4 occurred as the watershed transitioned from mountainous terrain to more gently sloping hillslopes. Though antecedent rainfall and discharge were greater at the downstream site, mean watershed slope decreased from 12.8 to 11.0 degrees, suggesting that stream slope may have declined enough to reduce the stream transport capacity below what was required to transport the incoming sediment supply. Though the transition between these sites appears to greatly reduce slump-sediment transport, the watershed area draining into site 4 only accounts for ~15 and 16% of the total area of all slumps and active slumps within the Stony Creek watershed. Past site 4, POC concentrations remain similar to or elevated along the remainder of the mainstem which suggests that sediment transport capacity changes little from this point towards the outlet. Mega-slumps (>20 ha), that can generate their own thaw-driven erosion feedbacks and can have retreat rates well above smaller slumps (Lacelle et al. 2015) occur within the lower eastern portion of the Stony Creek watershed where transition from water tracks to the mainstem has a less dramatic change in slope (Kokelj et al. 2017). Previous work has shown that Stony Creek outlet turbidity values can be comparable to values within mega-slumps impacted sub-catchments and exhibit the same diurnal patterns in turbidity (Kokelj et al. 2013). This highlights that, even under baseflow conditions, stream transport capacity may remain similar enough from slump-impacted eastern headwaters to the watershed outlet to prevent slump signals from becoming muted at the outlet. Furthermore, the recalcitrant nature of slump-origin POC (Shakil et al. 2021, Bröder et al. 2021, Keskitalo et al. 2021) potentially limits transformation of the suspended load prior to it reaching the outlet. While stream power has long been used as an important variable in sediment transport concepts, ample research has shown that a multitude of additional variables can significantly affect and complicate sediment transport and there is a need for new sediment transport theories to improve predictions of sediment transport associated with geomorphic change (Wainwright et al. 2015).

4.4.2. Changes in Peel River organic carbon loads (Goal 3)

Annual Peel River DOC loads exhibited a significant linear increase across the historical record available for the Peel River (1970s – 2017), while a significant linear increase was not detected in annual TSS loads, POC loads, or discharge. However, we did find abnormally high annual POC and TSS loads within the Peel River within the last decade. From 1986 – 2018, the area affected by thaw slumps on the Peel Plateau has increased by orders of magnitude and exhibited a nonlinear rate of increase with majority of the area and volume increasing occurring within the last decade (Kokelj et al. 2021). Thus, it may be that the abnormally high POC and TSS loads in the last decade highlight the beginning of a step-change in the Peel River organic carbon regime due to intensification in climate driven erosion across the Peel Plateau that would not be detectable in a linear trend assessment.

Linear models and compositional assessments in this study indicate that the trends in DOC and POC track different landscape level changes occurring across the Peel River watershed. As noted above, POC exiting the Stony Creek watershed appears almost entirely sourced from retrogressive thaw slump-origin material. In contrast, the age of DOC at the outlet of the Stony Creek (~655 – 790 ^{14}C yr BP) is closer to DOC ages observed in streams not affected by slumping (192 – 217 ^{14}C yr BP, Littlefair et al. 2017) than ages of DOC in rillwater tracks draining thaw slumps (1,157 – 9,592 ^{14}C yr BP). Furthermore, since slumping does not appear as a significant variable predicting DOC loads, we believe DOC entering the Peel River is primarily associated with leaching of modern terrestrial biomass or the contemporary active layer. The increase in annual DOC loads could be due to a multitude of landscape process changes that can interact including active layer deepening and prolonged freeze back that may both enhance subsurface leaching and flow (Beel et al. 2020, Spence et al. 2015), increased hydrological connectivity and wetland expansion associated with permafrost degradation (Connon et al. 2014), and increases in terrestrial productivity (Cameron and Lantz 2016, Chen et al. 2021, Mekonnen et al. 2021).

Multiple lines of evidence beyond this study support our interpretation of different processes accounting for changes in Peel River DOC and POC annual loads. Landscape vegetation and soil moisture metrics (NDVI, NDMI) have been found to be better predictors of DOC concentration along the Peel River than slump features in the landscape (Young et al. 2021). Guo et al. (2007) compared the ^{14}C ages of DOC (390 – 1,440 ^{14}C yr BP), riverine suspended POC and sediments (4430 to ~7970 ^{14}C yr BP) and organic carbon sources to Arctic rivers and suggested that DOC

was likely to be more influenced by changes to contemporary organic carbon sources with POC more likely to increase due to the melting of ice-bonded soils. Further, they suggested that low leachability of tundra soils meant that temporal changes in DOC may be primarily associated with increases in terrestrial primary production, including shifts from tundra to leaf bearing plants, while POC is more likely to track permafrost disturbance, though we note the POC exiting the Stony Creek outlet, as observed in this study, is far more aged (~17, 685 to 18650 ^{14}C yr BP) than riverine suspended POC and sediments in Guo et al. (2007).

Although multiple, broad-scale processes appear likely to affect DOC loads to the Peel River, acceleration of retrogressive thaw slumping affects <1% of the Peel River watershed. Yet, the increases in annual POC loads far outweigh any increase seen in annual DOC loads. This contrasts the short-lived and spatially limited effects of active layer detachments on suspended sediment fluxes for ~10 km^2 watersheds on Melville Island, Nunavut (Beel et al. 2018), likely due to the significant and sustained runoff sourced from massive ice-bodies exposed in retrogressive thaw slumps in this study (Rudy et al. 2017, Littlefair et al. 2017).

4.4.3. Implications for carbon cycling and downstream aquatic systems

Current assessments of the composition and biodegradability of POC mobilized from retrogressive thaw slumps on the Peel Plateau suggests that material is recalcitrant (Shakil et al. 2020, Bröder et al. 2021, Keskitalo et al. 2021) contributing minimally to organic carbon losses seen in incubation experiments (Shakil et al. 2020). Rather, the mineral surfaces associated with slump mobilized POC may be important sites of adsorption of DOC present within stream networks (Shakil et al. 2020, Littlefair et al. 2017). Numerical models of DOC concentrations along the Peel River highlight that adsorption to mineral surfaces are likely an important DOC removal process (Young et al. 2021). We note that these adsorption processes tend to selectively remove aromatic moieties that are often associated with lower lability (Groenveld et al. 2020), thus while the process may protect a portion of DOC, the portion that can readily be mineralized to CO_2 may remain available in the stream network. While rapid mineralization of organic carbon stores upon thaw have been a major point of concern (Schurr et al. 2015), burial of POC from the terrestrial biosphere is regionally and globally significant mechanism of carbon sequestration (Horan et al. 2019, Galy et al. 2015, Repasch et al. 2021). The balance between sequestration of POC from the terrestrial biosphere and oxidation of petrogenic organic carbon is a key term in

determining whether the Mackenzie River Basin is a net source or sink (Horan et al. 2019), and on geological timescales can set the magnitude of atmospheric carbon reservoirs (Burner and Raiswell 1983 in Galy et al. 2015). Low oxidation rates associated with the Mackenzie River suggest that there is efficient source-to-sink (i.e., headwater to ocean sediments) transit and burial of organic carbon (Repasch et al. 2021, Carvalhais et al. 2014) suggesting that intensification of climate-driven erosion may increase this carbon sink mechanism. However, quantification of changes in petrogenic oxidation rates (Horan et al. 2019) in slump-affected fluvial networks would best help estimate how enhanced erosion, which is also enhancing erosion of shale contained within permafrost (Shakil et al. 2020, Broder et al. 2021), will balance with burial of POC. Finally, enhanced POC mobilization is also associated with increased export of particulate nitrogen, particulate organic phosphorus, and particle-associated mercury (Shakil et al. 2020, St. Pierre, Zolkos, Shakil et al. 2018). Given that the particulate-associated carbon and nutrients are compositionally distinct from the dissolved organic matter present in non-slump affected networks (Shakil et al. 2020), research is needed on the role of nutrients and contaminants in this form in downstream aquatic food webs to assess how enhancement of particle dominance in the Peel River will translate to changes to food webs downstream.

4.4.4. Future research priorities

Change in the western Canadian Arctic is occurring rapidly and priorities for research need to focus on maximizing the efficiency with which we can detect change in a way that is relevant to local communities and is scalable across time and space so that effects on global biogeochemical cycles can also be quantified. Research is actively improving our conceptual understanding of the underlying geomorphic processes (Kokelj et al. 2017, Kokelj et al. 2021), our ability to detect features via remote sensing (Nitze et al. 2021), and our ability to quantify fine-scale geomorphic change via techniques using unmanned aerial vehicles (UAV) (van der Sluijs et al. 2018). However translating these physical changes to changes in water quality and aquatic system function requires: (a) quantification of time-variant sediment transit through fluvial networks including an ability to model fluxes and reservoir storage time of sediments across watershed scales; (b) biogeochemical rates and processes that may change when sediments are contained within reservoirs vs. in transit (here developments in aquatic redox concepts may be useful; Peiffer et al. 2021); and (c) improving our understanding and modelling of organo-mineral interactions (Opfergelt et al. 2020). Two

major limitations for modelling fluxes and reservoir storage time are a lack of sediment transport theories that can scale across time and space (Wainwright et al. 2015) alongside a lack of observations to develop empirical equations of stream flow and sediment loads in headwater streams on the Peel Plateau, particularly due to a lack of sampling during high flow periods such as the spring freshest and summer storm events. Developing this process-based understanding of change in the region can simultaneously help assess changes beyond risks associated with greenhouse gas emissions, including risks associated with contaminant mobilization (St. Pierre, Zolkos, and Shakil et al. 2018) and potential changes to aquatic food web structure that could affect food security.

4.5. Conclusion

Retrogressive thaw slumps are the primary source of POC, which comprises most of the TOC across slump-impacted watersheds on the Peel Plateau. Though most of the material eroded from slumps is retained within debris tongues at the valley-bottom in first to second order streams (Kokelj et al. 2021), the order of magnitude increase in TOC in suspension propagates to the Stony Creek outlet. This material is primarily composed of older and degraded organic carbon that is likely resistant to microbial breakdown during transport in streams (Shakil 2021). The intensification in slumping across the Peel Plateau appears to have resulted in a non-linear increase in annual POC loads in the Peel River, which will dramatically alter organic carbon and nutrient delivery to the Mackenzie Delta and to the Beaufort Sea in the Arctic Ocean.

4.6. Acknowledgements

This work took place within the Gwich'in Settlement region and we are thankful for support from the Tetlit Gwich'in Renwable Resources Council (RRC) and the Western Arctic Research Centre. We are further thankful for the field assistance of Christine Firth, Elizabeth Jerome, Billy Wilson, Keith Colin, Andrew Koe, Joyce Kendon, Luke Gjini, Maya Guttman, Lindsay Stephens, Rosemin Nathoo, and Erin MacDonald. Cara Littlefair provided invaluable advice on field logistics, and was involved in initial site selection of SD. Shawne Kokelj provided meteorological data. Christopher Osburn advised laboratory BEPOM analyses and he and Ashley Dubnick provided advice on PARAFAC modelling. Funding for this study was provided by the Natural Sciences and Engineering Research Council, Polar Continental Shelf Program (Natural Resources

Canada), Campus Alberta Innovates Program, CiCan Cleantech Internship Program, Environment Canada Science Youth Horizons Internship, Northern Scientific Training Program, University of Alberta and UAlberta North, and the Aurora Research Institute. Personal funding to S. Shakil was provided by the Natural Sciences and Engineering Research Council, the W. Garfield Weston, and the University of Alberta. Research for this paper was conducted under research licences: 15685 (2015); 15887 (2017).

4.8. Tables

Table 4-1. Explanatory variables used in pRDA analyses. For details on the calculation of variables, see Table A**3-3** in the supplementary. Chlorophyll α was not included as a water chemistry explanatory variable because concentrations were below detection limit (1 ug L^{-1}) for most sites.

Category	Variable	Variables with strong correlation (≥ 0.9)	Transformation
Water Chemistry	$\delta^{18}O$		none
	Ca yield	Na, Mg, SO_4^{2-}, Sr yields	log(x+2)
GIS: Soil and Geology	%shale (in bedrock) %colluvial %piedemont %moraine soil organic carbon in the top 100m		log(x+2)
GIS: Landcover	Mean watershed GPP	Mean watershed annual NPP, %shrub	log(x+2)
	%forest %grass %lichen %lake		
GIS: Thaw Slumping	% area active RTS 2017	% total area all RTS 2017	log(x+2)
	cumulative active RTS count	strahler impact accumulation	
Stream morphology	Stream power Stream slope		log(x+2)
Other	mean watershed slope	mean watershed roughness, mean watershed elevation, %barren land	log(x+2)
	Water yield Total Rain (past 96h)		

[a]$F^{14}C$ values are obtained from Shakil et al. (2020) and similar sites in Lacelle et al. (2019)

[b]$F^{14}C$ values based on Shakil et al. (2020) assuming a range from modern to observed DIC $F^{14}C$

[c]For $F^{14}C$, two samples consisted of end-member streambank types and two from different locations streambank locations near the Stony Creek outlet

Table 4-2. Comparison of end member source with streambank samples collected in 2017. End-member values were obtained from Shakil et al. (2020).

		Pleistocene[a]	Holocene[a]	Lower AL	Upper AL	Periphyton[b]	Streambank[c]
%SOC	Mean	1.79	1.73	2.89	19.04	13.75	2.47
	se	0.34	0.28	0.51	0.67	NA	0.31
	range	1.17 to 3.45	0.74 to 2.86	1.14 to 4.99	18.30 to 20.38	NA	0.59 to 7.39
$\delta^{13}C$	Mean	-26.76	-26.73	-26.48	-26.73	-33.39	-26.96
	se	0.06	0.06	0.09	0.03	2.10	0.17
	range	-26.57 to -27.01	-26.52 to -26.92	-26.06 to -26.91	-26.69 to -26.78	-30.02 to -38.83	-24.10 to -28.38
$F^{14}C$	Mean	0.005	0.112	0.603	0.987	~0.8	0.195
	se	0.001	0.095	NA	NA	NA	0.059
	range	0.003 to 0.007	0.007 to 0.491	NA	NA	0.673 to modern	0.086 to 0.323

4.9. Figures

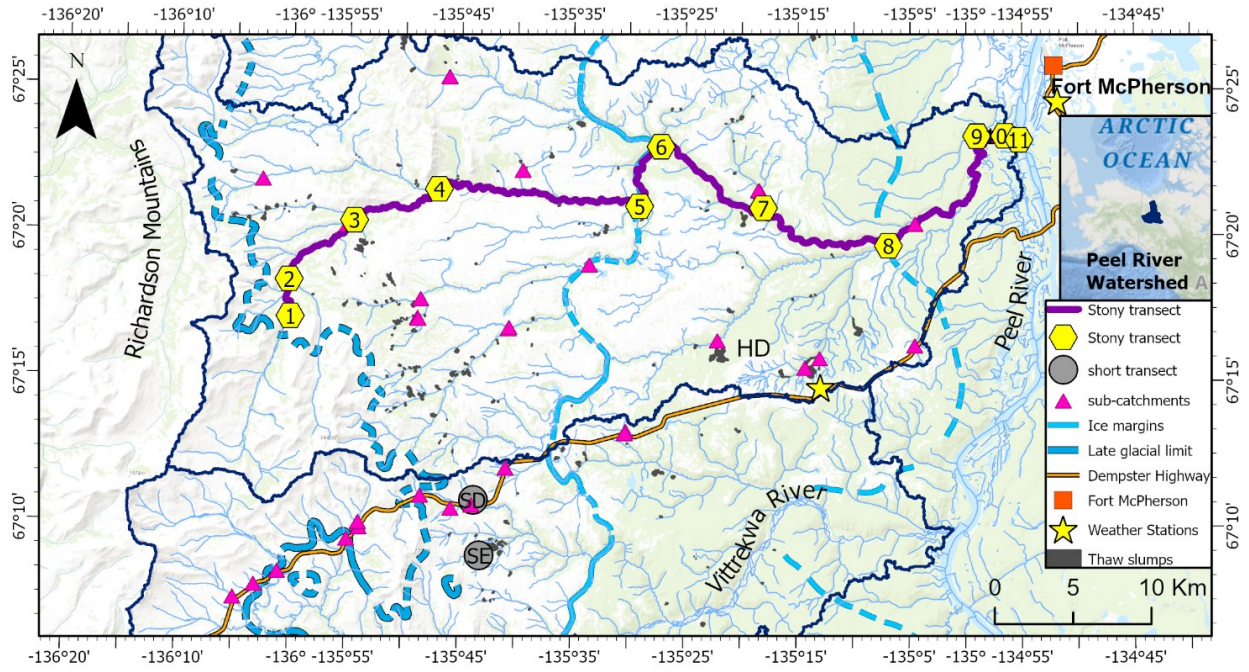

Figure 4-1. Map of sites and transects within the Stony Creek and Vittrekwa River Watersheds on the Peel Plateau.

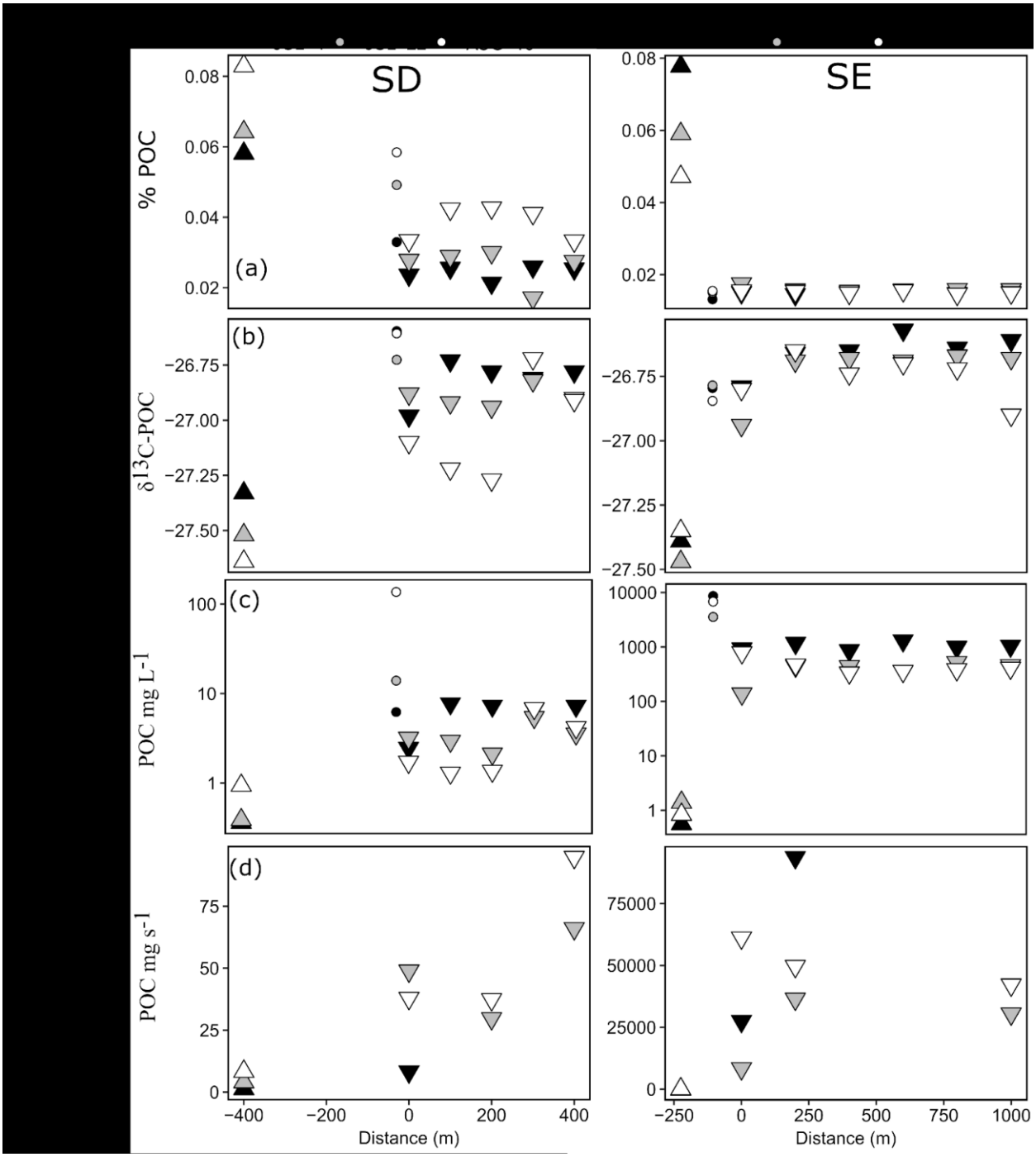

Figure 4-2. Short transects conducted in streams impacted by slumps SD and SE in 2015 showing (a-b) compositional changes via %POC and δ^{13}POC, (c) concentrations (mg L^{-1}), and (d) fluxes (mg s^{-1}). Note, there are no flux measurements past 0m downstream for SD on July 4 and past 250 m downstream SE on July 6.

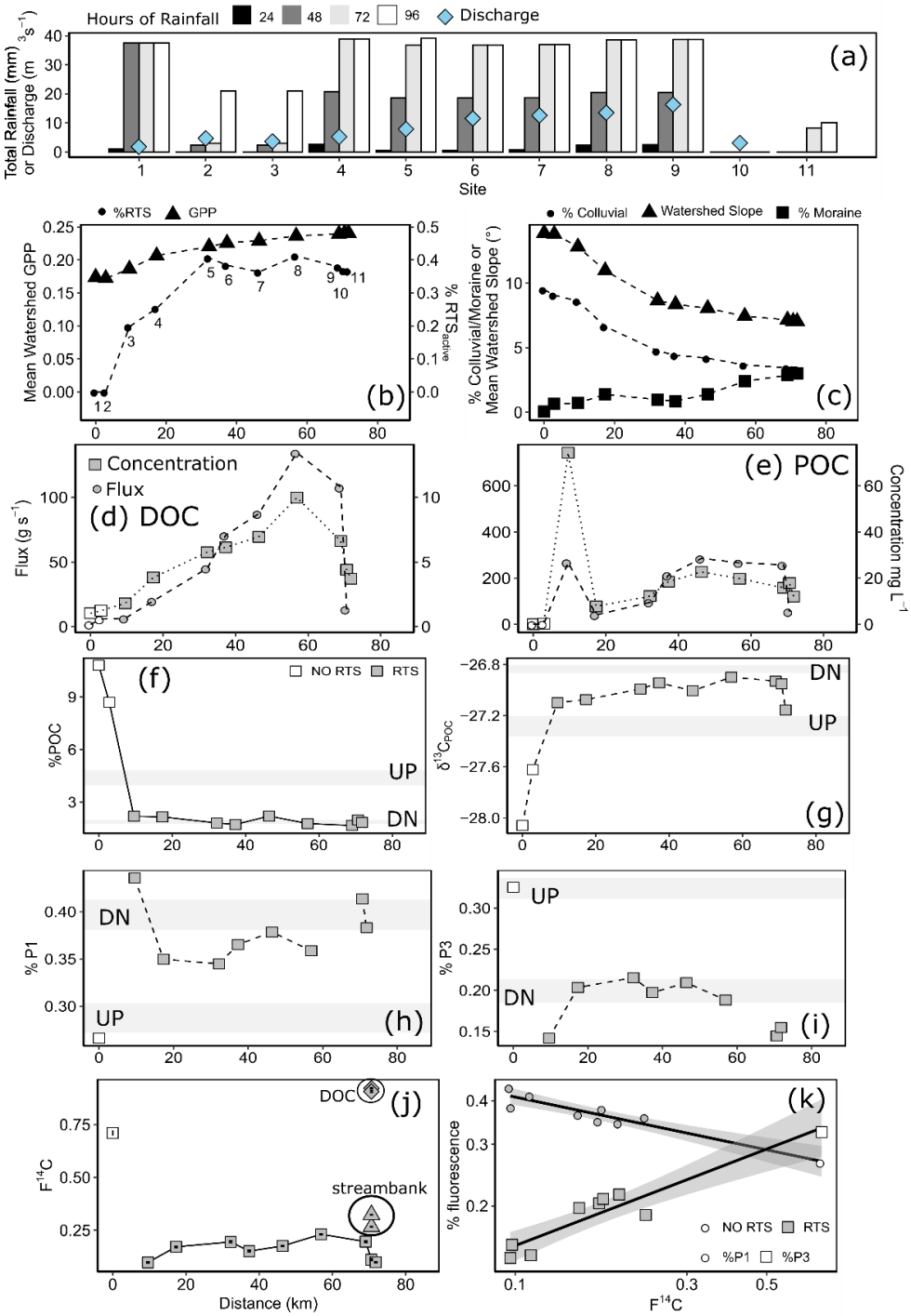

Figure 4-3. (a) Total rainfall over past 24, 48, 72, and 96 hours and discharge during transect sampling. Changes in geospatial variables (b-c), concentration and flux of DOC and POC (d-e), POM compositional metrics (f-i), and relationships between BEPOM fluorescence components and $F^{14}C_{POC}$ (k) across the Stony Creek mainstem. Error bars in (j) are 1σ of $F^{14}C$ for counting statistic errors. Grey bands in (f) through (i) show previously mean and standard error previously documented for analytes immediately upstream and downstream of thaw slumps (Shakil et al. 2020). Discontinuous lines indicate a missing site between points.

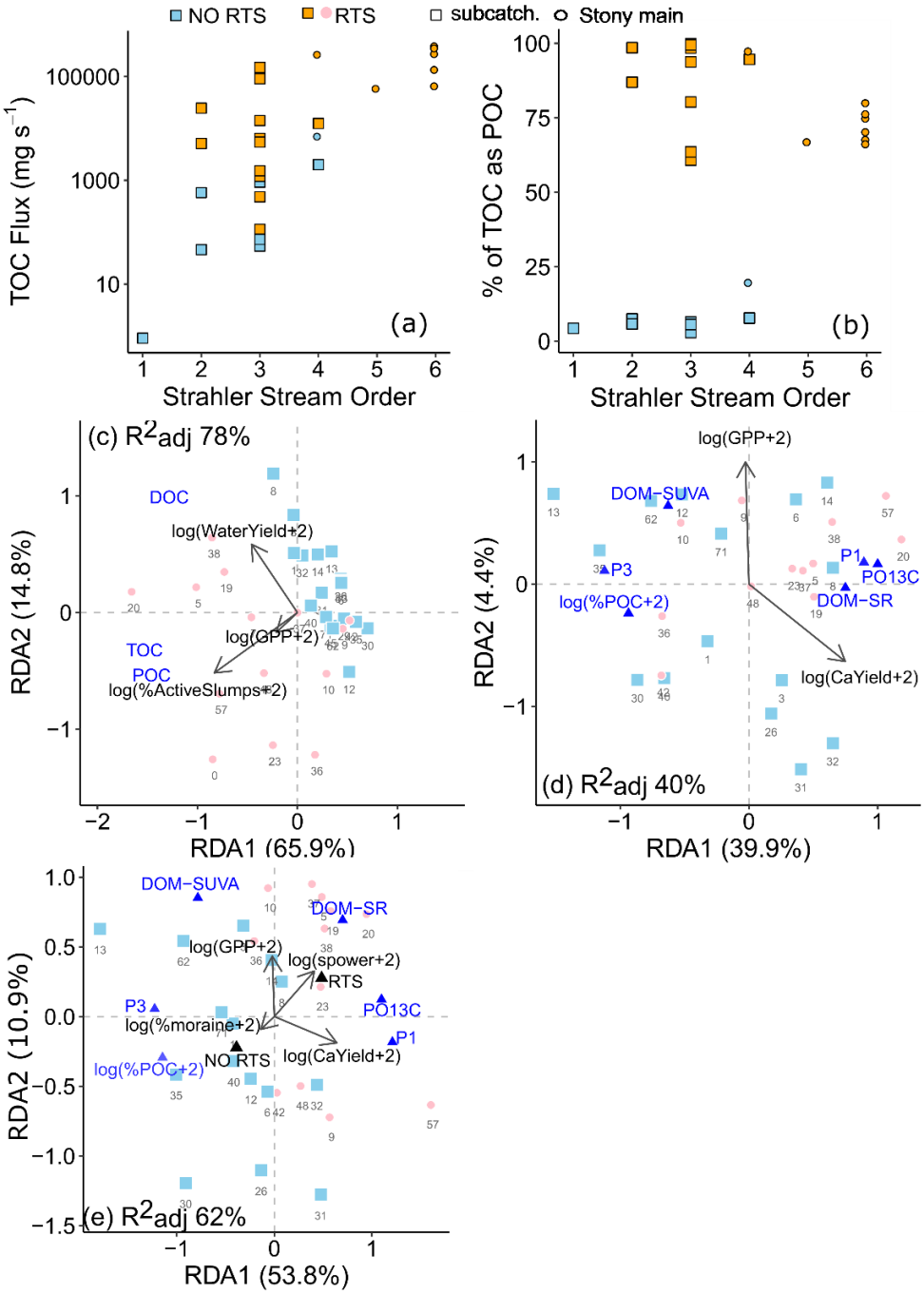

Figure 4-4. (a) TOC flux and (b) % of TOC as POC vs Strahler stream order for subcatchments and Stony Transect. (c-e) Biplots of RDAs showing relationship between explanatory variables and (c) OC yields and (d-e) OC composition. Plot (e) is modified from (d) to incorporate a categorical variable of RTS presence (see section 3.3). Arrows show biplot scores of explanatory variables retained after forward selection. Blue text or triangles show scores of response variables. Black triangles in (c) plot centroids of RTS presence. Sites are plotted as linear combinations of explanatory variables with pink dots and blue squares showing sub-catchments with (RTS) and without (NO RTS) active slumping. Axes % show biased proportions.

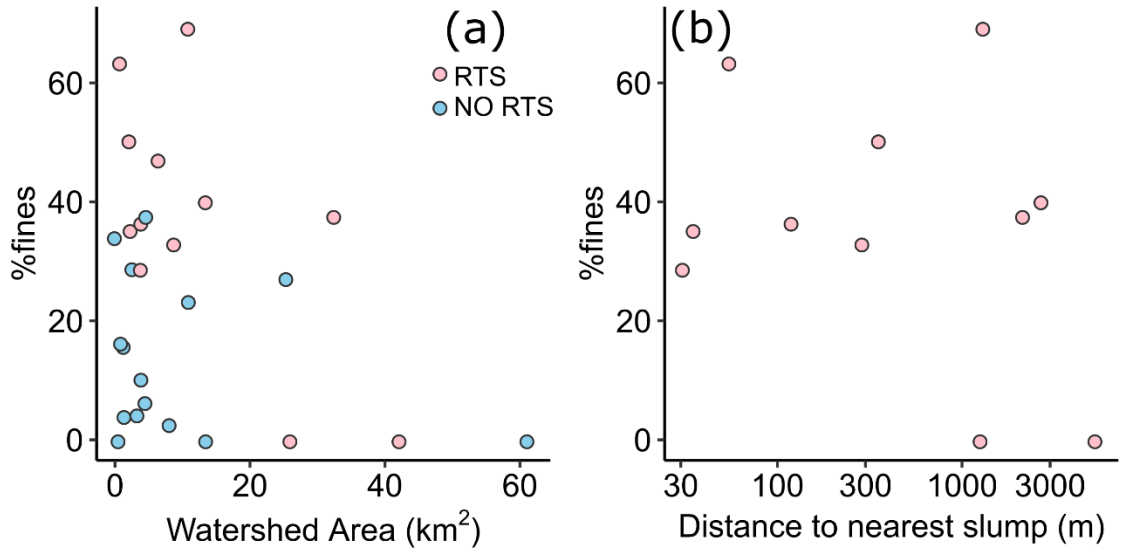

Figure 4-5. Percent fines of streambed material, as determined by Wolman pebble count vs. (a) watershed area and (b) distance from the nearest active slump.

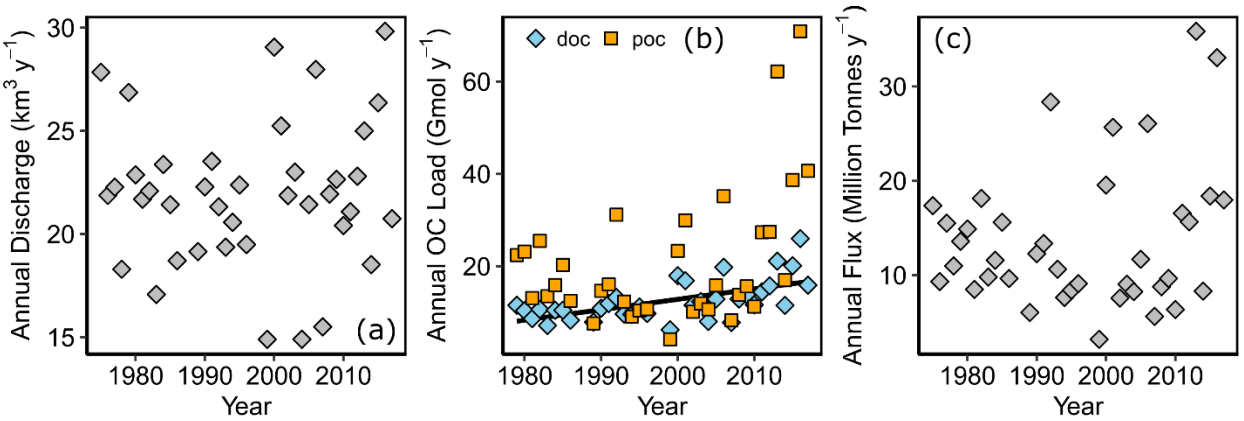

Figure 4-6. Annual discharge, **(b)** dissolved and particulate organic carbon loads, and **(c)** suspended sediment loads from 1975 – 2017.

Chapter 5.: General conclusions

5.1. Summary of Findings

This research investigated the effects of abrupt permafrost thaw, in the form of retrogressive thaw slumping, on fluvial organic carbon cycling, focusing on the often-understudied organic carbon partitioned as particulate organic carbon.

The results of Chapter 2 reveal that thaw slumps increase organic carbon, nitrogen, and phosphorus yields in streams by orders of magnitude, almost entirely due to the mobilization of particulate organic carbon (POC) and associated particulate nitrogen (PN) and phosphorus (POP) release. The magnitude of the increase in yields could vary in relation to slump characteristics (headwall height) and stream characteristics (stream power). Estimates of mid-June to mid-August yields downstream from even the smallest slump in the study were orders of magnitude greater than the combined dissolved and particulate carbon and nitrogen yields of any of the major Arctic rivers, including the Mackenzie. However, work from this chapter also revealed that the majority of the POC eroded from slumps will be sequestered for centuries to millenia within primary sediment stores in valley bottoms, where net accumulation is currently exceeding net erosion (see also Kokelj et al. 2021). Slump-mobilized POC was found to be compositionally distinct from its dissolved counterpart and appeared to contain relatively greater amounts of degraded organic matter, as inferred from base-extracted fluorescence of particulate organic matter, and thus is potentially more recalcitrant than POC present in non-slump affected stream networks.

In Chapter 3 I aimed to experimentally quantify changes in the biodegradability of organic carbon in streams due to the mobilization of POC. Using aerobic incubations including both DOC and POC from streams affected by thaw slumps we found that the slump-mobilized total organic carbon (TOC) undergoes minimal (~4%) oxidation over a 1-month period and that most of the mineralization was likely associated with DOC loss. In many experiments we found little to no change in organic carbon despite rapid consumption of oxygen. To our surprise, in many experiments we found significant organic carbon gains, with coupled analyses of redox-sensitive elements suggesting potentially significant chemolithoautotrophic processes may be promoted with the mobilization of mineral-rich tills to streams. These experiments suggest that the organic

carbon mobilized from thaw slumps may be predominantly re-sequestered at downstream points within the headwaters to ocean aquatic continuum after mobilization to streams.

In Chapter 4 we aimed to assess the downstream transport potential of organic carbon mobilized by thaw slumps, and the relative importance of slump-mobilized organic carbon across watershed scales including whether intensification of slumping across the Peel Plateau has affected the Peel River organic carbon regime. We find that the orders of magnitude increases in POC that were observed in Chapter 2 as a result of slumping do not drop off downstream of thaw slumps. Slump-mobilized POC is detectable at the point where an impacted watershed on the Peel Plateau drains into the larger Peel River, with this POC accounting for the majority of the organic carbon exiting this watershed. Preliminary analyses suggest that intensification in slumping has resulted in a non-linear increase in annual POC loads in the Peel River. Further the increase in annual POC loads exceeds increases in annual DOC loads over the course of the record. Changes in DOC could be due to a multitude of landscape factors, a likely one being increases in terrestrial primary production, while POC is likely linked to the intensification of slumping.

5.2. Future Research

Change in the western Canadian Arctic is occurring rapidly and priorities for research should therefore focus on maximizing the efficiency with which we can detect change in a way that is relevant to local communities and is scalable across time and space so that effects on global biogeochemical cycles can also be quantified. Research is actively improving our conceptual understanding of the underlying geomorphic processes (Kokelj et al. 2017, Kokelj et al. 2021), our ability to detect features via remote sensing (Nitze et al. 2021), and our ability to quantify fine-scale geomorphic change via UAV techniques (van der Sluijs et al. 2018). However translating these physical changes to changes in water quality and aquatic system function requires: (a) quantification of time-variant sediment transit through fluvial networks including an ability to model fluxes and reservoir storage time of sediments across watershed scales; (b) biogeochemical rates and processes that may change when sediments are contained within reservoirs vs. in transit (here developments in aquatic redox concepts may be useful; Peiffer et al. 2021); and (c) improving our understanding and modelling of organo-mineral interactions (Opfergelt et al. 2020) and particle-associated microbes. Developing this process-based understanding of change in the region can simultaneously help assess changes beyond risks associated with greenhouse gas emissions,

including risks associated with contaminant mobilization (St. Pierre, Zolkos, and Shakil et al. 2018) and potential changes to aquatic food web structure and food security.

Two major limitations for modelling fluxes and reservoir storage time are a lack of sediment transport theories that can scale across time and space (Wainwright et al. 2015) alongside a lack of observations to develop empirical equations of stream flow and sediment loads in headwater streams on the Peel Plateau, particularly due to a lack of sampling during high flow periods such as the spring freshest and summer storm events. Setting up continuous monitoring across headwaters of the Peel Plateau is logistically challenging because of the remote location and because installed sensors can be easily washed out with the high energy of the fluvial system (e.g., Kokelj et al. 2013) and active geomorphic change in the landscape. Suspended sediment loads can easily exceed the upper limit of turbidity sensors (Shakil et al. 2020, Kokelj et al. 2013) and both cameras and stream gauging stick we have attempted to install become buried under rapid movement of debris tongues, though automatic pump samplers have been successfully used in watersheds erosion via active layer detachments is occurring (Beel et al. 2018). Obtaining sediment cores within the slump scar zone and at various deposition points (lakes, alluvial fans) could be useful in constraining long term deposition rates at various points along the aquatic continuum, with differences in quantity potentially highlighting sediment storage time. The generally recalcitrant nature of POC mobilized from slumps suggests that it may be possible to track this form of POC, with the aided use of molecular analyses (e.g., Bröder et al. 2021). Compound-specific dating may also help quantify adsorption and sequestration of DOC into sediment repositories.

In Chapter 2, we highlighted that a multitude of processes beyond organic carbon decomposition may be impacting CO_2 release from streams affected by slumping that may need to be further explored (e.g., chemolithoautotrophy). However, we also note that our experiments did not quantify methane release, which can be substantially elevated in some downstream environments (Zolkos et al. 2018). The proportion of thawed permafrost carbon that can be released as methane versus carbon dioxide is an important unknown in current permafrost carbon models (IPCC 2021) and in these sediment-saturated systems methane could be a significant form of carbon release in areas such as the scar zone, streambed and streambank, and depositional points along the aquatic continuum. However, this methane release is likely most important near small slumps and in waterlogged scar zones where sediments have a higher concentration of organics

(Zolkos et al. 2018). Furthermore, our experiments only examine upstream processes occurring in suspended conditions. Biofilms dominate microbial life in stream ecosystems (Battin et al. 2016) and the dramatic change from cobble beds to unstable silty bottoms needs to be assessed to fully understand changes to stream function.

In Chapter 3, we also noted that while enhanced erosion to streams may be enhancing burial of biogenic carbon along the aquatic continuum, we do not have an assessment of petrogenic organic carbon oxidation rates, an important unknown with the likely enhanced erosion of shale contained within regional tills (Allen et al. 2015, Shakil et al. 2020, Bröder et al. 2021). Finally, we note that few studies have quantified changes in net ecosystem exchange in the scar zone (Abbott and Jones 2015) which is likely to vary with the nature of thaw and landscape properties (Tank et al. 2020) and at different stages of thaw slumping (original tundra versus debris versus different stages of revegetation), and this change is necessary to quantify the total magnitude of change to the carbon balance of an affected watershed.

This research highlights particle flux as a key variable in the release of permafrost carbon from abrupt thaw. Targeted quantification of the multitude of biotic and abiotic processes acting on the carbon, organic matter, and minerals associated with these particles will be of critical importance in accurately predicting the affect of continued regional permafrost erosion on the carbon cycle and aquatic systems affected.

BIBLIOGRAPHY

1-1. Abbott B W, Larouche J R, Jones J B, Bowden W B and Balser A W 2014 Elevated dissolved organic carbon biodegradability from thawing and collapsing permafrost Journal of Geophysical Research: Biogeosciences 119 2049–63

1-2. Aufdenkampe A K, Mayorga E, Raymond P A, Melack J M, Doney S C, Alin S R, Aalto R E and Yoo K 2011 Riverine coupling of biogeochemical cycles between land, oceans, and atmosphere Frontiers in Ecology and the Environment 9 53–60

1-3. Cole J J, Prairie Y T, Caraco N F, McDowell W H, Tranvik L J, Striegl R G, Duarte C M, Kortelainen P, Downing J A, Middelburg J J and Melack J 2007 Plumbing the Global Carbon Cycle: Integrating Inland Waters into the Terrestrial Carbon Budget Ecosystems 10 172–85

1-4. Battin T J, Luyssaert S, Kaplan L A, Aufdenkampe A K, Richter A and Tranvik L J 2009 The boundless carbon cycle Nature Geoscience 2 598–600

1-5. Battin T J, Kaplan L A, Findlay S, Hopkinson C S, Marti E, Packman A I, Newbold J D and Sabater F 2008 Biophysical controls on organic carbon fluxes in fluvial networks *Nature Geosci* **1** 95–100

1-6. Brown J, Romanovsky V. 2008. Report from the International Permafrost Association: state of permafrost in the first decade of the 21st century. Permafrost Periglacial Process. 19:255–60

1-7. Burd K, Estop-Aragonés C, Tank S E and Olefeldt D 2020 Lability of dissolved organic carbon from boreal peatlands: interactions between permafrost thaw, wildfire, and season Can. J. Soil. Sci. 1–13

1-8. Davidson E A and Janssens I A 2006 Temperature sensitivity of soil carbon decomposition and feedbacks to climate change Nature 440 165–73

1-9. Ewing S A, O'Donnell J A, Aiken G R, Butler K, Butman D, Windham-Myers L and Kanevskiy M Z 2015 Long-term anoxia and release of ancient, labile carbon upon thaw of Pleistocene permafrost Geophysical Research Letters 42 10,730-10,738

1-10. French H M 2013 Cold-Climate Weathering The Periglacial Environment (John Wiley & Sons, Ltd) pp 47–82 Online: http://onlinelibrary.wiley.com/doi/abs/10.1002/9781118684931.ch4

1-11. Gulev, S.K., P.W. Thorne, J. Ahn, F.J. Dentener, C.M. Domingues, S. Gerland, D. Gong, D.S. Kaufman, H.C. Nnamchi, J. Quaas, J.A. Rivera, S. Sathyendranath, S.L. Smith, B. Trewin, K. von Schuckmann, and R.S. Vose, 2021: Changing State of the Climate System. In Climate Change 2021: The Physical Science Basis. Contribution of Working Group I to the Sixth Assessment Report of the Intergovernmental Panel on Climate Change [Masson Delmotte, V., P. Zhai, A. Pirani, S.L. Connors, C. Péan, S. Berger, N. Caud, Y. Chen, L. Goldfarb, M.I. Gomis, M. Huang, K. Leitzell, E. Lonnoy, J.B.R. Matthews, T.K. Maycock, T. Waterfield, O. Yelekçi, R. Yu, and B. Zhou (eds.)]. Cambridge University Press. In Press.

1-12. Holmes, R. M. et al., 2018: River Discharge [Jeffries, M. O., J. Richter-Menge and J. E. Overland (eds.)]. Arctic Report Card, Update for 2018 [Available at: https://www.arctic.noaa.gov/Report-Card/Report-Card-2018/ArtMID/7878/ArticleID/786/River-Discharge%5D.

1-13. Hugelius G, Strauss J, Zubrzycki S, Harden J W, Schuur E A G, Ping C-L, Schirrmeister L, Grosse G, Michaelson G J, Koven C D, O'Donnell J A, Elberling B, Mishra U, Camill P, Yu Z, Palmtag J and Kuhry P 2014 Estimated stocks of circumpolar permafrost carbon with quantified uncertainty ranges and identified data gaps Biogeosciences 11 6573–93
1-14. Hutchins R H S, Tank S E, Olefeldt D, Quinton W L, Spence C, Dion N, Estop-Aragonés C and Mengistu S G 2020 Fluvial CO2 and CH4 patterns across wildfire-disturbed ecozones of subarctic Canada: Current status and implications for future change Global Change Biology 26 2304–19
1-15. IPCC, 2021: Summary for Policymakers. In: Climate Change 2021: The Physical Science Basis. Contribution of Working Group I to the Sixth Assessment Report of the Intergovernmental Panel on Climate Change [Masson Delmotte, V., P. Zhai, A. Pirani, S.L. Connors, C. Péan, S. Berger, N. Caud, Y. Chen, L. Goldfarb, M.I. Gomis, M. Huang, K. Leitzell, E. Lonnoy, J.B.R. Matthews, T.K. Maycock, T. Waterfield, O. Yelekçi, R. Yu, and B. Zhou (eds.)]. Cambridge University Press. In Press.
1-16. IPCC, 2019: Summary for Policymakers. In: IPCC Special Report on the Ocean and Cryosphere in a Changing Climate [H.-O. Pörtner, D.C. Roberts, V. Masson-Delmotte, P. Zhai, M. Tignor, E. Poloczanska, K. Mintenbeck, A. Alegría, M. Nicolai, A. Okem, J. Petzold, B. Rama, N.M. Weyer (eds.)]. In press.
1-17. Karlsson J, Serikova S, Vorobyev S N, Rocher-Ros G, Denfeld B and Pokrovsky O S 2021 Carbon emission from Western Siberian inland waters Nat Commun 12 825
1-18. Krasting, JPA, Broccoli, AJ, Dixon, KW, Lanzante, JR. 2013. Future changes in northern hemisphere snowfall. Journal of climate, 26 (20), 7813 – 7828, doi: 10.1175/jcli-d-12-008321.1.
1-19. Kokelj S V, Kokoszka J, van der Sluijs J, Rudy A C A, Tunnicliffe J, Shakil S, Tank S E and Zolkos S 2021 Thaw-driven mass wasting couples slopes with downstream systems, and effects propagate through Arctic drainage networks The Cryosphere 15 3059–81
1-20. Kokelj S V, Lantz T C, Tunnicliffe J, Segal R and Lacelle D 2017 Climate-driven thaw of permafrost preserved glacial landscapes, northwestern Canada Geology 45 371–4
1-21. Kokelj S V, Tunnicliffe J, Lacelle D, Lantz T C, Chin K S and Fraser R 2015 Increased precipitation drives mega slump development and destabilization of ice-rich permafrost terrain, northwestern Canada Global and Planetary Change 129 56–68
1-22. Littlefair C A and Tank S E 2018 Biodegradability of Thermokarst Carbon in a Till-Associated, Glacial Margin Landscape: The Case of the Peel Plateau, NWT, Canada Journal of Geophysical Research: Biogeosciences 123 3293–307
1-23. McClelland J W, Holmes R M, Dunton K H and Macdonald R W 2012 The Arctic Ocean Estuary Estuaries and Coasts 35 353–68
1-24. Meredith, M., M. Sommerkorn, S. Cassotta, C. Derksen, A. Ekaykin, A. Hollowed, G. Kofinas, A. Mackintosh, J. Melbourne-Thomas, M.M.C. Muelbert, G. Ottersen, H. Pritchard, and E.A.G. Schuur, 2019: Polar Regions. In: IPCC Special Report on the Ocean and Cryosphere in a Changing Climate [H.-O. Pörtner, D.C. Roberts, V. Masson-Delmotte, P. Zhai, M. Tignor, E. Poloczanska, K. Mintenbeck, A. Alegría, M. Nicolai, A. Okem, J. Petzold, B. Rama, N.M. Weyer (eds.)]. In press.
1-25. Natali S M, Holdren J P, Rogers B M, Treharne R, Duffy P B, Pomerance R and MacDonald E 2021 Permafrost carbon feedbacks threaten global climate goals Proc Natl Acad Sci USA 118 e2100163118

1-26. Santoro M, Cartus O, Carvalhais N, Rozendaal D M A, Avitabile V, Araza A, de Bruin S, Herold M, Quegan S, Rodríguez-Veiga P, Balzter H, Carreiras J, Schepaschenko D, Korets M, Shimada M, Itoh T, Moreno Martínez Á, Cavlovic J, Cazzolla Gatti R, da Conceição Bispo P, Dewnath N, Labrière N, Liang J, Lindsell J, Mitchard E T A, Morel A, Pacheco Pascagaza A M, Ryan C M, Slik F, Vaglio Laurin G, Verbeeck H, Wijaya A and Willcock S 2021 The global forest above-ground biomass pool for 2010 estimated from high-resolution satellite observations Earth System Science Data 13 3927–50
1-27. Schuur E A G and Mack M C 2018 Ecological Response to Permafrost Thaw and Consequences for Local and Global Ecosystem Services Annual Review of Ecology, Evolution, and Systematics 49 279–301
1-28. Segal R A, Lantz T C and Kokelj S V 2016 Acceleration of thaw slump activity in glaciated landscapes of the Western Canadian Arctic Environmental Research Letters 11 034025
1-29. Seneviratne, S.I., X. Zhang, M. Adnan, W. Badi, C. Dereczynski, A. Di Luca, S. Ghosh, I. Iskandar, J. Kossin, S. Lewis, F. Otto, I. Pinto, M. Satoh, S.M. Vicente-Serrano, M. Wehner, and B. Zhou, 2021: Weather and Climate Extreme Events in a Changing Climate. In Climate Change 2021: The Physical Science Basis. Contribution of Working Group I to the Sixth Assessment Report of the Intergovernmental Panel on Climate Change [Masson Delmotte, V., P. Zhai, A. Pirani, S.L. Connors, C. Péan, S. Berger, N. Caud, Y. Chen, L. Goldfarb, M.I. Gomis, M. Huang, K. Leitzell, E. Lonnoy, J.B.R. Matthews, T.K. Maycock, T. Waterfield, O. Yelekçi, R. Yu, and B. Zhou (eds.)]. Cambridge University Press. In Press.
1-30. Simon M, Grossart H, Schweitzer B and Ploug H 2002 Microbial ecology of organic aggregates in aquatic ecosystems Aquat. Microb. Ecol. 28 175–211
1-31. Spencer R G M, Mann P J, Dittmar T, Eglinton T I, McIntyre C, Holmes R M, Zimov N and Stubbins A 2015 Detecting the signature of permafrost thaw in Arctic rivers Geophysical Research Letters 42 2830–5
1-32. Strauss J, Schirrmeister L, Grosse G, Fortier D, Hugelius G, Knoblauch C, Romanovsky V, Schädel C, Schneider von Deimling T, Schuur E A G, Shmelev D, Ulrich M and Veremeeva A 2017 Deep Yedoma permafrost: A synthesis of depositional characteristics and carbon vulnerability Earth-Science Reviews 172 75–86
1-33. Tank S E, Vonk J E, Walvoord M A, McClelland J W, Laurion I and Abbott B W 2020 Landscape matters: Predicting the biogeochemical effects of permafrost thaw on aquatic networks with a state factor approach Permafrost and Periglacial Processes 31 358–70
1-34. Terhaar, J., Lauerwald, R., Regnier, P., Gruber, N., & Bopp, L. (2021). Around one third of current Arctic Ocean primary production sustained by rivers and coastal erosion. Nature Communications, 12(1), 169. https://doi.org/10.1038/s41467-020-20470-z
1-35. Turetsky M R, Abbott B W, Jones M C, Anthony K W, Olefeldt D, Schuur E A G, Grosse G, Kuhry P, Hugelius G, Koven C, Lawrence D M, Gibson C, Sannel A B K and McGuire A D 2020 Carbon release through abrupt permafrost thaw Nature Geoscience 13 138–43
1-36. Ussiri D A N and Lal R 2017 The Modern Carbon Cycle Carbon Sequestration for Climate Change Mitigation and Adaptation ed D A N Ussiri and R Lal (Cham: Springer International Publishing) pp 163–225 Online: https://doi.org/10.1007/978-3-319-53845-7_6
1-37. Vonk J E, Tank S E, Bowden W B, Laurion I, Vincent W F, Alekseychik P, Amyot M, Billet M F, Canário J, Cory R M, Deshpande B N, Helbig M, Jammet M, Karlsson J, Larouche J, MacMillan G, Rautio M, Walter Anthony K M and Wickland K P 2015

Reviews and syntheses: Effects of permafrost thaw on Arctic aquatic ecosystems Biogeosciences 12 7129–67
1-38. Vonk J E, Mann P J, Davydov S, Davydova A, Spencer R G M, Schade J, Sobczak W V, Zimov N, Zimov S, Bulygina E, Eglinton T I and Holmes R M 2013 High biolability of ancient permafrost carbon upon thaw Geophysical Research Letters 40 2689–93
1-39. Wickland K P, Waldrop M P, Aiken G R, Koch J C, Jorgenson M T and Striegl R G 2018 Dissolved organic carbon and nitrogen release from boreal Holocene permafrost and seasonally frozen soils of Alaska Environ. Res. Lett. 13 065011
2-40. Abbott B W, Jones J B, Godsey S E, Larouche J R and Bowden W B 2015 Patterns and persistence of hydrologic carbon and nutrient export from collapsing upland permafrost Biogeosciences 12 3725–40
2-41. Allen T L, Fraser T A, Hutchinson M P, Dolby G, Reyes J and Utting J 2015 OF2015-3.pdf (Yukon Geological Survey) Online: http://ygsftp.gov.yk.ca/publications/openfile/2015/OF2015-3.pdf
2-42. Armanini A 2018 Introduction to Sediment Transport Principles of River Hydraulics (Cham: Springer International Publishing) pp 33–47 Online: http://link.springer.com/10.1007/978-3-319-68101-6_2
2-43. Attermeyer K, Catalán N, Einarsdottir K, Freixa A, Groeneveld M, Hawkes J A, Bergquist J and Tranvik L J 2018 Organic Carbon Processing During Transport Through Boreal Inland Waters: Particles as Important Sites Journal of Geophysical Research: Biogeosciences 123 2412–28
2-44. Bates D, Mächler M, Bolker B and Walker S 2015 Fitting Linear Mixed-Effects Models Using lme4 Journal of Statistical Software 67 1–48
2-45. Beel C R, Lamoureux S F and Orwin J F 2018 Fluvial Response to a Period of Hydrometeorological Change and Landscape Disturbance in the Canadian High Arctic Geophysical Research Letters 45 10,446-10,455
2-46. Beel C R, Lamoureux S F, Orwin J F, Pope M A, Lafrenière M J and Scott N A 2020 Differential impact of thermal and physical permafrost disturbances on High Arctic dissolved and particulate fluvial fluxes Scientific Reports 10 11836
2-47. Blattmann T M, Letsch D and Eglinton T I 2018 On the geological and scientific legacy of petrogenic organic carbon Am J Sci 318 861–81
2-48. Bowden W B, Gooseff M N, Balser A, Green A, Peterson B J and Bradford J 2008 Sediment and nutrient delivery from thermokarst features in the foothills of the North Slope, Alaska: Potential impacts on headwater stream ecosystems Journal of Geophysical Research: Biogeosciences 113 n/a-n/a
2-49. Brett M T, Bunn S E, Chandra S, Galloway A W E, Guo F, Kainz M J, Kankaala P, Lau D C P, Moulton T P, Power M E, Rasmussen J B, Taipale S J, Thorp J H and Wehr J D 2017 How important are terrestrial organic carbon inputs for secondary production in freshwater ecosystems? Freshwater Biology 62 833–53
2-50. Bröder L, Davydova A, Davydov S, Zimov N, Haghipour N, Eglinton T I and Vonk J E Particulate organic matter dynamics in a permafrost headwater stream and the Kolyma River mainstem Journal of Geophysical Research: Biogeosciences n/a e2019JG005511
2-51. Brooker A, Fraser R H, Olthof I, Kokelj S V and Lacelle D 2014 Mapping the Activity and Evolution of Retrogressive Thaw Slumps by Tasselled Cap Trend Analysis of a Landsat Satellite Image Stack Permafrost and Periglacial Processes 25 243–56

2-52. Brym A, Paerl H W, Montgomery M T, Handsel L T, Ziervogel K and Osburn C L 2014 Optical and chemical characterization of base-extracted particulate organic matter in coastal marine environments Marine Chemistry 162 96–113
2-53. Burn C R 1997 Cryostratigraphy, paleogeography, and climate change during the early Holocene warm interval, western Arctic coast, Canada Can. J. Earth Sci. 34 912–25
2-54. Calmels D, Gaillardet J, Brenot A and France-Lanord C 2007 Sustained sulfide oxidation by physical erosion processes in the Mackenzie River basin: Climatic perspectives Geol 35 1003
2-55. Chin K S, Lento J, Culp J M, Lacelle D and Kokelj S V 2016 Permafrost thaw and intense thermokarst activity decreases abundance of stream benthic macroinvertebrates Global Change Biology 22 2715–28
2-56. Coch C, Juhls B, Lamoureux S F, Lafrenière M J, Fritz M, Heim B and Lantuit H 2019 Comparisons of dissolved organic matter and its optical characteristics in small low and high Arctic catchments Biogeosciences 16 4535–53
2-57. Duk-Rodkin A, & Hughes, O L 1992 Surficial geology, Fort McPherson-Bell River, Yukon-Northwest Territories. Geological Survey of Canada.
2-58. Dyke A 2005 Late Quaternary Vegetation History of Northern North America Based on Pollen, Macrofossil, and Faunal Remains gpq 59 211–62
2-59. Ewing S A, O'Donnell J A, Aiken G R, Butler K, Butman D, Windham-Myers L and Kanevskiy M Z 2015 Long-term anoxia and release of ancient, labile carbon upon thaw of Pleistocene permafrost Geophysical Research Letters 42 10,730-10,738
2-60. Finlay J C and Kendall C 2008 Stable Isotope Tracing of Temporal and Spatial Variability in Organic Matter Sources to Freshwater Ecosystems Stable Isotopes in Ecology and Environmental Science (John Wiley & Sons, Ltd) pp 283–333
2-61. Franklin O, Hall E K, Kaiser C, Battin T J and Richter A 2011 Optimization of biomass composition explains microbial growth-stoichiometry relationships Am. Nat. 177 E29-42
2-62. Fuchs M, Grosse G, Strauss J, Günther F, Grigoriev M, Maximov G M and Hugelius G 2018 Carbon and nitrogen pools in thermokarst-affected permafrost landscapes in Arctic Siberia Biogeosciences 15 953–71
2-63. Fuchs M, Lenz J, Jock S, Nitze I, Jones B M, Strauss J, Günther F and Grosse G 2019 Organic Carbon and Nitrogen Stocks Along a Thermokarst Lake Sequence in Arctic Alaska Journal of Geophysical Research: Biogeosciences 124 1230–47
2-64. Grandy A S and Neff J C 2008 Molecular C dynamics downstream: the biochemical decomposition sequence and its impact on soil organic matter structure and function Sci. Total Environ. 404 297–307
2-65. Guo L and Macdonald R W 2006 Source and transport of terrigenous organic matter in the upper Yukon River: Evidence from isotope (δ13C, Δ14C, and δ15N) composition of dissolved, colloidal, and particulate phases Global Biogeochem. Cycles 20 GB2011
2-66. Guo L, Ping C-L and Macdonald R W 2007 Mobilization pathways of organic carbon from permafrost to arctic rivers in a changing climate Geophysical Research Letters 34 L13603
2-67. Guo F, Kainz M J, Sheldon F and Bunn S E 2016 The importance of high-quality algal food sources in stream food webs – current status and future perspectives Freshwater Biology 61 815–31
2-68. Gundelwein A, Müller-Lupp T, Sommerkorn M, Haupt E T K, Pfeiffer E-M and Wiechmann H 2007 Carbon in tundra soils in the Lake Labaz region of arctic Siberia European Journal of Soil Science 58 1164–74

2-69. Helms J R, Stubbins A, Ritchie J D, Minor E C, Kieber D J and Mopper K 2008 Absorption spectral slopes and slope ratios as indicators of molecular weight, source, and photobleaching of chromophoric dissolved organic matter Limnology and Oceanography 53 955–69
2-70. Hemingway J D, Rothman D H, Grant K E, Rosengard S Z, Eglinton T I, Derry L A and Galy V V 2019 Mineral protection regulates long-term global preservation of natural organic carbon Nature 570 228–31
2-71. Hilton R G, Galy V, Gaillardet J, Dellinger M, Bryant C, O'Regan M, Gröcke D R, Coxall H, Bouchez J and Calmels D 2015 Erosion of organic carbon in the Arctic as a geological carbon dioxide sink Nature 524 84–7
2-72. Horan K, Hilton R G, Dellinger M, Tipper E, Galy V, Calmels D, Selby D, Gaillardet J, Ottley C J, Parsons D R and Burton K W 2019 Carbon dioxide emissions by rock organic carbon oxidation and the net geochemical carbon budget of the Mackenzie River Basin Am J Sci 319 473–99
2-73. Holmes R M, McClelland J W, Peterson B J, Shiklomanov I A, Shiklomanov A I, Zhulidov A V, Gordeev V V and Bobrovitskaya N N 2002 A circumpolar perspective on fluvial sediment flux to the Arctic ocean Global Biogeochemical Cycles 16 45-1-45–14
2-74. Jain A, Krishnan K P, Singh A, Thomas F A, Begum N, Tiwari M, Bhaskar V P and Gopinath A 2019 Biochemical composition of particles shape particle-attached bacterial community structure in a high Arctic fjord Ecological Indicators 102 581–92
2-75. Jones M K W, Pollard W H and Jones B M 2019 Rapid initialization of retrogressive thaw slumps in the Canadian high Arctic and their response to climate and terrain factors Environ. Res. Lett. 14 055006
2-76. Kokelj S V, Smith C a. S and Burn C R 2002 Physical and chemical characteristics of the active layer and permafrost, Herschel Island, western Arctic Coast, Canada Permafrost and Periglacial Processes 13 171–85
2-77. Kokelj S V, Lantz T C, Kanigan J, Smith S L and Coutts R 2009 Origin and polycyclic behaviour of tundra thaw slumps, Mackenzie Delta region, Northwest Territories, Canada Permafrost and Periglacial Processes 20 173–84
2-78. Kokelj S V and Jorgenson M T 2013 Advances in Thermokarst Research Permafrost and Periglacial Processes 24 108–19
2-79. Kokelj S V, Lacelle D, Lantz T C, Tunnicliffe J, Malone L, Clark I D and Chin K S 2013 Thawing of massive ground ice in mega slumps drives increases in stream sediment and solute flux across a range of watershed scales Journal of Geophysical Research: Earth Surface 118 681–92
2-80. Kokelj S V, Tunnicliffe J, Lacelle D, Lantz T C, Chin K S and Fraser R 2015 Increased precipitation drives mega slump development and destabilization of ice-rich permafrost terrain, northwestern Canada Global and Planetary Change 129 56–68
2-81. Kokelj S Va, Lantz T C, Tunnicliffe J, Segal R and Lacelle D 2017 Climate-driven thaw of permafrost preserved glacial landscapes, northwestern Canada Geology 45 371–4
2-82. Kokelj S Vb, Tunnicliffe J F and Lacelle D 2017 The Peel Plateau of Northwestern Canada: An Ice-Rich Hummocky Moraine Landscape in Transition Landscapes and Landforms of Western Canada ed O Slaymaker (Cham: Springer International Publishing) pp 109–22 Online: http://link.springer.com/10.1007/978-3-319-44595-3_7
2-83. Kokelj S V, Kokoszka J, van der Sluijs J, Rudy A C A, Tunnicliffe J, Shakil S, Tank S, and Zolkos S Under Review Slope thermokarst transforms permafrost preserved glacial

landscapes and effects propogate through Arctic drainage networks The Cryosphere Discussions
2-84. Lacelle D, Bjornson J, Lauriol B, Clark I D and Troutet Y 2004 Segregated-intrusive ice of subglacial meltwater origin in retrogressive thaw flow headwalls, Richardson Mountains, NWT, Canada Quaternary Science Reviews 23 681–96
2-85. Lacelle D, Lauriol B, Zazula G, Ghaleb B, Utting N and Clark I D 2013 Timing of advance and basal condition of the Laurentide Ice Sheet during the last glacial maximum in the Richardson Mountains, NWT Quaternary Research 80 274–83
2-86. Lacelle D, Fontaine M, Pellerin A, Kokelj S V and Clark I D 2019 Legacy of Holocene Landscape Changes on Soil Biogeochemistry: A Perspective From Paleo-Active Layers in Northwestern Canada Journal of Geophysical Research: Biogeosciences 124 2662–79
2-87. Lamoureux S F and Lafrenière M J 2014 Seasonal fluxes and age of particulate organic carbon exported from Arctic catchments impacted by localized permafrost slope disturbances Environmental Research Letters 9 045002
2-88. Lane L, Roots C and Fraser T 2012 Geology Herschel Island Qikiqtaryuk: A natural and cultural history of Yukon's Arctic island ed C Burn (Calgary, AB, Canada: University of Calgary Press)
2-89. Lenth R V 2016 Least-Squares Means: The R Package lsmeans Journal of Statistical Software 69 1–33
2-90. Lewkowicz A G and Way R G 2019 Extremes of summer climate trigger thousands of thermokarst landslides in a High Arctic environment Nature Communications 10 1–11
2-91. C A, Tank S E and Kokelj S V 2017 Retrogressive thaw slumps temper dissolved organic carbon delivery to streams of the Peel Plateau, NWT, Canada Biogeosciences 14 5487–505
2-92. Littlefair C A and Tank S E 2018 Biodegradability of Thermokarst Carbon in a Till-Associated, Glacial Margin Landscape: The Case of the Peel Plateau, NWT, Canada Journal of Geophysical Research: Biogeosciences 123 3293–307
2-93. Levenstein B, Culp J M and Lento J 2018 Sediment inputs from retrogressive thaw slumps drive algal biomass accumulation but not decomposition in Arctic streams, NWT Freshwater Biology 63 1300–15
2-94. Ma S, Chen Y, Lu X and Wang X 2018 Soil Organic Matter Chemistry: Based on Pyrolysis-Gas Chromatography- Mass Spectrometry (Py-GC/MS) Mini-Reviews in Organic Chemistry 15 389–403
2-95. Malone L, Lacelle D, Kokelj S and Clark I D 2013 Impacts of hillslope thaw slumps on the geochemistry of permafrost catchments (Stony Creek watershed, NWT, Canada) Chemical Geology 356 38–49
2-96. Mann P J, Sobczak W V, LaRue M M, Bulygina E, Davydova A, Vonk J E, Schade J, Davydov S, Zimov N, Holmes R M and Spencer R G M 2014 Evidence for key enzymatic controls on metabolism of Arctic river organic matter Global Change Biology 20 1089–100
2-97. Manning D W P, Rosemond A D, Kominoski J S, Gulis V, Benstead J P and Maerz J C 2015 Detrital stoichiometry as a critical nexus for the effects of streamwater nutrients on leaf litter breakdown rates Ecology 96 2214–24
2-98. McCallister S L, Ishikawa N F and Kothawala D N 2018 Biogeochemical tools for characterizing organic carbon in inland aquatic ecosystems Limnology and Oceanography Letters 3 444–57

2-99. McClelland J W, Holmes R M, Peterson B J, Raymond P A, Striegl R G, Zhulidov A V, Zimov S A, Zimov N, Tank S E, Spencer R G M, Staples R, Gurtovaya T Y and Griffin C G 2016 Particulate organic carbon and nitrogen export from major Arctic rivers Global Biogeochem. Cycles 30 2015GB005351
2-100. Moorhead D L and Sinsabaugh R L 2006 A Theoretical Model of Litter Decay and Microbial Interaction Ecological Monographs 76 151–74
2-101. Murphy K R, Stedmon C A, Graeber D and Bro R 2013 Fluorescence spectroscopy and multi-way techniques. PARAFAC Analytical Methods 5 6557
2-102. Murphy K R, Stedmon C A, Wenig P and Bro R 2014 OpenFluor– an online spectral library of auto-fluorescence by organic compounds in the environment Anal. Methods 6 658–61
2-103. Murton J B and Ballantyne C K 2017 Chapter 5 Periglacial and permafrost ground models for Great Britain Geological Society, London, Engineering Geology Special Publications 28 501–97
2-104. Norris D K 1985 Geology of the Northern Yukon and Northwestern District of Mackenzie Ottawa, Canada: Geological Survey of Canada
2-105. Olefeldt D, Goswami S, Grosse G, Hayes D, Hugelius G, Kuhry P, McGuire A D, Romanovsky V E, Sannel A B K, Schuur E A G and Turetsky M R 2016 Circumpolar distribution and carbon storage of thermokarst landscapes Nature Communications 7 13043
2-106. O'Neill H B, Burn C R, Kokelj S V and Lantz T C 2015 'Warm' Tundra: Atmospheric and Near-Surface Ground Temperature Inversions Across an Alpine Treeline in Continuous Permafrost, Western Arctic, Canada: Near-Surface Ground Temperatures Across an Alpine Treeline Permafrost and Periglacial Processes 26 103–18
2-107. C L, Handsel L T, Mikan M P, Paerl H W and Montgomery M T 2012 Fluorescence Tracking of Dissolved and Particulate Organic Matter Quality in a River-Dominated Estuary Environmental Science & Technology 46 8628–36
2-108. Panneer Selvam B, Lapierre J-F, Guillemette F, Voigt C, Lamprecht R E, Biasi C, Christensen T R, Martikainen P J and Berggren M 2017 Degradation potentials of dissolved organic carbon (DOC) from thawed permafrost peat Scientific Reports 7 1–9
2-109. Pautler B G, Simpson A J, Mcnally D J, Lamoureux S F and Simpson M J 2010 Arctic Permafrost Active Layer Detachments Stimulate Microbial Activity and Degradation of Soil Organic Matter Environ. Sci. Technol. 44 4076–82
2-110. Peter S, Isidorova A and Sobek S 2016 Enhanced carbon loss from anoxic lake sediment through diffusion of dissolved organic carbon Journal of Geophysical Research: Biogeosciences 121 1959–77
2-111. Plaza C, Pegoraro E, Bracho R, Celis G, Crummer K G, Hutchings J A, Hicks Pries C E, Mauritz M, Natali S M, Salmon V G, Schädel C, Webb E E and Schuur E A G 2019 Direct observation of permafrost degradation and rapid soil carbon loss in tundra Nat. Geosci. 12 627–31
2-112. Ramage J L, Irrgang A M, Morgenstern A and Lantuit H 2018 Increasing coastal slump activity impacts the release of sediment and organic carbon into the Arctic Ocean Biogeosciences 15 1483–95
2-113. Richardson D C, Newbold J D, Aufdenkampe A K, Taylor P G and Kaplan L A 2013 Measuring heterotrophic respiration rates of suspended particulate organic carbon from stream ecosystems: Measuring respiration rates of POC Limnology and Oceanography: Methods 11 247–61

2-114. Roiha T, Peura S, Cusson M and Rautio M 2016 Allochthonous carbon is a major regulator to bacterial growth and community composition in subarctic freshwaters Scientific Reports 6 1–12
2-115. Rudy A C A, Lamoureux S F, Kokelj S V, Smith I R and England J H 2017 Accelerating Thermokarst Transforms Ice-Cored Terrain Triggering a Downstream Cascade to the Ocean Geophys. Res. Lett. 44 11,080-11,087
2-116. Sardans J, Rivas-Ubach A and Peñuelas J 2012 The elemental stoichiometry of aquatic and terrestrial ecosystems and its relationships with organismic lifestyle and ecosystem structure and function: a review and perspectives Biogeochemistry 111 1–39
2-117. Schirrmeister L, Froese D, Tumskoy V, Grosse G and Wetterich S 2013 PERMAFROST AND PERIGLACIAL FEATURES | Yedoma: Late Pleistocene Ice-Rich Syngenetic Permafrost of Beringia Encyclopedia of Quaternary Science ed S Elisa and C Mock (Amsterdam: Elsevier) pp 542–52
2-118. Schimel J P and Weintraub M N 2003 The implications of exoenzyme activity on microbial carbon and nitrogen limitation in soil: a theoretical model Soil Biology and Biochemistry 35 549–63
2-119. Schubert C J and Calvert S E 2001 Nitrogen and carbon isotopic composition of marine and terrestrial organic matter in Arctic Ocean sediments:: implications for nutrient utilization and organic matter composition Deep Sea Research Part I: Oceanographic Research Papers 48 789–810
2-120. Segal R A, Lantz T C and Kokelj S V 2016 Acceleration of thaw slump activity in glaciated landscapes of the Western Canadian Arctic Environmental Research Letters 11 034025
2-121. Sinsabaugh R L and Follstad Shah J J 2010 Integrating resource utilization and temperature in metabolic scaling of riverine bacterial production Ecology 91 1455–65
2-122. Sinsabaugh R L and Follstad Shah J J 2011 Ecoenzymatic stoichiometry of recalcitrant organic matter decomposition: the growth rate hypothesis in reverse Biogeochemistry 102 31–43
2-123. Sinsabaugh R L and Follstad Shah J J 2012 Ecoenzymatic Stoichiometry and Ecological Theory Annu. Rev. Ecol. Evol. Syst. 43 313–43
2-124. Sinsabaugh R L, Manzoni S, Moorhead D L and Richter A 2013 Carbon use efficiency of microbial communities: stoichiometry, methodology and modelling Ecology Letters 16 930–9
2-125. Slaymaker O and Kovanen D J 2017 Long-Term Geomorphic History of Western Canada Landscapes and Landforms of Western Canada World Geomorphological Landscapes ed O Slaymaker (Cham: Springer International Publishing) pp 3–26 Online: https://doi.org/10.1007/978-3-319-44595-3_1
2-126. Spencer R G M, Mann P J, Dittmar T, Eglinton T I, McIntyre C, Holmes R M, Zimov N and Stubbins A 2015 Detecting the signature of permafrost thaw in Arctic rivers Geophysical Research Letters 42 2830–5
2-127. Stelzer R S, Heffernan J and Likens G E 2003 The influence of dissolved nutrients and particulate organic matter quality on microbial respiration and biomass in a forest stream Freshwater Biology 48 1925–37
2-128. Stock B C, Jackson A L, Ward E J, Parnell A C, Phillips D L and Semmens B X 2018 Analyzing mixing systems using a new generation of Bayesian tracer mixing models PeerJ 6 e5096

2-129. Strauss J, Schirrmeister L, Grosse G, Fortier D, Hugelius G, Knoblauch C, Romanovsky V, Schädel C, Schneider von Deimling T, Schuur E A G, Shmelev D, Ulrich M and Veremeeva A 2017 Deep Yedoma permafrost: A synthesis of depositional characteristics and carbon vulnerability Earth-Science Reviews 172 75–86
2-130. Stubbins A, Lapierre J-F, Berggren M, Prairie Y T, Dittmar T and del Giorgio P A 2014 What's in an EEM? Molecular Signatures Associated with Dissolved Organic Fluorescence in Boreal Canada Environmental Science & Technology 48 10598–606
2-131. Tank S E, Vonk J E, Walvoord M A, McClelland J W, Laurion I and Abbott B W 2020 Landscape matters: Predicting the biogeochemical effects of permafrost thaw on aquatic networks with a state factor approach Permafrost and Periglacial Processes n/a Online: http://onlinelibrary.wiley.com/doi/abs/10.1002/ppp.2057
2-132. Tanski G, Lantuit H, Ruttor S, Knoblauch C, Radosavljevic B, Strauss J, Wolter J, Irrgang A M, Ramage J and Fritz M 2017 Transformation of terrestrial organic matter along thermokarst-affected permafrost coasts in the Arctic Science of The Total Environment 581–582 434–47
2-133. Tanski G, Wagner D, Knoblauch C, Fritz M, Sachs T and Lantuit H 2019 Rapid CO2 Release From Eroding Permafrost in Seawater Geophysical Research Letters 46 11244–52
2-134. Turetsky M R, Abbott B W, Jones M C, Anthony K W, Olefeldt D, Schuur E A G, Grosse G, Kuhry P, Hugelius G, Koven C, Lawrence D M, Gibson C, Sannel A B K and McGuire A D 2020 Carbon release through abrupt permafrost thaw Nature Geoscience 13 138–43
2-135. van der Sluijs J, Kokelj S V, Fraser R H, Tunnicliffe J and Lacelle D 2018 Permafrost Terrain Dynamics and Infrastructure Impacts Revealed by UAV Photogrammetry and Thermal Imaging Remote Sensing 10 1734
2-136. Vonk J E, Sánchez-García L, van Dongen B E, Alling V, Kosmach D, Charkin A, Semiletov I P, Dudarev O V, Shakhova N, Roos P, Eglinton T I, Andersson A and Gustafsson ö. 2012 Activation of old carbon by erosion of coastal and subsea permafrost in Arctic Siberia Nature 489 137–40
2-137. Vonk J E, Mann P J, Davydov S, Davydova A, Spencer R G M, Schade J, Sobczak W V, Zimov N, Zimov S, Bulygina E, Eglinton T I and Holmes R M 2013 High biolability of ancient permafrost carbon upon thaw Geophysical Research Letters 40 2689–93
2-138. Vonk J E, Tank S E, Bowden W B, Laurion I, Vincent W F, Alekseychik P, Amyot M, Billet M F, Canário J, Cory R M, Deshpande B N, Helbig M, Jammet M, Karlsson J, Larouche J, MacMillan G, Rautio M, Walter Anthony K M and Wickland K P 2015 Reviews and syntheses: Effects of permafrost thaw on Arctic aquatic ecosystems Biogeosciences 12 7129–67
2-139. Ward C P and Cory R M 2015 Chemical composition of dissolved organic matter draining permafrost soils Geochimica et Cosmochimica Acta 167 63–79
2-140. Wauthy M, Rautio M, Christoffersen K S, Forsström L, Laurion I, Mariash H L, Peura S and Vincent W F 2018 Increasing dominance of terrigenous organic matter in circumpolar freshwaters due to permafrost thaw Limnology and Oceanography Letters 3 186–98
2-141. Welti N, Striebel M, Ulseth A J, Cross W F, DeVilbiss S, Glibert P M, Guo L, Hirst A G, Hood J, Kominoski J S, MacNeill K L, Mehring A S, Welter J R and Hillebrand H 2017 Bridging Food Webs, Ecosystem Metabolism, and Biogeochemistry Using Ecological Stoichiometry Theory Frontiers in Microbiology 8 Online: http://journal.frontiersin.org/article/10.3389/fmicb.2017.01298/full

2-142. Wild B, Andersson A, Bröder L, Vonk J, Hugelius G, McClelland J W, Song W, Raymond P A and Gustafsson Ö 2019 Rivers across the Siberian Arctic unearth the patterns of carbon release from thawing permafrost PNAS 116 10280–5
2-143. Zazula G D, MacKay G, Andrews T D, Shapiro B, Letts B and Brock F 2009 A late Pleistocene steppe bison (Bison priscus) partial carcass from Tsiigehtchic, Northwest Territories, Canada Quaternary Science Reviews 28 2734–42
2-144. Zolkos S, Tank S E and Kokelj S V 2018 Mineral Weathering and the Permafrost Carbon-Climate Feedback Geophysical Research Letters 45 9623–32
2-145. Zolkos S, Tank S E, Striegl R G and Kokelj S V 2019 Thermokarst Effects on Carbon Dioxide and Methane Fluxes in Streams on the Peel Plateau (NWT, Canada) Journal of Geophysical Research: Biogeosciences 124 1781–98
2-146. Zolkos, S., Tank, S.E. 2019. Permafrost geochemistry and retrogressive thaw slump morphology (Peel Plateau, Canada), v. 1.0 (2017-2017). Nordicana D45, doi: 10.5885/45573XD-28DD57D553F14BF0. Zolkos S and Tank S E 2020 Experimental Evidence That Permafrost Thaw History and Mineral Composition Shape Abiotic Carbon Cycling in Thermokarst-Affected Stream Networks Front. Earth Sci. 8 Online: https://www.frontiersin.org/articles/10.3389/feart.2020.00152/full
3-147. Abbott, B. W., Larouche, J. R., Jones, J. B., Bowden, W. B., and Balser, A. W.: Elevated dissolved organic carbon biodegradability from thawing and collapsing permafrost, J. Geophys. Res. Biogeosciences, 119, 2049–2063, https://doi.org/10.1002/2014JG002678, 2014.
3-148. Attermeyer, K., Catalán, N., Einarsdottir, K., Freixa, A., Groeneveld, M., Hawkes, J. A., Bergquist, J., and Tranvik, L. J.: Organic Carbon Processing During Transport Through Boreal Inland Waters: Particles as Important Sites, J. Geophys. Res. Biogeosciences, 123, 2412–2428, https://doi.org/10.1029/2018JG004500, 2018.
3-149. Berggren, M., Lapierre, J.-F., and del Giorgio, P. A.: Magnitude and regulation of bacterioplankton respiratory quotient across freshwater environmental gradients, ISME J., 6, 984–993, https://doi.org/10.1038/ismej.2011.157, 2012.
3-150. Bock, E. and Wagner, M.: Oxidation of Inorganic Nitrogen Compounds as an Energy Source, in: The Prokaryotes, edited by: Rosenberg, E., DeLong, E. F., Lory, S., Stackebrandt, E., and Thompson, F., Springer Berlin Heidelberg, Berlin, Heidelberg, 83–118, https://doi.org/10.1007/978-3-642-30141-4_64, 2013.
3-151. Bröder, L., Keskitalo, K., Zolkos, S., Shakil, S., Tank, S. E., Kokelj, S. V., Tesi, T., van Dongen, B. E., Haghipour, N., Eglinton, T. I., and Vonk, J. E.: Preferential export of permafrost-derived organic matter as retrogressive thaw slumping intensifies, Environ. Res. Lett., https://doi.org/10.1088/1748-9326/abee4b, 2021.
3-152. Coble, P. G.: Marine Optical Biogeochemistry: The Chemistry of Ocean Color, Chem. Rev., 107, 402–418, https://doi.org/10.1021/cr050350%2B, 2007.
3-153. Duk-Rodkin, A., and Hughes, O. L.: Surficial geology, Fort McPherson-Bell River, Yukon-Northwest Territories. Geological Survey of Canada, 1992.
3-154. Groeneveld, M., Catalán, N., Attermeyer, K., Hawkes, J., Einarsdóttir, K., Kothawala, D., Bergquist, J., and Tranvik, L.: Selective Adsorption of Terrestrial Dissolved Organic Matter to Inorganic Surfaces Along a Boreal Inland Water Continuum, J. Geophys. Res. Biogeosciences, 125, e2019JG005236, https://doi.org/10.1029/2019JG005236, 2020.
3-155. Hemingway, J. D., Rothman, D. H., Grant, K. E., Rosengard, S. Z., Eglinton, T. I., Derry, L. A., and Galy, V. V.: Mineral protection regulates long-term global preservation of

natural organic carbon, Nature, 570, 228–231, https://doi.org/10.1038/s41586-019-1280-6, 2019.
3-156. Hugelius, G., Strauss, J., Zubrzycki, S., Harden, J. W., Schuur, E. A. G., Ping, C.-L., Schirrmeister, L., Grosse, G., Michaelson, G. J., Koven, C. D., O'Donnell, J. A., Elberling, B., Mishra, U., Camill, P., Yu, Z., Palmtag, J., and Kuhry, P.: Estimated stocks of circumpolar permafrost carbon with quantified uncertainty ranges and identified data gaps, Biogeosciences, 11, 6573–6593, https://doi.org/10.5194/bg-11-6573-2014, 2014.
3-157. Keskitalo, K. H., Bröder, L., Shakil, S., Zolkos, S., Tank, S. E., van Dongen, B. E., Tesi, T., Haghipour, N., Eglinton, T. I., Kokelj, S. V., and Vonk, J. E.: Downstream Evolution of Particulate Organic Matter Composition From Permafrost Thaw Slumps, Front. Earth Sci., 9, https://doi.org/10.3389/feart.2021.642675, 2021.
3-158. Klatt, J. M. and Polerecky, L.: Assessment of the stoichiometry and efficiency of CO2 fixation coupled to reduced sulfur oxidation, Front. Microbiol., 6, https://doi.org/10.3389/fmicb.2015.00484, 2015.
3-159. Kokelj, S. V., Kokoszka, J., van der Sluijs, J., Rudy, A. C. A., Tunnicliffe, J., Shakil, S., Tank, S., and Zolkos, S.: Permafrost thaw couples slopes with downstream systems and effects propagate through Arctic drainage networks, Cryosphere Discuss., 1–43, https://doi.org/10.5194/tc-2020-218, 2020.
3-160. Kothawala, D. N., Kellerman, A. M., Catalán, N., and Tranvik, L. J.: Organic Matter Degradation across Ecosystem Boundaries: The Need for a Unified Conceptualization, Trends Ecol. Evol., 36, 113–122, https://doi.org/10.1016/j.tree.2020.10.006, 2021.
3-161. Lacelle, D., Fontaine, M., Pellerin, A., Kokelj, S. V., and Clark, I. D.: Legacy of Holocene Landscape Changes on Soil Biogeochemistry: A Perspective From Paleo-Active Layers in Northwestern Canada, J. Geophys. Res. Biogeosciences, 124, 2662–2679, https://doi.org/10.1029/2018JG004916, 2019.
3-162. Lenth, R. V.: emmeans: Estimated Marginal Means, aka Least-Squares Means. R package version 1.6.0. https://CRAN.R-project.org/package=emmeans, 2021.
3-163. Littlefair, C. A. and Tank, S. E.: Biodegradability of Thermokarst Carbon in a Till-Associated, Glacial Margin Landscape: The Case of the Peel Plateau, NWT, Canada, J. Geophys. Res. Biogeosciences, 123, 3293–3307, https://doi.org/10.1029/2018JG004461, 2018.
3-164. Littlefair, C. A., Tank, S. E., and Kokelj, S. V.: Retrogressive thaw slumps temper dissolved organic carbon delivery to streams of the Peel Plateau, NWT, Canada, Biogeosciences, 14, 5487–5505, https://doi.org/10.5194/bg-14-5487-2017, 2017.
3-165. Mann, P. J., Eglinton, T. I., McIntyre, C. P., Zimov, N., Davydova, A., Vonk, J. E., Holmes, R. M., and Spencer, R. G. M.: Utilization of ancient permafrost carbon in headwaters of Arctic fluvial networks, Nat. Commun., 6, 7856, https://doi.org/10.1038/ncomms8856, 2015.
3-166. Nelson, D. C., Jørgensen, B. B., and Revsbech, N. P.: Growth Pattern and Yield of a Chemoautotrophic Beggiatoa sp. in Oxygen-Sulfide Microgradients, Appl. Environ. Microbiol., 52, 225–233, 1986.
3-167. Olefeldt, D., Goswami, S., Grosse, G., Hayes, D., Hugelius, G., Kuhry, P., McGuire, A. D., Romanovsky, V. E., Sannel, A. B. K., Schuur, E. A. G., and Turetsky, M. R.: Circumpolar distribution and carbon storage of thermokarst landscapes, Nat. Commun., 7, 13043, https://doi.org/10.1038/ncomms13043, 2016.

3-168. Opfergelt, S.: The next generation of climate model should account for the evolution of mineral-organic interactions with permafrost thaw, Environ. Res. Lett., 15, 091003, https://doi.org/10.1088/1748-9326/ab9a6d, 2020.
3-169. Osburn, C. L., Handsel, L. T., Mikan, M. P., Paerl, H. W., and Montgomery, M. T.: Fluorescence Tracking of Dissolved and Particulate Organic Matter Quality in a River-Dominated Estuary, Environ. Sci. Technol., 46, 8628–8636, https://doi.org/10.1021/es3007723, 2012.
3-170. Percak-Dennett, E., He, S., Converse, B., Konishi, H., Xu, H., Corcoran, A., Noguera, D., Chan, C., Bhattacharyya, A., Borch, T., Boyd, E., and Roden, E. E.: Microbial acceleration of aerobic pyrite oxidation at circumneutral pH, Geobiology, 15, 690–703, https://doi.org/10.1111/gbi.12241, 2017.
3-171. Peter, S., Isidorova, A., and Sobek, S.: Enhanced carbon loss from anoxic lake sediment through diffusion of dissolved organic carbon, J. Geophys. Res. Biogeosciences, 121, 1959–1977, https://doi.org/10.1002/2016JG003425, 2016.
3-172. Richardson, D. C., Newbold, J. D., Aufdenkampe, A. K., Taylor, P. G., and Kaplan, L. A.: Measuring heterotrophic respiration rates of suspended particulate organic carbon from stream ecosystems: Measuring respiration rates of POC, Limnol. Oceanogr. Methods, 11, 247–261, https://doi.org/10.4319/lom.2013.11.247, 2013.
3-173. Schuur, E. A. G., McGuire, A. D., Schädel, C., Grosse, G., Harden, J. W., Hayes, D. J., Hugelius, G., Koven, C. D., Kuhry, P., Lawrence, D. M., Natali, S. M., Olefeldt, D., Romanovsky, V. E., Schaefer, K., Turetsky, M. R., Treat, C. C., and Vonk, J. E.: Climate change and the permafrost carbon feedback, Nature, 520, 171–179, https://doi.org/10.1038/nature14338, 2015.
3-174. Segal, R. A., Lantz, T. C., and Kokelj, S. V.: Acceleration of thaw slump activity in glaciated landscapes of the Western Canadian Arctic, Environ. Res. Lett., 11, 034025, https://doi.org/10.1088/1748-9326/11/3/034025, 2016.
3-175. Shakil, S., Tank, S. E., Kokelj, S. V., Vonk, J. E., and Zolkos, S.: Particulate dominance of organic carbon mobilization from thaw slumps on the Peel Plateau, NT: Quantification and implications for stream systems and permafrost carbon release, Environ. Res. Lett., 15, 114019, https://doi.org/10.1088/1748-9326/abac36, 2020.
3-176. Shakil, S., Tank, S., Vonk J.E., and Zolkos S.: Incubation Data Assessing Biodegradability of Organic Carbon Mobilized from Permafrost Thaw Slumps (Peel Plateau, NT, Canada). Waterloo, Canada: Canadian Cryospheric Information Network (CCIN). (DOI TBD), 2021.
3-177. Sinha, B. and Annachhatre, A. P.: Partial nitrification—operational parameters and microorganisms involved, Rev. Environ. Sci. Biotechnol., 6, 285–313, https://doi.org/10.1007/s11157-006-9116-x, 2007.
3-178. Spona-Friedl, M., Braun, A., Huber, C., Eisenreich, W., Griebler, C., Kappler, A., and Elsner, M.: Substrate-dependent CO2 fixation in heterotrophic bacteria revealed by stable isotope labelling, FEMS Microbiol. Ecol., 96, fiaa080, https://doi.org/10.1093/femsec/fiaa080, 2020.
3-179. Stolper, D. A., Revsbech, N. P., and Canfield, D. E.: Aerobic growth at nanomolar oxygen concentrations, Proc. Natl. Acad. Sci., 107, 18755–18760, https://doi.org/10.1073/pnas.1013435107, 2010.
3-180. Tank, S. E., Vonk, J. E., Walvoord, M. A., McClelland, J. W., Laurion, I., and Abbott, B. W.: Landscape matters: Predicting the biogeochemical effects of permafrost thaw on

aquatic networks with a state factor approach, Permafr. Periglac. Process., 31, 358–370, https://doi.org/10.1002/ppp.2057, 2020.
3-181. Tanski, G., Lantuit, H., Ruttor, S., Knoblauch, C., Radosavljevic, B., Strauss, J., Wolter, J., Irrgang, A. M., Ramage, J., and Fritz, M.: Transformation of terrestrial organic matter along thermokarst-affected permafrost coasts in the Arctic, Sci. Total Environ., 581–582, 434–447, https://doi.org/10.1016/j.scitotenv.2016.12.152, 2017.
3-182. Tanski, G., Wagner, D., Knoblauch, C., Fritz, M., Sachs, T., and Lantuit, H.: Rapid CO2 Release From Eroding Permafrost in Seawater, Geophys. Res. Lett., 46, 11244–11252, https://doi.org/10.1029/2019GL084303, 2019.
3-183. Tesi, T., Semiletov, I., Dudarev, O., Andersson, A., and Gustafsson, Ö.: Matrix association effects on hydrodynamic sorting and degradation of terrestrial organic matter during cross-shelf transport in the Laptev and East Siberian shelf seas, J. Geophys. Res. Biogeosciences, 121, 731–752, https://doi.org/10.1002/2015JG003067, 2016.
3-184. Turetsky, M. R., Abbott, B. W., Jones, M. C., Anthony, K. W., Olefeldt, D., Schuur, E. A. G., Grosse, G., Kuhry, P., Hugelius, G., Koven, C., Lawrence, D. M., Gibson, C., Sannel, A. B. K., and McGuire, A. D.: Carbon release through abrupt permafrost thaw, Nat. Geosci., 13, 138–143, https://doi.org/10.1038/s41561-019-0526-0, 2020.
3-185. Vachon, D., Sadro, S., Bogard, M. J., Lapierre, J.-F., Baulch, H. M., Rusak, J. A., Denfeld, B. A., Laas, A., Klaus, M., Karlsson, J., Weyhenmeyer, G. A., and Giorgio, P. A. del: Paired O2–CO2 measurements provide emergent insights into aquatic ecosystem function, Limnol. Oceanogr. Lett., 5, 287–294, https://doi.org/10.1002/lol2.10135, 2020.
3-186. Vonk, J. E., Tank, S. E., Mann, P. J., Spencer, R. G. M., Treat, C. C., Striegl, R. G., Abbott, B. W., and Wickland, K. P.: Biodegradability of dissolved organic carbon in permafrost soils and aquatic systems: a meta-analysis, Biogeosciences, 12, 6915–6930, https://doi.org/10.5194/bg-12-6915-2015, 2015a.
3-187. Vonk, J. E., Tank, S. E., Bowden, W. B., Laurion, I., Vincent, W. F., Alekseychik, P., Amyot, M., Billet, M. F., Canário, J., Cory, R. M., Deshpande, B. N., Helbig, M., Jammet, M., Karlsson, J., Larouche, J., MacMillan, G., Rautio, M., Walter Anthony, K. M., and Wickland, K. P.: Reviews and syntheses: Effects of permafrost thaw on Arctic aquatic ecosystems, Biogeosciences, 12, 7129–7167, https://doi.org/10.5194/bg-12-7129-2015, 2015b.
3-188. Weishaar, J. L., Aiken, G. R., Bergamaschi, B. A., Fram, M. S., Fujii, R., and Mopper, K.: Evaluation of Specific Ultraviolet Absorbance as an Indicator of the Chemical Composition and Reactivity of Dissolved Organic Carbon, Environ. Sci. Technol., 37, 4702–4708, https://doi.org/10.1021/es030360x, 2003.
3-189. Wologo, E., Shakil, S., Zolkos, S., Textor, S., Ewing, S., Klassen, J., Spencer, R. G. M., Podgorski, D. C., Tank, S. E., Baker, M. A., O'Donnell, J. A., Wickland, K. P., Foks, S. S. W., Zarnetske, J. P., Lee-Cullin, J., Liu, F., Yang, Y., Kortelainen, P., Kolehmainen, J., Dean, J. F., Vonk, J. E., Holmes, R. M., Pinay, G., Powell, M. M., Howe, J., Frei, R. J., Bratsman, S. P., and Abbott, B. W.: Stream Dissolved Organic Matter in Permafrost Regions Shows Surprising Compositional Similarities but Negative Priming and Nutrient Effects, Glob. Biogeochem. Cycles, 35, e2020GB006719, https://doi.org/10.1029/2020GB006719, 2021.
3-190. Zar, J. H.: Biostatistical Analysis, 5th ed., Prentice Hall, Upper Saddle River, N.J., 944 pp., 2010.

3-191. Zolkos, S. and Tank, S. E.: Experimental Evidence That Permafrost Thaw History and Mineral Composition Shape Abiotic Carbon Cycling in Thermokarst-Affected Stream Networks, Front. Earth Sci., 8, https://doi.org/10.3389/feart.2020.00152, 2020.
3-192. Zolkos, S., Tank, S. E., and Kokelj, S. V.: Mineral Weathering and the Permafrost Carbon-Climate Feedback, Geophys. Res. Lett., 45, 9623–9632, https://doi.org/10.1029/2018GL078748, 2018.
3-193. Zolkos, S., Tank, S. E., Striegl, R. G., and Kokelj, S. V.: Thermokarst Effects on Carbon Dioxide and Methane Fluxes in Streams on the Peel Plateau (NWT, Canada), J. Geophys. Res. Biogeosciences, 124, 1781–1798, https://doi.org/10.1029/2019JG005038, 2019.
3-194. Zolkos, S., Tank, S. E., Striegl, R. G., Kokelj, S. V., Kokoszka, J., Estop-Aragonés, C., and Olefeldt, D.: Thermokarst amplifies fluvial inorganic carbon cycling and export across watershed scales on the Peel Plateau, Canada, Biogeosciences, 17, 5163–5182, https://doi.org/10.5194/bg-17-5163-2020, 2020.
4-195. Beel C R, Lamoureux S F, Orwin J F, Pope M A, Lafrenière M J and Scott N A 2020 Differential impact of thermal and physical permafrost disturbances on High Arctic dissolved and particulate fluvial fluxes *Scientific Reports* **10** 11836
4-196. Biskaborn B K, Smith S L, Noetzli J, Matthes H, Vieira G, Streletskiy D A, Schoeneich P, Romanovsky V E, Lewkowicz A G, Abramov A, Allard M, Boike J, Cable W L, Christiansen H H, Delaloye R, Diekmann B, Drozdov D, Etzelmüller B, Grosse G, Guglielmin M, Ingeman-Nielsen T, Isaksen K, Ishikawa M, Johansson M, Johannsson H, Joo A, Kaverin D, Kholodov A, Konstantinov P, Kröger T, Lambiel C, Lanckman J-P, Luo D, Malkova G, Meiklejohn I, Moskalenko N, Oliva M, Phillips M, Ramos M, Sannel A B K, Sergeev D, Seybold C, Skryabin P, Vasiliev A, Wu Q, Yoshikawa K, Zheleznyak M and Lantuit H 2019 Permafrost is warming at a global scale *Nature Communications* **10** 264
4-197. Bowden W B, Gooseff M N, Balser A, Green A, Peterson B J and Bradford J 2008 Sediment and nutrient delivery from thermokarst features in the foothills of the North Slope, Alaska: Potential impacts on headwater stream ecosystems *Journal of Geophysical Research: Biogeosciences* **113** n/a-n/a
4-198. Bröder L, Keskitalo K, Zolkos S, Shakil S, Tank S E, Kokelj S V, Tesi T, Dongen B E V, Haghipour N, Eglinton T I and Vonk J E 2021 Preferential export of permafrost-derived organic matter as retrogressive thaw slumping intensifies *Environ. Res. Lett.* **16** 054059
4-199. Carvalhais N, Forkel M, Khomik M, Bellarby J, Jung M, Migliavacca M, Mu M, Saatchi S, Santoro M, Thurner M, Weber U, Ahrens B, Beer C, Cescatti A, Randerson J T and Reichstein M 2014 Global covariation of carbon turnover times with climate in terrestrial ecosystems *Nature* **514** 213–7
4-200. Cameron E A and Lantz T C 2016 Drivers of tall shrub proliferation adjacent to the Dempster Highway, Northwest Territories, Canada *Environ. Res. Lett.* **11** 045006
4-201. Casper A F, Rautio M, Martineau C and Vincent W F 2015 Variation and Assimilation of Arctic Riverine Sestonin the Pelagic Food Web of the Mackenzie River Delta and Beaufort Sea Transition Zone *Estuaries and Coasts* **38** 1656–63
4-202. Chen A, Lantz T C, Hermosilla T and Wulder M A 2021 Biophysical controls of increased tundra productivity in the western Canadian Arctic *Remote Sensing of Environment* **258** 112358

4-203. Chin K S, Lento J, Culp J M, Lacelle D and Kokelj S V 2016 Permafrost thaw and intense thermokarst activity decreases abundance of stream benthic macroinvertebrates *Global Change Biology* **22** 2715–28
4-204. Connon R F, Quinton W L, Craig J R and Hayashi M 2014 Changing hydrologic connectivity due to permafrost thaw in the lower Liard River valley, NWT, Canada *Hydrological Processes* **28** 4163–78
4-205. Dingman S L 2009 *Fluvial Hydraulics* (Oxford University Press)
4-206. Galy V, Peucker-Ehrenbrink B and Eglinton T 2015 Global carbon export from the terrestrial biosphere controlled by erosion *Nature* **521** 204–7
4-207. Groeneveld M, Catalán N, Attermeyer K, Hawkes J, Einarsdóttir K, Kothawala D, Bergquist J and Tranvik L 2020 Selective Adsorption of Terrestrial Dissolved Organic Matter to Inorganic Surfaces Along a Boreal Inland Water Continuum *Journal of Geophysical Research: Biogeosciences* **125** e2019JG005236
4-208. Hilton R G, Galy V, Gaillardet J, Dellinger M, Bryant C, O'Regan M, Gröcke D R, Coxall H, Bouchez J and Calmels D 2015 Erosion of organic carbon in the Arctic as a geological carbon dioxide sink *Nature* **524** 84–7
4-209. Horan K, Hilton R G, Dellinger M, Tipper E, Galy V, Calmels D, Selby D, Gaillardet J, Ottley C J, Parsons D R and Burton K W 2019 Carbon dioxide emissions by rock organic carbon oxidation and the net geochemical carbon budget of the Mackenzie River Basin *Am J Sci* **319** 473–99
4-210. Hugelius G, Strauss J, Zubrzycki S, Harden J W, Schuur E A G, Ping C-L, Schirrmeister L, Grosse G, Michaelson G J, Koven C D, O'Donnell J A, Elberling B, Mishra U, Camill P, Yu Z, Palmtag J and Kuhry P 2014 Estimated stocks of circumpolar permafrost carbon with quantified uncertainty ranges and identified data gaps *Biogeosciences* **11** 6573–93
4-211. Keskitalo K H, Bröder L, Shakil S, Zolkos S, Tank S E, van Dongen B E, Tesi T, Haghipour N, Eglinton T I, Kokelj S V and Vonk J E 2021 Downstream Evolution of Particulate Organic Matter Composition From Permafrost Thaw Slumps *Frontiers in Earth Science* **9** 181
4-212. Kokelj S V, Kokoszka J, van der Sluijs J, Rudy A C A, Tunnicliffe J, Shakil S, Tank S E and Zolkos S 2021 Thaw-driven mass wasting couples slopes with downstream systems, and effects propagate through Arctic drainage networks *The Cryosphere* **15** 3059–8
4-213. Kokelj S V, Lantz T C, Tunnicliffe J, Segal R and Lacelle D 2017 Climate-driven thaw of permafrost preserved glacial landscapes, northwestern Canada *Geology* **45** 371–4
4-214. Kokelj S V and Jorgenson M T 2013 Advances in Thermokarst Research *Permafrost and Periglac. Process.* **24** 108–19
4-215. Kokelj S V, Jenkins R E, Milburn D, Burn C R and Snow N 2005 The influence of thermokarst disturbance on the water quality of small upland lakes, Mackenzie Delta region, Northwest Territories, Canada *Permafrost Periglac. Process.* **16** 343–53
4-216. McClelland J W, Holmes R M, Peterson B J, Raymond P A, Striegl R G, Zhulidov A V, Zimov S A, Zimov N, Tank S E, Spencer R G M, Staples R, Gurtovaya T Y and Griffin C G 2016 Particulate organic carbon and nitrogen export from major Arctic rivers *Global Biogeochem. Cycles* **30** 2015GB005351
4-217. Lacelle D, Fontaine M, Pellerin A, Kokelj S V and Clark I D 2019 Legacy of Holocene Landscape Changes on Soil Biogeochemistry: A Perspective From Paleo-Active Layers in Northwestern Canada *Journal of Geophysical Research: Biogeosciences* **124** 2662–79

4-218. Lacelle D, Lauriol B, Zazula G, Ghaleb B, Utting N and Clark I D 2013 Timing of advance and basal condition of the Laurentide Ice Sheet during the last glacial maximum in the Richardson Mountains, NWT *Quaternary Research* **80** 274–83
4-219. Lacelle D, Bjornson J and Lauriol B 2010 Climatic and geomorphic factors affecting contemporary (1950–2004) activity of retrogressive thaw slumps on the Aklavik Plateau, Richardson Mountains, NWT, Canada *Permafrost and Periglacial Processes* **21** 1–15
4-220. Lacelle D, Bjornson J, Lauriol B, Clark I D and Troutet Y 2004 Segregated-intrusive ice of subglacial meltwater origin in retrogressive thaw flow headwalls, Richardson Mountains, NWT, Canada *Quaternary Science Reviews* **23** 681–96
4-221. Levenstein B M Impacts of retrogressive thaw slump disturbances on biological structure and function in Arctic streams, Peel Plateau, NWT 136
4-222. Littlefair C A, Tank S E and Kokelj S V 2017 Retrogressive thaw slumps temper dissolved organic carbon delivery to streams of the Peel Plateau, NWT, Canada *Biogeosciences* **14** 5487–505
4-223. Mekonnen Z A, Riley W J, Berner L T, Bouskill N J, Torn M S, Iwahana G, Breen A L, Myers-Smith I H, Criado M G, Liu Y, Euskirchen E S, Goetz S J, Mack M C and Grant R F 2021 Arctic tundra shrubification: a review of mechanisms and impacts on ecosystem carbon balance *Environ. Res. Lett.* **16** 053001
4-224. Nitze I, Heidler K, Barth S and Grosse G 2021 Developing and Testing a Deep Learning Approach for Mapping Retrogressive Thaw Slumps *Remote Sensing* **13** 4294
4-225. Opfergelt S 2020 The next generation of climate model should account for the evolution of mineral-organic interactions with permafrost thaw *Environ. Res. Lett.* **15** 091003
4-226. Peiffer S, Kappler A, Haderlein S B, Schmidt C, Byrne J M, Kleindienst S, Vogt C, Richnow H H, Obst M, Angenent L T, Bryce C, McCammon C and Planer-Friedrich B 2021 A biogeochemical–hydrological framework for the role of redox-active compounds in aquatic systems *Nat. Geosci.* **14** 264–72
4-227. Repasch M, Scheingross J S, Hovius N, Lupker M, Wittmann H, Haghipour N, Gröcke D R, Orfeo O, Eglinton T I and Sachse D 2021 Fluvial organic carbon cycling regulated by sediment transit time and mineral protection *Nat. Geosci.* **14** 842–8
4-228. R Core Team (2013). R: A language and environment for statistical computing. R Foundation for Statistical Computing, Vienna, Austria. ISBN 3-900051-07-0, URL http://www.R-project.org/.
4-229. Schuur E A G, McGuire A D, Schädel C, Grosse G, Harden J W, Hayes D J, Hugelius G, Koven C D, Kuhry P, Lawrence D M, Natali S M, Olefeldt D, Romanovsky V E, Schaefer K, Turetsky M R, Treat C C and Vonk J E 2015 Climate change and the permafrost carbon feedback *Nature* **520** 171–9
4-230. Shakil S, Tank S E, Kokelj S V, Vonk J E and Zolkos S 2020 Particulate dominance of organic carbon mobilization from thaw slumps on the Peel Plateau, NT: Quantification and implications for stream systems and permafrost carbon release *Environ. Res. Lett.* **15** 114019
4-231. Shogren A J, Zarnetske J P, Abbott B W, Iannucci F, Frei R J, Griffin N A and Bowden W B 2019 Revealing biogeochemical signatures of Arctic landscapes with river chemistry *Sci Rep* **9** 12894
4-232. Schuur E A G and Mack M C 2018 Ecological Response to Permafrost Thaw and Consequences for Local and Global Ecosystem Services *Annual Review of Ecology, Evolution, and Systematics* **49** 279–301

4-233. Schuur E A G, McGuire A D, Schädel C, Grosse G, Harden J W, Hayes D J, Hugelius G, Koven C D, Kuhry P, Lawrence D M, Natali S M, Olefeldt D, Romanovsky V E, Schaefer K, Turetsky M R, Treat C C and Vonk J E 2015 Climate change and the permafrost carbon feedback *Nature* **520** 171–9
4-234. Spence C, Kokelj S V, Kokelj S A, McCluskie M and Hedstrom N 2015 Evidence of a change in water chemistry in Canada's subarctic associated with enhanced winter streamflow *Journal of Geophysical Research: Biogeosciences* **120** 113–27
4-235. St. Pierre K A, Zolkos S, Shakil S, Tank S E, St. Louis V L and Kokelj S V 2018 Unprecedented Increases in Total and Methyl Mercury Concentrations Downstream of Retrogressive Thaw Slumps in the Western Canadian Arctic *Environmental Science & Technology* Online: http://pubs.acs.org/doi/10.1021/acs.est.8b05348
4-236. Terhaar J, Lauerwald R, Regnier P, Gruber N and Bopp L 2021 Around one third of current Arctic Ocean primary production sustained by rivers and coastal erosion *Nat Commun* **12** 169
4-237. Turetsky M R, Abbott B W, Jones M C, Anthony K W, Olefeldt D, Schuur E A G, Grosse G, Kuhry P, Hugelius G, Koven C, Lawrence D M, Gibson C, Sannel A B K and McGuire A D 2020 Carbon release through abrupt permafrost thaw *Nature Geoscience* **13** 138–43
4-238. Walvoord M A and Kurylyk B L 2016 Hydrologic Impacts of Thawing Permafrost—A Review *Vadose Zone Journal* **15** vzj2016.01.0010
4-239. Wainwright J, Parsons A J, Cooper J R, Gao P, Gillies J A, Mao L, Orford J D and Knight P G 2015 The concept of transport capacity in geomorphology *Reviews of Geophysics* **53** 1155–202
4-240. Whiteside J H, Olsen P E, Eglinton T I, Cornet B, McDonald N G and Huber P 2011 Pangean great lake paleoecology on the cusp of the end-Triassic extinction *Palaeogeography, Palaeoclimatology, Palaeoecology* **301** 1–17
4-241. van der Sluijs J, Kokelj S V, Fraser R H, Tunnicliffe J and Lacelle D 2018 Permafrost Terrain Dynamics and Infrastructure Impacts Revealed by UAV Photogrammetry and Thermal Imaging *Remote Sensing* **10** 1734
4-242. Vonk J E, Tank S E and Walvoord M A 2019 Integrating hydrology and biogeochemistry across frozen landscapes *Nat Commun* **10** 5377
4-243. Young E W 2021 *Predicting DOC Concentration in the Peel River with a Mechanistic Numerical Model* (Utrecht University)
4-244. Yue S, Pilon P, Phinney B and Cavadias G 2002 The influence of autocorrelation on the ability to detect trend in hydrological series *Hydrological Processes* **16** 1807–29
4-245. Zolkos S, Tank S E, Striegl R G, Kokelj S V, Kokoszka J, Estop-Aragonés C and Olefeldt D 2020 Thermokarst amplifies fluvial inorganic carbon cycling and export across watershed scales on the Peel Plateau, Canada *Biogeosciences* **17** 5163–82
5-246. Abbott B W and Jones J B 2015 Permafrost collapse alters soil carbon stocks, respiration, CH4, and N2O in upland tundra *Global Change Biology* **21** 4570–87
5-247. Allen T L, Fraser T A, Hutchinson M P, Dolby G, Reyes J and Utting J 2015 *OF2015-3.pdf* (Yukon Geological Survey) Online: http://ygsftp.gov.yk.ca/publications/openfile/2015/OF2015-3.pdf
5-248. Battin T J, Besemer K, Bengtsson M M, Romani A M and Packmann A I 2016 The ecology and biogeochemistry of stream biofilms *Nat Rev Microbiol* **14** 251–63

5-249. Beel C R, Lamoureux S F and Orwin J F 2018 Fluvial Response to a Period of Hydrometeorological Change and Landscape Disturbance in the Canadian High Arctic *Geophysical Research Letters* **45** 10,446-10,455
5-250. Bröder L, Keskitalo K, Zolkos S, Shakil S, Tank S E, Kokelj S V, Tesi T, Dongen B E V, Haghipour N, Eglinton T I and Vonk J E 2021 Preferential export of permafrost-derived organic matter as retrogressive thaw slumping intensifies *Environ. Res. Lett.* **16** 054059
5-251. Opfergelt S 2020 The next generation of climate model should account for the evolution of mineral-organic interactions with permafrost thaw *Environ. Res. Lett.* **15** 091003
5-252. Peiffer S, Kappler A, Haderlein S B, Schmidt C, Byrne J M, Kleindienst S, Vogt C, Richnow H H, Obst M, Angenent L T, Bryce C, McCammon C and Planer-Friedrich B 2021 A biogeochemical–hydrological framework for the role of redox-active compounds in aquatic systems *Nat. Geosci.* **14** 264–72
5-253. Kokelj S V, Kokoszka J, van der Sluijs J, Rudy A C A, Tunnicliffe J, Shakil S, Tank S E and Zolkos S 2021 Thaw-driven mass wasting couples slopes with downstream systems, and effects propagate through Arctic drainage networks *The Cryosphere* **15** 3059–81
5-254. Kokelj S V, Lantz T C, Tunnicliffe J, Segal R and Lacelle D 2017 Climate-driven thaw of permafrost preserved glacial landscapes, northwestern Canada *Geology* **45** 371–4
5-255. Kokelj S V, Lacelle D, Lantz T C, Tunnicliffe J, Malone L, Clark I D and Chin K S 2013 Thawing of massive ground ice in mega slumps drives increases in stream sediment and solute flux across a range of watershed scales: FLUVIAL IMPACTS OF THERMOKARST *Journal of Geophysical Research: Earth Surface* **118** 681–92
5-256. Nitze I, Heidler K, Barth S and Grosse G 2021 Developing and Testing a Deep Learning Approach for Mapping Retrogressive Thaw Slumps *Remote Sensing* **13** 4294
5-257. Shakil S, Tank S E, Kokelj S V, Vonk J E and Zolkos S 2020 Particulate dominance of organic carbon mobilization from thaw slumps on the Peel Plateau, NT: Quantification and implications for stream systems and permafrost carbon release *Environ. Res. Lett.* **15** 114019
5-258. St. Pierre K A, Zolkos S, Shakil S, Tank S E, St. Louis V L and Kokelj S V 2018 Unprecedented Increases in Total and Methyl Mercury Concentrations Downstream of Retrogressive Thaw Slumps in the Western Canadian Arctic *Environmental Science & Technology* Online: http://pubs.acs.org/doi/10.1021/acs.est.8b05348
5-259. Tank S E, Vonk J E, Walvoord M A, McClelland J W, Laurion I and Abbott B W 2020 Landscape matters: Predicting the biogeochemical effects of permafrost thaw on aquatic networks with a state factor approach *Permafrost and Periglacial Processes* **31** 358–70
5-260. van der Sluijs J, Kokelj S V, Fraser R H, Tunnicliffe J and Lacelle D 2018 Permafrost Terrain Dynamics and Infrastructure Impacts Revealed by UAV Photogrammetry and Thermal Imaging *Remote Sensing* **10** 1734
5-261. Wainwright J, Parsons A J, Cooper J R, Gao P, Gillies J A, Mao L, Orford J D and Knight P G 2015 The concept of transport capacity in geomorphology *Reviews of Geophysics* **53** 1155–202
5-262. Zolkos S, Tank S E and Kokelj S V 2018 Mineral Weathering and the Permafrost Carbon-Climate Feedback *Geophysical Research Letters* **45** 9623–32

Appendix.1. Supporting information for Chapter 2

A1.1 Geochemical Analyses

A1.1.1 Suspended Particulate Matter (> 0.7 µm, >2.2 µm PO14C)

Filters for POC, POδ^{13}C, and PO^{14}C were oven dried at 60 °C for 24 hours, weighed, and fumigated under heat (60 °C) for 24 hours by placing 25 mL of 12M HCl into a desiccator in an oven to remove carbonates and dolomites (Whiteside et al. 2011). Following fumigation, samples were air dried in a second desiccator and were then re-oven dried at 60 °C for 24 hours (Whiteside et al. 2011). Dried filters were packed into tin capsules and analyzed for POC and POδ^{13}C on an elemental analyzer interfaced to a PDZ Europa 20-20 isotope ratio mass spectrometer (UC Davis Stable Isotope Facility). A duplicate set of un-acidified filters were similarly analyzed for PN and Pδ^{15}N. PO^{14}C was analyzed by Accelerator Mass Spectrometry following pellitization at the University of Ottawa (A.E. Lalonde AMS Laboratory). Particulate organic phosphorus (POP) was analyzed following the chemical wet oxidation method as outlined in Labry et al. (2013). We chose to not determine POP by subtracting particulate inorganic phosphorus (PIP) from total particulate phosphorus (TPP), as also outlined by Labry et al. (2013), since the PIP method is inefficient in digesting inorganic phosphates in clay structures (Suzumura 2008), which we believe leads to overestimates of POP in our mineral rich samples (see S8 below). While it is common to use elemental combustion analysis to measure particulate nitrogen as an analogue to particulate organic nitrogen (Lee et al. 2016, Huang et al. 2018), and there is no evidence of mineral nitrogen in XRD (Zolkos and Tank 2020) or XRF (Malone et al. 2013) scans of RTS sediments, it is possible that a significant portion of particulate nitrogen could be composed of inorganic nitrogen adsorption to clay structures (Schubert and Calvert 2001). Thus we offer both TDN and DON as dissolved comparisons to particulate nitrogen.

A1.1.2 Filtrate (< 0.7 µm)

Dissolved organic carbon (DOC) concentration was determined as non-purgeable organic carbon from 3 injections with a coefficient of variation <2%, or most similar 3 of 5 injections, on a Shimadzu TOC-V analyzer. DIN, determined as the sum of ammonia and nitrate/nitrite analyses, and TDN were analyzed colorimetrically via flow injection analysis on a Lachat QuikChem 8500 FIA automated ion analyzer in the Canadian Association for Laboratory Accreditation-certified Biogeochemical Analytical Service Laboratory (BASL; University of Alberta). Ammonia and TDN were determined following methods modified from APHA (2012) and nitrate/nitrite was analyzed following O'Dell (1996). SRP samples were analyzed via colorimetry using a molybdate-ascorbic acid method modified from Stainton et al. (1977; see Soluble Reactive Phosphorus section below). Analysis for SRP occurred using a Genesys 10 UV-VIS scanning spectrophotometer and a 50 mm cylindrical quartz cell. Since SRP samples were stored filtered and frozen, analysis occurred within 1 month of sample collection (Dore et al. 1996 and within-lab testing at BASL). DOC samples were stored in pre-combusted (500°C, 5h) 40 mL borosilicate glass vials, acidified to a pH of 2 (Vonk et al. 2015). Total dissolved nitrogen (TDN) samples were stored in acid-leached 60 mL HDPE bottles. TDN and DOC were stored in the dark at ~4 °C. Dissolved inorganic nitrogen (DIN) samples were filtered into acid-leached polypropylene centrifuge tubes (Corning®). Total dissolved phosphorus (TDP), and soluble reactive phosphorus (SRP) were stored in acid-leached HDPE bottles. DIN, TDP, and SRP were stored frozen and in the dark. All sample bottles were triple rinsed with sample water prior to being filled. Dissolved organic nitrogen (DON) and phosphorus (DOP) were calculated as the difference between TDN and DIN and TDP and SRP, respectively. Any analytes below detection limits determined by BASL were replaced by half of the detection limit value. Any DOP concentrations below 4.9 µg L^{-1} were replaced with half this value, since this is the limit of quantitation for TDP, as determined by BASL. This replaced negative values and DOC:DOP ratios that were asymptotic around 0 µg L^{-1} DOP, which were 36 out of 63 samples. One DON value (FM3-DN-2015-08-14) was negative beyond limits of detection or quantitation and was removed. All C:N and C:P ratios were calculated as atomic ratios.

A1.2 Base-extracted particulate organic matter

A1.2.1 Base extractions and optical analyses

Filters collected in 2016 were thawed and immediately placed in 10 mL of 0.1 M NaOH (standard solution obtained from ACROS organics, CAT# AC124190010) for extraction in the dark at 4°C for 24 hours in a 15 mL centrifuge tube (Corning®). After 24 hours, extractions were filtered through 0.2 μm polyether sulfone syringe filters (EMD Millipore Millex®, 33mm, CAT#SLGP033NB) into a new 15 mL centrifuge tube and neutralized to a pH ranging between 6.2 and 7.8 using trace metal grade HCl, with added volumes always below 0.2 mL (Osburn et al. 2012). Filtered extracts were analysed for absorbance from 240 – 800 nm at 1 nm increments in a 10 mm cuvette using an integration time of 0.1 seconds (Horiba Aqualog). The same sample was then analyzed for fluorescence at excitation wavelengths of 230 – 800 nm at 5nm increments, and emission wavelengths 153.16 – 930.03 at 2.52 nm increments, with an integration time of 2 seconds and Medium CCD Gain. Samples for absorbance and fluorescence were diluted when optical density was greater than 0.4 at 240 nm (Osburn et al. 2012), and/or the sum of absorbance at a pair of wavelengths was greater than 1.5 (Kothawala et al. 2013), or if counts on the machine exceeded 50,000 outside of the Rayleigh scatter lines (nearing the maximum number of counts the machine can record). Due to error during lab analysis (e.g. samples were not diluted below 1.5 total absorbance threshold), the following samples were lost or removed from the dataset: (a) FM2-UP, and (b) SE-UP and SE-IN collected on August 9, 2016. We retained the downstream sample collected on August 9, 2016. Since site SE happened to be visited twice in 2016, we used data available for 2016-06-17.

A1.2.2 Absorbance spectra corrections

Prior to calculations, absorption spectra were dilution corrected and then baseline corrected using the mean absorbance between 700 and 800 nm respective to each spectrum (Helms et al. 2008). Minor structures were apparent in the absorption spectra in the form of broad peaks near 280 nm, and an approximation of the first order derivative of each absorption spectra indicated that the peak generally occurs ca. 280-285 nm (Brym et al. 2014). Following Brym et al. (2014), we excised values between 280-301 nm in this region and replaced it with non-linear interpolation to smooth out the absorbance spectra and re-calculated spectral slopes. Spectral slopes and slope ratios were linearly correlated with the calculations from non-interpolated values (R^2 >0.9). Slope ratios were ~14% lower when absorption spectra were smoothed due to an ~15% decrease in S_{275-}

$_{295}$ that were also offset by ~0.002 nm^{-1}. However, neither calculation method resulted in changes in inference when comparing slope ratios upstream, within, and downstream of slumps, and thus the uncorrected slope ratios are reported.

A1.2.3 Excitation-emission matrices corrections

Prior to these calculations, raw excitation-emission matrices were corrected using the following standard procedures outlined by Murphy et al. (2013): (a) neutralized 0.1 M NaOH blanks were subtracted from respective samples (i.e. *blank corrected*); (b) inner filter effects were corrected using matching absorbance measurements also collected at 5nm increments; (c) fluorescence data were normalized to Raman Units by dividing by the Raman area of pure water integrated over λ_{em} range 384 to 423 nm at λ_{ex} 350 nm (RU_{350}). Additionally, RU_{350}-normalized fluorescence units were divided by the volume of stream water filtered and multiplied by the volume of extractant used to account for large variability in the volume of sample filtered at each site (Brym et al. 2014). Finally, first and second order Rayleigh and Raman scatter were excised, and all excised scatter was interpolated over except for first order Rayleigh scatter.

A1.2.4 Statistical modelling of fluorescence data (PARAFAC)

To identify 'components' within excitation-emission matrices, parallel factor analysis (PARAFAC) modelling was completed using the drEEM toolbox (Murphy et al. 2013) in MATLAB (Mathworks, Inc., Natick, MA). To increase the sample size for a more robust model, samples collected upstream, within, and downstream of thaw slump sites in 2016 (n=17) were combined with samples collected in 2017 from streams with and without active slumps in the watershed across the Stony Creek and Vittrekwa (n = 39; thus n_{total} = 56). Prior to fitting a model, data were assessed for outlier samples and wavelengths, both by assessing leverages of samples and wavelengths after fitting preliminary models, and by testing whether changes in the model occurred after removal of samples. While no samples were removed as outliers, emission and excitation wavelengths with more noise than signal were removed. For this dataset, this involved removing emission wavelengths <280 and >600 and excitation wavelengths <240 and > 500. Excitation-emission matrices were also normalized by dividing by the sum of the squared value of all fluorescence intensities in the matrix (*normeem*, Murphy et al. 2013).

A 5-component model was chosen as the best fit to the data based on: (a) a large decrease in the sum of squared residuals relative to fewer-component models; and (b) less residual structure per sample relative to fewer-component models. The 5-component model only passed 2 of three split half validation tests (S4C6T3 configuration, Murphy et al. 2013), and attempts to remove outliers in the splits did not enable a pass of all 3 tests. However, split-half validations can be difficult to pass for small sample sizes (n=56 in this study) and heterogeneous datasets (Stedmon and Bro 2008, Murphy et al. 2013). The presence of a residual structure in the residuals of multiple samples against a 4-component model indicated an additional component needed to be added to the model. When components were increased above 5, several issues were apparent in the models: (1) core-consistencies dropped to near 0 and modelled components changed substantially when 1-2 samples were removed, showing instability in the higher component models; (2) components began exhibiting more atypical spectral features (Murphy et al. 2013); and (3) peaks emerged in modelled samples along Rayleigh scatter lines that were not present in the original sample, suggesting modelling of noise. All extracted components compared well with previously identified components in the OpenFluor database (Table A**1-1**).

A1.2.5 Calculation of additional indices

Several commonly used fluorescence indices were additionally calculated to aid in the interpretation of fluorescent components (Table A**1-2**). Initially, this list of indices included the freshness index, which is positively associated with recent biological activity (Parlanti et al. 2000, Wilson and Xenopolous 2009) and the fluorescence index, which is positively associated with increasing contributions of microbial original fluorescent moieties when differentiating between microbial and higher plant origin (McKnight et al. 2001, Cory and McKnight 2005). However, we decided to remove these two indices for the following reason. The indices were developed on the ratio of two peaks found in samples of dissolved organic matter from diverse environments. Further examination of the points used to calculate the indices on our BEPOM samples suggests that the calculation is only the ratio of a shoulder and its peak across the excitation wavelength used for the calculation (Figure S3). %C1 was highly correlated with both indices ($r>0.9$), so it is likely that they are simply tracking the relative intensity of this component.

A1.3 Principal components analysis

A1.3.1 Corrections and imputations to geochemical data

For five headwall samples, % carbon of acidified sediment samples was greater than for non-acidified samples suggesting an error during the acidification process. Therefore %POC and POδ^{13}C values for these samples were removed, and imputed in R using aregImput() from R package Hmisc (Harrell 2020). This function uses bootstrapping to resample for multiple imputations. Then additive regression is used comparing replacement vs. non-missing values. Finally, missing values were imputed with predictive mean matching. Missing values (%POC, POδ^{13}C, POC:POP, and POC:PN) were predicted using the combined stream POM and headwall sample dataset and including variables P^{15}N, %PN, and %POP. R^2 for predicting non-missing values for each variable using last imputations of predictors were 0.921 (POC:POP), 0.878 (POC:PN), 0.604 (POδ^{13}C), and 0.991 (%POC). Only 2/9 lower active-layer, 1/6 Pleistocene, 1/3 upper active layer, and 1/6 Holocene samples were imputed. Imputation was conducted since PCA cannot handle missing values and is often preferred to complete removal of subjects with missing values (e.g. complete case analysis) as the latter can cause biased results and difficulty in interpreting the population of subjects (van der Heijden et al. 2006).

A1.3.2 BEPOM PCA

A principal components analysis was used to examine relationships between commonly used absorbance- and fluorescence-based indices (Table A**1-2**) and components and find major gradients of variation in the sample set. PCA is based on a pearson correlation coefficient matrix and pearson correlations can be affected by outliers and skewed distribution (Zar 2010). Therefore, we transformed any highly skewed or non-normal variables. This resulted only in the transformation of %C4 to $(\%C4)^2$. The first two axes explained 84% of the variation in the dataset and were the only components explaining a greater proportion of variance than a random division of total variance amongst components, as shown by greater inertia than their counterpart of a broken stick model (**Figure A1-4**, Jackson et al. 1993). The two downstream samples collected on different days for site SE (see section S2.1) were averaged prior to the PCA analysis.

A1.4 Quantification of organic carbon delivery

A1.4.1 Discharge measurements

Instantaneous discharge was determined at each sampling point on each collection day using pygmy or Redback "AA" current meters and the velocity-area method (Gordon et al. 2005, pg. 93 – 96). Stream channel sections were modified if necessary, to remove objects creating turbulence (rocks, twigs) and divided into equal subsections. A single velocity measurement was obtained for each subsection by recording the number of revolutions of a current meter at 0.6x the depth. Where the AA meter profile was too large for the stream section, a pygmy meter was used. Where both AA meter and pygmy meter widths or heights were too large (i.e. very narrow or shallow streams) the float-area method was used to determine velocity in each subsection, where a small buoyant object (short twigs) was placed on the water surface at the center of the subsection and the time it took to travel a known distance was recorded.

A1.4.2 Instantaneous yield calculations

Instantaneous fluxes of suspended and dissolved parameters were calculated by:

$F = Q * [a]$ **(Eq. 1)**

where Q is discharge (L s^{-1}), $[a]$ is the concentration of any parameter of interest in the appropriate concentration units, and F is the flux of the parameter of interest in the appropriate mass units per second.

Instantaneous yields were then calculated by:

$Y_i = F/A$ **(Eq. 2)**

where F is the flux calculated in Eq. 1, and A is the area (km^2) of the watershed draining to the point sampled.

A1.4.3 Determination of watershed areas

Watershed delineations were based on gridded (30 m) Canadian Digital Elevation Model (CDEM) products from Natural Resources Canada (NRCan; *https://open.canada.ca*), stream networks vectorized in the National Hydro Network, and visible in multispectral imagery from Copernicus Sentinel data (2017; European Space Agency, https://sentinel.esa.int/; St. Pierre, Zolkos, and Shakil et al. 2018). Stream networks were delineated from the CDEM. Prior to delineation, CDEM

data were reconditioned using stream vectors from the NRCan National Hydro Network (NHN). Prior to reconditioning, these stream vectors were modified solely for the sampled sites to match current stream networks. This was done by overlaying NHN networks on multispectral imagery from Copernicus Sentinel data (2017) (European Space Agency, http://sentinel.esa.int/). Stream networks in the 2017 Sentinel-2 imagery were found to match 2015 and 2016 stream networks and was used to ensure consistency in the stream network delineation used for related projects spanning 2015 – 2017 on the Peel Plateau.

A1.5 Linear mixed modelling

We examined the effect of retrogressive thaw slumps (RTS sites) on total organic carbon yield and stream geochemistry using linear mixed effects models fitted using the R package *lme4* (Bates et al. 2015) and tested the significance of parameters using Satterthwaite's method with the *lmerTest* package (Kuznetsova et al. 2017). Linear mixed effects models account for dependencies due to repeated measures and nested designs and are suitable for unbalanced designs (different sample sizes, *n*) (Zuur et al. 2009).

For each parameter, we attempted to fit the model with the maximal random structure that matched the study design (Barr et al. 2013). For this study, the aim of this structure was:

$$y \sim StreamLoc + (1 + StreamLoc|SlumpSite) + (1|JDay) \qquad \textbf{(Eq. 3)}$$

where *y* is a dependent variable (Table 2), *StreamLoc* is the fixed effect of stream location relative to the slump site (upstream, within, downstream), *(1 + StreamLoc | SlumpSite)* is a random slope and intercept term per slump site, and *(1| JDay)* is a random intercept term for Julian Day. In some cases, datasets were unable to be fit with this maximal model due to singular fit and convergence failure issues, thus models were simplified as needed while still maintaining slump site grouping of the dataset (i.e. random intercept per slump site).

Model fits were inspected visually using histogram and residual plots. In some cases, dependent variables were transformed to meet assumptions of independent and homoscedastic residuals, as noted in Table 2.

For follow-up linear models assessing the effect of landscape, morphological, and meteorological variables on slump effect, to minimize multicollinearity issues, we removed any explanatory variables with $r \geq 0.9$ prior to fitting any models (i.e. Area, $r_{\text{Area: Debris Tongue}} = 0.9$). We dropped individual explanatory variables from the model one by one, beginning with least significant terms

(greatest p values) and using *anova* and a p=0.05 threshold, refitting the model each time. We confirmed a lack of patterns and normality of residuals, and variance inflation factors of remaining explanatory variables were <3. All explanatory variables were scaled and centered using *scale* in R and standardized beta coefficients are reported for these results (i.e. slopes of standardized predictors, β_{std}).

A1.6 Organic matter source sample collection and analysis

A1.6.1 Bulk periphyton

Submerged rocks on the streambed were collected in whirl-pak bags along with stream water until they could be processed (within 24 hours) at our field camp. Rocks were scrubbed with a clean toothbrush over a 25mm filter tower assembly containing a pre-combusted (450°C, 5h) GF/F filter. The brush and filter were rinsed 3 times with deionized water, and the filter was stored frozen until analysis for POδ^{13}C as described in supplementary S1.

A1.6.2 Headwall samples

Samples from headwalls were obtained from the active layer (AL), "Holocene-age permafrost" (HOL); and Pleistocene-age permafrost (PLE) sediments at FM2, FM3, SE, SD, SH, and SF. At least 5-10 cm of exposed, outer material was chiseled off and discarded prior to chiseling out sample material into a Whirl-Pak bag. If distinct layers were present in the active layer (e.g. organic and mineral horizons) separate samples were collected from each band. At the sampling points within this study, no distinct layers were immediately noted within the (HOL) and (PLE) units. Upon return to camp, headwall samples were thawed at ~4°C for less than 24 hours, at which time any clear supernatant generated from thaw of ice was discarded, which we assume had negligible particulate organic matter. The settled sediments were then stored frozen until return to the University of Alberta where they were freeze dried and stored at room temperature until analysis. Freeze dried samples were processed for C, N, and P content, POδ^{13}C, and Pδ^{15}N. Samples from site FM2 and FM3 were additionally processed for PO^{14}C.

A portion of each freeze-dried headwall sample was subsampled using a pre-combusted stainless-steel scoopula into a new 15 mL centrifuge tube (Corning®) for radiocarbon analysis. The remainder of material was dis-aggregated and passed through a 2mm sieve to remove large debris.

Material <2mm was finely ground to powder using a stainless-steel coffee grinder, which was cleaned between samples using 5% v/v HCl and deionized Milli-Q water. Analyses of POP, POC, POδ^{13}C, PN, and Pδ15N were conducted as described for suspended particulates using powdered material. However, for acidification of sediments prior to POC and POδ^{13}C analysis, powdered material was weighed into 10 x 10 mm Ag capsule and contained within pre-combusted glass vials during fumigation.

Material subsampled for radiocarbon analysis was spread on pre-combusted glass petri-dishes and examined under a dissecting microscope to remove any large debris or material (e.g. twigs, large rocks) that contrasted with the bulk background sediments. Subsamples of sediments were then pre-treated to remove carbonates using heated acid washes (HCl, 1M, 80ºC, 30 min; "A" treatment from Crann et al. 2017). Acid washes were repeated until effervescence stopped occurring in the samples; across all samples, two rounds of acid washes were sufficient.

A1.7 Calculation of source contributions

A1.7.1A1.7.1 End Member values

For headwall end member samples, while all sites sampled were analyzed for POδ^{13}C, POΔ14C are obtained from a subset of two slump sites (*FM2, FM3*). To increase the robustness of our end-member values, we added in POδ^{13}C and POΔ14C values reported by Lacelle et al. (2019) from unit 2 (Holocene) and unit 3 (Pleistocene) from sites Wilson and CB (Table 1 in Lacelle et al. 2019). We did not add unit 1 (active layer) since we were not sure how this would equate to our upper and lower active layer groupings. To obtain Δ14C values from Lacelle et al. (2019), F^{14}C values were back-calculated from reported values of ^{14}C yr B.P. following:

$$^{14}\text{C yr. B.P.} = -8033\ln(F^{14}C) \qquad \textbf{(Eq. 4)}$$

Δ^{14}C were then calculated from F^{14}C following:

$$\Delta 14\text{C} = \left(\left(F^{14}C * e^{\left(\frac{1950-y}{8267}\right)}\right) - 1\right) * 1000 \qquad \textbf{(Eq. 5)}$$

Where y is sample collection year. For Lacelle et al. (2019), we assumed samples were collected and analyzed in 2017. However, even a 10 year error on the year of sample collection results in less than 0.01% error in the Δ^{14}C values.

Since POΔ14C values were not measured for periphyton samples, we spanned our end-member values for this to range from a DIC measurement obtained from FM2 in August, 2015 (Δ14C=-332.271 ± 2.4 σ) to modern day atmospheric $\Delta^{14}C$ values (2010 Δ14C=42; Hua et al. 2013). Since a mean and standard deviation is required for IsoError, to reflect the uncertainty of the probability of where the true end member occurs between these two values, we used a large standard deviation equivalent to the mean of the two values (145.135). Mean and standard deviations of values used for the mixing model are shown in Table A**1-3**.

A1.7.2 Mixing Model

A dual-carbon isotope ($PO\delta^{13}C$ and POΔ14C) was used to distinguish between proposed sources using MixSIAR (Stock et al. 2018). To account for potential fractionation of $\delta^{13}C$, the MixSIAR package was run including discrimination factors set to ±1‰. The model was run with stream location as a fixed effect, slump site as a random effect, with process error (Stock et al. 2018), and with mean and standard deviation of sources using samples obtained from this study and Lacelle et al. (2019). Model convergence was confirmed using Gelman-Rubin and Geweke diagnostic tests (Stock et al. 2016). Due to large variations in carbon-rich vs. poor sources, models were run with a concentration dependence using the average % organic carbon of each source, including matching % organic carbon for samples obtained from Lacelle et al. (2019).

A1.8 Repeated measures ANOVA for assessment of differences in BEPOM between stream locations

We used a repeated measures ANOVA, with stream location as a within subjects (slump site) factor to assess whether the differences between stream locations along %C1, a variable that represented the gradient of separation in our PCA analysis, was significant. Prior to the analysis, we imputed a missing value for the SB upstream sample, which was lost due to human error during analysis, using the average upstream values of the two sites closest to this sampling location (SA and SC). Based on our field observations of watershed vegetation and channel characteristics (e.g. flow, streambed, size) these sites also most closely resembled the SB upstream site relative to other sites. Imputation was conducted since repeated measures ANOVA cannot handle missing values. Imputation is often preferred to complete removal of subjects with missing values (e.g. complete

case analysis) as the latter can cause biased results and difficulty in interpreting the population of subjects (van der Heijden et al. 2006).

A1.9 Landscape and environmental explanatory variables

A series of morpholoical, meteorological, and landscape variables were used to examine the relative importance of these factors on slump effects (see section 2.8). Meteorological data were obtained from a GNWT-operated weather station located near FM3. The 96 hour antecedant rainfall period was chosen due to previous observations of strong correlations with sediment transport (Kokelj et al. 2015). Longitude was used to approximate landscape factors correlated to east-west gradients in surficial geology and vegetation across the study area (section 2.1), and stream power (only used in the upstream vs. downstream models) accounted for sediment transport mechanics in stream networks (supplementary S9). Longitude was strongly correlated to elevation and distance from maximum glacial limit (table 1) but was chosen as an all-encompassing landscape variable due to sample size limitations. Scar zone area and average air temperature over the past 96 hours were strongly correlated to debris tongue length and total rainfall respectively ($|r|>0.8$), thus were not used.

Downstream unit stream power was calculated following:

$$\boldsymbol{\Omega = \rho g Q S} \qquad \text{(Eq. 6)}$$

Where Ω is unit stream power (W m^{-2}), $\boldsymbol{\rho}$ is the density of water (1000 kg m^{-3}), g is acceleration due to gravity (9.8 m s^{-2}), Q is discharge (m^3 s^{-1}) and S is the channel slope. Since we did not have channel slopes paired with each measurement date, average channel slopes for the entire season were used. Average channel slopes were obtained for sites from Table S3 in Zolkos et al. (2019).

Maximum elevations near slump headwalls were calculated as the maximum elevation with ~50m of the slump headwall. High resolution digital elevation models (2m pixel size) containing the slump site of interest were exported out of the Arctic DEM explorer (https://livingatlas2.arcgis.com/arcticdemexplorer/). Polygons, within ~50m of the headwall, were traced around slump headwalls (e.g. figure S5 and the maximum elevations were extracted from within the polygon in ArcGIS using Zonal Statistics. Elevation was strongly correlated ($r>0.9$) to longitude of sites, which also coincided with west-to-east recession of the Laurentide Ice Sheet and ice-margin environments (figure 1). Thus, longitude was used as an all-encompassing variable

for east-west gradients on the Peel Plateau. Maximum slopes across the scar zone to valley bottom (e.g. figure S5) were obtained by delineating the area of interest over Arctic DEM exports in ArcGIS. DEMs were then converted to slope rasters, and maximum slopes within delineated polygons were extracted using Zonal Statistics.

A1.10 Approximation of seasonal POC flux downstream of slump SD

For continuous monitoring of turbidity downstream of two slump site end members (SE and SD) we installed 2 YSI Data Sondes (600 OMS, 6920VS). Matching dip samples were collected to measure TSS downstream of SE and SD four and five times respectively (figure S6). We did not use sensor data downstream of SE to estimate POC flux since it did not consistently record turbidity (Figure S6). This was likely due to sediment loads being well above the turbidity sensor maximum limit (spot samples indicated sediment concentrations were often well above 8000 mg L^{-1}). However, due to the high energy braided stream downstream of SE, we sometimes found the sensor out of water.

For SD turbidity data, we excised data 4 hours before and after removal and deployment times respectively to avoid deployment and removal effects. We then interpolated higher resolution turbidity data from measured 40-minute intervals to 2-minute intervals using *na_interpolation* (TSimpute package, R; Moritz 2017) (figure S6), also extrapolating out to the excised deployment and removal times to match TSS measurements. We repeated the interpolation step two more times after removing areas of data we believed to be erroneous (turbidity < 5.4, turbidity measurements when conductivity was 0, figure S6). Final interpolated turbidity data was regressed against 5 instantaneous flux measurements (figure S7c). Since the system is not sediment limited, total suspended sediment (TSS) concentration increased with TSS flux (figure S7a), thus turbidity generally related to TSS concentration and flux in a similar manner (figure S7c-d). To avoid negative sediment flux measurements, we set the intercept in the linear relationship between turbidity and TSS flux to 0 and used only the slope of the relationship to convert turbidity measurements to instantaneous TSS flux measurements. We then summed calculated TSS flux data for the deployment period (June 23rd, 2015 – August 16th, 2015). While there was a single outlier driving the relationship, we did not remove this data point as it provided a data point during high transport, and we acknowledge that the estimate of flux we present will substantially improve with more robust datasets (i.e. more samples with greater coverage across transport conditions).

We chose not to extrapolate for the entire thaw season of the Peel Plateau (April 30th – Sept. 30th inclusive, O'Neill et al. 2015) due to the flashy nature of turbidity measurements (figure S6), and acknowledge that this could be half the annual flux downstream of SD. Furthermore, we note that a comparison between scaling up the average of spot measurements of POC flux (red diamonds, figure S6), to the period of sensor deployment results in half the flux estimated using sensor data (used here), likely due to spot samples falling at baseflow periods.

A1.11 Analytical methods for phosphorus

A1.11.1 Analysis of soluble reactive phosphorus

Soluble reactive phosphorus (SRP) was determined via colorimetry following Stainton et al. (1977). Briefly, 2.5 mL of a mixed molybdate reagent for orthophosphate determination (4 parts pre-mix reagent, 1-part ascorbic acid solution) was added to 25 mL of sample. Samples then sat for 20 minutes and the absorbance was read at 885 nm within 1 hour using a 5 mm quartz cuvette. Colour corrections for each sample were also determined by adding 2.5 mL of mixed molybdate reagent for natural colour determination (4 parts pre-mix reagent, 1-part distilled water) to 25 mL of sample. The absorbance of the colour correction was only subtracted from the absorbance for orthophosphate determination if it constituted more than 10% of the orthophosphate absorbance. The pre-mix reagent consisted of 140 mL concentrated H_2SO_4 diluted in 140 mL deionized water, which, after cooling, was mixed with 15 g ammonium molybdate and 0.34 g antimony potassium tartrate dissolved in 1.2 L deionized water. The ascorbic acid solution consisted of 5.17 g of ascorbic acid dissolved in 100 mL deionized water.

A1.11.2 Analysis of particulate organic phosphorus

Particulate organic phosphorus (POP) was determined using the chemical wet oxidation as outlined by Labry et al. (2013), which is modified from Raimbault et al. (1999). The method uses a persulfate oxidizing reagent buffered to maintain alkaline conditions. For every 250 mL of reagent, 30 g of disodium tetraborate and 15 g of potassium persulfate ($K_2S_2O_8$) are dissolved in deionized water following steps detailed by Labry et al. (2013) and Raimbault et al. (1999). The buffered reagent is intended to minimize the acid hydrolysis of particulate inorganic phosphorus sources that can lead to overestimates of POP (Labry et al. 2013).

Samples were placed into pre-leached (HCl, 24h) and pre-combusted (500°C, 2h) borosilicate test tubes, followed by 40 mL of deionized water and 5 mL of oxidizing reagent. Tubes are capped with un-lined polypropylene caps (VWR, Cat #16153-483) and autoclaved for 30 minutes at 120°C. Prior to autoclaving, caps were tightened and then loosened one turn to enable ventilation which prevents tubes from exploding. Since ventilation results in loss of water volume, volumes in test tubes were marked prior to autoclaving. Tubes were then allowed to cool down to room temperature and those that had volumes below the marked line were topped up with deionized water. 10 mL of digested sample water was then decanted into 15 mL centrifuge tubes (Corning) and analyzed for SRP concentrations within 24 hours of digestion using a 10 mm quartz cuvette and methods for SRP analysis (section S11.1).

To remove interference of particulate material, after the addition of reagents for SRP analysis, samples were centrifuged at 3322 rcf (4000 rpm, Thermo Scientific SH-300 rotator r_{max} = 185.4, Thermo Scientific Sorvall Legend T+) for 5 minutes. Standard curves of 0, 25, 50, 100, 250, 400, 500, and 750 ug L^{-1} were run using non-digested standards prior to each analysis. Since we found non-linear relationships between absorbance and known phosphate concentrations above 750 ug L^{-1}, due to consumption of reagent chemicals, samples with an absorbance above the 750 ug L^{-1} standard were diluted to be within the standard range. A standard curve replicating the concentrations was also run through the digestion protocol. Standard curves run through the digested protocol were offset in a similar manner where lower concentrations had higher absorbance values, altering the slope and intercept of the standard curve (Figure A**1-8**a, Table A**1-6**). To account for this digestion effect on samples, the digested standard curve was used to calculate sample phosphate concentrations.

A1.11.3 Comparison of methods for the determination of POP

Labry et al. (2013) recommended determining POP concentrations by first determining total particulate phosphorus (TPP) concentrations and particulate inorganic phosphorus (PIP) concentrations, then determining POP by subtracting PIP from TPP (henceforth referred to as TPP-PIP method). This recommendation was largely due to concerns about overestimation of POP using the chemical wet oxidation method due to its ability to hydrolyze inorganic particulate phosphorus sources even under alkaline buffered conditions. However, the PIP method outlined by Labry et al. (2013) may be inefficient at hydrolysing phosphate bound to clay minerals that can

be released during the TPP procedure (Suzumura 2008). This can have little effect when particulate samples are pre-dominantly of biotic origin (e.g. algal species, bacterioplankton) as is the case for samples examined by Labry et al. (2013), but in mineral rich systems, the inefficiency of the PIP method may likely result in an even greater overestimate of POP. This would be of concern in this study since thaw slumps can erode large volumes of sediments from glacial till deposits.

To assess the most appropriate method for our system, we tested the three methods outlined by Labry et al. (2013) on a sample collected from a stream impacted by thaw slump site *SE*. If the TPP – PIP method underestimated phosphate bound to clay minerals to a greater degree than the CWO method hydrolyzed inorganic phosphorus sources, then POP would represent a greater proportion of the total phosphorus with the TPP-PIP method. Phosphorus concentrations produced by the CWO, PIP, and TPP method were 5.15 ± 0.218 mg/L *(mean, standard error of the mean, n=4)*, 9.00 ± 0.175 mg/L *(mean, standard error of the mean, n=4)*, and 81.8 ± 0.861 mg/L *(mean, standard error of the mean, n=4)* respectively. The CWO method suggested that 6 ± 0.3 % *(mean, standard error of the mean, n=4)* of the phosphorus in the sediments were from organic material, while the TPP-PIP method suggested that 89 ± 0.2 % *(mean, standard error of the mean, n=4)* was organic (figure S8b). We believe this large discrepancy is due to large amounts of phosphorus being bound to clays that can be released in the TPP digestion but not in the PIP digestion, thus resulting in a large overestimate of POP. We therefore chose to use the CWO method for determining POP concentrations.

A1.12 Tables

Table A1-1. Description of components in 5-Component PARAFAC model.

Comp.	Excitation wavlength* (nm)	Emission Wavelength* (nm)	Resemblance to previously identified peak labels (*general descriptions used*)	OpenFluor Matches TCC >0.95	OpenFluor Matches 0.95 < TCC >0.9	Assignment Corresponding to Previous studies
1	290	413	A[a] with a long excitation tail *(UVC humic-like*)	31	32	terrestrial humic-like (e.g. Painter et al. 2018); microbially- or photo-chemically altered organic matter (Yamashita et al. 2013)
2	255	523	E[b] (soil fulvic-like)	14	8	terrestrial humic/fulvic-like (e.g. Walker et al. 2013)
3	310	439	Combined A[a] and C[a] (*UVA humic-like*)	13	10	terrestrial, humic/fulvic-like (e.g. Søndergaard et al. 2003)
4	375	476	Combined A[a] and C[a]	1	4	likely terrestrial humic-like (e.g. Walker et al. 2013)
5	275	299	B[a] (tyrosine-like, protein-like)	0	5	tyrosine-like, protein-like (e.g. Stedmon and Markager 2005)

TCC is the tucker congruence correlation coefficent of Excitation and Emission spectra (TCC_{ExEm})
*maximum wavelength is shown
[a]Coble et al. (2007); [b]Stedmon et al. (2003).

Table A1-2. Candidate variables for linear discriminant analysis of difference in BEPOM optical properties upstream, within, and downstream of slumps.

	Index or Component	Calculation	Reference	Description / Purpose	Assumptions to interpretation
Abs. Based	S_R	$S_{275-295}$ / $S_{350-400}$	Helms et al. (2008)	Shown to be negatively correlated to DOM molecular weight and to generally decrease on irradiation	Molecules with higher molecular weight were formed during decay processes or were resistant to decay processes (2) Majority of compounds are not breaking down to lower molecular weight during the extraction process
	$a_{tot/TSS}$ (m^{-1}/mg/L)	Total absorbance[a] between wavelengths 250 - 450, divided by suspended sediment concentration.	Modified from Helms et al. (2008)	Helms et al. (2008) use the total absorbance in this wavelength range to calculate mass balances of chromophoric dissolved organic matter. Here we use it to show extractable chromophoric organic mater per unit of sediment collected on a filter. Greater values indicate greater extractable chromophoric material per unit of particulate material in the water column which may, like %POC, indicate earlier stages in diagenesis of sediments.	(1) Particles with greater absorbance of extracts (either due to amount or structure of compounds) are not associated with particles with lower % organic carbon. (2) Absorbance of chromophoric organic matter can be related to concentration of chromophoric organic matter across particulate types.

Fluor. Based	Humification Index[b]	$\sum I_{em\ 435-480}$ / ($\sum I_{em\ 300-345}$ + $\sum I_{em\ 435-480}$) at ex. 254	Ohno et al. (2002)	Ranges from 0 to 1, with increasing values associated with a "red-shift" or shift to longer wavelengths, potentially due to lower molecular ratios of hydrogen to carbon. May indicate relative abundance of compounds generated through polycondensation reactions. This could indicate material further in the progression in organic matter decay and greater relative abundance of compounds more resistant to breakdown (refractory).	Low hydrogen to carbon ratios were generated from polycondensation reactions. Polycondensation reactions occur as 'fresh' organic material is exposed to biochemical reactions. The end product is a less biochemically reactive pool.
	Peak ratio (A:B)	Ratio of peak A (ex260/max. em. 400:460) to Peak B (ex275/em305) intensity	Coble et al. 2007; Hansen et al. 2016 (note, Hansen refers to Coble Peak B as Peak T)	The ratio of degraded organic material (associated with peak A) to fresh-like material (associated with peak T)	(1) Compounds associated with fresh/degraded material are dominantly confined to their respective peaks (A vs T). (2) Compounds for each peak are extracted proportional to their presence in the particulate phase and aren't transformed to fluoresce outside their peak region.
	Peak ratio (C:B)	Ratio of Peak C (max. ex. 320:360 / max. em. 420:460) to Peak B (ex275/em305) intensity	Coble et al. 2007; Hansen et al. 2016 (note, Hansen refers to Coble Peak B as Peak T)	The ratio of degraded organic material (associated with peak A) to fresh-like material (associated with peak T)	(1) Compounds associated with fresh/degraded material are dominantly confined to their respective peaks (C vs T). (2) Compounds for each peak are extracted proportional to their presence in the particulate phase and aren't transformed to fluoresce outside their peak region.
	Peak ratio (T:C)	Ratio of Peak T (ex275/em340) to	Coble et al. 2007; Gabor	Hudson et al. (2008) showed a strong correlation between peak T	Assumes peak T intensity is associated with compounds that

	Peak C (max. ex. 320:360 / max. em. 420:460) intensity	et al. 2014 (sec. 9.2.5 and references therein)	fluorescence and biological oxygen demand (BOD) in river waters and final treated sewage effluents, whereas peak C intensity tends to correlate with dissolved organic matter concentration. Thus, the ratio of the two may indicate BOD/DOC ratios in terrestrial waters.	increase in relative abundance due to biological activity that will consume oxygen. Further assumes correlations between peaks and BOD and dissolved organic matter concentrations are maintained within this study.

[a]Further detailed accounts of marked indices can be found in Gabor et al. (2014).
[b]Note, absorbance units for base-extracted material were normalized for volume filtered.

Table A1-3. Mean and standard deviation set for end member values for mixing model. Number of samples for mixing model purposes was set to n=1000. %OC is percent organic carbon.

Source	$\delta^{13}C$ (*mean*)	$\delta^{13}C$ (*sd*)	$\Delta^{14}C$ (*mean*)	$\Delta^{14}C$ (*sd*)	%OC
Pleistocene Permafrost	-26.77	0.15	-995.08	1.99	1.37
Holocene Permafrost	-26.64	0.11	-888.70	210.85	1.16
Upper Active Layer	-26.73	0.07	10.42	44.66	19.34
Lower Active Layer	-26.50	0.35	-545.65	203.48	2.34
Periphyton	-33.39	4.19	-145.14	145.14	13.75

Table A1-4. Radiocarbon results of bulk sediments from thaw slump headwall layers.

Lab ID	Layer	Approx. depth (m)	14C yr B.P.	±	Range yr cal B.P.
FM2					
UOC-7474	Upper Active Layer	0.05	107	37	271 - 186 (31.2 %)
UOC-7474	(O-Horizon)				150 - 11 (64.2 %)
UOC-7475	Lower Active Layer	0.40	9331	43	10677 - 10412 (95.4 %)
UOC-7476	Holocene	0.65 - 0.70	5710	37	6628 - 6585 (8.6 %)
UOC-7476					6569 - 6409 (86.8 %)
UOC-7477	Pleistocene	5.80	44798	556	49680 - 46708 (95.4 %)
FM3					
UOC-7471	Lower Active Layer	0.39 - 0.53	4062	37	4802 - 4761 (10.4%)
UOC-7471					4693 - 4675 (2.1%)
UOC-7471					4645 - 4429 (82.9%)
UOC-7472	Holocene	1.60 - 1.70	40344	351	44646 - 43216 (95.4%)
UOC-7473	Pleistocene	4.50	47803	763	49162 - 46661 (95.4%)

Table A1-5. Mean (and standard deviations) of source contributions to stream POM, as determined by MixSIAR. FM2, FM3, and SD are sorted by decreasing headwall height. All refers to overall mixing model results upstream, within, and downstream of the three sites.

		Upstream					Within					Downstream				
	Site	In situ peri.	Active Layer upper	Active Layer lower	Permafrost hol.	Permafrost ple.	In situ peri.	Active Layer upper	Active Layer lower	Permafrost hol.	Permafrost ple.	In situ peri.	Active Layer upper	Active Layer lower	Permafrost hol.	Permafrost ple.
	all	10%	41%	21%	16%	12%	8%	22%	17%	22%	30%	10%	19%	20%	24%	28%
	sd	15%	24%	21%	16%	12%	13%	17%	17%	20%	21%	11%	13%	15%	17%	17%
Decreasing headwall height -------->	FM2	4%	26%	21%	26%	24%	1%	7%	11%	32%	50%	2%	6%	13%	32%	47%
	sd	8%	19%	28%	29%	17%	2%	5%	18%	34%	35%	3%	5%	19%	33%	33%
	FM3	3%	12%	23%	32%	30%	2%	4%	13%	31%	50%	2%	3%	15%	33%	46%
	sd	4%	10%	24%	30%	23%	2%	4%	16%	32%	29%	3%	4%	16%	31%	27%
	SD	4%	64%	21%	8%	4%	3%	44%	26%	15%	12%	4%	35%	29%	19%	14%
	sd	7%	24%	27%	8%	5%	6%	21%	31%	17%	11%	5%	15%	30%	19%	15%

Table A1-6. Standard Curve equations and regression coefficients for digested and non-digested standards.

	Not Digested		Digested	
	Run 1	Run 2	Run 1	Run 2
R^2	0.9997	0.9999	0.9966	0.9605
Regression Coefficient	0.00062	0.00062	0.00053	0.00048
Regression Intercept	-0.0011	-0.0014	0.07409	0.09242

A1.13 Figures

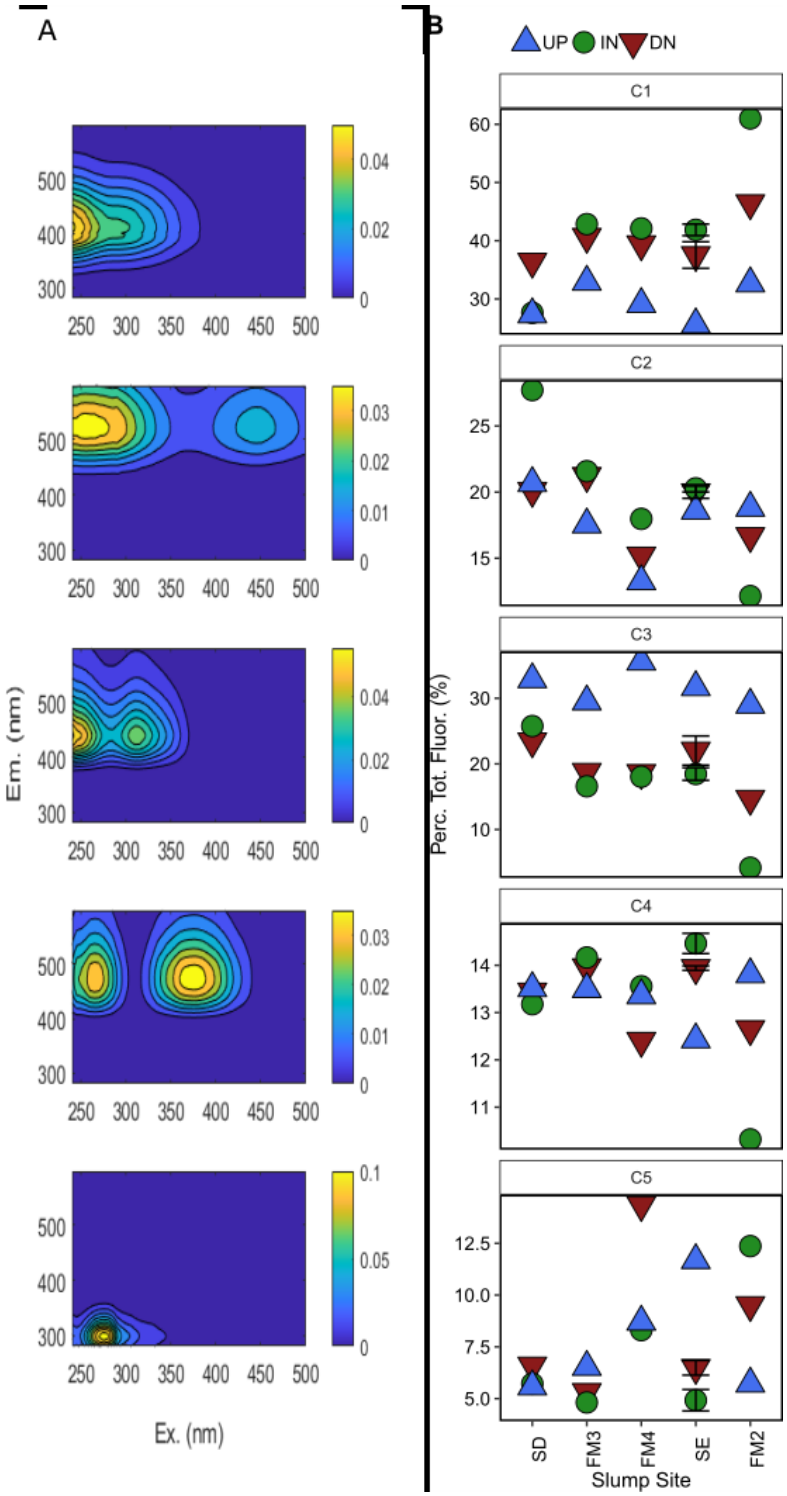

Figure A1-1. Contour plots and **(b)** Component distributions ($Fmax_{nj}/\sum_{nj}^{1j} Fmax$) upstream, within, and downstream of slump sites. Error bars show standard error of the mean for two samples within and downstream of *SE*.

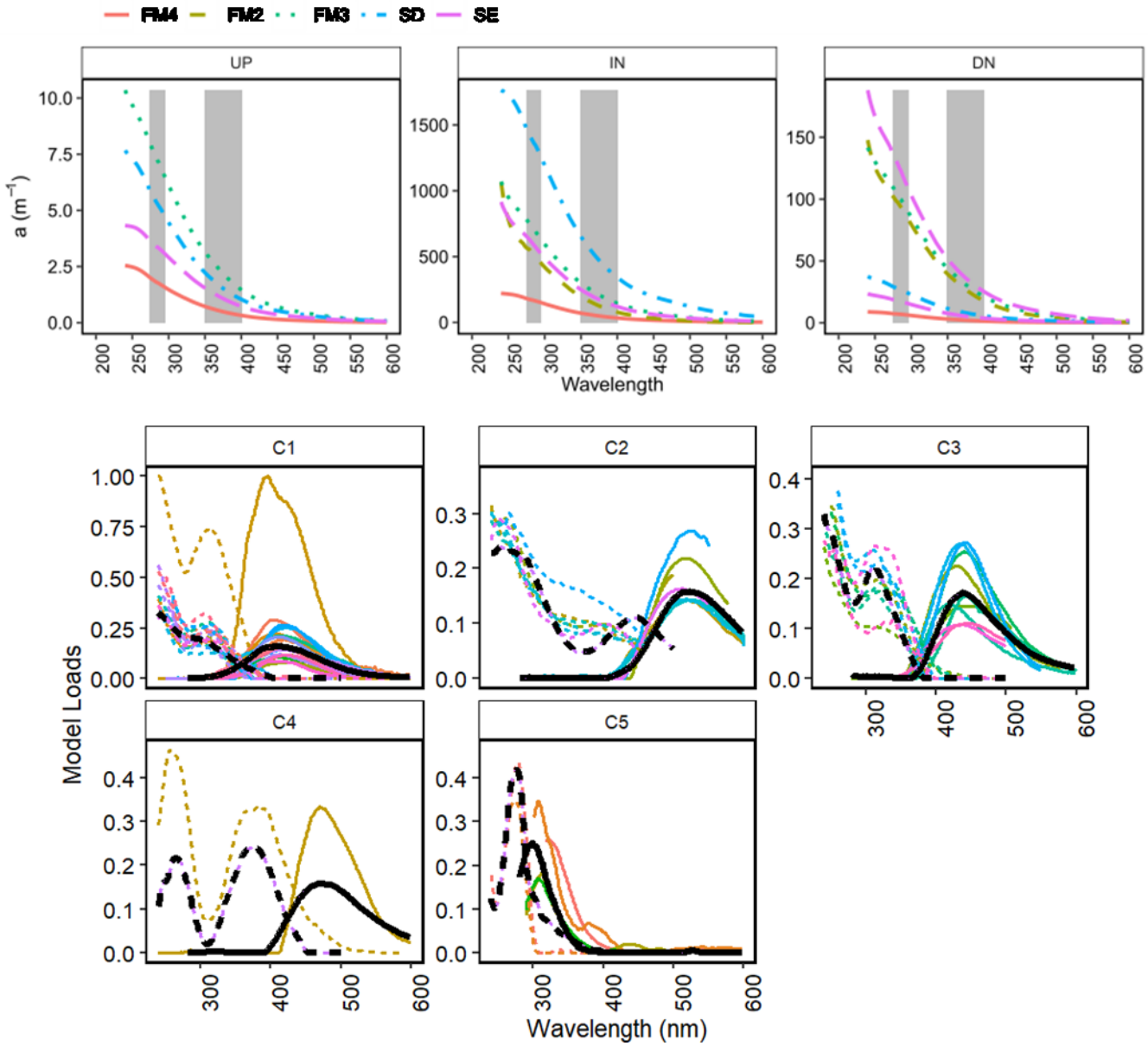

Figure A1-2. Top row: BEPOM absorbance spectra upstream, within, and downstream of slump sites. Shaded areas represent regions used to calculate S_R. Note, two samples collected early and late in the thaw season are shown for sampling downstream of *SE*. **C1 – C5**: Excitation (dashed lines) and emission (solid lines) spectral loadings of model components. Thick black lines are loadings from this study. All other lines are OpenFluor model components where TCC_{ExEm}>0.95. Matches where 0.95> TCC_{ExEm} >0.9 are shown for component 4 (1 match) and component 5 (all matches).

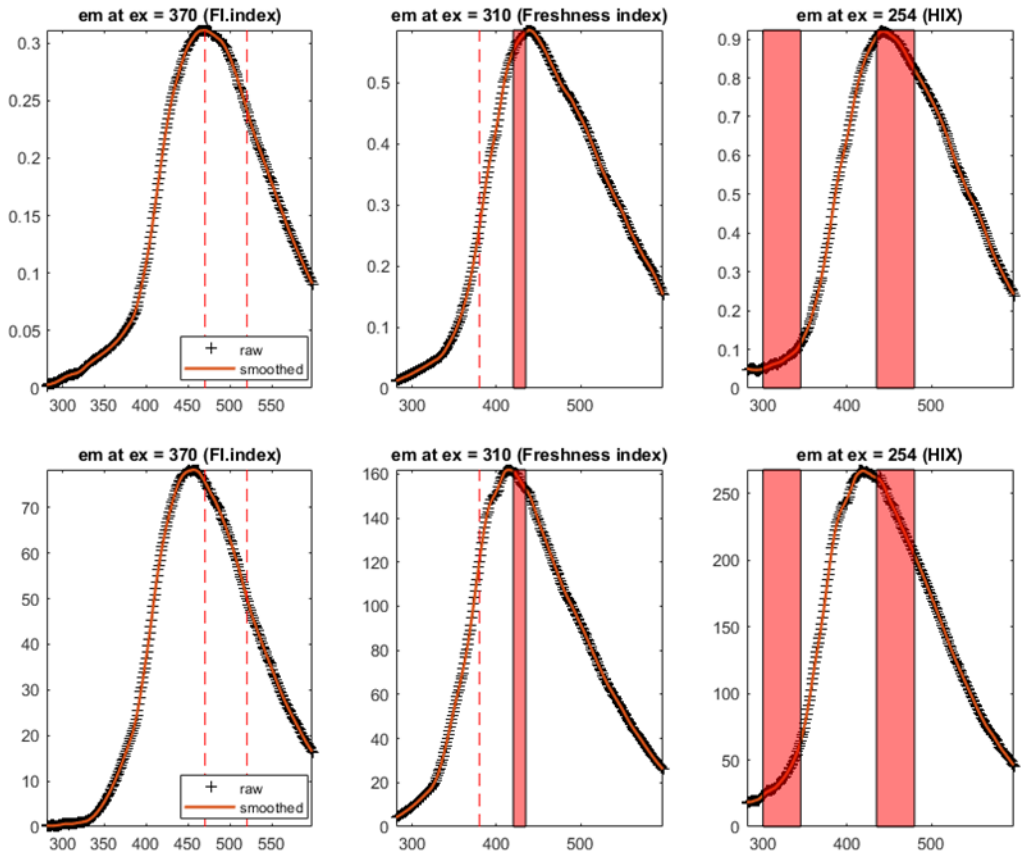

Figure A1-3. Emission points used for the calculation of fluorescence (FI), freshness, and humificaion (HIX) indices at excitations of 370, 310, and 254 nm, respectively. Spectra for FM2-UP (top) and FM2-IN (bottom) are shown.

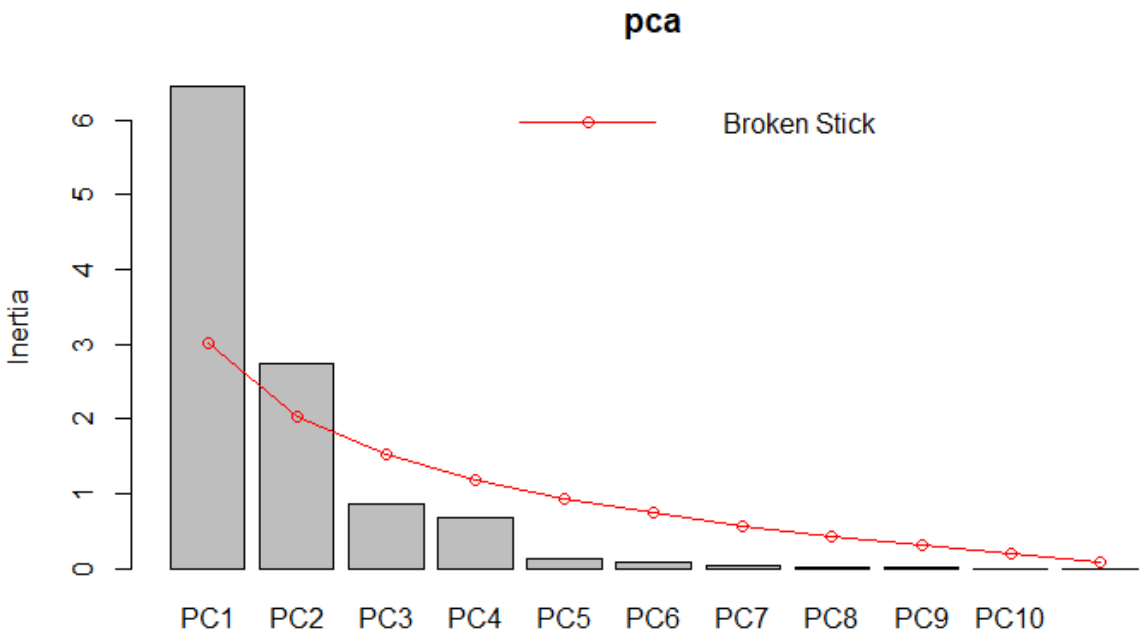

Figure A1-4. Inertia of broken stick model compared to principal components derived from principal component analysis of BEPOM variables.

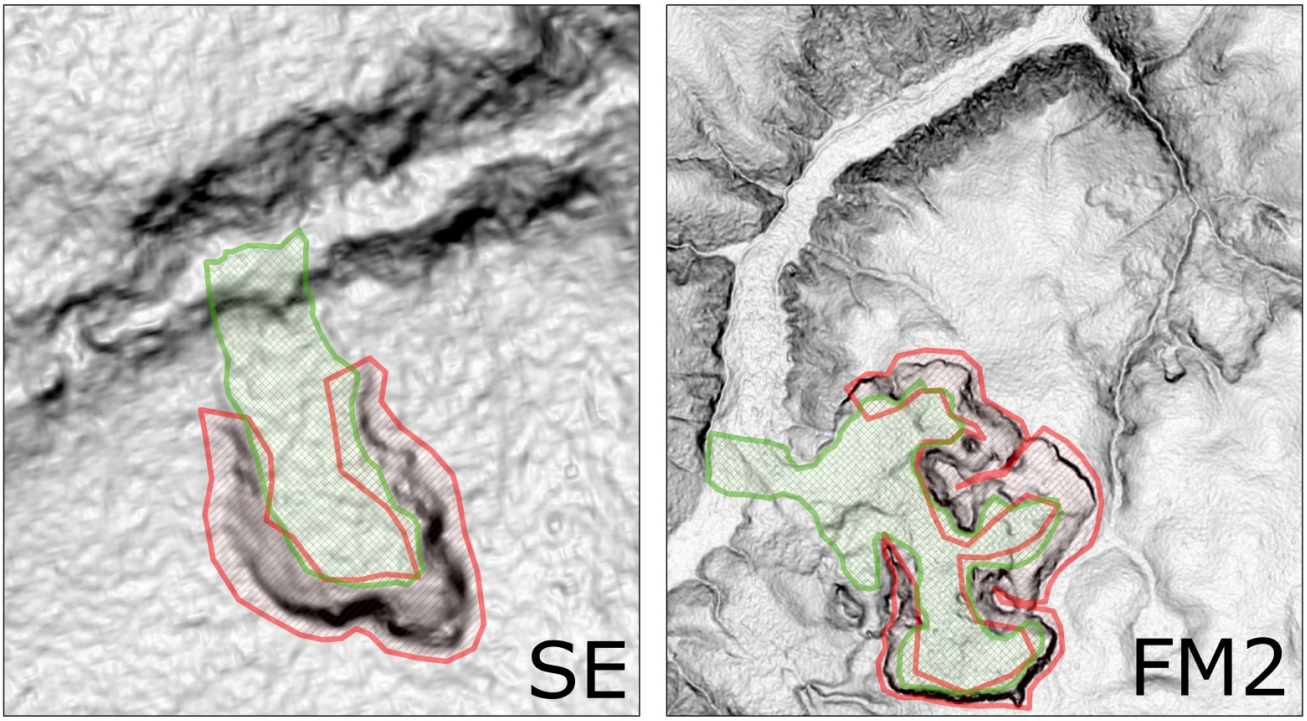

Figure A1-5. Slope rasters derived from Arctic DEM models for SE and SB. The red slashed area demarcates the area delineated around the headwall to extract maximum elevations. The green cross-hatched area demarcates the scar zone to valley bottom area used to extract the maximum slope.

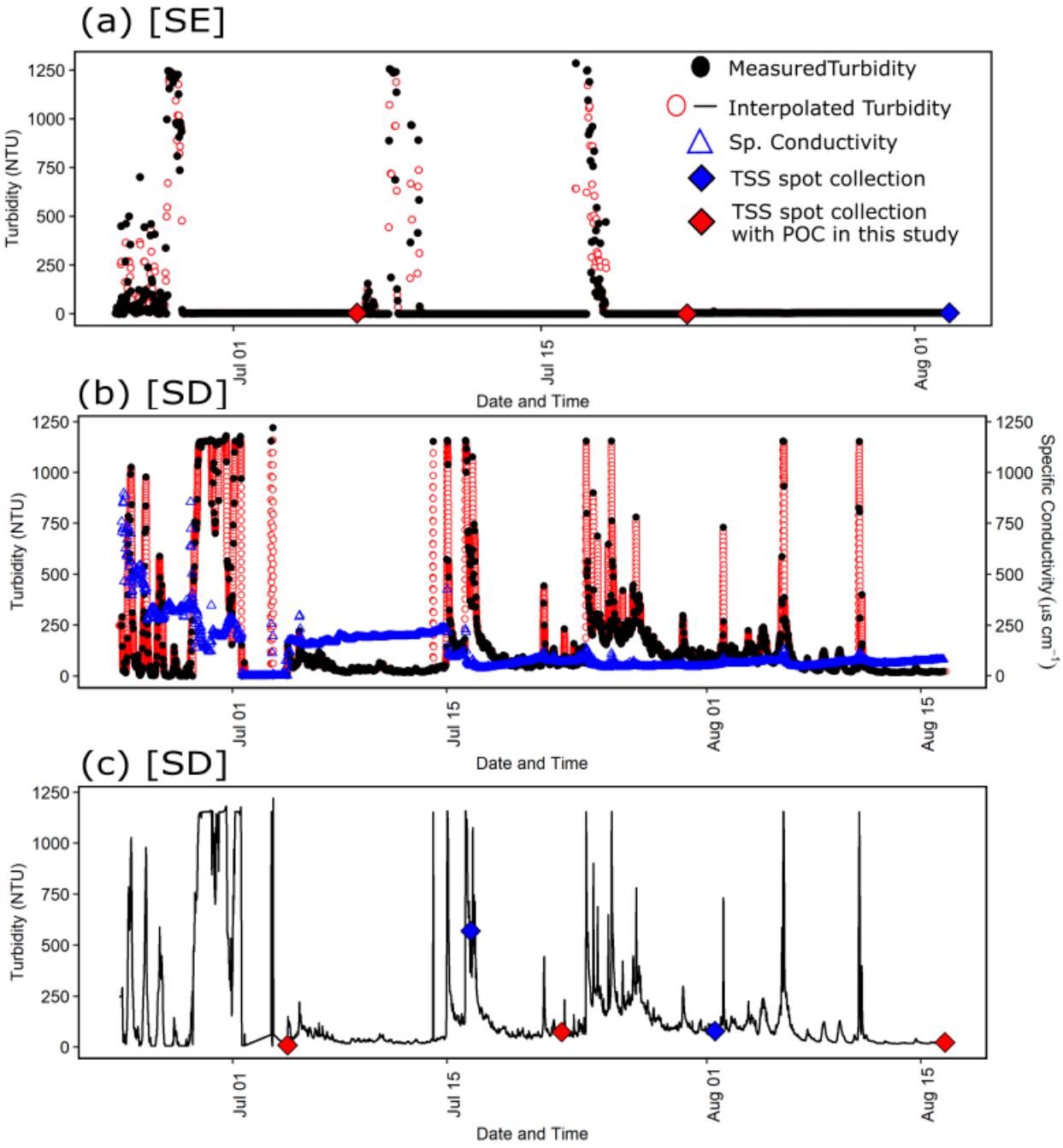

Figure A1-6. (a) Turbidity and TSS spot sample measurements (diamonds) downstream of slump SE. (b) Turbidity and conductivity measurements downstream of slump SD. (c) Turbidity interpolated to 2-minute resolution and TSS spot sample measurements (diamonds) downstream of SD. For a and b, black, filled dots show measured turbidity, red, open dots show measurements interpolated to 20 min. (SE – for matching spot TSS samples) and 2 min. resolution (SD). Open blue triangles in b show conductivity. Red diamonds in a and c show TSS samples matching POC samples in this study, and blue diamonds show additional TSS measurements without matching POC. The legend for all panels is as in panel (a).

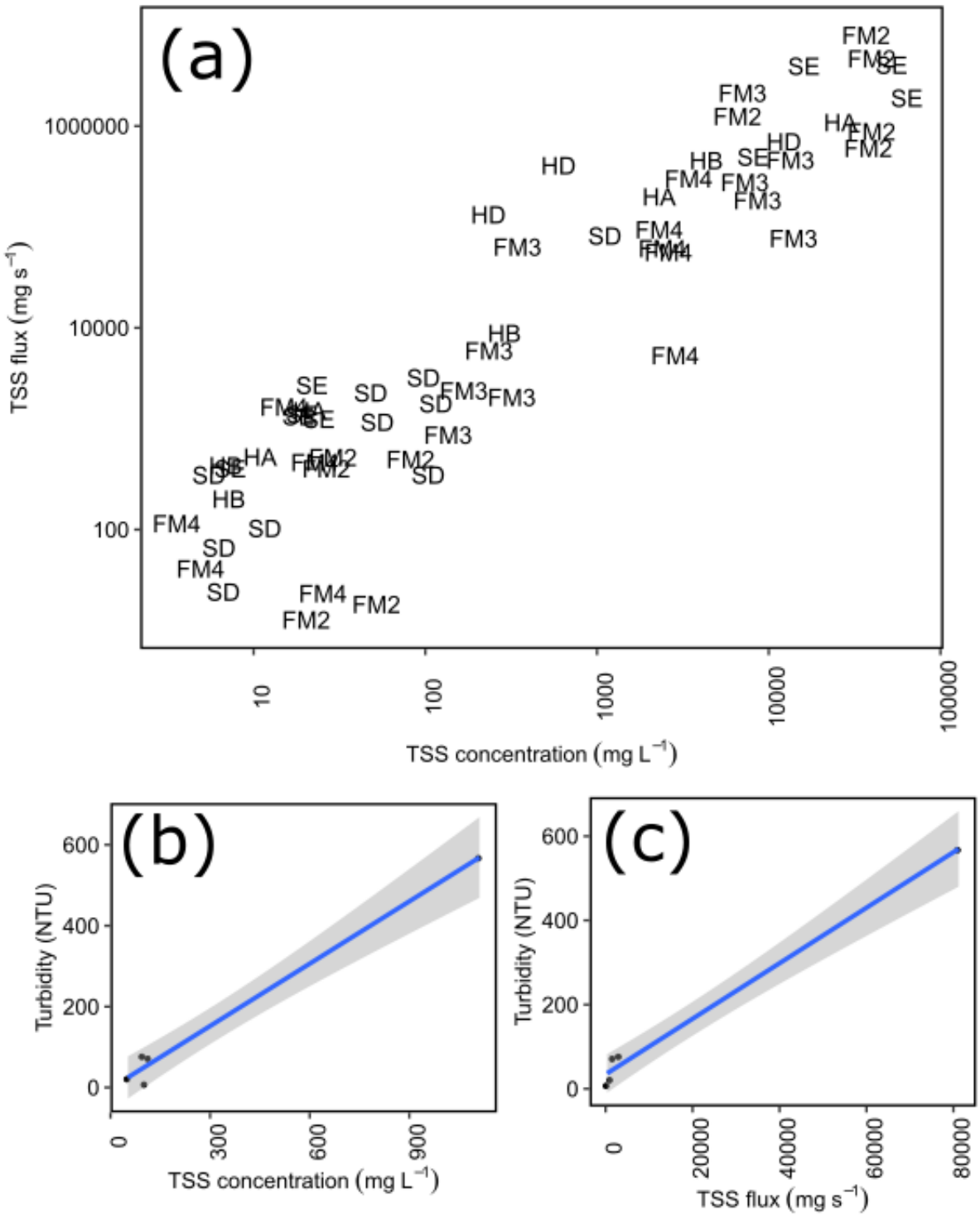

Figure A1-7. (a) Instantaneous TSS flux vs. TSS concentrations across slump sites. (b) Turbidity (from 2 min. interpolated data) vs. TSS concentration downstream of SD. (c) Turbidity (from 2 min. interpolated data) vs. instantaneous TSS flux downstream of SD.

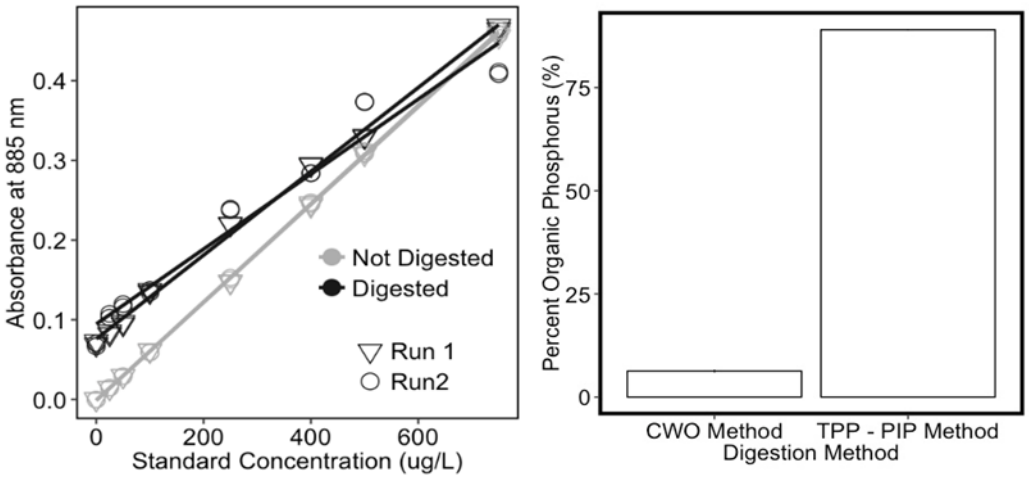

Figure A1-8. (a) Comparison of Standard Curves for digested and non-digested standards for POP analysis. (b) Comparison of percent POP determined from chemical wet oxidation (CWO) digestion method and from subtraction of PIP from TPP (TPP – PIP Method).

Appendix.2. Supporting information for Chapter 3

A2.1 Field Processing

Stream water upstream and downstream of slump sites were collected in 10L and 4L LDPE cubitainers respectively (pre-leached with deionized water for ~24hrs). Within-slump samples were collected in acid-leached 250 – 500 mL HDPE/polyethylene bottles. In 2016, additional samples were taken at downstream sites in acid-leached 500 mL HDPE cubitainers to add as unfiltered water. All containers were triple sample rinsed. All samples were processed within 24 hours of collection, apart from within-slump and downstream samples collected for unfiltered treatments in 2016 that were stored in the dark at 4ºC until the start of the experiment.

Cubitainers containing upstream water were thoroughly shaken and a portion was decanted into a clean 4L LDPE cubitainer and stored in the dark at 4ºC until the start of the experiment. The remaining portion was geo-pump filtered through Masterflex tubing and a 1 μm pore-size Geotech filter, then filtered through pre-combusted (450°C, 5h) glass fibre filters (Whatman, GF/F, 0.7 μm) into another clean 4L LDPE cubitainer.

A2.2 Detailed Experimental Set-up

Prior to the start of the experiment, all sample water was brought to room temperature (~20 – 25 ºC) to prevent changing oxygen concentrations and volumes over the course of bottle filling. Experiment bottles were first filled with filtered water by drawing the appropriate filtered water sample from the cubitainer through pre-vacuumed Tygon tubing. The outlet of this tubing was placed at the bottom of bottle to prevent air bubble formation. Due to the extremely low particulate concentrations in upstream samples, unfiltered upstream bottle treatments were also filled this way, with cubitainers gently shaken to maintain homogeneity of unfiltered water. For slump-affected treatments, unfiltered slump runoff and/or downstream water was pipetted into bottles filled with the respective filtered water. This tended to result in particulate concentrations being more dilute than *in situ* measurements. Particle suspension was maintained prior to pipetting either by inverting bottles several times prior to pipetting or using a magnetic stir bar. Pipette tips were cut to prevent clogging. Cutting tips did not affect the volume of water drawn up, which we tested by pipetting deionized water volumes with cut tips on a weigh scale. Bottles also contained pre-sterilized and pre-combusted glass beads (MP Biomedicals, Roll & Grow™ Plating Beads,

MP115000550) to ensure particle suspension. In 2015, the 120 mL serum bottles were sealed with Balch blue butyl stoppers. In 2016, glass BOD bottles were used so bottles were sealed with glass stoppers wetted around the rim to ensure an air-tight seal and capped with a plastic cap to prevent any evaporation. In 2019, 120 mL serum bottles were used again and capped with grey chlorobutyl isopropene stoppers (Niemann et al. 2015).

Experiment bottles were set up in replicates of 3 – 4, with bottles processed immediately and at the end of the experiment for changes in organic carbon concentrations. Bottles processed at the end of the experiment contained oxygen sensor spots (details below) to continuously monitor oxygen concentrations during the experiment. In 2015, we intended to process bottles after 7 and 28 days, following timepoints recommended for BDOC incubations (Vonk et al. 2015) and previously used for BDOC incubations in our study region (Littlefair et al. 2017). However, due to rapid oxygen consumption at some sites, experiment bottles intended for 28 days of incubations had to be removed at 11 days to prevent anoxic conditions in the bottles that would not be reflective of stream water column conditions. Thus, for 2015 experiments we present results after 7 days of incubation. For following experiments, we aimed to conduct incubations for long enough to see a detectable change in carbon measurements, based on the declines in oxygen concentrations, while preventing experiments from going below 2 mg L^{-1}. This resulted in an incubation duration of 8 days in 2016 and 27 days in 2019.

For the fractionation experiment, slump runoff collected in 2016 was stored in the dark at ~4°C until fractionation which was conducted the day after collection. Briefly, 0.5 mL was poured sequentially through a 2mm 3'' SS mesh sieve, a 63 µm sieve, and a 20 µm sieve and shaken with a cover and pan. Material the passed through the 20 µm sieve was passed through a 0.65-micron PES filter on a filter tower, with material passed through the filter discard and material collected on the filter rinsed into a beaker for use in the fractionation experiment. GF/F filtered water collected immediately downstream of slump SE was used to help rinse particles through the fractionation process and make each fraction back up to an appropriate volume to compare with the unfractionated treatment.

Bottles were suspended either by placing them on a PVC pipe (Figure S10) that was placed on rollers and rotated at 4 rpm (2015, 2016 bottles had to be placed sideways) or by placing them on a shaker table (2018 – 225 rpm, 2019 - ~70 rpm).

A2.3 Characterization of each size fraction

Material from each sieve size fraction was retained to determine particles size, ^{14}C age of associated organic matter, percent POC (i.e., POC: TSS), and absorbance and fluorescence spectra of base-extracted particulate organic matter (BEPOM). Size fractions with lower particles sizes had lower organic matter content (lower percent organic carbon) and associated organic matter had a greater ^{14}C age (Table **3-5**). Extraction of size fractions was done in triplicate, but one replicate of the size fraction > 63 µm had to be removed due to optical density concerns (see section 4). A biplot of PCA components 1 and 2 that explained 92% of the variation in optical indices of BEPOM revealed that extractions of organic matter in the clay and silt size fractions had a greater relative contribution of UVA humic-like peak C (Figure **3-6**), which has been characterized as terrigenous organic matter that has undergone less chemical reworking than peak A (Stubbins et al. 2014). While peak C was not negatively correlated with peak A, it was strongly correlated with total absorbance per unit of sediment extracted (Table A**2-6**). Altogether, this suggests that smaller size fractions had lower organic carbon content that was older and potentially more degraded.

A2.4 Laboratory Analyses

A2.4.1 Oxygen

Oxygen concentrations were measured within air-tight bottles with SP-PSt3-PSUP-YOP-D5 oxygen sensor spots (PreSens GmbH, Regensburg, Germany, Warkentin et al., 2007). These sensor spots were attached to the inner wall of glass bottles with silicone glue. Molecular oxygen quenches the luminescence of inert metal porphyrine complex immobilized in an oxygen-permeable matrix. The photoluminescence lifetime of the luminophore within the sensor spot was measured by a fiber-optic oxygen meter (Fibox 3; PreSens GmbH) placed at the center of the spot sensor outside of the glass bottle. Excitation light (505 nm) was supplied by a glass fiber, which also transported the emitted fluorescence signal (>600 nm) back to the oxygen meter. The method does not consume any oxygen. The average of ~5 fluorescence measurements was used to determine the oxygen concentration at a timepoint. The standard deviation of these replicate measurements was always less than 0.35 mg/L. There are three factors that can interfere with oxygen measurements: (1) temperature, (2) pressure, and (3) salinity. Temperature can affect the

fluorescence lifetime and the solubility of oxygen in water. Both effects are compensated for using simultaneous measurements from the temperature probe placed in an identical water experiencing the same environmental conditions as experimental bottles. Pressure does not affect the spot sensor's measurements of mg/L of oxygen in a closed container. For our 2019 experiment, we added 1 mL of 3.6 M $ZnCl_2$ solution to sterilize half of our bottles so we corrected all bottles for a potential "salting-out-effect" oxygen (Lang and Zander 1986) sterilized with $ZnCl_2$ in 2019 using a salinity value of 4.1 ‰.

A2.4.2 Organic Carbon

Filters for POC were oven dried at 60 °C for 24 hours, weighed, and fumigated under heat (60 °C) for 24 hours by placing 25 mL of 12M HCl into a desiccator in an oven to remove carbonates and dolomites (Whiteside et al. 2011). Following fumigation, samples were air dried in a second desiccator and were then re-oven dried at 60 °C for 24 hours (Whiteside et al. 2011). Dried filters were packed into silver capsules, with a second layer of tin capsules to promote combustion and shipped to the GG Hatch Laboratory (now Jan Veizer Stable Isotope Laboratory, University of Ottawa) for elemental analysis on an Elementar Isotope Cube. The amount of carbon was converted to bottle POC concentrations by dividing by bottle volumes determined gravimetrically. In some cases, the entire bottle could not be filtered, and filtered volumes were determined volumetrically via a graduated cylinder. DOC concentration was determined as non-purgeable organic carbon from 3 injections with a coefficient of variation <2%, or most similar 3 of 5 injections, on a Shimadzu TOC-V analyzer at the University of Alberta. Total organic carbon concentrations were determined as the sum of the two.

A2.4.3 Nitrogen, Sulfur, cations, and trace metals (2019 test)

Samples for dissolved inorganic nitrogen (DIN: ammonium, nitrate, nitrite), SO_4^-, and trace metals were filtered through pre-combusted GF/F filters on a filter tower and stored in triple sample rinsed 15 mL centrifuge tubes. DIN tubes were pre-leached with acid and stored frozen (-20 ºC) until analysis at the Canadian Association of Laboratory Accreditation (CALA)-certified Biogeochemical Analytical Service Laboratory (BASL; University of Alberta, Edmonton, AB, Canada). Out of each tube, concentrations of ammonium (NH_4^+), nitrate (NO_3^-), and nitrite (NO_2^-) were determined. SO_4 tubes were pre-leached with deionized water and stored in the dark at 4 ºC

until analysis at BASL. Trace metals (Na, K, Ca, Mg, Fe, Al, Sr, Se, Zn, Si, Ba, Mn, Ni, P, Ti, V, Rb, Li) tubes were pre-leached with acid and stored in the dark at 4 ºC. To prevent binding to the container, 4 drops of 18% trace-metal grade nitric acid was added to each tube. Samples were analyzed by inductively coupled plasma mass spectrometer (Perkin Elmer Elan 6000 Quadrupole ICP-MS) at the University of Alberta Canadian Centre for Isotope Microanalysis, following Cooper et al. (2008).

A2.4.4 XRD (2019 test)

A subset of experimental water was filtered through a pre-combusted and pre-weighed 25 mm GF/F filter from two bottles at the beginning of the experiment to determine the mineralogy of sediments and assess whether changes in mineralogy occurred due to sterilization procedures. Filters were dried at 50-60 ºC for 24 h and weighed to record sediment weights. Mineralogy was analyzed from sediments collected on a 25 mm glass fibre filter (Whatman, GF/F) at the University of Alberta by XRD (Rigaku Ultimate IV). The radiation source used was a Cobalt tube at 38 kV and 38 mA. Filters were mounted on a zero-background plate and scans were conducted using Bragg-Brentano parafocusing geometry, from 5 to 90° at 0.02° steps with a scan speed of 2.00 degrees per minute (0.6 s/step). Presence of minerals was determined using JADE 9.6 software with the 2019 ICDD Database PDF 4+, and 2018-1 ICSD databases. Detection limit of the analyses is typically between 1-5%. Organic matter was not removed prior to analysis, but organic matter content of samples was below 5%. XRD analysis did not reveal any changes in mineral presence due to sterilization procedures.

A2.4.5 Dissolved inorganic carbon (2019 test)

Dissolved inorganic carbon samples were obtained by filtering incubation water through a 0.45 µm PES syringe filter into pre-acid-leached (10% v/v HCl, 24 hours) and pre-combusted 12 mL glass vials. Vials were sealed airtight with butyl-lined screw caps and stored in the dark at 4°C. Samples were taken in quadruplicate. In two of the replicates, we added 0.05-0.1 mL of 3.6 M $ZnCl_2$ to assess whether there was any difference in storage. Samples were measured on an Apollo SciTech DIC analyzer. For all samples, the coefficient of variance between machine replicates was less than 0.1% and the standard deviation was less than 5 µM. For all samples without the addition of $ZnCl_2$, the coefficient of variances between tube replicates was less than 5%, and the standard

deviation was less than 24 μM. We found $ZnCl_2$ has significantly lower DIC concentrations in samples and noticed precipitation of salts at the bottom of several tubes, thus we do not report DIC concentrations from DIC tubes with $ZnCl_2$ added after collection from incubation bottles.

A2.4.6 Optical Analyses

Dissolved organic matter composition in experimental bottles for all experiments was characterized using absorbance measurements (see 4.1 for further details). In 2019, we additionally characterized DOM fluorescence and base-extractions of particulate organic matter (BEPOM, Osburn et al. 2012) in experimental bottles. For BEPOM, additional bottles at the beginning and end of the experiment were filtered through pre-combusted glass fibre filters (Whatman, GF/F), and filters were stored frozen until extraction in 10 mL of 0.1 N NaOH. Further extraction details are in section S2.1 of the supplementary of Shakil et al. (2020). BEPOM was also used to characterize the organic matter pools associated with different sieve size fractions used in the 2016 experiment.

A2.4.7 Absorbance measurements

In 2015 and 2016, absorbance was measured at 254 nm and 750 nm on a Genesys 10 UV spectrophotometer using a 1-cm quartz cuvette. In 2019, absorbance was measured at 240-800 nm at 1nm increments in a 1-cm quartz cuvette using an integration time of 0.1 seconds (Horiba Aqualog). Absorbance values were baseline corrected either using absorbance at 750 nm (2015-16) or the mean absorbance from 700 – 800 nm (2019). Absorbance values were then converted to both decadal and Napierian absorption coefficients for calculating absorbance indices (see 4.9).

A2.4.8 Fluorescence measurements

BEPOM samples, and 2019 DOM samples were also analysed for fluorescence (Horiba Aqualog at excitation wavelengths of 230 – 800 nm at 5nm increments, with an integration time of 2 seconds. Emission wavelengths spanned 117.27 – 826.70 for 2016, and 118.78 – 828.18 for 2019, both with an increment of 2.39, an integration time of 2 seconds and Medium CCD Gain. Samples were diluted when optical density was: (a) greater than 0.4 at 240 nm (Osburn et al. 2012) and/or the sum of absorbance at a pair of wavelengths was greater than 1.5 (Kothawala et al. 2013), and (b) if counts on the machine exceeded 50,000 outside the Rayleigh scatter lines (nearing the

maximum number of counts the machine can record). Excitation and emission spectra were corrected using drEEM version 0.6.3 (Murphy et al. (2013). Briefly, spectra were: (a) blank corrected, using 18.2 MΩ Milli-Q water for DOM samples and neutralized 0.1 M NaOH blanks for BEPOM samples; (b) inner filter effects were corrected using matching absorbance measurements also collected at 5 nm increments; (c) fluorescence data sets were normalized to Raman Units by dividing by the Raman area of pure water integrated of a λ_{em} range 383/384 to 420/425 nm at λ_{ex} 350 nm (RU_{350}) for BEPOM and DOM samples, respectively.

A2.4.9 Optical Indices

For all DOM samples, we calculate $SUVA_{254}$ by normalizing the decadal absorbance at 254 nm to DOC concentrations (mg L^{-1}, Weishaar et al. 2003). $SUVA_{254}$ values were corrected for Fe concentrations estimated to be within bottles (Poulin et al. 2014) either calculated from *in situ* Fe measurements or measurements made on a subset of bottles. Using absorbance spectra, we calculated spectral slope ratios (Helms et al. 2008) for 2019 DOM samples and all BEPOM samples. From fluorescence matrices we picked the maximum fluorescence of common peaks (Coble 2007) and normalized them to the maximum samples fluorescence to assess their relative contribution to the fluorescence landscape. We also calculated humification index for all samples, along with the biological index for DOM samples. Indices used are detailed in Table A**2-5**.

A2.4.10 Radiocarbon analyses

Size fraction material retained for characterization was stored frozen (-20°C) until it was freeze dried at the University of Alberta. A portion of each freeze-dried material was subsampled using a pre-combusted stainless-steel scoopula into a new 15 mL centrifuge tube (Corning®) for radiocarbon analysis. Material subsampled for radiocarbon analysis was spread on pre-combusted glass petri-dishes and examined under a dissecting microscope to remove any large debris or material (e.g., twigs, large rocks) that contrasted with the bulk background sediments. Subsamples of sediments were then pre-treated to remove carbonates using heated acid washes (HCl, 1M, 80ºC, 30 min; "A" treatment from Crann et al. 2017). Acid washes were repeated until effervescence stopped occurring in the samples; across all samples, two rounds of acid washes were sufficient. ^{14}C was then analyzed by Accelerator Mass Spectrometry following pellitization at the University of Ottawa (A.E. Lalonde AMS Laboratory).

A2.5 Sterile Experiment Details

In 2018, to test the rate of oxygen consumption on sterilized sediments, we placed 0.15 g of sterilized sediment each in 5 replicate 60 mL glass BOD bottle containing an oxygen sensor spot and glass beads to enable particle suspension, to achieve a concentration mimicking typical in-situ total suspended sediment concentrations. Bottles were filled 18.2 MΩ Milli-Q water (TOC <10ppb, sterilized in the Milli-Q system with UV-light). Bottles were sealed with a glass stopper with water placed around the rim to prevent gas exchange, along with a cap to hold the stopper in place. An additional set of 5 replicate bottles were prepared in parallel containing only Milli-Q water. All bottles and tools were sterilized with 95% ethanol which was evaporated in a fumehood. Sediment was obtained from a parallel study (Zolkos and Tank 2020) and sterilized using dry heat in an oven set at 200°C for 24h. This sterilization procedure was validated by mixing sterilized sediment with DI water and placing 1 mL of the slurry onto a nutrient-rich agar plate at 37°C for 7 days. No colonies were observed.

In 2019, sterilization of bottles was achieved by autoclaving filtered water collected downstream of site FM3, and unfiltered water collected within slump FM3 runoff using a 30-minute sterilization procedure at 18 psi and 121°C to kill the native bacterial population. To ensure no bacterial growth if any microorganisms were introduced as the experiment was set up, we added 1 mL of ~3.6M $ZnCl_2$ solution to ensure even minimal introduction of microbes during experiment set-up would not result in rapid growth of microbes due to the absence of the original microbial community. We recognize that this removes our ability to assess whether non-stream microorganisms were introduced into the unsterilized bottles during incubation set up. We assumed that the biotic effect of microbes introduced into unsterilized bottles during set-up would be minimal since all tools and surfaces were sterilized with 95% ethanol prior to incubation set-up and there is a microbial community present to compete with. To test sterilization, 1 mL of incubation water was pipetted onto a nutrient-rich "plate-count" agar plate, from both sterilized (see above) and unsterilized treatments. This water was removed from a bottle dedicated to BEPOM analyses where quantification of particles was not required. A sterilized glass spreader, 95% ethanol and a lighter, was then used to spread the drop around the plate evenly. The plates were then incubated under the same conditions as the incubation (20°C, in the dark). Colonies were observed to form on plates with water from unsterilized bottles, but none formed with water

from sterilized bottles (Figure A**2-9**). This test was done using bottles at the beginning and end of the experiment and still showed colony formation for unsterilized bottles but none for sterilized ones.

A2.6 Additional processes outside of heterotrophic respiration

Based on orders of magnitude increases in ammonium concentrations downstream of thaw slumps (Shakil et al. 2020) and prevalence of sulfide oxidation across the Peel Plateau (Zolkos et al. 2018) we believed that nitrification (eqs. S1) and sulfide oxidation (eq. S2) could have contributed to organic carbon gains observed in 2015 and 2016 experiments. Note that equation 4 is a general equation of chemolithoautotrophic reduced sulfur oxidation that can have a variable stoichiometry, and assumes sulfur oxidizing bacteria exclusively produce SO_4^{2-}, rather than both SO_4^{2-} and S^0 (Klatt and Polerecky 2015, Nelson et al. 1986). Equation S3 shows a net reaction for a model of pyrite oxidation at circumneutral-pH (Percak-Dennet et al. 2015). This sulfide oxidation can generate sulfuric acid that can weather carbonates (e.g., eq. S4) or silicates (Zolkos et al. 2020).

$NH_3 + 1.5O_2 \leftrightarrow NO_2^- + H^+ + H_2O$ (eq. S1a)

$NO_2^- + 0.5O_2 \leftrightarrow NO_3^-$ (eq. S1b)

$CO_2 + H_2S + O_2 + H_2O \leftrightarrow [CH_2O] + H_2SO_4$ (eq. S2)

$FeS_2 + 3.75O_2 + 3.5H_2O \leftrightarrow + 2H_2SO_4 + Fe(OH)_3$ (eq. S3)

$H_2SO_4 + 2(Ca,Mg)CO_3 \leftrightarrow 2(Ca^{2+},Mg^{2+}) + SO_4^{2-} + 2HCO_3^-$ (eq. S4)

A2.7 Data Analysis

The percent change of OC was used to measure differences in biodegradability:

$$\%\boldsymbol{\Delta OC} = \frac{(\boldsymbol{OC_{T_n}} - \boldsymbol{OC_{TOaverage}})}{\boldsymbol{OC_{TOaverage}}} \text{ (eq. S5)}$$

In eq. 1 above, $\boldsymbol{OC_{T_n}}$ is the DOC, POC, or TOC measured at an end time point, and $\boldsymbol{OC_{TOaverage}}$ is the mean OC measured at the beginning of the experiment. Since multiple outcomes were tested for ANOVAs, p-values of main tests were corrected for false discovery rate using padjust() from R package "emmeans" (Lenth 2021). For 2015, main tests were corrected for 19 tests since SU treatments was tested in 4 comparisons and 3-4 outcomes were tested per comparison. For 2016, main tests were corrected for 4-5 tests since 4-5 outcomes were tested per

ANOVA. Follow-up Tukey or GamesHowell adjusted pairwise t-tests were conducted only when an interaction or main test of interest was significant.

We used principal components analysis (PCA) to visualize differences between groups. Prior to our PCA we (a) used Pearson correlations to remove variables such that no variables within the PCA had a Pearson correlation greater than 0.9; (b) log-transformed all variables to prevent skew and (c) conducted a detrended correspondence analysis to ensure linearity of the dataset.

A2.8 Appendix 2 Tables

Table A2-1. Oxygen consumption rates and absolute changes in oxygen during experiments. Note, MQ indicates 18.2 MΩ water from the Milli-Q system (described above).

Year	Treatment	Site	# days	t-half[a]		k[a]		ΔO_2 (µM)		
				mean	se	mean	se	mean	se	n[b]
2015	Filtered upstream (F)	HA	7	49.1	5.1	0.014	0.00	-33	4	3
		HA	11	57.4	3.2	0.012	0.00	-33	1	3
		HB	7	74.8	8.9	0.01	0.00	-20	1	3
		HB	11	56.0	3.4	0.012	0.00	-34	1	3
		HD	7	35.3	4.5	0.02	0.00	-47	6	3
		HD	11	36.1	6.5	0.02	0.00	-55	8	3
	Unfiltered upstream (U)	HA	7	35.5	3.1	0.02	0.00	-39	3	3
		HA	11	38.0	1.3	0.018	0.00	-51	2	3
		HB	7	65.7	1.6	0.011	0.00	-24	2	3
		HB	11	62.1	5.7	0.011	0.00	-38	5	3
		HD	7	8.6	0.8	0.082	0.01	-135	11	3
		HD	11	7.7	0.2	0.09	0.00	-194	6	3
	Slump in filtered upstream (SU)	HA	7	6.5	0.5	0.108	0.01	-178	10	3
		HA	11	6.2	0.8	0.116	0.01	-239	20	3
		HB	7	10.1	1.7	0.073	0.02	-121	16	3
		HB	11	12.2	0.2	0.057	0.00	-139	3	3
		HD	7	11.2	0.9	0.062	0.01	-115	10	3
		HD	11	8.0	0.6	0.088	0.01	-214	18	3
	Slump in filtered downstream (SD)	HA	7	6.4	0.5	0.109	0.01	-171	12	3
		HA	11	6.8	-	0.103	-	-226	-	1
		HB	7	10.6	0.1	0.065	0.00	-110	4	3
		HB	11	7.9	1.2	0.09	0.01	-203	33	2
		HD	7	11.7	0.4	0.059	0.00	-104	5	3
		HD	11	10.0	0.1	0.069	0.00	-178	5	3
	SU settle (SS)	HA	7	14.5	0.4	0.048	0.00	-83	5	3
		HA	11	14.8	1.1	0.047	0.00	-117	6	3
		HB	7	21.0	0.5	0.033	0.00	-57	4	3
		HB	11	21.3	0.7	0.033	0.00	-90	4	3
		HD	7	17.3	0.4	0.04	0.00	-68	3	3
		HD	11	16.5	1.0	0.042	0.00	-116	11	3
2016	Unfractionated	SE	8	6.5	0.8	0.11	0.01	-211	7	3
	2 - 0.063 mm (SN)	SE	8	23.9	2.4	0.03	0.00	-98	6	4
	0.063 - 0.020 mm (SL)	SE	8	23.8	2.0	0.03	0.00	-102	6	4
	< 0.020 mm (SMSC)	SE	8	10.1	0.3	0.069	0.00	-168	3	4
	Upstream	SE	8	63.0	13.4	0.013	0.00	-64	6	4
	Upstream filtered control	SE	8	171.8	20.6	0.004	0.00	-44	3	4

	Downstream	SE	8	13.8	2.7	0.057	0.01	-148	16	4
	Downstream filtered control	SE	8	61.6	5.1	0.012	0.00	-65	5	4
	2.79k Downstream		8	30.4	4.0	0.024	0.00	-93	4	4
	2.79k Downstream filtered control		8	109.7	32.9	0.008	0.00	-50	4	4
	MQ control		8	96.6	30.6	0.008	0.00	-44	5	2
2018	Sterile HD debris sediments	HD	7	-	-	-	-	-226	2	5
	MQ control		7	-	-	-	-	-18	4	5
2019	Stream	SC	27	36.4	1.5	0.02	0.00	-124	7	12
	Sterile control	SC	27	100.3	35.4	0.005	0.00	-15	3	12
	MQ control	NA	27	-657.9	2400.6	0	0.00	-8	5	6

[a]If k and t-half are not shown, exponential model was not an appropriate fit for data

Table A2-2. Comparison of 2015 TSS concentrations (mg L^{-1}) in experiment bottles at T0 vs. in situ.

Year	Site	Location	In situ		Experiment	sd	n	Exp:InSitu
2015	HA	Up	10.90		3.40	0.5	3	0.31
		DN[a]	2298		2100	1240	9	0.91
	HB	UP	6.87		0.62	0.5	3	0.09
		DN[a]	4330		1400	55.8	8	0.32
	HD	UP	97.1		100	0.8	3	1.03
		DN[a]	12300		1090	23.4	9	0.09
2016	SE	UP	112		104	17.3	4	0.93
		DN	46300	unfractionated[b]	52600	2290	4	1.14
				0.63 - 2 mm[b]	340	70.4	4	
				0.22 - 0.63 mm[b]	880	21.0	4	
				<0.22 mm[b]	30900	3740	4	
				sum of fractionated bottles	32120	3741		
				transect[c]	1190	51.6	4	0.03
		DN - 3km	20400		617	5.0	4	0.03
2018	HD	Debris Tongue			2500			
2019	SC	DN	4152		675	74.6	24	0.16

[a]SU, SS, and SD treatments were mimicking downstream conditions.
[b]used within-slump particles and downstream filtrate (fractionation experiment)
[c]used donwstream particles and filtrate (for transect experiment)
note: low Exp:InSitu ratios for upstream locations with low TSS values may be detection limit issues of TSS
In Situ TSS measurements at many upstream sites required filtering of upwards of 1-2 L of water. Experimental bottle volumes were 60-120 mL.

Table A2-3. Presence of minerals, as detected by XRD analysis, of sediments in bottles at the beginning of the experiment.

	Treatment	Stream		Sterile	
	Rep	A	B	A	B
Calcite	$Ca(CO_3)$	Y	Y	Y	Y
Pyrite	FeS_2	Y	Y	Y	Y
Gypsum	$CaSO_4 \cdot 2H_2O$	N	N	N	N
Quartz	SiO_2	Y	Y	Y	Y
Muscovite	$KAl_2(Si,Al)_4O_{10}(OH_2)$	Y	Y	Y	Y
Albite	$NaAlSi_3O_8$	Y	Y	Y	Y
Clinochlore	$(Mg,Fe,Al)_6(Si,Al)_4O_{10}(OH)_8$	Y	Y	Y	Y
Kaolonite	$Al_2Si_2O_5(OH)_4$	Y	Y	Y	N
Microcline	$K(AlSi_3O_8)$	Y	Y	Y	Y

Table A2-4. Estimated initial ammonium concentrations associated with experiments where gains in organic carbon were significantly greater than zero.

Year	Treatment	Site	# days	n	ΔTOC (μM)	ΔTOC CI error	Oxygen consumed (μM)	CI error	Estimated initial NH_4^+ (μM)
2015	Filtered (F)	HB	11	3	130	67	34	4	0.53
	Unfiltered Upstream (U)	HD	11	3	150	28	194	24	3.3
	Slump in filtered upstream (SU)	HA	7	3	269	250	178	43	1.4
		HB	11	3	335	296	140	14	0.65
	Slump in filtered downstream (SD)	HA	7	3	337	285	171	50	7.9
		HA[a]	11	1	418	-	226	-	7.9
	SU settled (SS)	HB	7	3	164	164	57	16	0.65
2016 - Fractionation	<0.020 mm	SE	8	4	601	459	168	8	not collected
2016 - Transect	Upstream	SE	8	4	75	60	64	20	not collected
	Upstream filtered control	SE	8	4	37	36	44	9	
	~3k Downstream		8	4	60	50	93	13	not collected

Milli-Q water control	8	3	83	71	44	59	0.0

[a] only 1 sample because other bottle replicates went before 2 mg L^{-1}

Table A2-5. Description of optical indices used.

	Index or Component	Calculation	Reference	Description / Purpose
Abs-based	S_R	$S_{275-295}$ / $S_{350-400}$	Helms et al. (2008)	Shown to be negatively correlated to DOM molecular weight and to generally decrease on irradiation
	$a_{Tot.\ 250-450}$ (m^{-1}, TSS standardized)	Total absorbance between wavelengths 250 - 450, divided by suspended sediment concentration. Note, absorbance units for base-extracted material were normalized for volume filtered.	Modified from Helms et al. (2008)	Greater values indicate greater extractable chromophoric material per unit of particulate material in the water column which may, like %POC, indicate earlier stages in diagenesis of sediments.
Fluor. Based	Humification Index (HIX)*	$\sum I_{em\ 435-480}$ / ($\sum I_{em\ 300-345}$ + $\sum I_{em\ 435-480}$) at ex. 254	Ohno et al. (2002)	Ranges from 0 to 1, with increasing values associated with a "red-shift" or shift to longer wavelengths, potentially due to lower molecular ratios of hydrogen to carbon. May indicate relative abundance of compounds generated through polycondensation reactions. This could indicate material further in the progression in organic matter decay and greater relative abundance of compounds more resistant to breakdown (refractory).
	Biological Index (BIX)*	$I_{em\ 380}$ / $I_{em\ 430}$ at ex. 310	Huguet et al. (2009)	Modified from the original freshness index (see Freshness Index) to account for broadening of 'humic' region by presence of α peak. In this study, freshness index and biological index are perfectly correlated.
	Common Coble peaks normalized to maximum Fluorescence			
	B	Ex: 275, Em: 305	Coble et al. 2007	tyrosine-like, protein-like

T	Ex: 275, Em: 340	Coble et al. 2007	tryptophan-like, protein-like
A	Ex: 260, Em: 400-460	Coble et al. 2007	UVC-humic-like
C	Ex: 320-360, Em: 420-460	Coble et al. 2007	UVA humic-like
M	Ex: 290-310, Em: 370-410	Coble et al. 2007	UVA humic-like
Components based on previous PARAFAC analyses normalized to maximum Fluorescence			
C1		Shakil et al. 2020	degraded terrestrial-like; similar to Coble peak A
C3		Shakil et al. 2020	fresher terrestrial-like (relative to C1), similar to Coble peak C
C5		Shakil et al. 2020	protein-like

Table A2-6. Final list of optical indices input to the PCA analysis, and their relationship to indices that were removed due to strong correlation. See Table A**2-5** for abbreviations.

Group	Optical Indices	Other Indices with Pearson correlation >0.9
2016 Experiment Size Fractions	S_R	Peaks B, M
	HIX	none
	Peak A	none
	Peak C	$a_{Tot.\ 250450}$
2019 Experimental DOM samples	$SUVA_{254}$	HIX, A
	S_R	none
	Peak C	Peak A
	Peak M	Peak T
	BIX	Peaks B, T
2019 Experimental BEPOM Samples	S_R	none
	HIX	Peak C, Component C3
	Peak M	none
	C1	Peaks A, B, T, Component C5
	C2	Peaks A, B, C5

A2.9 Appendix 2 Figures

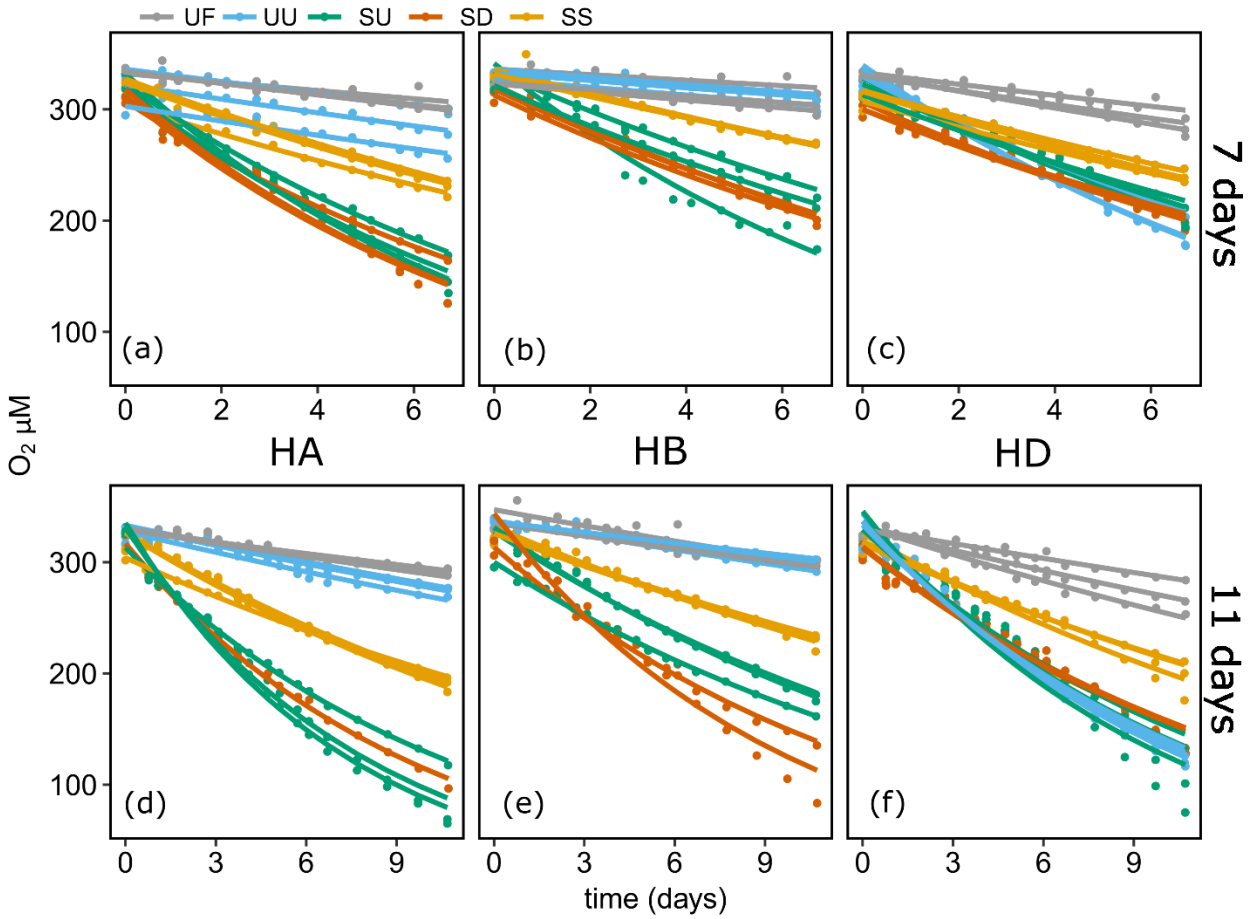

Figure A2-1. 2015 experiment oxygen concentrations (µM) for bottles incubated for 7 days (a-c) and 11 days (d-f). Dots show measured concentrations and lines show modelled measurements based on first order exponential decay. HA, HB, and HD differentiate slump sites. Codes: filtered (UF) and unfiltered (UU) upstream, slump material in upstream (SU) and downstream (SD) filtrate, and SU settled out (SS).

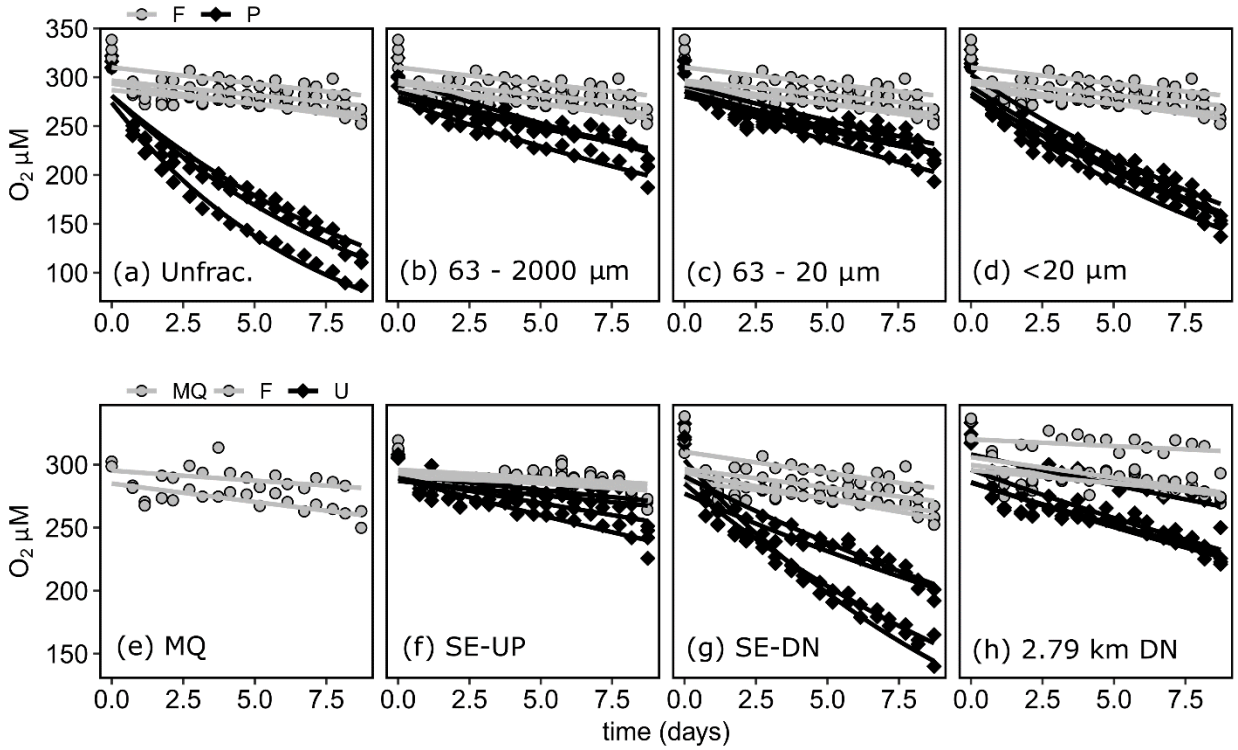

Figure A2-2. 2016 experiment oxygen concentrations for fractionation experiment (a-d) and transect validation experiment (e-h). Codes in a-d differentiate filtered controls (F) and particle containing bottles (P) and codes for e-h differentiate Milli-Q control (MQ) filtered controls (F) and unfiltered treatments (U). Note that F in a-d and g are from the same samples, but repeatedly shown for easy comparison. Dots show measured concentrations and lines show modelled concentrations based on first order exponential decay.

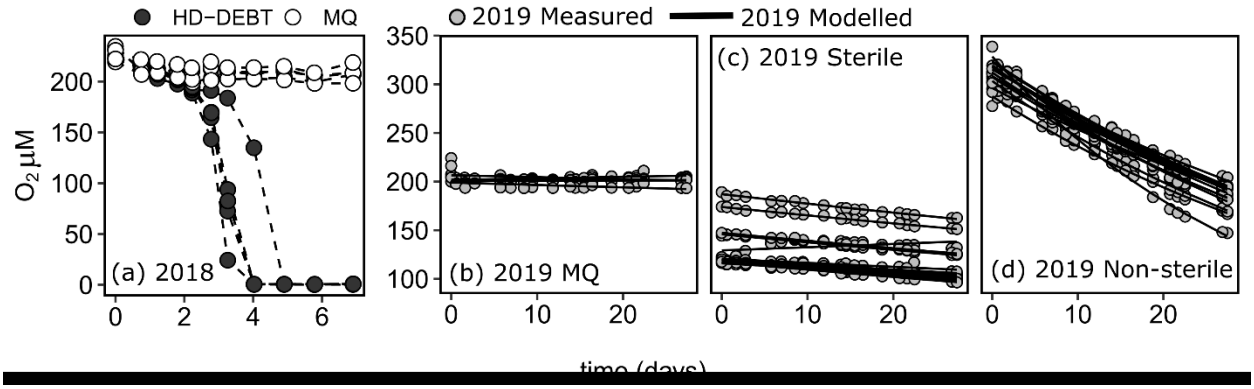

Figure A2-3. 2018 (a) and 2019 (b-d) oxygen concentrations (µM). Dots show measured concentrations. Dashed lines in (a) are just used to connect repeat measurements from the same bottle while solid lines in b-d show modelled measurements based on first order exponential decay. HB-DEBT = HD debris sediments, MQ=Milli-Q water.

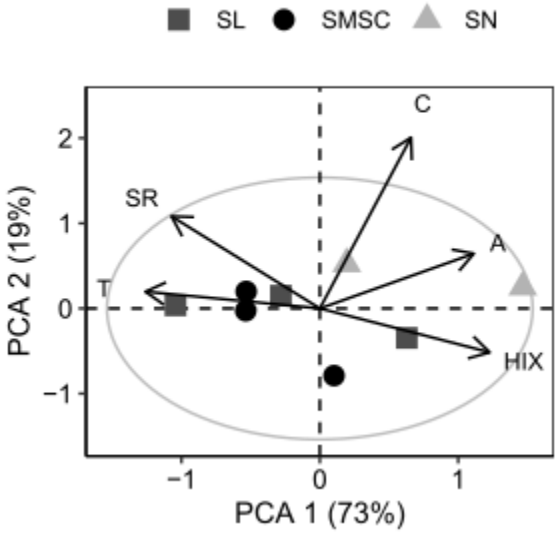

Figure A2-4. Principal components analysis of optical indices for BEPOM of different size fractions. PCA is shown in scaling 1. The grey circle marks the circle of equilibrium contribution. Constituent abbreviations are as in Table A**2-6**.

Figure A2-5. Damming of upstream flow by HD debris and possible encroachment of slump material into the upstream site.

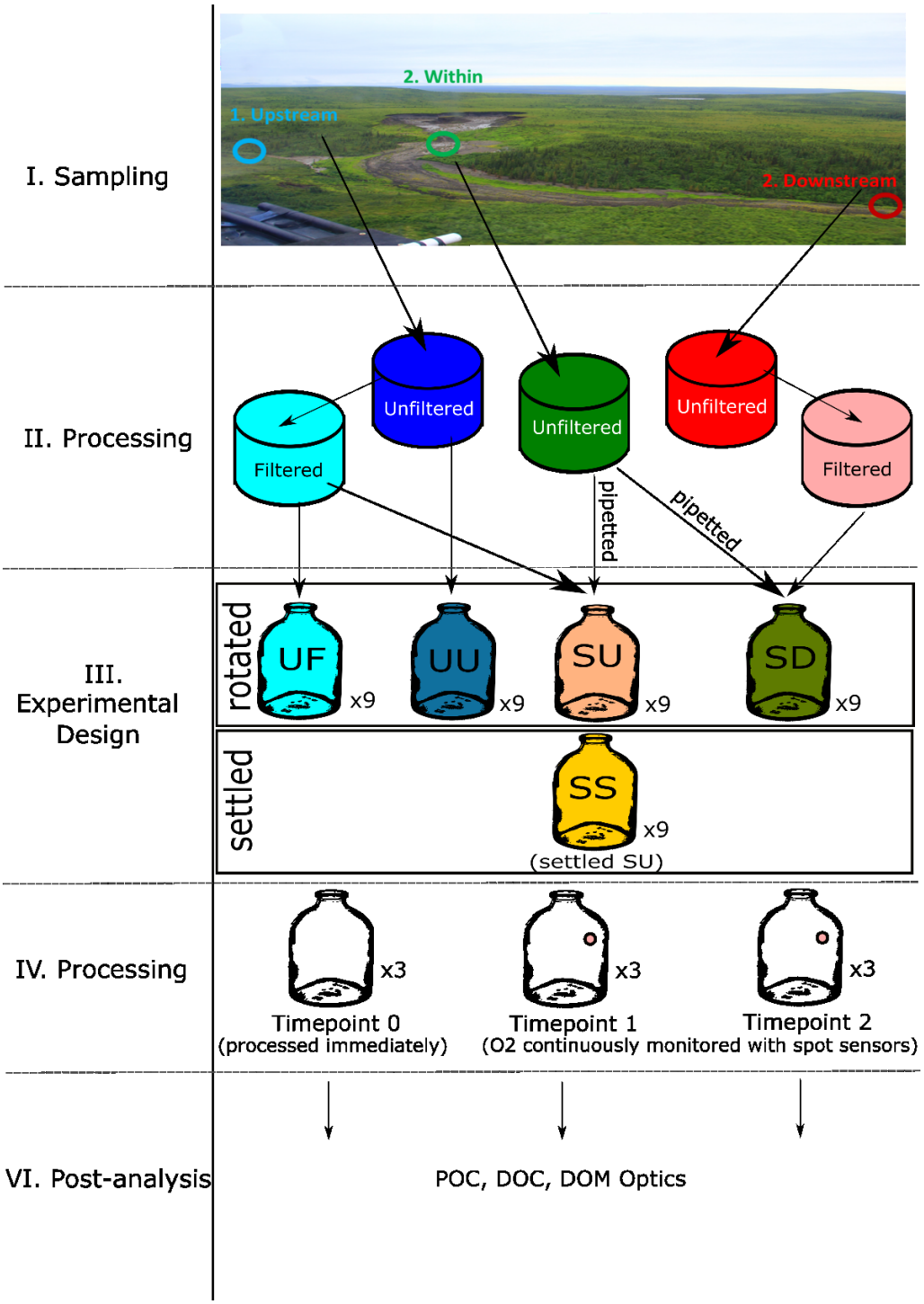

Figure A2-6. Flow chart for processing of 2015 experiment. Note, timepoint 2 did not last for much longer than timepoint 1 due to rapid oxygen loss. Due to this, and the fact that some bottle replicates had to be removed because of anoxia, data is not presented. Analyses show particulate (POC) and dissolved (DOC) organic carbon and dissolved organic matter (DOM) optics ($SUVA_{254}$).

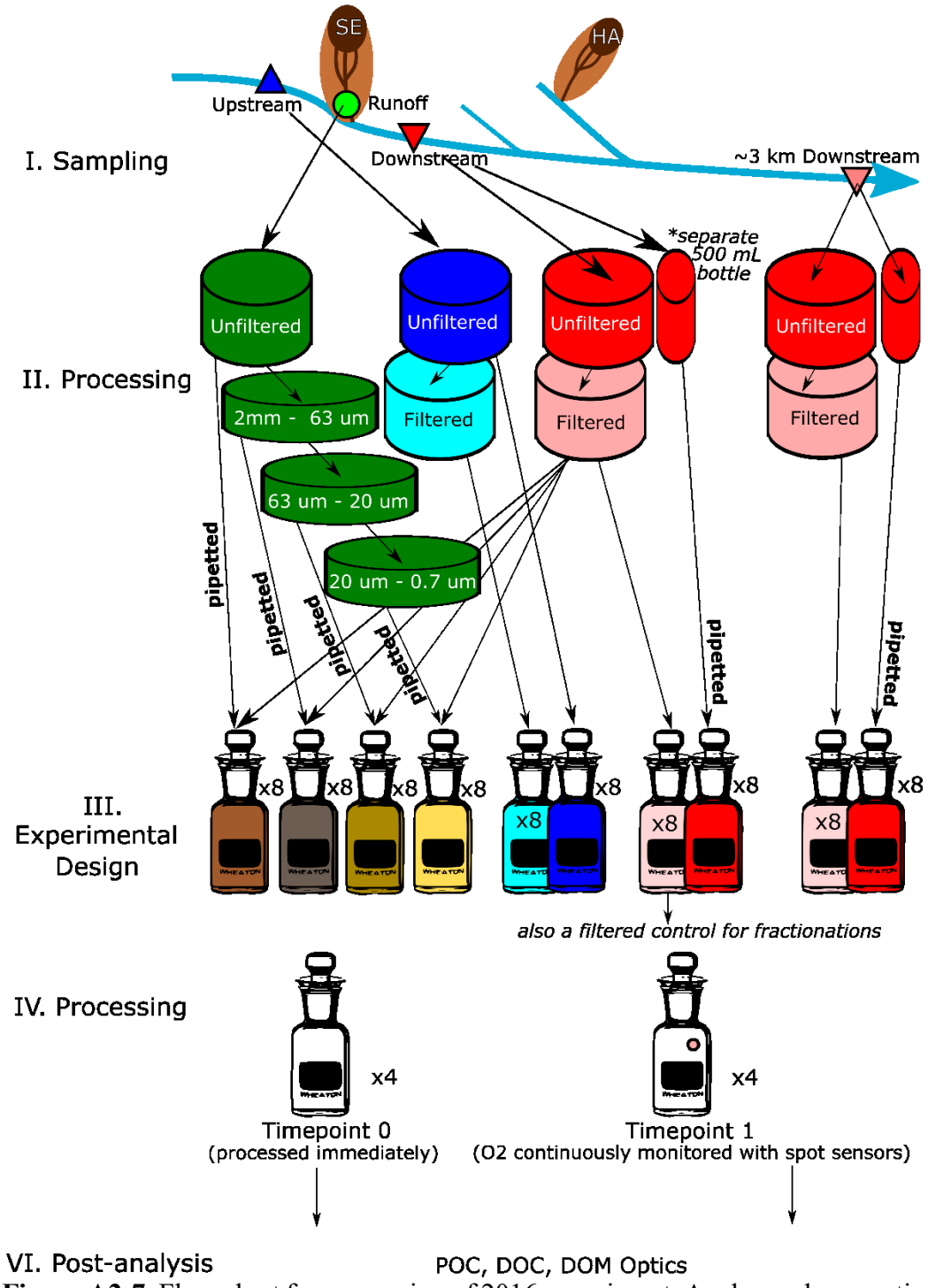

Figure A2-7. Flow chart for processing of 2016 experiment. Analyses show particulate (POC) and dissolved (DOC) organic carbon and dissolved organic matter (DOM) optics ($SUVA_{254}$).

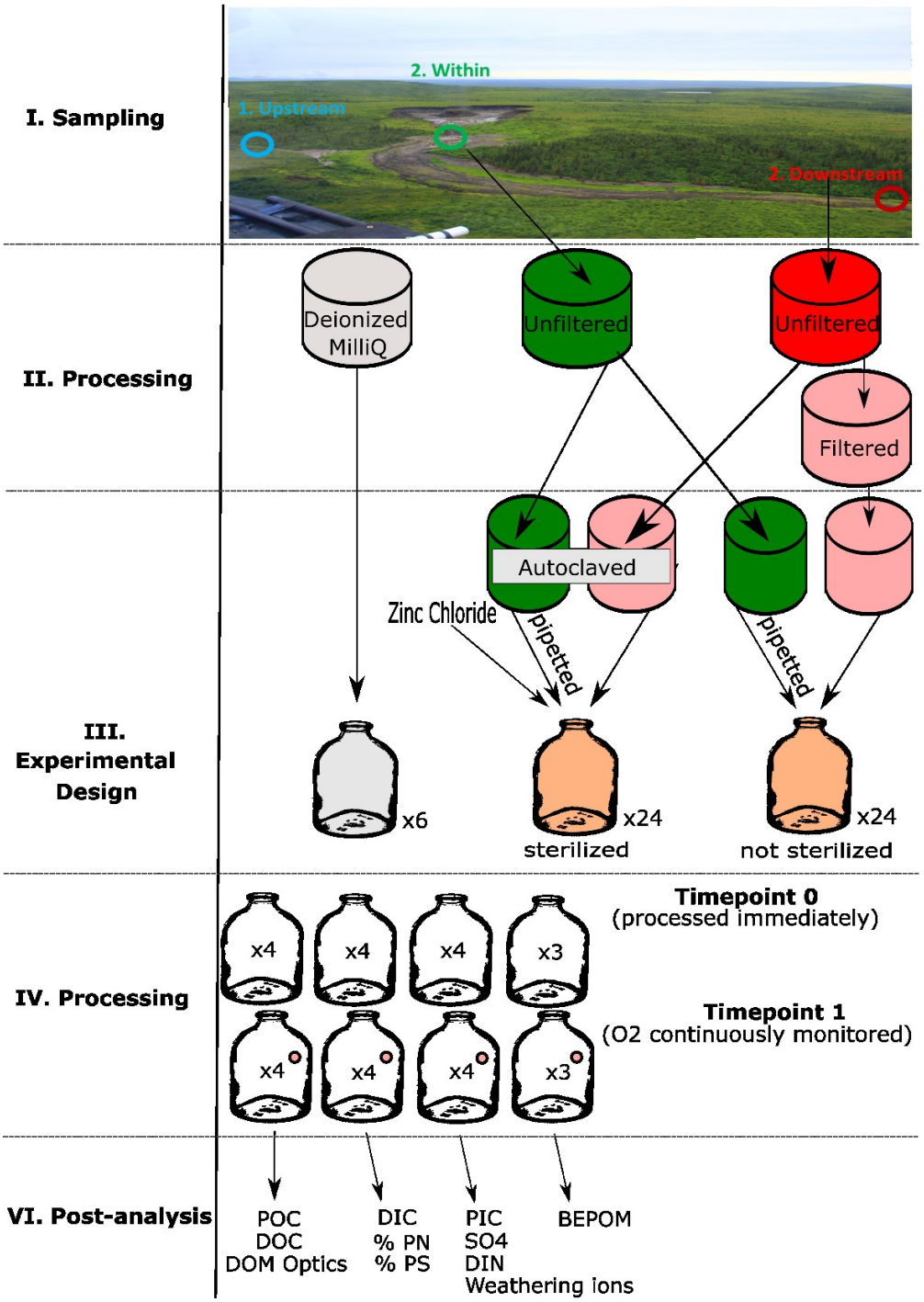

Figure A2-8. Flow chart for processing of 2019 experiment. Note, that only 2 bottle replicates were used to assess changes in BEPOM for sterilized treatments. Analyses show particulate (POC) and dissolved (DOC) organic carbon, dissolved organic matter (DOM) optics (absorbance and fluorescence), dissolved (DIC) and particulate (PIC) inorganic carbon, % particulate nitrogen (PN) and sulfur (PS), dissolved inorganic nitrogen (DIN), SO_4^{2-}, weathering ions, and base-extracted particulate organic matter (BEPOM).

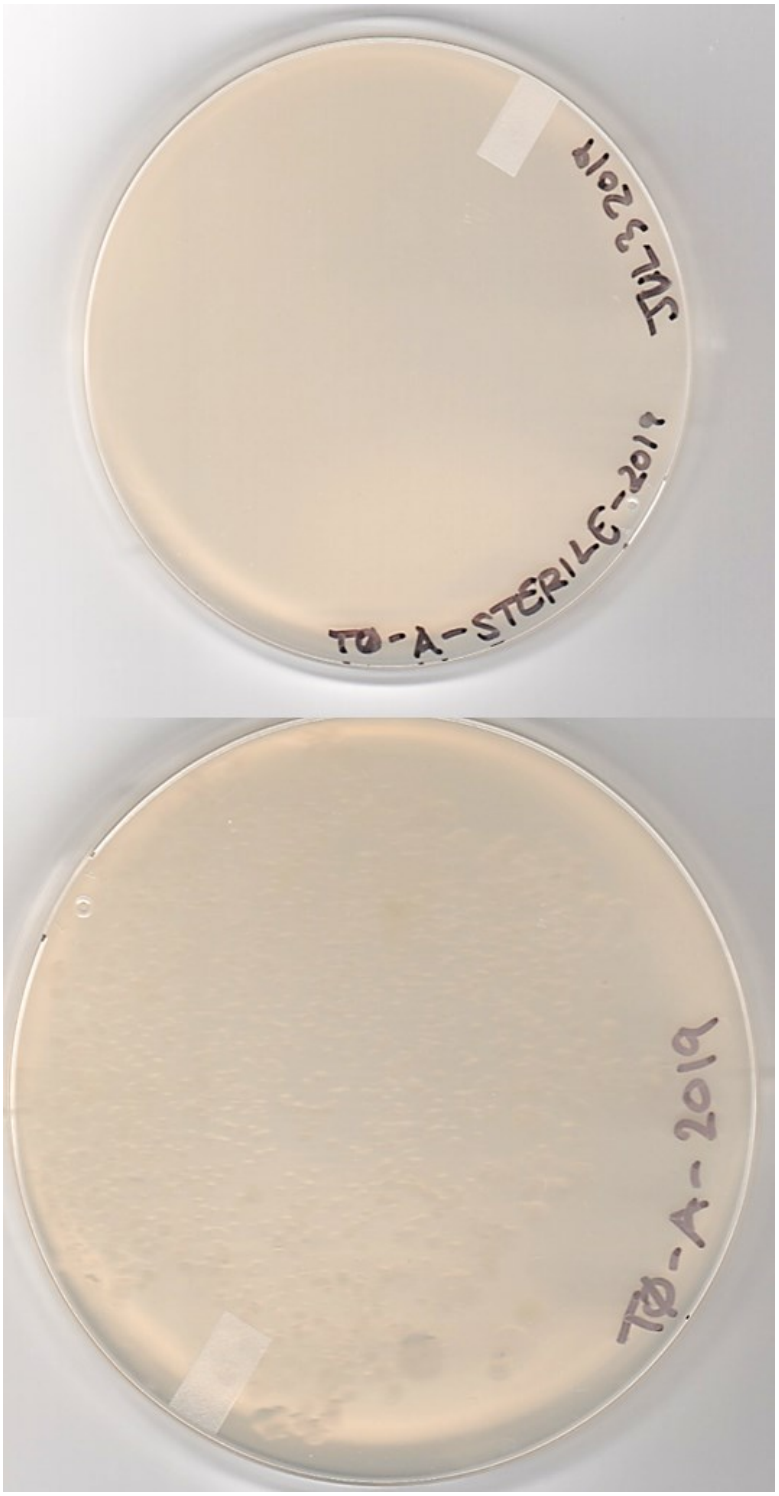

Figure A2-9. Microbial count of sterilized (top) and unsterilized (bottom) bottles from the 2019 experiments. Note on bottom, light coloured bumps represent microbial colonies.

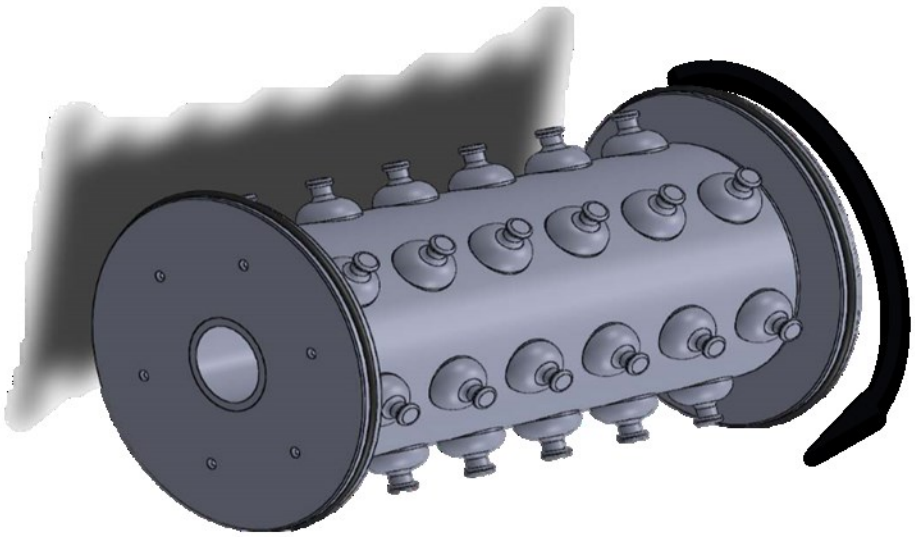

Figure A2-10. Schematic diagram of rotator used for particle suspension in 2015.

Appendix.3. Supporting information for Chapter 4

Table A3-1. Study design. YSI measurements included conductivity (µS cm^{-1}), dissolved oxygen (%saturation and mg L^{-1}, excluding 2015), and temperature (°C).

Goal	Year	Site	Sampling Dates	Field Measurements	Analyses/Chemical Data
(1)	2015	SD Transect (UP - 400m DN)	JUL-04, JUL-22, AUG-16	Discharge (Q) at select points, YSI	POC, %POC, $\delta^{13}C_{POC}$
		SE Transect (UP - 1000m DN)	JUL-06, JUL-21, AUG-21		
	2017	Stony Creek Transect	JUL	Q, YSI	POC, DOC, Q, BEPOM, $F^{14}C_{POC}$, $F^{14}C_{DOC}$, Chlα
(2)	2017	Subcatchments (n=34)	JUL - AUG	Q, channel slope (S), Wolman pebble count, YSI	POC, DOC, Q, BEPOM, DOM, $\delta^{18}O_{H2O}$, streambank %SOC, $\delta^{13}C_{SOC}$, Chlα
(3)	~1960s - 2019	Peel River Station 10MC0001	Any data available Jan. – Dec.	Not Applicable	DOC, POC, TSS, Q

Table A3-2. Additional details of Stony Creek transect sampling.

Site #	Sampling Day	Strahler Order	Transect distance (km)	Watershed Area (km^2)	Area RTS_{active} (km)	Cumulative $\#RTS_{active}$
1	22-Jul	4	0	61	0	0
2	27-Jul	4	3	108	0	0
3	27-Jul	4	10	143	28	7
4	25-Jul	5	17	236	60	15
5	25-Jul	6	32	479	195	52
6	25-Jul	6	37	595	228	60
7	25-Jul	6	46	666	242	65
8	25-Jul	6	57	917	378	94
9	25-Jul	6	69	998	378	94
10	10-Jul	6	71	1029	378	94
11	07-Aug	6	72	1030	378	94

Table A3-3. Geospatial data used.

Category	Parameters	Base datasets	Datasource	Spatial Resolution (scale)	Calculation Method
Terrain	mean watershed slope, mean watershed elevation, mean terrain roughness	CDEM	Canadian Digital Elevation Model	30m	Slope (planar) and Zonal Statistics Tools, ArcGIS Pro 2.8.0; Roughness Tool from Geomorphic Gradients Metrics Toolbox (Evans et al. 2014)
Geology: Landscape position	Distance from maximum westward extent of Laurentide Ice Sheet	Duk-Rodkin and Hughes (1992) Surficial Geology Map	Duk-Rodkin and Hughes (1992)	~125m (1:250,000)	Orthorectified Duk-Rodkin Imagery in ArcGIS Desktop, Delineated glacial limits in area of interest, and calculated distance of sampling points from delineated lines using "Near" (Analysis Tool) in ArcGIS Pro 2.8.0
Geology: Bedrock	%shale	Norris (1985) Bedrock Geology Map	Norris (1985)	~250m (1:500,000)	Orthorectified Norris Imagery in ArcGIS Desktop, Delineated Features and Intersected with delineated watersheds in ArcGIS Pro 2.8.0
Geology: Surficial	%Piedmont, %Alluvial, %Bedrock, %Fluvial, %Glaciogenic, %Moraine, %Organic	Duk-Rodkin and Hughes (1992) Surficial Geology map	Côté et al. (2013)	~125m (1:250,000)	Intersected with delineated watersheds in ArcGIS Pro 2.8.0
Geology: Soil organic carbon content (1m)	Soil organic carbon content (1m)	Canadian portion is based off digital soil map by	Hugelius et al. (2013)	~500m (1 : 1 000 000)	Intersected with delineated watersheds in ArcGIS Pro 2.8.0

		Tarnocai and Lacelle (1996)			
Landcover	%forest, %grassland, %lichen/moss, %shrubland, %water, %urban/built-up, %wetland		Latifovic (2019)	30m	Intersected with delineated watersheds in ArcGIS Pro 2.8.0
Landcover: Lake coverage	%lake	NHN Network modified to Sentinel-2 satellite imagery from 2017	National Hydro Network Dataset, Sentinel-2 2017 imagery	~25m (1:50,000)	Manually adjusted NHN lakes dataset using Sentinel-2 imagery, Intersected updated lakes and ponds with delineated watershed, ArcGIS Pro 2.8.0
Landcover: Productivity	Gross Primary Productivity, Net Primary Productvity	MODIS/Terra	(1) GPP: Running et al. (2015), (2) NPP: Running et al. (2019)	500m	Google Earth Engine
Retrogressive thaw slumping	%slump area, cumulative slump count	Sentinel-2 (2016, 2017) 10m	Kokoszka and Kokelj (2021)	~1m (1:2000)	Intersection of digitized slumping area with watershed area. Cumulative count details are outlined in Zolkos et al. (2020)